CERN-ACC-Note-2019-XXX
Geneva, November 25, 2019

The Large Hadron-Electron Collider at the HL-LHC

From resolving the partonic structure of matter to Higgs and BSM physics

LHeC Collaboration

Submitted to J.Phys. G

Abstract

This is our abstract.

Foreword [Herwig Schopper]

This is the 2019 CDR of the LHeC. Thumbs up!

Preface

This is the 2019 CDR of the LHeC.

Contents

Space for ‘back of the envelope’ calculations.

Chapter 1

Executive Summary [Oliver Bruening, Max Klein]

Put your text here! this goes up to Q^2.

Chapter 2

Introduction [Max Klein]

An example citation [1]

Chapter 3

The Large Hadron Collider at High Luminosity [Oliver Bruening]

Example reference: LHeC [1]

3.1 The Accelerator - Parameters and Timeline [Oliver Bruening]

3.2 Physics Expectations [Monica D'Onofrio]

Chapter 4

Main Characteristics of the LHeC [Oliver Bruening, Max Klein]

4.1 Kinematics and Reconstruction of Final States [Max Klein]

4.1.1 Nominal Beam Energies

4.1.2 Reduced Electron or Proton Beam Energy

4.2 A Summary of the LHeC Configuration and Parameters [Max Klein]

4.2.1 Introduction

The Conceptual Design Report (CDR) of the LHeC was published in 2012 [1]. The CDR default configuration uses a 60 GeV energy electron beam derived from a racetrack, three-turn, intense energy recovery linac (ERL) achieving a cms energy of $\sqrt{s} = 1.3\,\text{TeV}$, where $s = 4E_pE_e$ is determined by the electron and proton beam energies, E_e and E_p. In 2012, the Higgs boson, H, was discovered which has become a central topic of current and future high energy physics. The Higgs production cross section in charged current (CC) deep inelastic scattering (DIS) at the LHeC is roughly 100 fb. The Large Hadron Collider has so far not led to the discovery of any exotic phenomenon. This forces searches to be pursued, in pp but as well in ep, with highest achievable precision in order to access a maximum range of phase space and possibly rare channels. The DIS cross section at large x roughly behaves like $(1-x)^3/Q^4$ demanding very high luminosities for exploiting the unknown regions of Bjorken x near to 1 and very high Q^2, the negative four-momentum transfer squared between the electron and the proton. For the current update of the design of the LHeC this has set a luminosity goal in excess of the $10^{33}\,\text{cm}^{-2}\text{s}^{-1}$ as had been adopted for the CDR. There arises the potential, as will be detailed in Sect.**??**, to transform the LHC into a high precision electroweak, Higgs and top quark physics facility.

The ep Higgs production cross section rises approximately with E_e. New physics may be related to the heaviest known elementary particle, the top quark, the ep production cross section of which rises stronger than linear with E_e in the LHeC kinematic range which is not very far from the $t\bar{t}$ threshold. Searches for heavy neutrinos, SUSY particles etc. are the more promising the higher the energy is. Access in DIS to very low Bjorken x requires high energies because of $x = Q^2/s$, for inelasticity $y = 1$. In DIS, one needs $Q^2 > M_p^2 \simeq 1\,\text{GeV}^2$. Physics therefore requires a maximally large energy. However, cost and effort set realistic limits such that twice the HERA electron beam energy, of about 27 GeV, appeared as a reasonable and affordable target value.

In the CDR the default electron energy was chosen to be 60 GeV. This can be achieved with an ERL

circumference of 1/3 of that of the LHC [1]. Recently the cost was estimated. This has defined a new default configuration of $E_e = 50\,\text{GeV}$ and a circumference of 5.4 km which is 1/5 of the LHC length. The decision on E_e is not taken now. This paper comprises studies with different energy configurations, mainly $E_e = 50$ and 60 GeV, which are close in their cms energy values of 1.2 and 1.3 TeV, respectively.

Given the non-linear dependence of the cost on E_e, for energies larger than about 60 GeV, significantly larger electron beam energy values may only be justified by overriding arguments, such as, for example, the existence of leptoquarks [1]. Higher values of $\sqrt{s}$ are also provided with enlarged proton beam energies by the High Energy LHC ($E_p = 13.5\,\text{TeV}$) and the FCC-pp with E_p between 20 and possibly 150 TeV, depending on the dipole magnet technology.

4.2.2 Cost Estimate, Default Configuration and Staging

In 2018 a detailed cost estimate has been performed [2] following the guidance and practice of CERN accelerator studies. The assumptions were also compared with the DESY XFEL cost. The result was that for the 60 GeV configuration about half of the total cost was due to the two SC linacs. The cost of the arcs decreases stronger than linear with decreasing energy, about $\propto E^4$ for synchrotron radiation losses and $\propto E^3$ when emittance dilution is required to be preserved [3]. It was therefore considered to set a new default of 50 GeV with a circumference of 1/5 of that of the LHC, see Sect. **??**, compared to 1/3 for 60 GeV. Furthermore, an initial phase at 30 GeV was considered, within the 1/5 configuration but with less equipped linacs. The HERA electron beam energy was 27 GeV. The main results, taken from [2] are reproduced in Tab. 4.1.

Item Mode	60 GeV CDR	30 GeV stage 1	50 GeV default
SRF System	805	402	670
SRF R+D and Prototyping	31	31	31
Injector	40	40	40
Arc Magnets and Vacuum	215	103	103
SC IR Magnets	105	105	105
Source and Dump System	5	5	5
Cryogenic Infrastructure	100	41	69
General Infrastructure and Installation	69	58	58
Civil Engineering	386	289	289
Total Cost	1756	1075	1371

Table 4.1: Summary of cost estimates, in MSF, from [2]. The 60 GeV configuration is built with a 9 km triple racetrack configuration as was considered in the CDR [1]. It is taken as the default configuration for FCC-eh, with an additional CE cost of 40 MSF due to the larger depth on point L (FCC) as compared to IP2 (LHC). Both the 30 and the 50 GeV assume a 5.4 km configuration, i.e. the 30 GeV is assumed to be a first stage of LHeC upgradeable to 50 GeV ERL. Whenever a choice was to be made on estimates, in [2] the conservative number was chosen.

The choice of a default of 50 GeV at 1/5 of the LHC circumference results, as displayed, in a total cost of 1.075 MSF for the initial 30 GeV configuration and an additional, upgrade cost to 50 GeV of 296 MSF. If one restricted the LHeC to a non-upgradeable 30 GeV only configuration one would, still in a triple racetrack configuration, come to roughly a 1 km long structure with two linacs of about 500 m length, probably in a

[1] If these existed with a mass of say $M = 1.5\,\text{TeV}$ this would require, at the LHC with $E_p = 7\,\text{TeV}$, to choose E_e to be larger than 90 GeV, and to pay for it. Leptoquarks would be produced by ep fusion and appear as resonances, much like the Z boson in e^+e^- and would therefore fix E_e (given certain E_p which at the FCC exceeds 7 TeV). The genuine DIS kinematics, however, is spacelike, the exchanged four-momentum squared $q^2 = -Q^2$ being negative, which implies that the choice of the energies is less constrained than in an e^+e^- collider aiming at the study of the Z or H bosons.

single linac tunnel configuration. The cost of this version of the LHeC is roughly 800 MSF, i.e. about half the 60 GeV estimated cost. However, this would essentially reduce the LHeC to a QCD and electroweak machine, still very powerful but accepting substantial losses in its Higgs, top and BSM programme.

Choices on the final energy will be made later. They not only depend on a budget but also on the future development of particle physics at larg. For example, it may turn out that the community for a foreseeable future may not find the O(10) GSF required to build any of the e^+e^- colliders currently considered. Then the only way to improve on the Higgs measurements beyond HL-LHC substantially is the high energy (50-60 GeV), high luminosity ($\int L = 1\,\mathrm{ab}^{-1}$) LHeC. Obviously, physics and cost are intimately related. Based on such considerations, but also taking into account technical constraints as resulting from the amount of synchrotron radiation losses in the interaction region and the arcs, we have chosen 50 GeV in a 1/5 of U(LHC) configuration as the new default. This economises about 400 MSF as compared to the CDR configuration.

If the LHeC ERL was built, it may later be transferred, with some reconfiguration and upgrades, to the FCC to serve as the FCC-eh. The FCC-eh has its own location, L, for the ERL which requires a new accelerator tunnel. It has been decided to keep the 60 GeV configuration for the FCC, as described in the recently published CDR of the FCC [4]. The LHeC ERL configuration may be used later as a top-up injector for the Z and possibly WW phase of the FCC-ee, should the FCC-ee indeed preceed the FCC-hh/eh phase.

4.2.3 Configuration Parameters

A possible transition from the 60 GeV to the 50 GeV configuration of the LHeC has been envisaged already in 2018, as considered in the paper submitted to the European strategy [5]. The machine layout shown in that paper is reproduced in Fig. 4.1. It is a rough sketch illustrating the reduction from a 60 GeV to a 50 GeV configuration, which results not only in a reduction of capital costs, as discussed above, but also of efforts.

The ERL configuration has been recently revisited [3] considering its dependence on the electron beam energy. Applying a dimension scaling which preserves the emittance dilution, the results have been obtained as are summarised in Tab. 4.2. The 1/5 configuration is chosen as the new LHeC default while the CDR

item circumference [U(LHC)]	1/3	1/4	1/5	1/6
Energy [GeV]	61.1	54.2	49.1	45.2
Linac length [m] x 2	1025	909	829	758
Arc radius [m] x 2 π	1058	737	536	427
Spreader and Recombiner length [m] x 4	76	76	76	76
Circumference [m]	9000	6750	5332	4500

Table 4.2: Scaling of the electron beam energy, linac and further accelerator element dimensions with the choice of the total circumference in units $1/n$ of the LHC circumference. For comparison, the CERN SPS has a circumference of 1/4 of that of the LHC.

on the LHeC from 2012 and the recent CDR on FCC-eh have used the 1/3 configuration. The energy and configuration may be decided as physics, cost and effort dictate when a decision is taken eventually.

4.2.4 Luminosity

The luminosity L for the LHeC in its linac-ring configuration is determined as

$$L = \frac{N_e N_p f \gamma_p}{4\pi\epsilon_p \beta^*} \cdot \prod_{i=1}^{3} H_i,$$

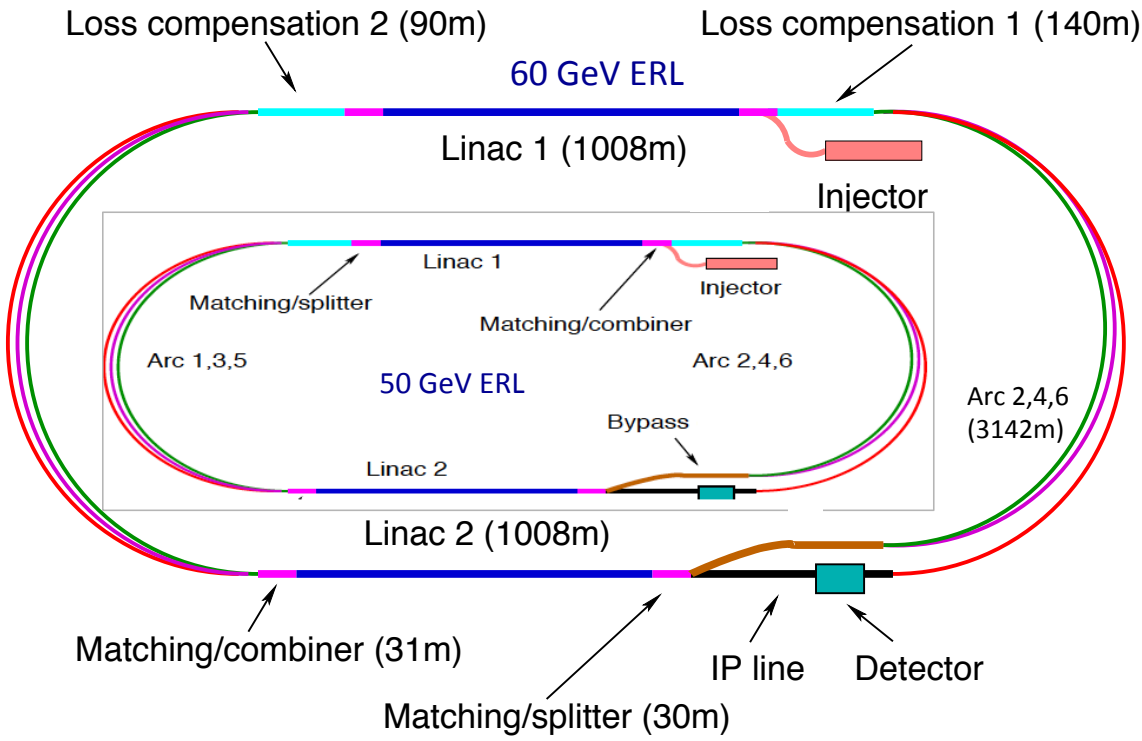

Figure 4.1: Schematic view of the three-turn LHeC configuration with two oppositely positioned electron linacs and three arcs housed in the same tunnel. Two configurations are shown: Outer: Default $E_e = 60\,\text{GeV}$ with linacs of about 1 km length and 1 km arc radius leading to an ERL circumference of about 9 km, or 1/3 of the LHC length. Inner: Sketch for $E_e = 50\,\text{GeV}$ with linacs of about 0.8 km length and 0.55 km arc radius leading to an ERL circumference smaller than the SPS size, i.e. 5.4 km or 1/5 of the LHC length. The 1/5 circumference configuration is flexible: it entails the possibility to stage the project as funds of physics dictate by using only partially equipped linacs, and it also permits upgrading to somewhat higher energies if one admits increased synchrotron power losses and operates at higher gradients.

where $N_{e(p)}$ is the number of electrons (protons) per bunch, $f = 1/\Delta$ the bunch frequency with the bunch distance Δ, equal to 25 ns at the LHC, and γ_p the relativistic factor E_p/M_p of the proton beam. Further, ϵ_p denotes the normalized proton transverse beam emittance and β^* the proton beta function at the IP, assumed to be equal in x and y. The luminosity is moderated by the hourglass factor, $H_1 = H_{geo} \simeq 0.9$, the pitch or beam-beam correction factor, $H_2 = H_{b-b} \simeq 1.3$, and the filling factor $H_3 = H_{coll} \simeq 0.8$. The product of these factors is estimated to be one and the factors are therefore not listed in the subsequent tables.

The electron beam current is given as

$$I_e = eN_e f.$$

The current for the LHeC is limited by the charge delivery of the source. In the new default design we have $I_e = 20\,\text{mA}$ which results from a charge of 500 pC for the bunch frequency of 40 MHz. It is one of the tasks of the PERLE facility to investigate the stability of the 3-turn ERL configuration in view of the challenge for each cavity to hold the sixfold current due to the simultaneous acceleration and deceleration of 3 bunches.

Electron-Proton Collisions

The design parameters of the luminosity have been recently provided in a note describing the FCC-eh configuration [**?**], including the LHeC. The following table, Tab. 4.3, represents an update comprising in

addition the initial 30 GeV configuration and the lower energy FCC-pp version based on the LHC magnets [2]. For the LHeC, as noted above, we assume $E_e = 50\,\text{GeV}$ while for FCC-eh we stick to 60 GeV. Since the source limits the electron current, the peak luminosity may be assumed not to depend on E_e. Studies of the interaction region design, presented in this paper, show that one may be confident in reaching a β^* of 10 cm, while it will be a challenge to reach values below. Similarly, it will be quite a challenge to operate with a current beyond 20 mA. That has yet been considered in the dedicated operation mode, in which, it has been assumed [**?**] that the LHeC would possibly operate for a few years when the *pp* program has ended.

E_p [TeV]	7	7	7	7	20	50
E_e [GeV]	60	30	50	50	60	60
mode	CDR	initial	default	dedicated	design	design
N_p [10^{11}]	1.7	2.2	2.2	2.2	1	1
ϵ_p [μm]	3.7	2.5	2.5	2.5	2.2	2.2
I_e [mA]	6.4	15	20	50	20	20
N_e [10^9]	1	2.3	3.0	7.8	3.0	3.0
β^* [cm]	10	10	7	7	12	15
Luminosity [$10^{33}\,\text{cm}^{-2}\text{s}^{-1}$]	1	5	9	23	8	15

Table 4.3: Summary of luminosity parameter values for the LHeC and FCC-eh. Left: CDR from 2012; Middle: LHeC in three stages, an initial low energy run, the default 50 GeV, both concurrently with the LHC, and a final, dedicated, stand-alone *ep* phase ; Right: FCC-eh with a 20 and a 50 TeV proton beam, in synchronous operation.

The peak luminosity values exceed those at HERA by 2-3 orders of magnitude. The operation of HERA in its first, extended running period, 1992-2000, provided an integrated luminosity of about $0.1\,\text{fb}^{-1}$ for the collider experiments H1 and ZEUS. This may now be expected to be taken in a day of initial LHeC operation.

Electron-Ion Collisions

The design parameters of the luminosity have recently been also provided [**?**] for the electron-lead ion scattering. The following table, Tab. 4.4, is a slight update of the numbers presented in there also introducing the $E_p = 20\,\text{TeV}$ FCC-hh configuration. A year of eA operation, possibly distributed over some smaller bits of operation thus has the potential to provide an integrated data set of about 5 (25) fb^{-1} for the LHeC (FCC-eh), resp. This exceeds the HERA *ep* luminosity values about tenfold and the fixed target nuclear DIS experiment kinematics by about $3-4$ orders of magnitude. These energy frontier electron-ion configurations therefore have the potential to establish a much different view on nuclear structure and parton dynamics as the current one. This is discussed in Sect.XX.

4.2.5 Linac Parameters

The brief summary of the main LHeC characteristics here concludes with the main ERL parameters, for the novel default of 50 GeV. Tab. 4.5, which are discussed in much detail in Sect.YY.

[2] The low energy FCC-pp collider, as of today, uses a 6 T LHC magnet in a 100 km tunnel. If within decades ahead high field magnets may become available based on HTS technology, then a 20 TeV proton beam energy may also be achievable in the LHC tunnel. To this extent the here considered low energy FCC and an HTS based HE-LHC represent much comparable options in terms of their energy reach.

parameter [unit]	LHeC	FCC-eh	FCC-eh
E_p [TeV]	7	20	50
E_{Pb} [PeV]	0.574	1.64	4.1
E_e [GeV]	50	50	50
$\sqrt{s_{eN}}$ electron-nucleon [TeV]	0.8	1.4	2.2
bunch spacing [ns]	50	100	100
no. of bunches	1200	2072	2072
ions per bunch [10^8]	1.8	1.8	1.8
$\gamma\epsilon_A$ [μm]	1.5	0.9	0.9
electrons per bunch [10^9]	6.2	12.5	12.5
electron current [mA]	20	20	20
IP beta function β_A^* [cm]	7	10	15
luminosity [$10^{32}\mathrm{cm}^{-2}\mathrm{s}^{-1}$]	10	18	54

Table 4.4: Baseline parameters of future electron-ion collider configurations based on the electron ERL, in concurrent eA and AA operation mode with the LHC and the two versions of a future hadron collider at CERN.

item	dimension	value
Frequency	MHz	801.58
Bunch charge	pC	499
Bunch spacing	ns	24.95
Electron current	mA	20
Injector energy	MeV	500
Gradient	MV/m	19.73
Cavity length, active	m	0.918
Cavity length, flange-to-flange	m	1.5
Cavities per cryomodule		4
Length of cryomodule	m	7
Acceleration per cryomodule	MeV	72.45
Total number of cryomodules		112
Acceleration energy per pass	GeV	8.1

Table 4.5: Basic LHeC ERL characteristics for the default configuration using two such linacs located opposite to each other in a racetrack of 5.3 km length. Each linac is passed three times.

4.3 Operation Schedule [Oliver Bruening]

4.4 Summary of Acceptance, Resolution and Calibrations [Peter Kostka]

Chapter 5

Precision Standard Model Physics with LHeC

[Daniel Britzger, Fred Olness]

Example reference: LHeC [1]

5.1 Sample PDF Figures: *... for consideration*

Note: these are sample PDF figures to include per discussion of the PDF & Low x Working group discussion (Fred 6 Oct. 2019)

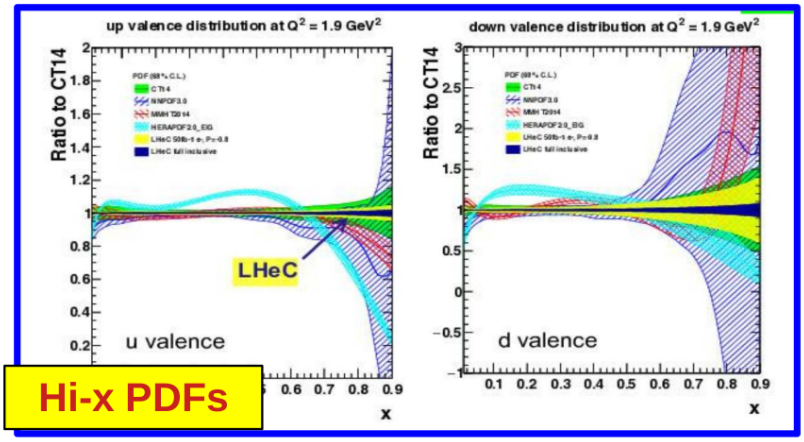

Figure 5.1: PDF constraints from LHeC at hi-x.

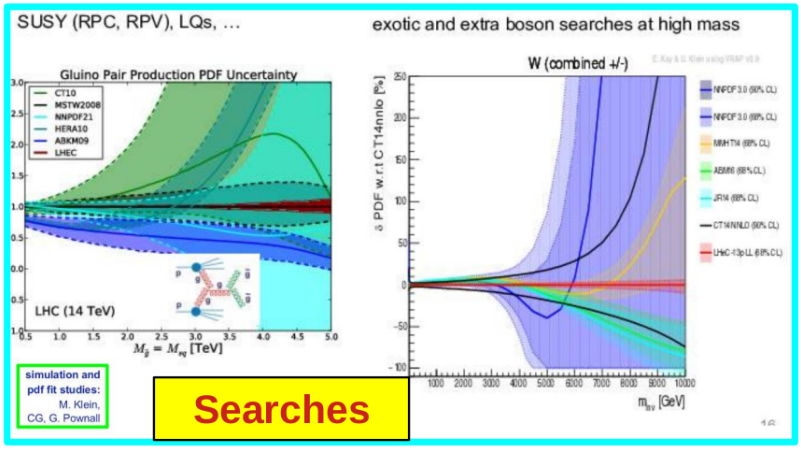

Figure 5.2: Impact of PDF constraints on BSM searches: i) gluion production; ii) extra W production

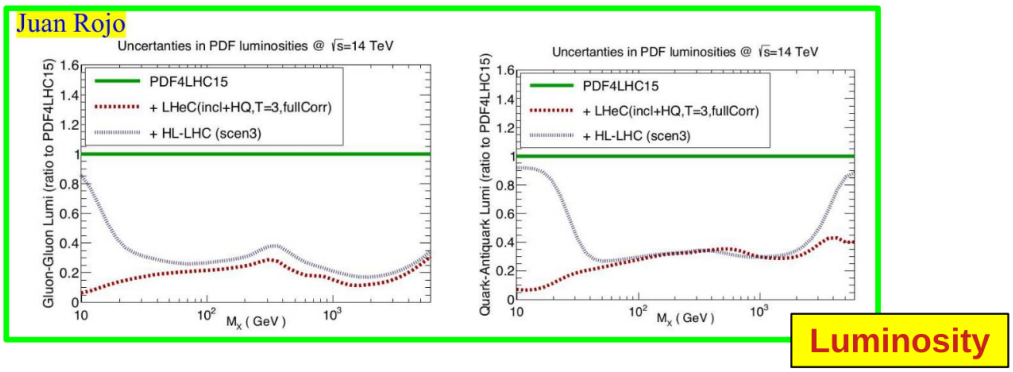

Figure 5.3: Impact of PDF constraints on BSM searches: luminosity constraints for M_X production

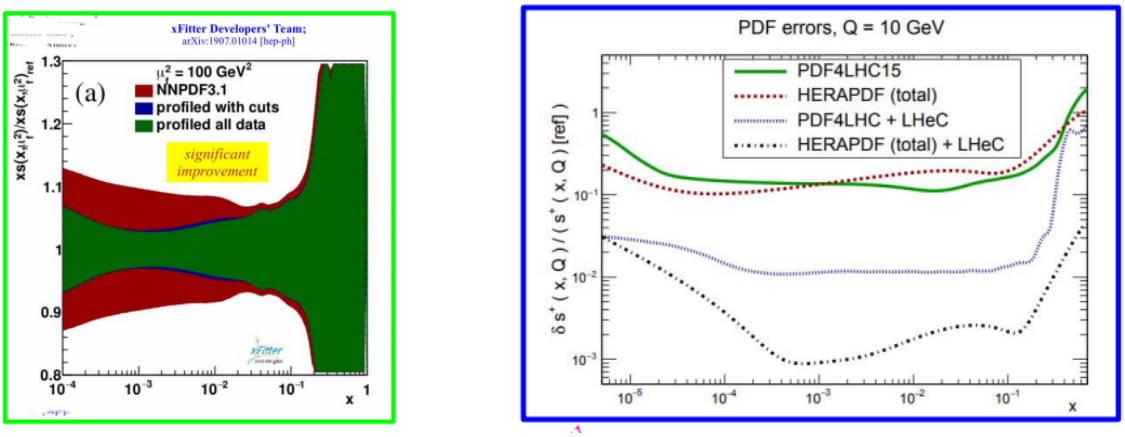

Figure 5.4: Constraints on the strange quark PDF from Refs. [6, 7]

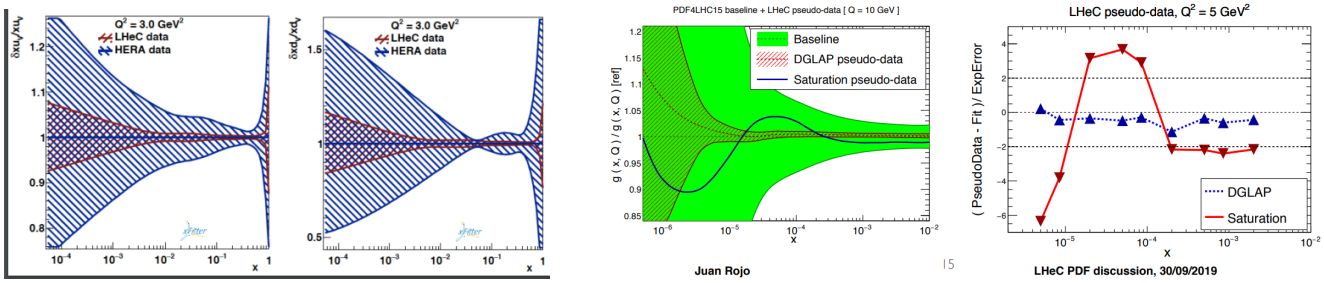

Figure 5.5: Constraints at small x, and impact from saturation.

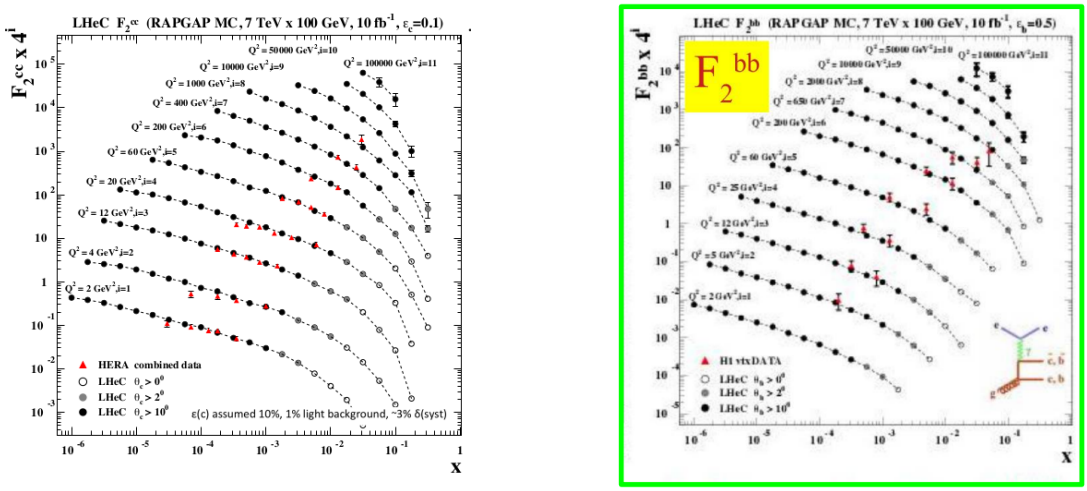

Figure 5.6: Heavy quark structure functions $F_2^{c\bar{c}}$ and $F_2^{b\bar{b}}$.

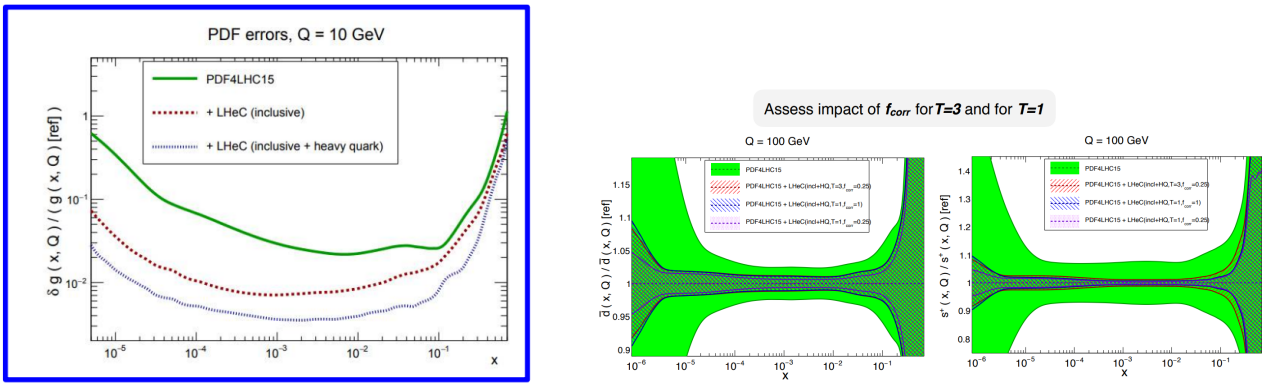

Figure 5.7: a) Impact on the gluon uncertainty including heavy quark (HQ) data. b) Impact of tolerance parameter on resulting PDF uncertainties.

5.2 Challenging the Standard Model through High Precision and Energy

5.3 Resolving the Parton Substructure of the Proton [Claire Gwenlan, Fred Olness]

5.3.1 Simulated Data [Max Klein]

5.3.2 PDFs from early LHeC Data [Claire Gwenlan]

5.3.3 Complete Unfolding of PDFs [Claire Gwenlan]

5.3.4 Strange Quark Density [Mandy Cooper Sarkar]

5.4 Discovery through Precision QCD

5.4.1 Determination of the strong coupling constant [Daniel Britzger]

Strong coupling is most important QCD parameter...

Running...

Different processes can be considered for an $\alpha_s(M_Z)$-determation.

Strong coupling from inclusive jet cross sections Inclusive jet cross sections are measured in the Breit frame of reference. They are proportional to $\alpha_s(M_Z)$ already in leading order pQCD.

Here, we show the cross sections as a function of P_T, where P_T denotes the jet transverse momentum in the Breit frame.

Kinematic cuts...

Pseudo data and JES scale uncertainties

All other uncertainties.

NNLO predictions are shown in figure 5.8, where also estimates for jet-energy scale uncertainties of 0.5 % are displayed.

Methodology for $\alpha_s(M_Z)$ fit....

Using a double-differential inclusive jet cross section measurement as function of P_T and Q^2, the strong coupling constant can be determined with an experimental precision up to

$$\delta\alpha_s(M_Z) = 0.00013\,(exp)$$

NNLO scale uncertainties are large ($\delta\alpha_s(M_Z) = 0.0035\,(NNLO)$) but can be reduced with a suitable cuts in P_T and Q^2 up to $\delta\alpha_s(M_Z) \approx 0.0010$. New predictions with resummed contributions or N3LO predictions will further improve this value.

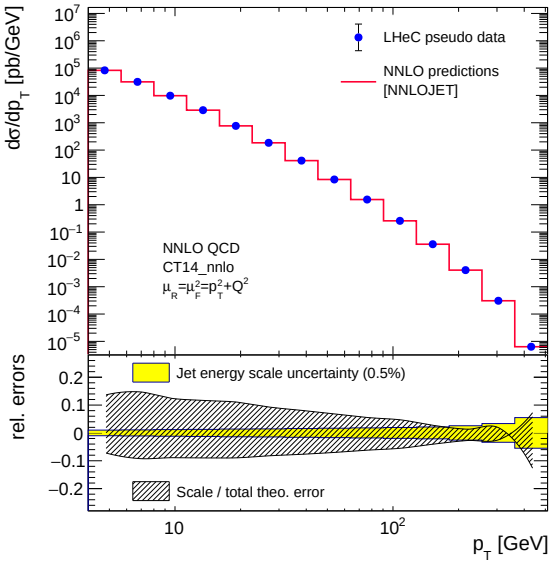

Figure 5.8: NNLO inclusive jet cross section as a function of the jet transverse momentum in the Breit frame, p_{T}.

Strong coupling from inclusive NC DIS cross sections Inclusive DIS cross sections are sensitive to the strong coupling through higher order corrections, the contributions of the F_L structure function and the scale-dependent cross section at high-x ('scaling violations').

Methodology: PDF+α_{s} fit to inclusive NC and CC DIS data, similar to section 5.3.3. Different than above, the value of the strong coupling constant is an additional parameter in the fit. Fits are done in VFN-scheme at NNLO accuracy and the full set of simlulated uncertainties are taken into account.

The 1D profile likelihood is displayed in figure 5.10 for different electron beam energies (see section **??**.

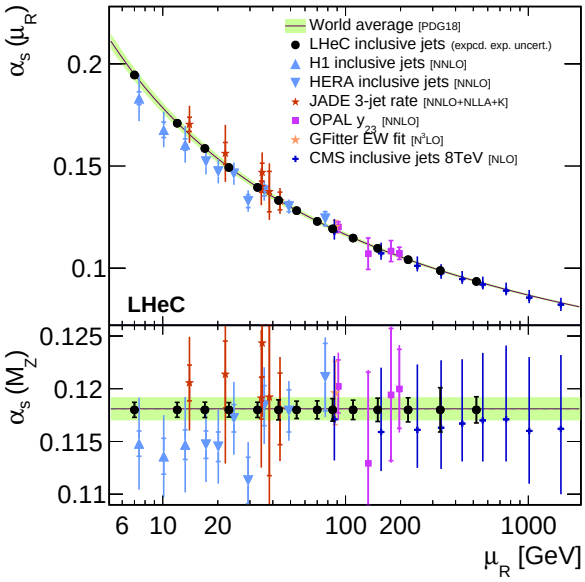

Figure 5.9: Constraints on $\alpha_S(\mu^2)$ from LHeC.

Strong coupling from further processes Most noteworthy: multi-jet cross sections: di-jet cross sections

three-jet, and four-jet cross section with increased sensitivity to $alpha_s$ and well defined pQCD order. However, higher order corrections beyond NLO theory will become challenging for theory colleagues. At HERA, these measurement were limited by kinematic reach and the recorded luminosity

event shape observables...

Substructure of jets...

Further precision measurements at the LHeC will become sensitive to the value of $\alpha_s(M_Z)$. These could be heavy-flavor cross sections, such as charm and bottom cross section measurements.

Photo-production cross sections provide a great opportunity for precision measurments of $\alpha_s(M_Z)$. Also its running can be greatly measured since the scale of the process is well estimated by the transverse momentum of the jets μ_R P_T. ... photon PDFs...

Diffractive dijets.

Dedicated high-x low-Q^2 cross sections.

Discussion of $\alpha_s(M_Z)$ determinations at LHeC Values from inclusive jet cross sections and from PDF fits with inclusive DIS data are compared in figure 5.10 and 5.11.

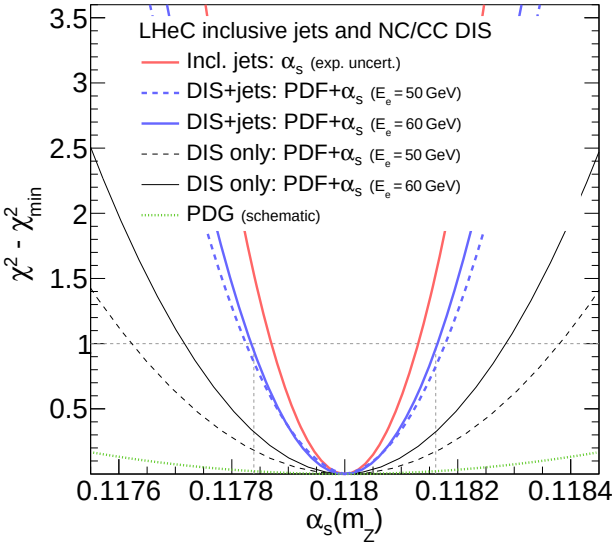

Figure 5.10: Estimates for the determination of the strong coupling constant $\alpha_s(M_Z)$ with inclusive DIS and/or with inclusive jet cross sections. Also estimates from different electron beam energies are displayed.

5.4.2 Grand Unification [Claire Gwenlan]

5.4.3 New QCD Dynamics at Small x [Anna Stasto]

The LHeC machine will offer access to a completely novel kinematic regime of DIS characterized by very small values of x. From the kinematical plane in (x, Q^2) depicted in Fig. **??** ***Here we need to refer to the Figure with kinematic plane for ep at LHeC*** , it is clear that the LHeC will be able to probe Bjorken-x values as low as 10^{-6} for perturbative values of Q^2. At low values of x different phenomena may occur which go beyond the standard collinear perturbative description based on DGLAP evolution. Since the seminal works of Balitsky, Fadin, Kuraev and Lipatov [8, 9, 10], it has been known that at large values

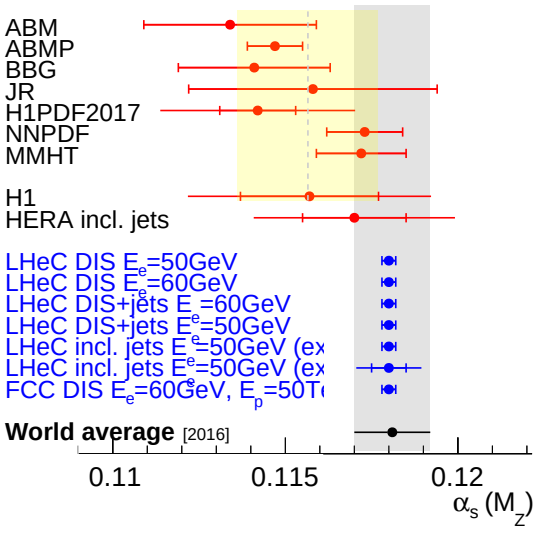

Figure 5.11: Summary of $\alpha_s(M_Z)$ values in comparison with nowadays values. The figure is just a place-holder for th final plot.

of centre-of-mass energy $\sqrt{s}$ or, to be more precise, in the Regge limit, there are large logarithms of energy which need to be resummed. Thus, even at low values of the strong coupling α_s logarithms of energy $\ln s$ may be sufficiently large there, such that terms like $(\alpha_s \ln s)^n$ will start to dominate the cross section.

The calculation of the scattering amlitudes in the multi-Regge kinematics and the resummation of $(\alpha_s \ln s)^n$ series in the leading logarithmic order was performed in [8, 9, 10] and it resulted in the famous BFKL evolution equation. This small x evolution equation, written for the so-called gluon Green's function or the unintegrated gluon density, is a differential equation in $\ln 1/x$. An important property of this equation is that it keeps the transverse momenta unordered along the gluon cascade. This has to be contrasted with the DGLAP evolution which is differential in the hard scale Q^2 and relies on the strong ordering in the transverse momenta of the exchanged partons in the parton cascade. The solution to the BFKL equation is a gluon density which grows sharply with decreasing x, as a power i.e. $\sim x^{-\omega_{IP}}$, where ω_{IP} is the hard Pomeron intercept, and in the leading logarithmic approximation equals $\frac{N_c \alpha_s}{\pi} 4 \ln 2$, which gives value of about 0.5 for typical values of the strong coupling. The leading logarithmic (LLx) result yielded a growth of the gluon density which was too steep for the experimental data at HERA. The next-to-leading logarithmic (NLLx) calculation performed in the late 90s [11, 12] resulted in large negative corrections to the LLx value of the hard Pomeron intercept and yielded some instabilities in the cross section [13, 14, 15, 16, 17].

The appearance of the large negative corrections at NLLx motivated the search for the appropriate resummation which would stabilize the result. It was understood very early that the large corrections which appear in BFKL at NLL are mostly due to the kinematics [18, 19, 20] as well as DGLAP terms and the running of the coupling. First attempts at combining the BFKL and DGLAP dynamics together with the proper kinematics [21] yielded encouraging results, and allowed to describe the HERA data on structure functions with good accuracy. The complete resummation program was developed in a series of works [22], [23, 24, 25, 26, 27, 28], [29, 30, 31, 32, 33], [34],[35]. In these works the resummation for the gluon Green's function and the splitting functions was developed.

The low-x resummation was recently applied to the description of structure function data at HERA using the methodology of NNPDF [36]. It was demonstrated that the resummed fits provide a better description of the structure function data than the DGLAP based fits at fixed NNL order. In particular, it was shown that the χ^2 of the fits does not vary appreciably when more small x data are included in the case of the fits

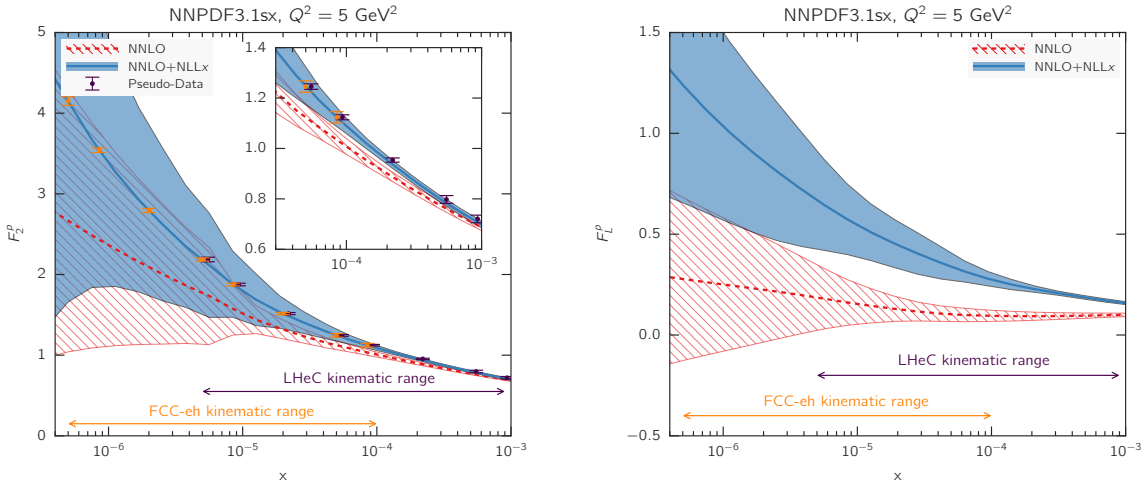

Figure 5.12: Predictions for the F_2 and F_L structure functions using the NNPDF3.1sx NNLO and NNLO+NLLx fits at $Q2 = 5\text{GeV}^2$ for the kinematics of the LHeC and FCC-eh. In the case of F_2, we also show the expected total experimental uncertainties based on the simulated pseudo-data, assuming the NNLO+NLLx values as central prediction. A small offset has been applied to the LHeC pseudo-data as some of the values of x overlap with the FCC-eh pseudo-data points. The inset in the left plot shows a magnified view in the kinematic region $x > 3 \times 10^{-5}$, corresponding to the reach of HERA data. Figure from [36]. ***Warning: I have taken the caption literally from paper [36]. Needs to modify?***

which include the effects of the resummation. On the other hand, the fits based on NNLO DGLAP evolution exhibit a worsening of their quality in the region of low x and low to moderate values of Q^2. This indicates that there is some tension in the fixed order fits, and that resummation alleviates it. In addition, it was shown that the description of the longitudinal structure function F_L from HERA data is improved in the fits with the small x resummation. This analysis strongly suggests that the small x resummation effects are indeed visible in the HERA kinematics. Such effects will thus be strongly magnified in the LHeC kinematics, which probes values of x of the order of magnitude lower than HERA. The NNPDF group also performed simulation of the structure functions F_2 and F_L with and without resummation in the LHeC range as well as for the next generation electron-hadron collider FCC-eh [36]. The predictions for the structure functions as a function of x for fixed values of Q^2 are shown in Figs. 5.12.

The simulations were done using APFEL [37] together with the HELL package [38] which implements the small x resummation. From Fig. 5.12 it is clear that LHeC will have much higher sensitivity to discriminate between fixed order and resummed scenarios than the HERA collider. The differences between central values for both predictions are of the order of 15% for the case of F_2 and this is larger than the projected error bar on the reduced cross section or structure function F_2 which could be measured at LHeC. For comparison, the simulated pseudodata for F_2 are shown together with the expected experimental uncertainties. The total uncertainties of the simulated pseudo-data are at the few percent level at most, and therefore much smaller than the uncertainties coming from the PDFs in most of the kinematic range.

Thus, fits to the LHeC data will have power to discriminate between the different frameworks. In the right plot in Fig. 5.12, the predictions for the longitudinal structure function are shown. We see that in the case of the F_L structure function, the differences between the fixed order and resummed predictions are even larger, consistently over the entire range of x. This indicates the importance of the measurement of the longitudinal structure function F_L which can provide further vital constraints on the QCD dynamics in the low x region due to its sensitivity to the gluon density in the proton.

To further illustrate the power of the high energy DIS collider like LHeC in exploring the dynamics at low x, fits which include the simulated data were performed. The NNLO+NLLx resummed calculation was

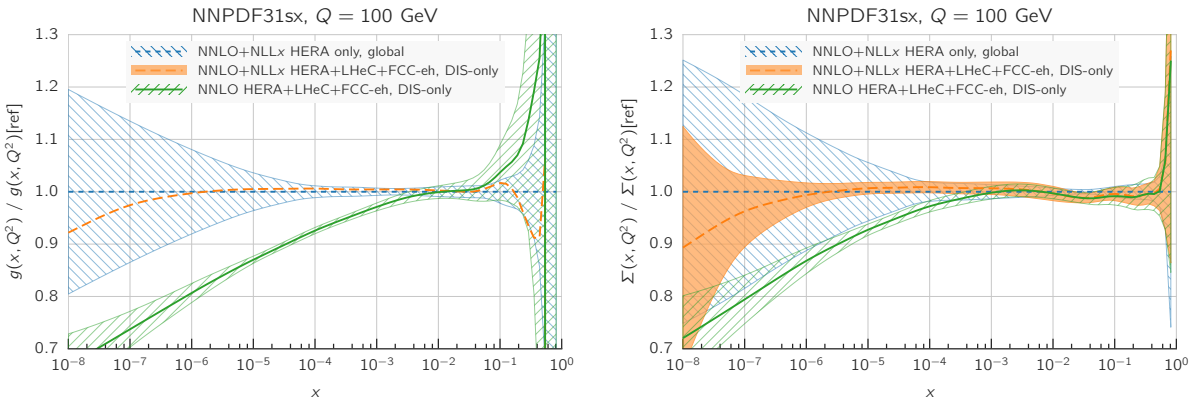

Figure 5.13: Comparison between the gluon (left plot) and the singlet (right plot) PDFs in the NNPDF3.1sx NNLO+NNLx fits without and with the LHeC+FCC-eh pseudo-data on inclusive structure functions. For completeness, we also show the results of the corresponding NNPDF3.1sx NNLO fit with LHeC+FCC-eh pseudo-data. Figure from [36] ***Warning: I have taken the caption literally from paper [36]. Needs to modify?***

used to obtain the simulated pseudodata, both for the LHeC, in a scenario of 60 GeV electron beam on a 7 TeV proton beam as well as in the case of the FCC-eh scenario with the 50 TeV proton beam. All the experimental uncertainties for the pseudodata have been added in quadrature. Next, fits were performed to the DIS HERA as well as pseudodata using the theory with and without the resummation at low x. The hadronic data were not included for this analysis but, as demonstrated in [36], these data do not have much of the constraining power at low x, and thus the results of the analysis at low x are independent of the additional non-DIS data sets. The quality of the fits characterized by the χ^2 was markedly worse when the NNLO DGLAP was used to fit the HERA data and the pseudodata from LHeC and/or FCC-eh with resummation. To be precise, the χ^2 for the HERA data set was equal to 1.22 for the NNLO fit, and 1.07 for the resummed fit. For the case of the LHeC/FCC-eh the χ^2 was equal to 1.71/2.72 and 1.22/1.34 for NNLO and NNLO+resummation fits, respectively. These results demonstrate the huge discriminatory power of the new DIS machines between the DGLAP and resummed frameworks, and the large sensitivity to the low x region while simultaneously probing low to moderate Q^2 values.

In Fig. 5.13 the comparison of the gluon and quark distribution from the NNLO + NLLx fits is shown at $Q = 100$ GeV as a function of x, with and without including the simulated pseudodata from LHeC as well as FCC-eh. The large differences at large x are due to the fact that only DIS data were included in the fits, and not the hadronic data. The central values of the extracted PDFs using only HERA or using HERA and the simulated pseudodata coincide with each other, but a large reduction in uncertainty is visible when the new data are included. The uncertainties from the fits based on the HERA data only increase sharply already at $x \sim 10^{-4}$. On the other hand, including the pseudodata from LHeC and/or FCC-eh can extend this regime by order(s) of magnitude down in x. Furthermore, fits without resummation, based only on NNLO DGLAP, were performed to the HERA data and the pseudodata. We see that in this case the extracted gluon and singlet quark densities differ significantly from the fits using the NNLO+NLLx. Already at $x = 10^{-4}$ the central values of the gluon differ by 10% and at $x = 10^{-5}$, which is LHeC regime, the central values for the gluon differ by 15%. This difference is much larger than the accuracy with which the gluon can be extracted from the DIS data, which is of the order of $\sim 1\%$.

The presented analysis demonstrates, that the fixed order prediction based on the DGLAP evolution would likely fail to describe accurately the structure function data in the new DIS machines and in that regime new dynamics, resummation, is mandatory for quantitative predictions. Therefore the LHeC machine has an unprecedented potential to pin down the details of the QCD dynamics at low values of Bjorken x.

5.4.4 Pinning Down the Low x Gluon with F_2 and F_L Measurements [Max Klein]

5.4.5 The 3D Structure of the Proton [Anna Stasto]

As evident from the discussion in the previous sections, the LHeC machine will be able to measure the collinear parton distribution functions with unprecedented accuracy, in the extended range of x and Q^2. Thus, it will allow to gain the new insight into the details of the one-dimensional structure of the proton and nuclei, including possibility of exploring novel phenomena at low x. In addition to collinear dynamics, LHeC machine opens a new window into the proton and nuclear structure by allowing to precisely investigate the partonic structure in more than just one dimension of the longitudinal momentum. The precision DIS thus gives access to multidimentional aspects of the hadron structure. This can be achieved by precisely measuring processes with more exclusive final states, like production of jets, semi-inclusive production of hadrons and exclusive processes, in particular the elastic diffractive production of vector mesons and the deeply virtual Compton (DVCS) scattering. These processes have a potential to provide the information not only about the longitudinal distribution of partons in the proton or nucleus but also information about the dependence of the parton distribution on the transverse momenta as well as the momentum transfer. Thus LHeC can open a unique window into the details of the 3D structure of hadrons.

The most general quantity that can be defined in QCD, that would contain very detailed information about the partonic content of the hadron, is the Wigner distribution [39]. This function $W(x, \mathbf{k}, \mathbf{b})$ is a 1+4 dimensional function that contains rich information about the hadron structure. One can think of that quantity as the mother or master parton distribution, from which lower-dimensional distributions can be obtained. In the definition of the Wigner function, $\mathbf{k}$ is the transverse momentum of the parton and $\mathbf{b}$ is the 2-dimensional impact parameter, which can be defined as a Fourier conjugate to the momentum transfer of the process. The other, lower dimensional, parton distributions can be obtained by integrating out different variables. And thus, the transverse momentum dependent parton (TMD) distributions (or unintegrated parton distribution functions) $f_{\rm TMD}(x, \mathbf{k})$ can be obtained by integrating out the impact parameter $\mathbf{b}$ in Wigner function, while the generalized parton densities (GPD), $f_{\rm GPD}(x, \mathbf{b})$, can be obtained from Wigner function through the integration over the transverse momentum $\mathbf{k}$. In the regime of small x, or high energy, a suitable formalism is that of the dipole picture, where the fundamental quantity which contains the details of the partonic distribution is the dipole amplitude $N(x, \mathbf{r}, \mathbf{b})$. This object contains the dependence on the impact parameter $\mathbf{b}$ as well as another transverse size, the so-called dipole size, which can be related to the transverse momentum of the parton $\mathbf{k}$ through the Fourier transform. The important feature of the dipole amplitude is that it should obey the unitarity limit $N \leq 1$. The dipole amplitude N within this formalism, can be roughly interpreted as a Wigner function in the high energy limit, as it contains the information about the spatial distribution of the partons in addition to the dependence on the longitudinal momentum fraction x.

Detailed simulations of the elastic diffractive J/ψ vector meson production were performed for the LHeC kinematics and beyond [1], using the formalism of the dipole picture. This particular process is shown in Fig.5.14, left plot. The proton is scattered elastically with the momentum transfer t, and the vector meson is produced, which is separated from the final state proton by a rapidity gap. Of particular importance is the measurement of the t slope of this process, since it can be related directly to the impact parameter distribution of the partonic density in the target. The first type of analysis like this, in the context of the elastic scattering was performed by Amaldi and Schubert [40], where it was demonstrated that the Fourier transform of the elastic cross section yields access to the impact parameter profile of the scattering amplitude. This method can be utilized in the context of the vector meson scattering in Deep Inelastic Scattering, where the transverse distribution of partons, in the perturbative regime, can be extracted through the appropriate Fourier transform []. The additional advantage of studying the diffractive vector meson production is the fact that the partonic distribution can be studied as a function of the hard scale in this process given by the mass of the vector meson in the photoproduction case or the Q^2 (or more precisely combination of Q^2

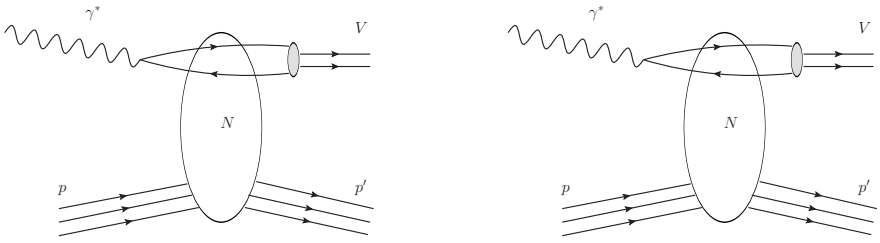

Figure 5.14: Left: the diagram for the elastic diffractive production of the vector meson. Right: schematic illustration of the elastic diffractive vector meson production in the dipole picture. The initial virtual photon, fluctuates into the quark - antiquark pair which then scatters off the hadronic target and the forms the vector meson. The details of the hadronic interaction of the dipole with the target are encoded in hte dipole amplitude N.

and M_V^2) in the case of the diffractive DIS production of the vector meson, as well as the energy W of the photon-proton system available in the process.

The differential cross section for the elastic vector meson production can be expressed in the following form

$$\frac{d\sigma^{\gamma^* p \to J/\psi p}}{dt} = \frac{1}{16\pi}|\mathcal{A}(x,Q,\Delta)|^2 \,, \tag{5.1}$$

where the amplitude for the process of elastic diffractive vector meson production in the high energy limit, within the framework of the dipole picture, is given by

$$\mathcal{A}(x,Q,\Delta) \;=\; \sum_{h\bar{h}} \int d^2\mathbf{r} \int dz \Psi^*_{h\bar{h}}(z,\mathbf{r},Q)\, \mathcal{N}(x,\mathbf{r},\Delta)\, \Psi^V_{h\bar{h}}(z,\mathbf{r}) \,. \tag{5.2}$$

In the above formula, $\Psi^*_{h\bar{h}}(z,\mathbf{r},Q)$ is the photon wave function, which describes the dissociation of the virtual photon γ^* into a $q\bar{q}$ pair. This wave funtion can be calculated from the perturbative QCD. The function $\Psi^V_{h\bar{h}}(z,\mathbf{r})$ is the wave function of the vector meson. Finally, $\mathcal{N}(x,\mathbf{r},\Delta)$ is the dipole amplitude, which contains all the information about the interaction of the quark-antiquark dipole with the target. The formula (5.2) can be interpreted as a process of the fluctuation of the virtual photon into a $q\bar{q}$ pair, which is subsequently interacting with the target through the dipole amplitude $\mathcal{N}$ and the formation of the vector meson, given by the amplitude Ψ^V, see Fig.5.14, right plot. The two integrals in the definition (5.2) are performed over the dipole size which is denoted by $\mathbf{r}$, and z which is the longitudinal momentum fraction of the photon carried by the quark. The scattering amplitude depends on the value of the momentum transfer Δ, which is related to the Mandelstam variable $t = -\Delta^2$. The sum is performed over the helicity states of $quarkandantiquark$.

The dipole amplitude $\mathcal{N}(x,\mathbf{r},\Delta)$ can be related to the dipole amplitude in the coordinate space through the appropriate Fourier transform

$$N(x,\mathbf{r},\mathbf{b}) = \int d^2\Delta\, e^{i\Delta\cdot\mathbf{b}} \mathcal{N}(x,\mathbf{r},\Delta) \,. \tag{5.3}$$

We stress, that **r** and **b** are two different transverse sizes here. The dipole size **r** is conjugated to the transverse momentum of the partons **k**, whereas the impact parameter is roughly the distance between the center of the scattering target to the center-of-mass quark-antiquark dipole and is related to the Fourier conjugate variable momentum transfer Δ.

Dipole amplitude $N(x, \mathbf{r}, \mathbf{b})$ contains rich information about the dynamics of the hadronic interaction. It is 5-dimensional function and it depends on the longitudinal momentum fraction, and two two-dimensional coordinates. The dependence on the longitudinal momentum fraction is obviously related to the evolution with the center-of-mass energy of the process, the dependence on the **b** provides information about the spatial distribution of the partons in the target. Within this framework, it is mainly the distribution of gluons in the impact parameter space. The dipole amplitude has a nice property that its value should be bounded from above by unitarity requirement $N \leq 1$. The complicated dependence on energy, dipole size and impact parameter of this amplitude can provide a unique insight into the dynamics of QCD, and approach to the dense partonic regime.

From Eqs.(5.1),(5.2) and (5.3) it is evident that the information about the spatial distribution in impact parameter **b** is related through the Fourier transform to the dependence of the cross section on the momentum transfer $t = -\Delta^2$.

To see how the details of the distribution, and in particular the approach to the unitarity can be studied through the VM elastic production, calculations based on the dipole model were performed [41], and extended to energies which can be reached at LHeC as well as the FCC-eh.

The prametriztions used in the calculation were IP-Sat model [42, 43] and b-CGC model [44]. In both cases the impact parameter dependence has to be modelled phenomenologically. In the IP-Sat model the dipole amplitude has the following form

$$N(x, \mathbf{r}, \mathbf{b}) \;=\; 1 - \exp[-\frac{\pi^2 r^2}{2N_c}\alpha_s(\mu^2) x g(x, \mu^2) T_G(b)] \;, \tag{5.4}$$

with the impact parameter profile for the gluon

$$T_G(b) \;=\; \frac{1}{2\pi B_G}\exp(-b^2/2B_G) \;.$$

The function $xg(x, \mu^2)$ is the collinear gluon density, evolved using LO DGLAP evolution (without the quarks), from initial scale μ_0^2 up to scale μ^2 set by the dipole size $\mu^2 = \frac{4}{r^2} + \mu_0^2$. $\alpha_s(\mu^2)$ is the strong coupling. The parametrization of the gluon density at the initial scale μ_0^2 is given by

$$xg(x, \mu_0^2) = A_g x^{-\lambda_g}(1-x)^{5.6} \;.$$

The alternative parametrization used is given by the b-CGC model [44] which has the form

$$N(x, \mathbf{r}, \mathbf{b}) \;=\; \begin{cases} N_0 \left(\frac{rQ_s}{2}\right)^{2\gamma_{\rm eff}} & \text{for} \quad rQ_s \leq 2 \;, \\ 1 - \exp(-\mathcal{A}\ln^2(\mathcal{B}rQ_s)) & \text{for} \quad rQ_s > 2 \;, \end{cases} \tag{5.5}$$

where the effective anomalous dimension $\gamma_{\rm eff}$ and the saturation scale Q_s of the proton explicitly depend on the impact parameter and are defined as

$$\begin{aligned} \gamma_{]\rm eff} \;&=\; \gamma_s + \frac{1}{\kappa\lambda \ln 1/x}\ln\left(\frac{2}{rQ_s}\right) \;, \\ Q_s(x,b) \;&=\; \left(\frac{x_0}{x}\right)^{\lambda/2}\exp\left[-\frac{b^2}{4\gamma_s B_{\rm CGC}}\right] \quad \text{GeV} \;, \end{aligned} \tag{5.6}$$

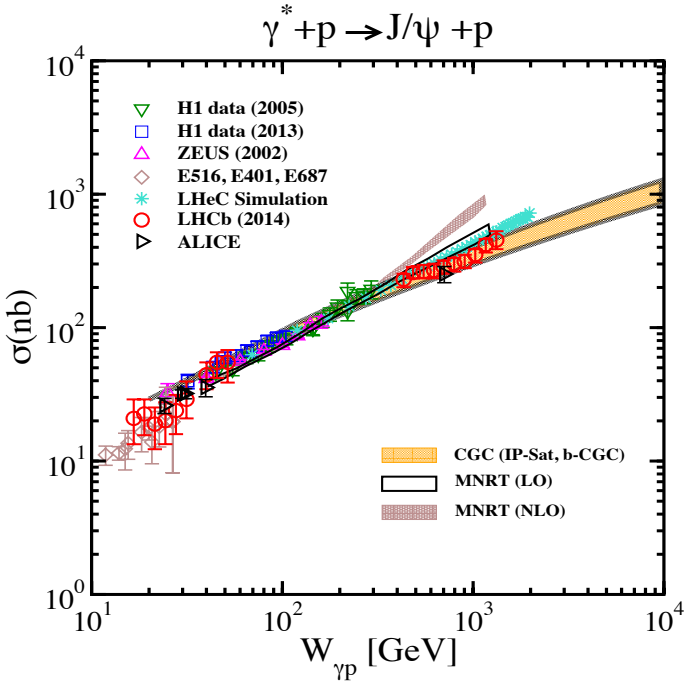

Figure 5.15: Total J/ψ cross-section as a function of center-of-mass photon-proton energy W, compared to results from the b-CGC and IP-Sat models with parameters of the models determined via a fit to the data from HERA [11, 12] and the old F2 structure function [15] (dashed-dotted line, labeled b-CGC 2008). The data are from fixed target experiments [45] [46], the H1, ZEUS [47, 48, 49, 50], LHCb [51] and ALICE [52] Collaborations. We also show the LHeC pseudo-data obtained from a simulation [1]. Figure reproduced from [41].

where $\kappa = \chi''(\gamma_s)/\chi'(\gamma_s)$, with $\chi(\gamma)$ being the leading-logarithmic BFKL kernel eigenvalue function [10]. The parameters $\mathcal{A}$ and $\mathcal{B}$ in Eq.(5.5) are determined uniquely from the matching of the dipole amplitude and its logarithmic derivatives at limiting value of $rq_s = 2$. The b-CGC model is constructed by smoothly interpolating between two analytically known limiting cases [44], namely the solution of the BFKL equation in the vicinity of the saturation line for small dipole sizes $r < 2/Q_s$, and the solution of the BK equation deep inside the saturation region for large dipole sizes $r > 2/Q_s$.

Parameters μ_0, A_g, λ_g of the IP-Sat model and $N_0, \gamma_s, x_0\lambda$ of the b-CGC model were fitted to obtain the best description of the inclusive data for the structure function F_2 at HERA. The slope parameters, which control the b -dependence in both models, B_g and $B_{\rm CGC}$ were fitted to obtain the best description of the elastic diffractive J/ψ production, in particular the t-dependence, at small values of t.

The calculations from the model for the cross section for the elastic J/ψ production as a function of the energy, in the photoproduction case $Q^2 \simeq 0$, are shown in Fig.**??**. Comparison is shown with the fixed target, HERA data as well as the LHCb and ALICE data, from ultra-peripheral collisions at the LHC. Previous estimates for the LHeC are shown as well [1]. The band includes uncertainty due to the choice of models as well as the variation in the charm quark mass within the range $m_c = 1.2 - 1.4$ GeV. In addition, comparison with the calculations based on the perturbative QCD at LO and NLO [53], without parton saturation effects are shown. The calculations are in a very good agreement with the HERA data as well as previous estimates for the LHeC. On the other hand we see some discrepancy between the calculations which include the saturation and the ones which do not, in particular LO estimates [53]. The slower growth with energy, of the calculation with saturation included, highlights the importance of the non-linear effects at higher energies.

In Figs. 5.16 we show the differential cross section $d\sigma/dt$ as a function of $|t|$ of and study its variation with

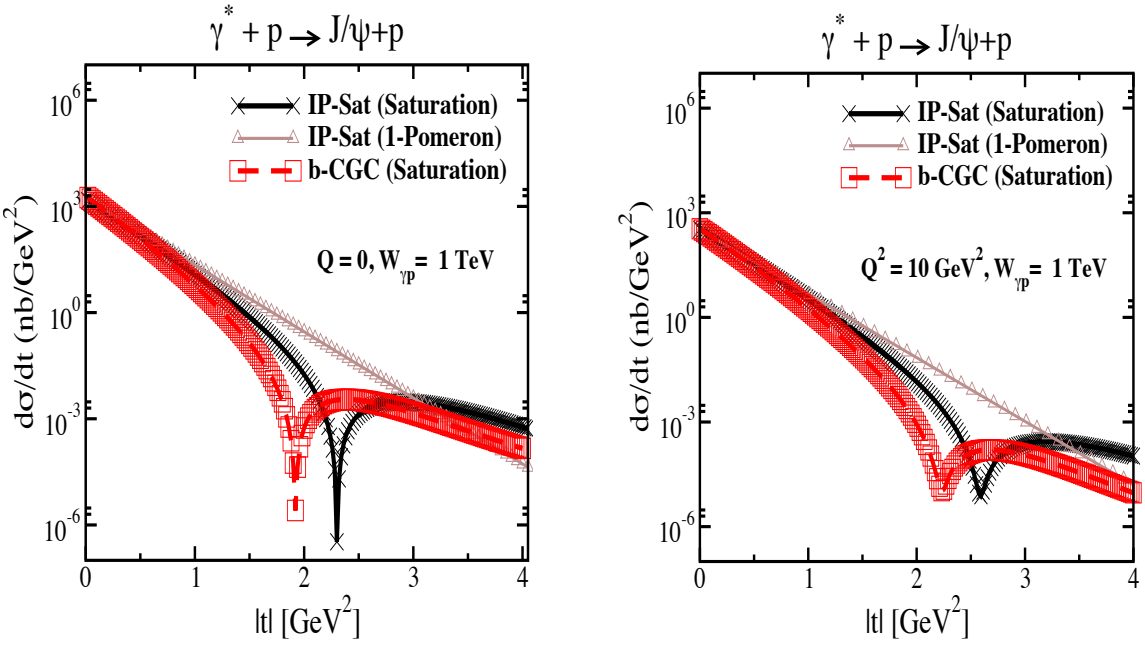

Figure 5.16: Differential cross section for the elastic J/ψ production as a function of $|t|$ within the IP-Sat (saturation), b-CGC and 1-Pomeron models at a fixed $W\gamma p = 1$TeV and for two different values of photon virtuality $Q = 0$ and $Q^2 = 10$ GeV^2. The thickness of points includes the uncertainties associated with our freedom to choose different values for the charm quark mass within the range $m_c = 1.2 - 1.4$ GeV.

energies, virtualities as well as model dependence. First, in Fig.5.16 we show the differential cross section as a a function of t for fixed energy $W = 1$ TeV, in the case of the photoproduction of J/Psi (left plot) and for the case of DIS with $Q^2 = 10\,\mathrm{GeV}^2$. There are three different calculations in each plot, using IP-sat model, b-CGC model and the 1-Pomeron approximation. The last one is obtained when just keeping the first nontrivial term in the expansion of the eikonalized formula of the IP-Sat amplitude (5.4). First, let us observe that all three models coincide for very low values of t, where the dependence on t is exponential. This is because for low $|t|$, relatively large values of impact parameter are probed in Eq.(5.2) where the amplitude is small, and therefore the tail in impact parameter is Gaussian in all three cases. Since the Fourier transform of the Gaussian in b is a function which is exponential in t, the result at low t follows. On the other hand, the three scenarios differ significantly for large values of $|t|$. In the case of the 1-Pomeron approximation the dependence is still exponential, without any dips, which is easily understood since the impact parameter profile is Gaussian in this case. For the two other scenarios, dips in t emerge. They signal the departure from the Gaussian profile in b for small values of b where the system is dense. Similar pattern can be observed when performing the Fourier transform of the Wood-Saxon distribution, which is typical distribution used for the description of the matter density in nuclei. When Q^2 is increased the pattern of dips also changes. This is illustrated in Fig.5.16. It is seen that dips move to the higher values of $|t|$ for DIS as compared with the photoproduction. This can be understood from the dipole formula Eq. 5.2 which contains the integral over the dipole size. The larger values of Q^2 select the smaller values of dipole size r, where the amplitude is smaller and thus in the dilute regime, where the profile in b is again Gaussian. On the other hand small scales select large dipole sizes for which the dipole amplitude is larger and thus the saturation effects more prominent, leading to the distortion of the impact parameter profile and therefore emergence of dips in t.

In the next figure Fig.5.17 we show the same calculation but for higher energy $W = 2.5$ TeV. In this case we see that the dips move to the lower values of $|t|$. This can be easily understood, as with the increasing energy the dipole scattering amplitude increases, and thus the dilute-dense boundary shifts to larger values of b, meaning that the $t$dependence deviation from the exponential fall off occurs for smaller values of $|t|$.

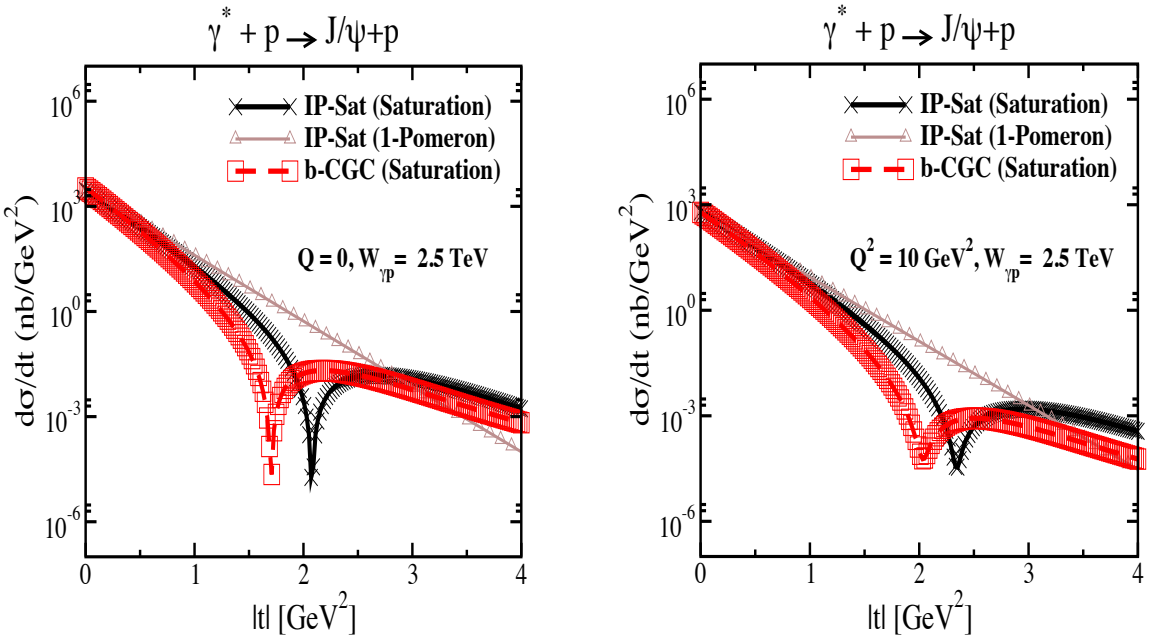

Figure 5.17: Differential cross section for the elastic J/ψ production as a function of $|t|$ within the IP-Sat (saturation), b-CGC and 1-Pomeron models at a fixed $W\gamma p = 2TeV$ and for two different values of photon virtuality $Q = 0$ (left plot) and $Q^2 = 10$ GeV^2 (right plot). The thickness of points includes the uncertainties associated with our freedom to choose different values for the charm quark mass within the range $m_c = 1.2 - 1.4$ GeV .

Similar studies [41] show also the change of the position of the dips with the mass of the vector meson, for the lighter vector mesons, like ρ, ω, ϕ the dips occur earlier in t than for the heavier vector mesons J/ψ or Υ. We note that of course the details of the position of the dips depend crucially on the details of the models, which are currently not constrained by the existing HERA data.

We thus see that the precise measurement of the t-slope in the elastic diffractive production of vector mesons at the LHeC, and its variation with x and scales, provide unique opportunity to explore the transition between the dilute and dense partonic regime. As mentioned earlier, the elastic diffractive production is one among several different measurements which can be performed to explore the 3D structure of the hadron. Another one is the Deeply Virtual Compton Scattering which a process sensitive to the spatial distribution of quarks inside the hadron. Preliminary analyses [1] indicate huge potential of LHeC for the measurements of DVCS. Another example of a process that could be studied at the LHeC, is the diffractive dijet production. It has been suggested [54] that this process is sensitive to the Wigner function, and that both the transverse momentum and spatial distribution of partons can be extracted by measuring this process. The transverse momentum of the jets would be sensitive to the transverse momentum of the participating partons, whereas the momentum transfer of the elastically scattered proton would give a handle on the impact parameter distribution of the partons in the target, thus giving a possibility to extract the information about the Wigner distribution.

5.4.6 Diffraction [Paul Newman]

Here we talk about the inclusive diffraction, shall we change the title to 'Inclusive diffraction' ?

5.5 Electroweak Physics [Daniel Britzger]

Since the discovery of the Standard Model (SM) Higgs boson at the CERN LHC experiments and subsequent measurement of its parameters, all fundamental parameters of the SM have been measured directly and with remarkable precision. To further establish the validity of the theory of electroweak interactions, validate the mechanism of electroweak symmetry breaking and the mechanism of the generation of particle masses, further high-precision electroweak measurements have to be performed. Such high-precision measurements are also often considered as a portal to new physics, since non-SM contributions, as for instance loop-insertions, may yield significant deviations for some precisely measurable and calculable observables. The greatly enlarge kinematic reach to higher scales in comparison to HERA and the large targeted luminosity will allow for the first time high-precision electroweak measurements in ep.

The LHeC experimental conditions offer the opportunity for unique measurements of electroweak parameters, which are often complementary to other experiments, such as proton-proton or electron-positron collider experiments or low energy neutrino or muon scattering experiments. Among many other quantities, unique measurements of the weak couplings of the light quarks, u and d, can be performed due to the important contributions of valence quarks in the initial state, as well as scale dependent measurements of weak interactions, since deep-inelastic ep scattering is mediated through space-like momentum transfer (t-channel exchange).

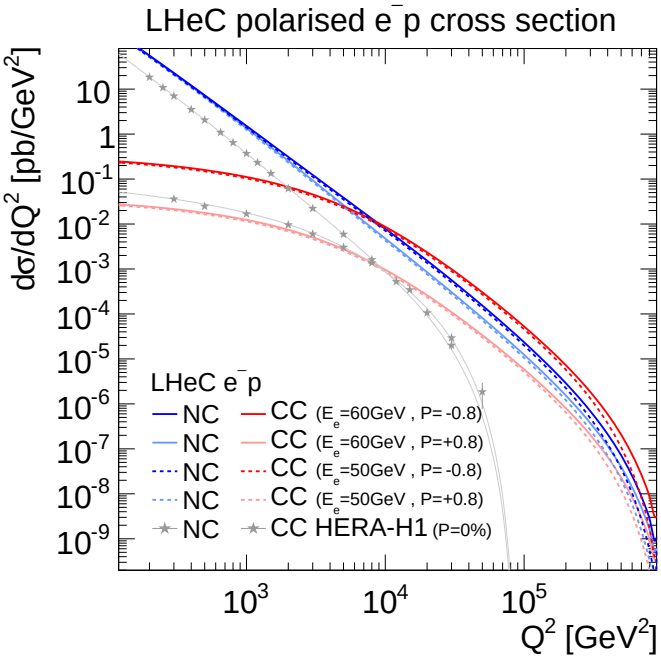

Figure 5.18: Single differential cross sections for polarised e^-p NC and CC DIS at LHeC for two different electron beam energies (E_e). Cross sections for longitudional electron beam polarisations of $P_e = +0.8$ and -0.8 are displayed. For comparison also measurements at center-of-mass energies of $\sqrt{s} = 920$ by H1 at HERA for unpolarised ($P = 0\,\%$) electron beams are displayed.

In this section we study the sensitivity of inclusive NC and CC cross section at LHeC to electroweak parameters. Inclusive NC DIS interactions in $e^{\pm}p$ scattering are mediated by a virtual photon (γ) or the Z boson in the t-channel. Inclusive CC DIS interactions are mediated exclusively by the W boson as a purely *weak* process. The single-differential inclusive NC and CC DIS cross sections for polarised e^-p scattering as function of Q^2 are displayed in figure 5.18. The targeted longitudional polarisation states of the LHeC electron beam of $P_e \pm 0.8$ will considerably alter the CC DIS cross section as it scales linearly with P_e and

also for NC cross section polarisation effects are significant in kinematic regions, where γZ and pure Z exchange are important. Albeit the impact of a reduced electron beam energy of $E_e = 50\,\text{GeV}$ appears to the very small, a higher electron beam energy may yield higher precision for electroweak parameters, since these are predomonintly sensitive to the cross sections at highest scales.

5.5.1 Theory of elecectroweak effects in inclusive NC and CC DIS cross sections

Inclusive NC DIS cross sections are expressed in terms of generalised structure functions $\tilde{F}_2^{\pm}$, $x\tilde{F}_3^{\pm}$ and $\tilde{F}_{\text{L}}^{\pm}$ at EW leading order (LO) as

$$\frac{d^2\sigma^{\text{NC}}(e^{\pm}p)}{dxdQ^2} = \frac{2\pi\alpha^2}{xQ^4}\left[Y_+\tilde{F}_2^{\pm}(x,Q^2) \mp Y_- x\tilde{F}_3^{\pm}(x,Q^2) - y^2\tilde{F}_{\text{L}}^{\pm}(x,Q^2)\right] ,$$

where α denotes the fine structure constant and x the Bjorken scaling variable. The terms $Y_{\pm} = 1 \pm (1-y)^2$ contain the helicity dependence of the process, where y denotes the inelasticity of the process. The generalised structure functions are then separated into contributions from pure γ- and Z-exchange and their interference [55]:

$$\begin{aligned}
\tilde{F}_2^{\pm} &= F_2 - (g_V^e \pm P_e g_A^e)\varkappa_Z F_2^{\gamma Z} + \left[(g_V^e g_V^e + g_A^e g_A^e) \pm 2P_e g_V^e g_A^e\right]\varkappa_Z^2 F_2^Z ,\\
\tilde{F}_3^{\pm} &= -(g_A^e \pm P_e g_V^e)\varkappa_Z F_3^{\gamma Z} + \left[2g_V^e g_A^e \pm P_e(g_V^e g_V^e + g_A^e g_A^e)\right]\varkappa_Z^2 F_3^Z .
\end{aligned} \tag{5.7}$$

Similar expressions hold for $\tilde{F}_L$. In the naive quark-parton model, which corresponds to the LO QCD approximation, the structure functions are calculated as

$$\begin{aligned}
\left[F_2, F_2^{\gamma Z}, F_2^Z\right] &= x\sum_q \left[Q_q^2, 2Q_q g_V^q, g_V^q g_V^q + g_A^q g_A^q\right]\{q+\bar{q}\} ,\\
x\left[F_3^{\gamma Z}, F_3^Z\right] &= x\sum_q \left[2Q_q g_A^q, 2g_V^q g_A^q\right]\{q-\bar{q}\} ,
\end{aligned}$$

and it is easily recognized that those are closely related to the quark and anti-quark momentum distributions, xq and $x\bar{q}$. In eqs. (5.7) and (5.8), the variables $g_V^{e/q}$ and $g_A^{e/q}$ stand for the vector and axial-vector couplings of the lepton or quarks to the Z boson, and the coefficient $\varkappa_Z$ accounts for the Z-boson propagator and the normalisation of the weak contributions. Both parameters are given by electroweak theory. The (effective) coupling parameters depend on the electric charge, $Q_{q/e}$, in units of the positron charge, and on the third component of the weak-isospin of the fermion, $I^3_{\text{L},q/e}$. In terms of $\sin^2\theta_{\text{W}}$, they are given by

$$\begin{aligned}
g_A^{q/e} &= \sqrt{\rho_{\text{NC},q/e}}\, I^3_{\text{L},q/e} ,\\
g_V^{q/e} &= \sqrt{\rho_{\text{NC},q/e}}\left(I^3_{\text{L},q/e} - 2Q_{q/e}\kappa_{\text{NC},q/e}\,\sin^2\theta_{\text{W}}\right) .
\end{aligned} \tag{5.8}$$

The coefficient $\varkappa_Z$ is calculated as

$$\varkappa_Z(Q^2) = \frac{Q^2}{Q^2+M_Z^2}\frac{1}{4\sin^2\theta_{\text{W}}\cos^2\theta_W} = \frac{Q^2}{Q^2+M_Z^2}\frac{G_{\text{F}}M_Z^2}{2\sqrt{2}\pi\alpha} ,$$

i.e. taking into account either the weak mixing angle, $\sin^2\theta_{\text{W}} = 1 - M_{\text{W}}^2/M_{\text{Z}}^2$, which is calculated from the the W and Z boson masses M_{W} and M_{Z}, or alternatively using the Fermi coupling constant G_{F}.

In order to perform predictions in LO electroweak theory only two independent parameters are needed in addition to α. At higher orders, loop corrections involve a non-negligible dependence on further (mass) parameters, where the most important ones are M_t and M_H and hadronic contributions. Due on the renormalisation of the corrections and the choice of input parameters the calculations become scheme dependent. Here we adopt the on-shell scheme using M_{Z} and M_{W} as input parameters to the calculations.

Subsequently, the cross section and also all other parameters are predictions within the EW formalism and can be used to test the validity of the electroweak theory. Reasonable examples are determinations of (all) the weak neutral current couplings, g_A^f and g_V^f with $f = (e, \mu, \tau, u, d, s, c, b, t)$, or more general the $\rho_{\mathrm{NC},f}$ and $\kappa_{\mathrm{NC},f}$ factors. These can be done either in the scale-indpendent LO approximation, by taking the scale-dependent loop corrections from theory, or their effective values can be determined at different scales. More commonly though, the effective weak mixing angle $\sin\theta^{\mathrm{eff}}_{\mathrm{W},f} := \kappa_{\mathrm{NC},q/e}\ \sin^2\theta_{\mathrm{W}}$ is tested at different scales, while also this quantity has an important scheme dependent component (see Ref. **??** for a concise dicsuccion). Noteworthy, most of the precision measurements are performed in the time-like domain, i.e. $+\mu^2$, whereas DIS is mediated by space-like momentum transfer, $Q^2 = -q^2$. In DIS at the LHeC, in addition, a large kinematic range can be tested.

Complementary, the measurement of the weak boson masses yields an interesting testing case of the theory, in particular the measurement of M_{W}. This is because M_{W} can be considered as input parameter to the formalism, or alternatively, if the precision measurement of G_{F} is been taken as input [56], then M_{W} becomes a prediction and can be confronted with the measurement directly.

[57]

5.5.2 Methodology of a combined EW and QCD fit

The expected uncertainties of the electroweak parameters are obtained in a combined fit of electroweak parameters and the PDFs, where the inclusive NC and CC DIS pseudo-data (see sect. 5.3.1) are taken as data. In this way, uncertainties from the PDFs are taken into account, which is very reasonable, since the PDFs will predominantly be determined from those LHeC data in the future. The details of the PDF fit are altogether fairly similar to the PDF fits outlined in sect. 5.3.3, but additionally EW effects are included into the calculation by considering the full set of 1-loop electroweak corrections [**?**]. The pQCD predictions are performed in the zero-mass VFN-scheme, and the χ^2 quantity, which is input to the minimisation and error propagation is based on normal-distributed relative uncertainties, such avoiding a dependence on the actual size of the cross sections.

5.5.3 Weak boson masses M_W and M_Z

The expected uncertainties for a determination of M_{W} and M_{Z}, are determined in the PDF+EW-fit, where one of the masses is determined together with the PDFs, while the other mass parameter as taken as external input. The expected uncertainties of M_{W} are

$$\Delta M_{\mathrm{W}}(\text{LHeC-60}) = \pm 14_{(\mathrm{exp})} \pm 10_{(\mathrm{PDF})}\,\mathrm{MeV} \quad \text{and}$$
$$\Delta M_{\mathrm{W}}(\text{LHeC-50}) = \pm 14_{(\mathrm{exp})} \pm 10_{(\mathrm{PDF})}\,\mathrm{MeV}$$

for LHeC with $E_e = 60\,\mathrm{GeV}$ or $50\,\mathrm{GeV}$, respectively. The breakdown into experimental and PDF uncertainties is obtained by repeating the fit with PDF parameters fixed. These uncertainties are displayed in figure 5.20 and compared to the value obtained by H1 [58] and to the PDG value [**?**]. In addition, uncertainties when performing our PDF+EW-fit to the final combined HERA data [**?**] or to the simulated FCC-eh data are shown. In case, the dominating uncorrelated uncertainties can be reduced from the prospected $\Delta\sigma = 0.5\,\%$ to $\Delta\sigma = 0.25\,\%$, a precision of M_{W} of up to

$$\Delta M_{\mathrm{W}}(\text{LHeC-60}) = \pm 14_{(\mathrm{exp})} \pm 10_{(\mathrm{PDF})}\,\mathrm{MeV} \quad \text{and}$$
$$\Delta M_{\mathrm{W}}(\text{LHeC-50}) = \pm 14_{(\mathrm{exp})} \pm 10_{(\mathrm{PDF})}\,\mathrm{MeV}$$

for LHeC-60 and LHeC-50 may be achieved, respectively. A complete dependence of ΔM_{W} on the size of the uncorrelated uncertainty, and the normalisation uncertainty is diplayed in figure **??**. The prospected

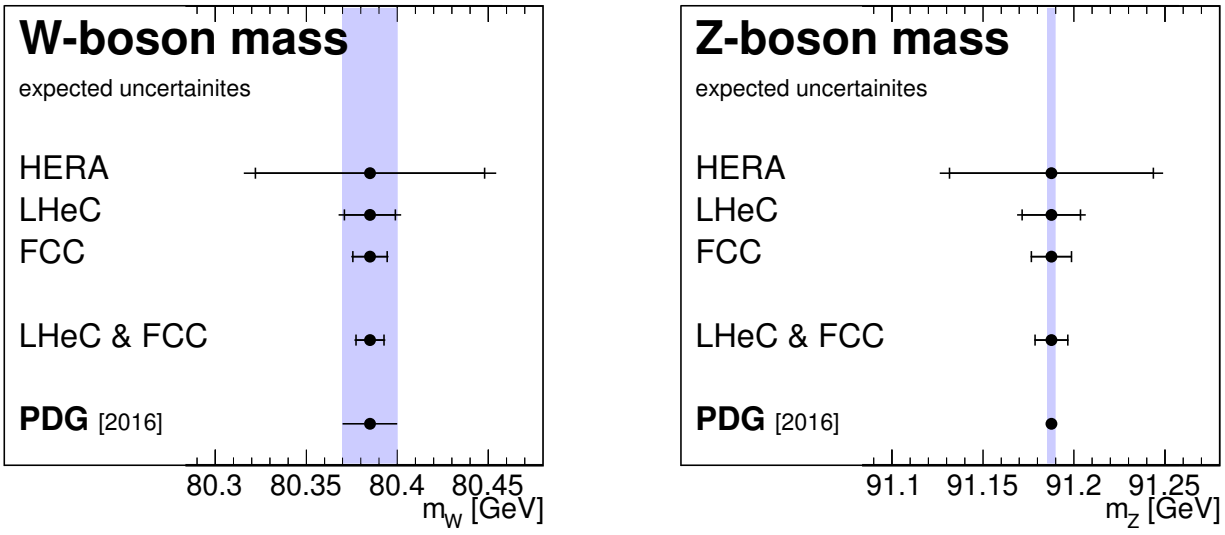

Figure 5.19: Measurements of the W-boson mass (left) and Z-boson mass (right) from HERA, LHeC and FCC-eh (simulated) data and compared to the PDG values.

Figure 5.20: Comparison of the precision for M_{W} for LHeC for different sizes of the uncorrelated or normalisation uncertainty.

measurement of the W-boson mass with LHeC data will be among the most precise measurements and will significantly improve the world average value of M_{W}, which is currently dominated by the ATLAS measurement [59].

While the measurement of M_{W} are competitive with other measurements, the expected uncertainties of M_{Z} are about 19 MeV and 11 MeV for LHeC-60 and LHeC-50, respectively, and are thus of similar size than those of M_{W}. Therefore, the precision of M_{Z} cannot compete with the precise measurements at the Z-pole by LEP+SLD, and future e^+e^- colliders may even improve on that.

5.5.4 Further mass determinations

The inclusive DIS data are sensitive to the top-quark mass M_t through radiative corrections, and the M_t dependent terms are the dominant corrections for the vertex and the propagator self-energies. They are considered in the ρ and κ parameters and in the correction factor Δr, where and the leading contributions are proportional to $G_{\mathrm{F}} M_t^2$. This allows for an indirect determination of the top-quark mass using LHeC inclusive DIS data, and an uncertainty of $\Delta M_t = 888$ GeV can be achieved. In case, the dominating uncorrelated uncertainties of the DIS data can be reduced to $\Delta\sigma = 0.25$, ΔM_t becomes as small as 888 GeV. This would greatly improve over the limited precision obtained with the final H1 data [**?**], and would represent a very precise indirect determination of the top-quark mass.

More generally, and to some extent dependent on the choice of the renormalisation scheme, the leading self-energy and vertex corrections are proportional to $\frac{M_t^2}{M_{\mathrm{W}}^2}$ and thus a simultaneous determination of M_t and M_{W} is desirable. The prospects for a simultaneous determination of M_t and M_{W} is displayed in figure 5.21. It is remarakable, that the precision of the LHeC is expected to be superior than the the LEP combination, which combines results from all of the four LEP experiments and the SLD experiment. In figure 5.21, also the 68 % confidence level is displayed for a fit without PDF parameters. This result suggests, that the

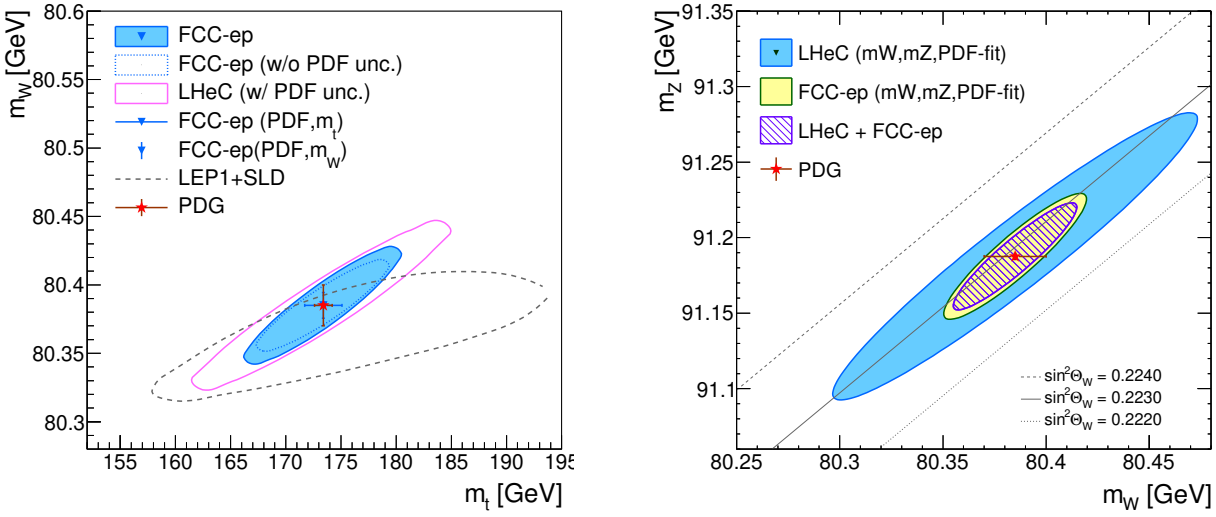

Figure 5.21: Simultaneous determination of the top-quark mass and W-boson mass from LHeC-50 or LHeC-60 data (left). Simultaneous determination of the W-boson and Z-boson masses from LHeC-50 or LHeC-60 data (right).

determination of the EW parameters is to a large extent independent on the QCD phenomenology and the PDFs.

The subleading contributions to the vertex and self-energy corrections have a Higgs-boson mass dependence and are proportional to $\log \frac{M_H^2}{M_W^2}$. When fixing all other parameters the Higgs boson mass could be determined indirectly through these loop corrections with a precision of $\Delta m_H = 888\,\text{GeV}$ and $\Delta m_H = 888\,\text{GeV}$ for $E_e = 60\,\text{GeV}$ or $50\,\text{GeV}$, respectively.

5.6 Direct W and Z production

5.6.1 Anomalous Triple Gauge Couplings

5.7 Top-Quark Physics [Christian Schwanenberger]

This is from the EURO2020. SM top quark production at a future ep collider is dominated by single top quark production, mainly via CC DIS production. The total cross section is 1.73 pb at the LHeC [?] with an electron beam energy of 60 GeV. The other important top quark production mode is $t\bar{t}$ photoproduction with a total cross section of 23 fb at the LHeC [?]. This makes a future LHeC collider a top quark factory and an ideal tool to analyze top quarks with a high precision, in particular their electroweak interaction. Top quark physics at the LHeC represents a very rich and diverse field of research involving not only high precision measurements of top quark properties, but also senstive searches for new physics as outlined here.

One flagship measurement is the direct measurement of the CKM matrix element $|V_{tb}|$, i.e. without making any model assumptions such as on the unitarity of the CKM matrix or the number of quark generations. A detailed analysis of the single top quark CC DIS process at the LHeC shows that already at 100 fb^{-1} of integrated luminosity an uncertainty of 1% can be expected. This compares to a total uncertainty of 4.1% of the currently most accurate result at the LHC Run-I performed by the CMS experiment. The same analysis can also be used to search for anomalous left-handed (L), and right-handed (R) Wtb vector (1) and tensor (2) couplings $f_{L,R}^{1,2}$ [?]. In the SM $f_L^1 = 1$ (with $f_L^1 \equiv 1 + \Delta f_L^1$), and $f_R^1 = f_L^2 = f_R^2 = 0$. Using

hadronic top quark decays only, the expected accuracies in a measurement of these couplings as a function of the integrated luminosity are presented in Fig. **??** (right). The couplings can be measured at the per cent level at 1 ab^{-1}. Similarly, the CKM matrix elements $|V_{tx}|$ ($x = d, s$) can be extracted through the analysis of W boson and bottom (light) quark associated production channels, where the W boson and b-jet (light jet) final states can be produced via s-channel single top quark decay or t-channel top quark exchange [**?**]. At 1 ab^{-1} of integrated luminosity and an electron polarization of 80%, the 2σ limits improve on existing limits from the LHC by almost an order of magnitude, and will therefore represent a direct high precision measurement of this important top quark property. In these studies, upper limits at the 2σ level down to $|V_{td}| < 0.06$ and $|V_{ts}| < 0.06$ can be achieved.

5.7.1 Single and Pair Top Production in DIS

5.7.2 Wtq Couplings

5.7.3 FCNC Top Quark Couplings

5.7.4 Top Quark Measurements and Searches for New Physics

5.8 Disentangling non-linear QCD dynamics at the LHeC [Juan Rojo, et al.]

Introduction. The LHeC will extend the kinematic reach of HERA at small-x by one order of magnitude in the perturbative regime $Q \gtrsim 1$ GeV [1]. This extension will allow unprecedented tests of the strong interaction in this extreme region, where deviations from the linear DGLAP evolution are expected to appear. In particular, it has been argued that the strong growth of the gluon PDF at small-x should eventually lead to gluon recombination [60] to avoid violating the unitary bounds. The onset of such non-linear dynamics, also known as saturation, has been extensively searched but so far there is no conclusive evidence of its presence, at least within the HERA inclusive structure function measurements. In this context, the extended kinematic range of the LHeC provides unique avenues to explore the possible onset of non-linear QCD dynamics at small-x. The discovery of saturation, a radically new regime of QCD, would then represent an important milestone in our understanding of the strong interactions.

The main challenge in disentangling saturation lies in the fact that non-linear corrections are expected to be moderate even at the LHeC, since they are small (if present at all) in the region covered by HERA. Therefore, great care needs to be employed in order to separate such effects from those of standard DGLAP linear evolution. Indeed, it is well known that HERA data at small-x in the perturbative region can be equally well described, at least at the qualitative level, both by PDF fits based on the DGLAP framework as well as by saturation-inspired models. However, rapid progress both in theory calculations and methodological developments have pushed QCD fits to a new level of sophistication, and recently it has been shown that subtle but clear evidence of BFKL resummation at small-x is present in HERA data, both for inclusive and for heavy quark structure functions [61, 62]. Such studies highlight how it should be possible to tell apart non-linear from linear dynamics using state-of-the-art fitting methods even if these are moderate, provided that they are within the LHeC reach.

Here we want to assess the sensitivity of the LHeC to detect the possible onset of non-linear saturation dynamics. This study will be carried out by generalizing a recent analysis [7] that quantified the impact of LHeC inclusive and semi-inclusive measurements on the PDF4LHC15 PDFs [63, 64] by means of Hessian profiling [65]. There, the LHeC pseudo-data was generated assuming that linear DGLAP evolution was valid in the entire LHeC kinematic range using the PDF4LHC15 set as input. To ascertain the possibility of pinning down saturation at the LHeC, here we have revisited this study but now generating the LHeC

pseudo-data by means of a saturation-inspired calculation. By monitoring the statistical significance of the tension that will be introduced (by construction) between the saturation pseudo-data and the DGLAP theory assumed in the PDF fit, we aim to determine the likelihood of disentangling non-linear from linear evolution effects at the LHeC. See also [66] for previous related studies along the same direction.

Analysis settings. In this study we adopt the settings of [67, 7], to which we refer the interested reader for further details. In [7] the impact on the proton PDFs of inclusive and semi-inclusive neutral-current (NC) and charged current (CC) DIS structure functions from the LHeC was quantified. These results were then compared with the corresponding projections for the PDF sensitivity of the High-Luminosity upgrade of the LHC (HL-LHC). In the left panel of Fig. 5.22 we display the kinematic range in the (x, Q^2) plane of the LHeC pseudo-data employed in that analysis, which illustrated how the LHeC can provide unique constraints on the behaviour of the quark and gluon PDFs in the very small-x region.

Since non-linear dynamics are known to become sizable only at small-x, for the present analysis it is sufficient to consider the NC $e^- p$ inclusive scattering cross-sections from proton beam energies of $E_p = 7$ TeV and $E_p = 1$ TeV. In the right panel in Fig. 5.22 we show the bins in (x, Q^2) for which LHeC pseudo-data for inclusive structure functions has been generated according to a saturation-based calculation. Specifically, we have adopted here the DGLAP-improved saturation model of Ref. [68], in which the scattering matrix is modeled through eikonal iteration of two gluon exchanges. This model was further extended to include heavy flavour in [69]. The specific parameters that we use were taken from Fit 2 in [70], where parametrisations are provided that can be used for $x < 0.01$ and $Q^2 < 700$ GeV^2. These parameters were extracted from a fit to the HERA legacy inclusive structure function measurements [71] restricted to $x < 0.01$ and $0.045 < Q^2 < 650$ GeV^2. In contrast to other saturation models, the one we assume here [70] provides a reasonable description for large Q^2 in the small x region, where it ensure a smooth transition to standard fixed-order perturbative results.

In Fig. 5.23 we compare the $F_2(x, Q^2)$ inclusive structure function (left panel) and its logarithmic slope in x (right panel) as a function of Q^2, comparing the results of the DGLAP and GBW (saturation) approaches. We can observe that the main qualitative difference between the two predictions is the different scaling with Q^2, where the saturation (GBW) approach predicts a softer growth of F_2 with Q^2 at small-x as compared to the DGLAP approach. Indeed, non-linear effects damp the growth of F_2, reducing it by up to a factor 2 at small-x and large Q^2. Further differences are found for the longitudinal structure function $F_L(x, Q^2)$ to which we are also sensitive in our analysis, given that the LHeC pseudo-data corresponds to the reduced cross-section $\widetilde{\sigma}^{ep}_{NC}$ which receives contributions both from F_2 and F_L. As we will shown below, the fact that the two formalisms lead to different scalings with Q^2 is crucial in order to disentangle them at the LHeC.

Note that the above discussion refers only to the generated LHeC pseudo-data: all other aspects of the QCD analysis of [7] are left unchanged. In particular, the PDF profiling will be carried out using theory calculations obtained by means of DGLAP evolution with the NNLO PDF4LHC15 set (see also [72]), with heavy quark structure functions evaluated by means of the FONLL-B general-mass variable flavour number scheme [73]. In order to ensure consistency with the PDF4LHC15 prior, here we will replace the DGLAP pseudo-data by the saturation calculation only in the kinematic region for $x \lesssim 10^{-4}$, rather than for all the bins indicated in red in Fig. 5.22. The reason for this choice is that PDF4LHC15 already includes HERA data down to $x \simeq 10^{-4}$ which is successfully described via the DGLAP framework, and therefore if we assume departures from DGLAP in the LHeC pseudo-data this should only be done for smaller values of x.

Results and discussion. Using the analysis settings described above, we have carried out the profiling of PDF4LHC15 with the LHeC inclusive structure function pseudo-data, which for $x \leq 10^{-4}$ ($x > 10^{-4}$) has been generated using the GBW saturation (DGLAP) calculations, and compare them with the results of the profiling where the pseudo-data follows the DGLAP prediction. We have generated $N_{\rm exp} = 500$

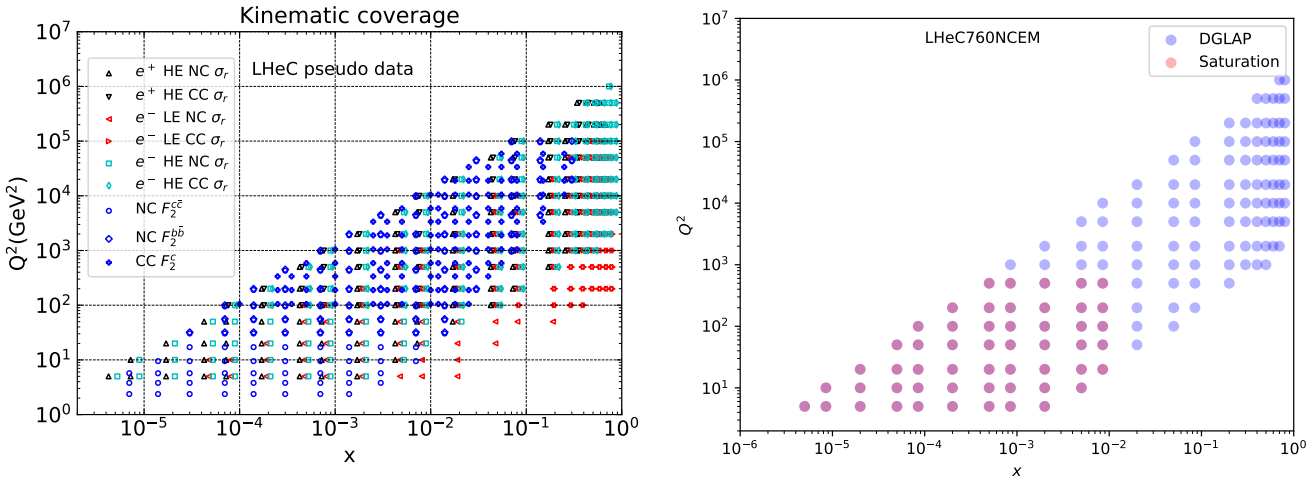

Figure 5.22: Left plot: the kinematic range in the (x, Q^2) plane of the LHeC pseudo-data on inclusive and semi-inclusive DIS structure functions used in the PDF projections of [7]. Right plot: the kinematic coverage of the NC e^-p scattering pseudo-data at the LHeC, where the blue (red) points indicate those bins for which DGLAP (saturation) predictions are available.

independent sets LHeC pseudo-data, each one characterised by different random fluctuations (determined by the experimental uncertainties) around the underlying central value.

To begin with, it is instructive to compare the data versus theory agreement, $\chi^2/n_{\rm dat}$, between the pre-fit and post-fit calculations, in order to assess the differences between the DGLAP and saturation cases. In the upper plots of Fig. 5.24 we show the distributions of pre-fit and post-fit values of $\chi^2/n_{\rm dat}$ for the $N_{\rm exp} = 500$ sets of generated LHeC pseudo-data. We compare the results of the profiling of the LHeC pseudo-data based on DGLAP calculations in the entire range of x with those where the pseudo-data is based on the saturation model in the region $x < 10^{-4}$. Then in the bottom plot we compare of the post-fit χ^2 distributions between the two scenarios. Note that in these three plots the ranges in the x axes are different.

From this comparison we can observe that for the case where the pseudo-data is generated using a consistent DGLAP framework (PDF4LHC15) as the one adopted for the theory calculations used in the fit, as expected the agreement is already good at the pre-fit level, and it is further improved at the post-fit level. However the situation is rather different in the case where a subset of the LHeC pseudo-data is generated using a saturation model: at the pre-fit level the agreement between theory and pseudo-data is poor, with $\chi^2/n_{\rm dat} \simeq 7$. The situation markedly improves at the post-fit level, where now the $\chi^2/n_{\rm dat}$ distributions peaks around 1.3. This result implies that the DGLAP fit manages to absorb most of the differences in theory present in the saturation pseudo-data. This said, the DGLAP fit cannot entirely "fit away" the non-linear corrections: as shown in the lower plot of Fig. 5.24, even at the post-fit level one can still tell apart the $\chi^2/n_{\rm dat}$ distributions between the two cases, with the DGLAP (saturation) pseudo-data peaking at around 0.9 (1.3). This comparison highlights that it is not possible for the DGLAP fit to completely absorb the saturation effects into a PDF redefinition.

In order to identify the origin of the worse agreement between theory predictions and LHeC pseudo-data in the saturation case, it is illustrative to take a closer look at the pulls defined as

$$P(x, Q^2) = \frac{\mathcal{F}_{\rm fit}(x, Q^2) - \mathcal{F}_{\rm dat}(x, Q^2)}{\delta_{\rm exp}\mathcal{F}(x, Q^2)}\,, \tag{5.9}$$

where $\mathcal{F}_{\rm fit}$ is the central value of the profiled results for the observable $\mathcal{F}$ (in this case the reduced neutral current DIS cross-section), $\mathcal{F}_{\rm dat}$ is the corresponding central value of the pseudo-data, and $\delta_{\rm exp}\mathcal{F}$ represents the associated total experimental uncertainty. In Fig. 5.25 we display the pulls between the post-fit prediction

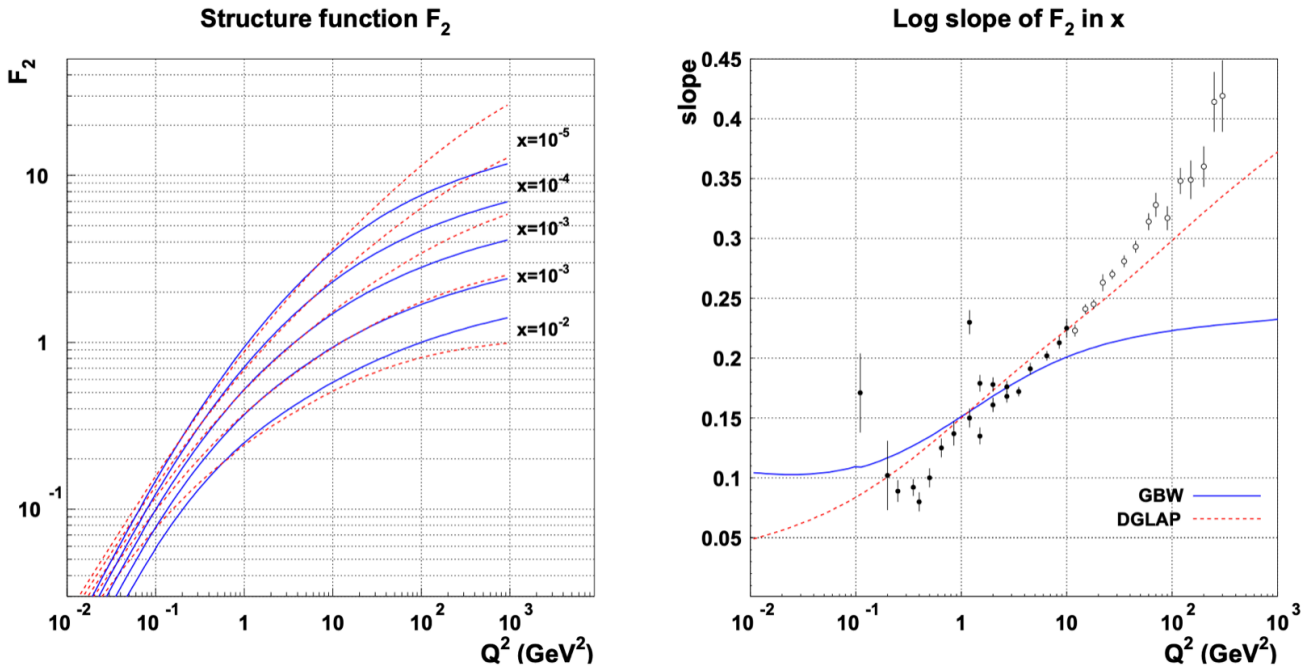

Figure 5.23: The $F_2(x, Q^2)$ inclusive structure function (left) and its logarithmic slope in x (right plot) as a function of Q^2 comparing the results of the DGLAP and GBW (saturation) approaches. In the latter case we also compare the theory calculations with available H1 and ZEUS measurements. Figure taken from Ref. [70]

and the central value of the LHeC pseudo-data for different bins in Q^2. We compare the cases where the pseudo-data has been generated using a consistent theory calculation (DGLAP) with that based on the GBW saturation model.

The comparisons in Fig. 5.25 show first of all that in the DGLAP case the pulls are $\mathcal{O}(1)$ in the entire kinematical range. This is of course expected, given that the LHeC pseudo-data is generated using the same theory as the one subsequently used for the fit. In the case where the pseudo-data has been partially generated with the saturation calculation, on the other hand, one finds a systematic tension between the theory used for the fit (DGLAP) and the one used to generate the pseudo-data (saturation). Indeed, we find that at the smallest values of x the theory prediction undershoots the data by a significant amount, while at higher x the opposite behaviour takes place. One can also see that in the region $10^{-4} \lesssim x \lesssim 10^{-3}$ the fit overshoots the pseudo-data by a large amount.

These comparisons highlight how a QCD fit to the saturation pseudo-data is obtained as a compromise between opposite trends: the theory wants to overshoot the data at very small x and overshoot it at larger values of x. These tensions result in a distorted fit, explaining the larger $\chi^2/n_{\rm dat}$ values as compared to the DGLAP case. Such a behaviour can be partially traced back by the different scaling in Q^2 between DGLAP and GBW shown in Fig. 5.23: while a difference x dependence could eventually be absorbed into a change of the PDFs at the parametrisation scale Q_0, this is not possible with a Q^2 dependence.

The pull analysis of Fig. 5.25 highlights how in order to tell apart linear from non-linear QCD evolution effects at small-x it would be crucial to ensure a lever arm in Q^2 as large as possible in the perturbative region. This way it becomes possible to disentangle the different scaling in Q^2 for the two cases. The lack of a sufficiently large lever arm in Q^2 at HERA at small x could explain in part why both frameworks are able to describe the same structure function measurements at the qualitative level. Furthermore, we find that amplifying the significance of these subtle effects can be achieved by monitoring the χ^2 behaviour in the Q^2 bins more affected by the saturation corrections. The reason is that the total χ^2, such as that reported in

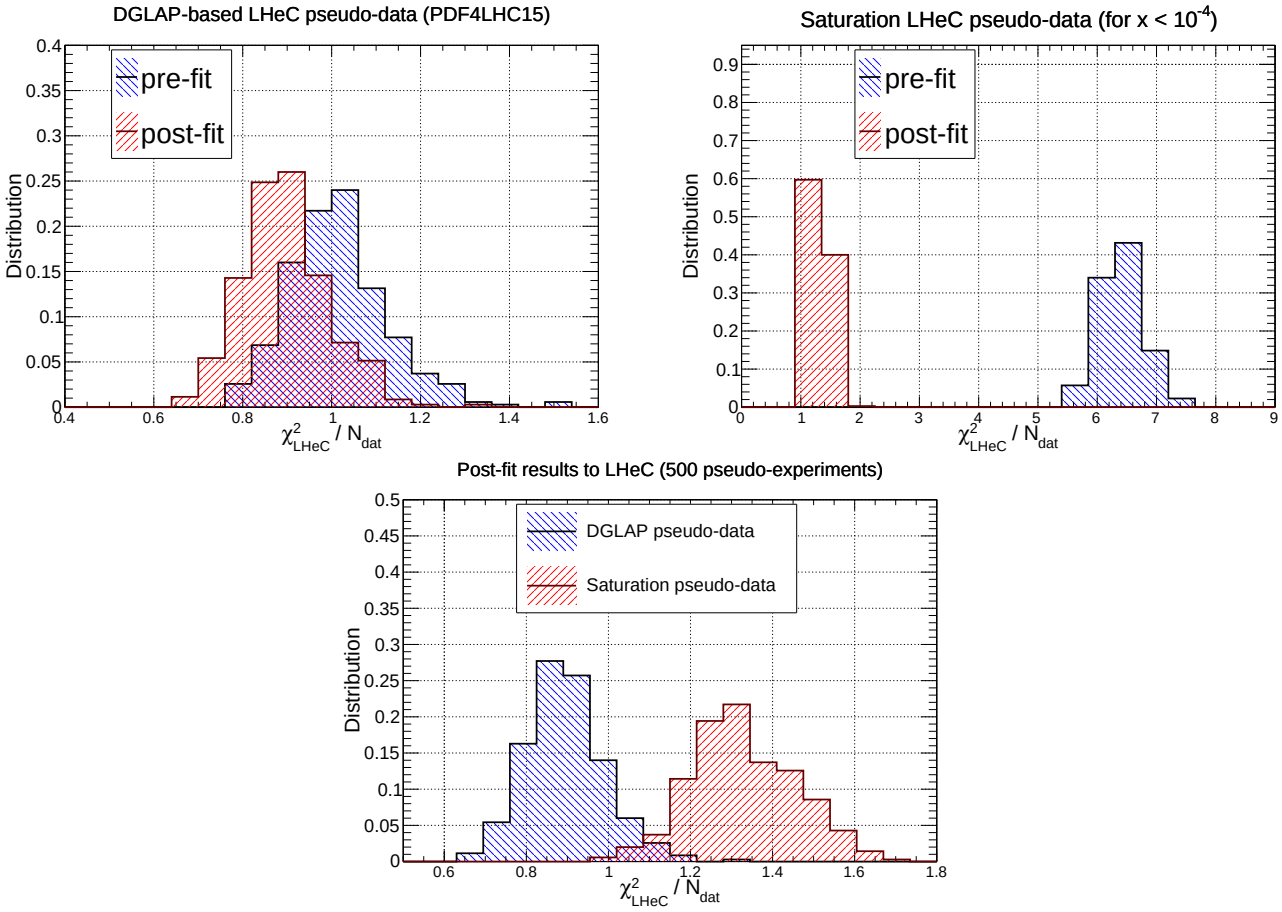

Figure 5.24: Upper plots: the distribution of pre-fit and post-fit values of $\chi^2/n_{\rm dat}$ for the $N_{\rm exp} = 500$ sets of generated LHeC pseudo-data. We compare the results of the profiling of the LHeC pseudo-data based on DGLAP calculations in the entire range of x (left) with those where the pseudo-data is based on the saturation model in the region $x < 10^{-4}$ (right plot). Bottom plot: comparison of the post-fit $\chi^2/n_{\rm dat}$ distributions between these two scenarios for the pseudo-data generation.

Fig. 5.24, is somewhat less informative since the deviations at small-Q are washed out by the good agreement between theory and pseudo-data in the rest of the kinematical range of the LHeC summarised in Fig. 5.22.

To conclude this analysis, in Fig. 5.26 we display the comparison between the PDF4LHC15 baseline with the results of the PDF profiling of the LHeC pseudo-data for the gluon (left) and quark singlet (right) for $Q = 10$ GeV. We show the cases where the pseudo-data is generated using DGLAP calculations and where it is partially based on the GBW saturation model (for $x \lesssim 10^{-4}$). We find that the distortion induced by the mismatch between theory and pseudo-data in the saturation case is typically larger than the PDF uncertainties expected once the LHeC constraints are taken into account. While of course in a realistic situation such a comparison would not be possible, the results of Fig. 5.26 show that saturation-induced effects are expected to be larger than the typical PDF errors in the LHeC era, and thus that it should be possible to tell them apart using for example tools such as the pull analysis of Fig. 5.25 or other statistical methods.

Summary. Here we have assessed the feasibility of disentangling DGLAP evolution from non-linear effects at the LHeC. By means of a QCD analysis where LHeC pseudo-data is generated using a saturation model, we have demonstrated that the LHeC should be possible to identify non-linear effects with large statistical significance, provided their size is the one predicted by current calculations such as the that of [70] that

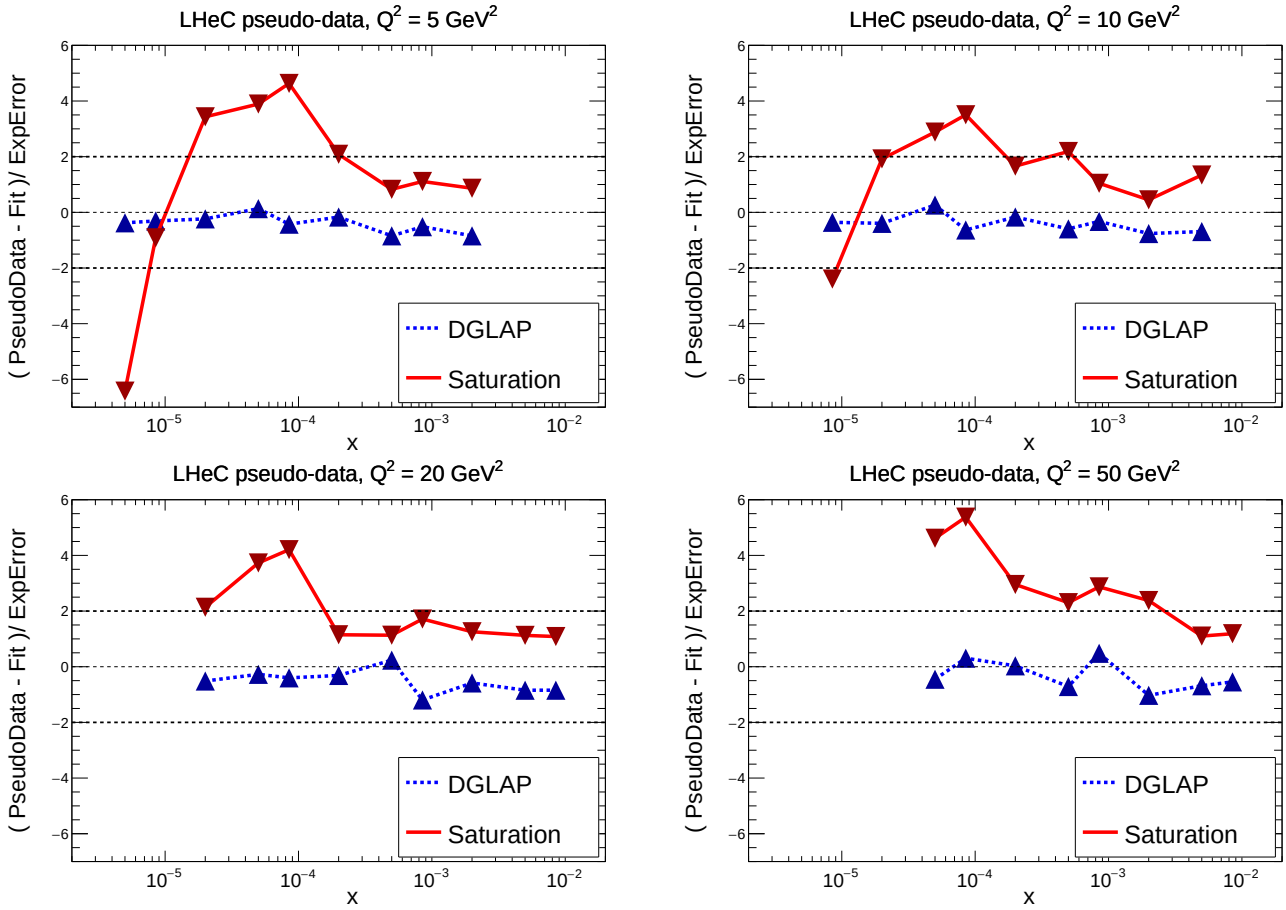

Figure 5.25: The pulls between the post-fit prediction and the central value of the LHeC pseudo-data, Eq. (5.9), for four different bins in Q^2. We compare the results of the profiling where the LHeC pseudo-data has been generated using a consistent DGLAP theory with that partially based on the saturation calculations.

have been tuned to HERA data. A more refined analysis would require to study whether or not small-x BFKL resummation effects can partially mask the impact of non-linear dynamics, though this is unlikely since the main difference arises in their Q^2 scaling. The discovery of non-linear dynamics would represent an important milestone for the physics program of the LHeC, demonstrating the onset of a new gluon-dominated regime of the strong interactions and paving the way for detailed studies of the properties of this new state of matter. Such discovery would have also implications outside nuclear and particle physics, for instance it would affect the theory predictions for the scattering of ultra-high energy neutrinos with matter [74].

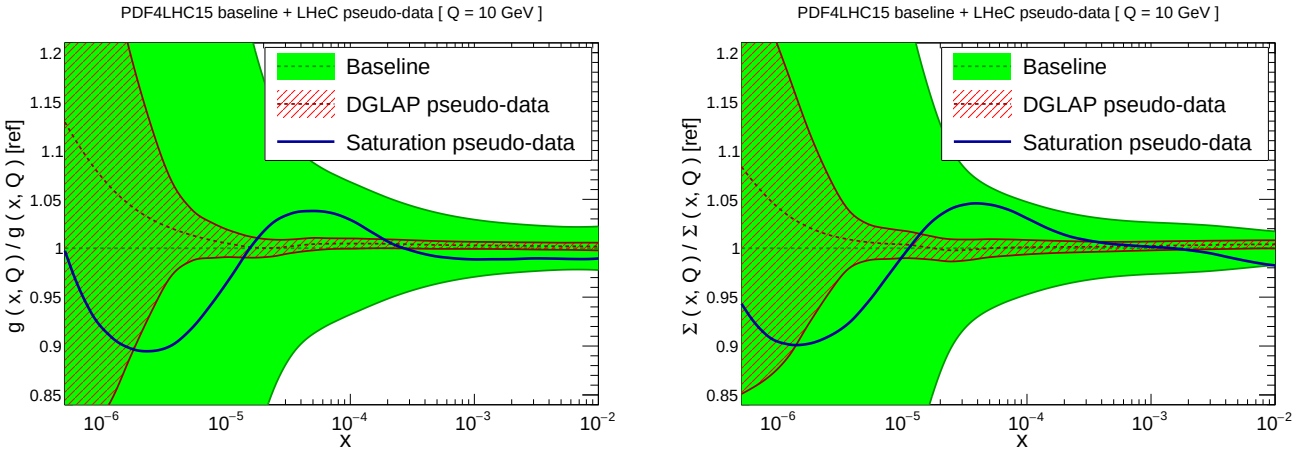

Figure 5.26: Comparison between the PDF4LHC15 baseline (green band) with the results of the profiling of the LHeC pseudo-data for the gluon (left) and quark singlet (right) for $Q = 10$ GeV. We show the cases where the pseudo-data is generated using DGLAP calculations (red hatched band) and where it is partially based on the GBW saturation model (blue curve).

Chapter 6

Nuclear Particle Physics with Electron-Ion Scattering at the LHeC [Nestor Armesto]

Example reference: LHeC [1]

6.1 Introduction [Anna Stasto]

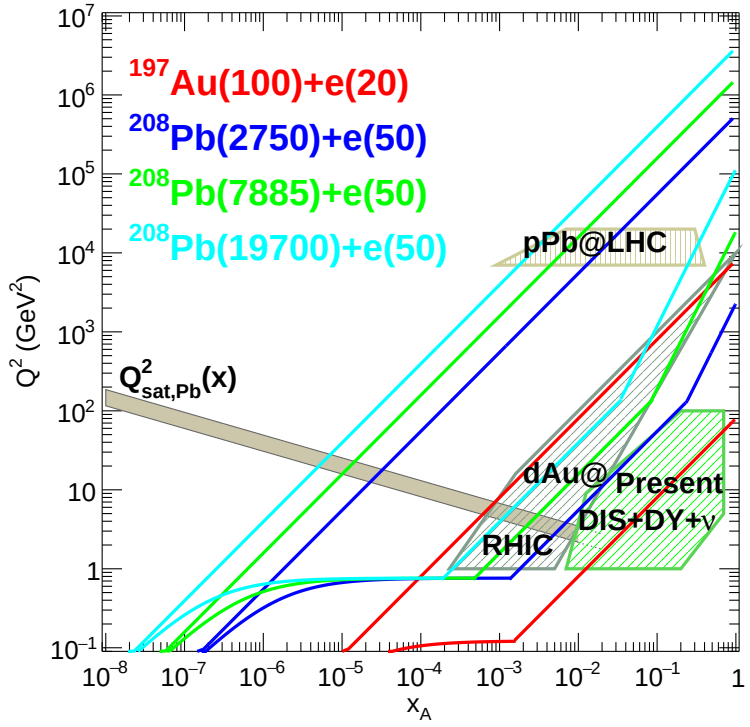

Figure 6.1: Kinematic regions in the $x - Q^2$ plane explored by different data sets (charged lepton and neutrino DIS, DY, dAu at RHIC and pPb at the LHC) used in present nPDF analyses [75], compared to the ones achievable at the EIC (red), the LHeC (ERL against the HL-LHC beams, dark blue) and two FCC-eh versions ($E_p = 20\,\text{TeV}$ - green and $E_p = 50\,\text{TeV}$ - light blue). Acceptance of the detector for the electrons is taken to be $1^\circ < \theta < 179^\circ$, and $0.01(0.001) < y < 1$ for the EIC (all other colliders).

Here we should discuss the different subjects along the sections, their theoretical relevance, present status and prospects for the LHeC. The kinematic plot has been updated to include the 40 TeV option.

6.2 Nuclear Parton Densities [Nestor Armesto]

PDFs are essential ingredients in our understanding of the dynamics of strong interaction. First, they encode important information about the structure of hadrons [76, 77]. Second, they are indispensable for the description of hadronic collisions within standard collinear factorisation [78]. Concerning nuclei, it has been known for more than 40 years that structure functions are affected by the nuclear environment [79, 80] so that they cannot be interpreted as a superposition of structure functions of free nucleons. In the standard approach, within the collinear factorization, the nuclear modification is included in the parametrization of the parton densities. This means that the parton densities in a bound nucleon are different than those in a free nucleon, and the difference is enoded in the non-perturbative initial conditions of the parton densities at some low, initial scale Q_0^2. The present status of nuclear parton densities (nPDFs), see for example [**?**, 81], can be summarised as follows:

- Modern analysis [82, 83, 84, 75] are performed at next-to-leading order (NLO) and next-to-next-to-leading order (NNLO) [85, 86]. Differences between them mainly arise from the different sets of data included in the analysis[1] and from the different functional forms employed for the initial conditions.
- Many sets of data are presented as ratios of cross section for a given nucleus over that in deuterium. Therefore, it has become customary to work in terms of ratios of nPDFs:

$$R_i(x,Q^2) = \frac{f_i^{\rm A}(x,Q^2)}{A f_i^{\rm p}(x,Q^2)} \ , \quad i = u,d,s,c,b,g,\ldots ,$$

  with $f_i^{{\rm p}(A)}(x,Q^2)$ the corresponding parton density in a free proton p or in nucleus A. These nuclear modification factors are parametrised at some initial scale Q_0^2 (assuming isospin symmetry to hold). The nPDFs are then obtained multiplying the nuclear modification factors by some given set of free proton PDFs.
- Data come from a large variety of nuclei and the number of data points for any of them is very small compared to the proton analysis. The most up to date analyses include between 1000 and 2000 data points for 14 nuclei. In particular, for the Pb nucleus, there are less than 50 points coming from the fixed target Deep Inelastic Scattering (DIS) and Drell-Yan (DY) experiments and from particle production data in pPb collisions at the Large Hadron Collider (LHC). The fit for a single nucleus is therefore impossible and the modelling of the A-dependence of the parameters in the initial conditions becomes mandatory [75, 84].
- The kinematic coverage in Q^2 and x with existing data is very small compared to the requirements of present hadronic colliders. The ultimate precision and large coverage of the kinematic plane for nPDFs can only be provided by the high energy electron-ion collider. Meanwhile, the only experimental collision system where nPDFs can be potentially be constrained are hadronic and ultraperipheral collisions (UPCs). It is important to stress though, that extracting PDFs from these collisions presents many theoretical challenges. These are related to the question of applicability of the collinear factorization for nuclear collisions, higher twist effects, scale choices and other theoretical uncertainties.

All in all, all parton species are very weakly constrained at small $x < 10^{-2}$ [87], gluons at large $x > 0.2$, and the flavour decomposition is largely unknown - a natural fact for u and d due to the approximate isospin symmetry in nuclei[2]. The impact of presently available LHC data, studied using reweighting [65, 88]

[1] The main difference lies on the use or not of neutrino-Pb cross sections from CHORUS and π^0 transverse momentum spectra from dAu collisions at the Relativistic Heavy Ion Collider (RHIC).

[2] The u-d difference is suppressed by a factor $2Z/A - 1$.

in [89, 90] and included in the fit in [75], is quite modest with some constrains on the gluon and the strange quark in the region $0.01 < x < 0.3$. On the other hand, theoretical predictions for nuclear shadowing of quark and gluon PDFs based on s-channel unitarity and diffractive nucleon PDFs are available down to $x \sim 10^{-4} - 10^{-5}$ [91, 92].

Future runs at the LHC will offer several possibilities for improving our knowledge on nPDFs [93]. But the ideal place to determine parton densities is DIS. Either the electron-ion colliders at the US, the Electron Ion Collider (EIC) [94] or, in a much larger kinematic domain (see Fig. 6.1), at the LHeC. DIS measurements in such configurations offer unprecedented possibilities to enlarge our knowledge on parton densities through a complete unfolding of all flavours.

In the following, we show the possibilities for constraining the PDFs for a Pb nucleus at the LHeC. In the next subsection, Subec. 6.2.1 we discuss the corresponding pseudodata for the inclusive cross section in electron-nucleus scattering. Next, in Subsec. 6.2.2, we discuss how the pseudodata will be introduced in a global nPDF fit. Finally in Subsec. 6.2.3, it is demonstrated how the PDF of Pb can be extracted with a very good precision from the LHeC data only, without any resource to any other set of data.

6.2.1 Pseudodata [Max Klein]

The LHeC provides measurements of eA scattering cross sections in the deep inelastic scattering region $Q^2 > 1\,\mathrm{GeV}^2$ reaching to values of Q^2 up to about $5 \cdot 10^5\,\mathrm{GeV}^2$ and corresponding x values between a few times 10^{-6} and near to $x = 1$. This enables the determination of a complete set of nPDFs in electron-lead scattering at the LHC from the inclusive neutral and charged current cross sections with a clean separation of up and down valence and sea quark distributions. The very high Q^2 which reaches much beyond the W mass squared makes the CC measurements extremely valuable for the separation of different flavours when taken together with the NC, from photon and Z boson exchange. Charm tagging in CC determines the anti-strange quark distribution in a wide kinematic range to typically $10 - 20\,\%$ precision, while charm and beauty tagging in NC provide high precision determinations of xc and xb from nuclei. Using coherent data from just this, one experiment the uncertainties of these nPDFs will follow from a straightforward $\Delta\chi^2 = 1$ criterion.

The QCD analyses illustrated subsequently of pseudo LHeC cross section data employ sets of simulated NC and CC measurements under assumptions which are summarised in Table 6.1, see [95]. The cross section simulation was done numerically employing derivative formulae from [96] and found to compare well to a detailed Monte Carlo simulation when tested for the conditions of the H1 experiment. The assumptions made are all reasonable when comparing with the H1 achievements, which shall probably be exceeded owing to new detector techniques and higher statistics. The control of radiative corrections in eA scattering is a special challenge as these grow $\propto Z^2$. The LHeC detector thus needs to be equipped with reliable photon detectors and the exploitation of the energy-momentum conservation, via the $E - p_z$ cut, should further reduce the effect of photon radiation to a few per cent level. It is also to be noted that the semi-inclusive measurements of the s, c and b quark distributions carry additional uncertainties for tagging, acceptance and background influences.

Fig. 6.2 illustrates the kinematic reach of the NC+CC pseudodata at the LHeC and the FCC-eh, in ep and ePb collisions. Besides, The LHeC is the ideal environment to determine the strange, charm and beauty (also the top) PDFs. The principal technique is charm tagging (in CC for xs, in NC for xc) and beauty tagging (in NC for xb). The beam spot of the LHeC has the transverse extension of about $(7\,\mu\mathrm{m})^2$. Modern Silicon detectors have a resolution of a few microns to be compared with typical decay lengths of charm and beauty particles of hundreds of μm. The experimental challenges then are the beam pipe radius, coping at the LHeC with strong synchrotron radiation effects, and the forward tagging acceptance, similar to the HL-LHC challenges.

Table 6.1: Summary of assumed uncertainties for future inclusive cross section measurements at the LHeC.

Source of uncertainty	Error on the source or cross section
scattered electron energy scale	0.1 %
scattered electron polar angle	0.1 mrad
hadronic energy scale	0.5 %
calorimeter noise ($y < 0.01$)	1-3 %
radiative corrections	1-2 %
photoproduction background	1 %
global efficiency error	0.7 %

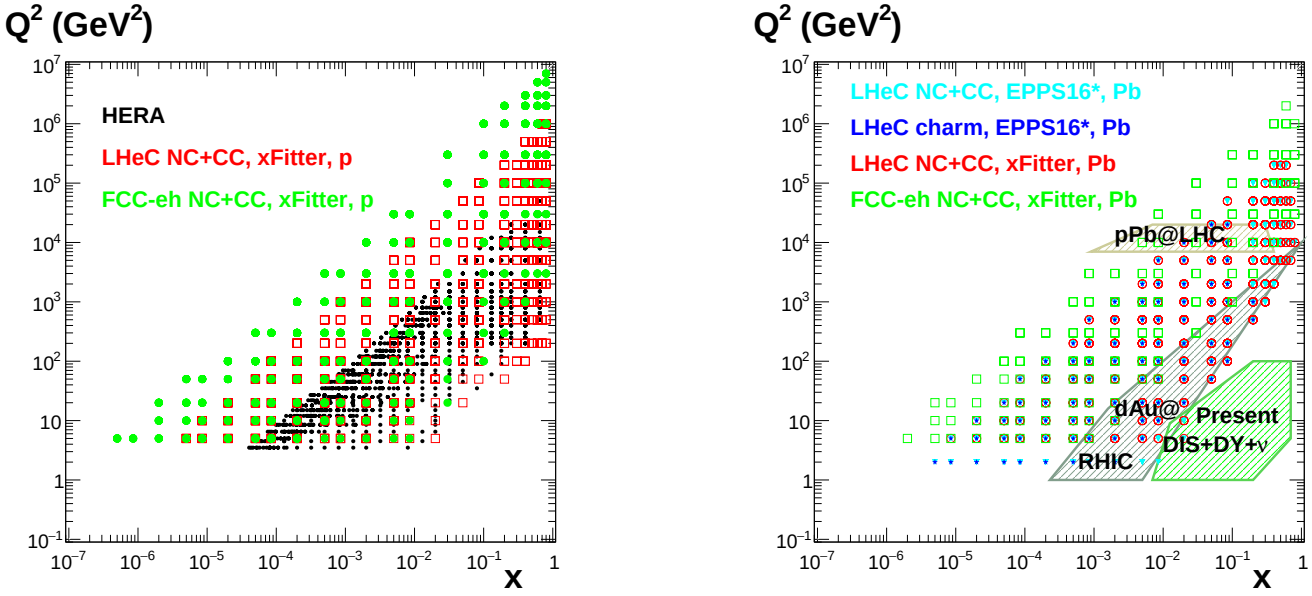

Figure 6.2: *Left*: kinematic $x - Q^2$ plot of the NC+CC pseudodata on a proton at the LHeC (red symbols) and the FCC-eh (green symbols) used in the xFitter analysis in Subsec. 6.2.3; data used in analysis at HERA (black symbols) are shown for comparison. *Right*: kinematic $x - Q^2$ plot of the pseudodata on Pb used in the EPPS16 analysis at the LHeC (NC+CC, light blue symbols, and charm, dark blue symbols) in Subsec. 6.2.2, and in the xFitter analysis in Subsec. 6.2.3 (at the LHeC, red symbols, and the FCC-eh, green symbols); the regions explored by currently available data sets (charged lepton and neutrino DIS, DY, dAu at RHIC and pPb at the LHC) used in present nPDF analyses [75] are shown for comparison.

A study was made of the possible measurements of the anti-strange density (Fig. 6.3 top) using impact parameter tagging in eA CC scattering, and of the charm and beauty structure functions in NC (Figs. 6.3 middle and 6.3 bottom respectively). Following experience on heavy flavour tagging at HERA and ATLAS, assumptions were made on the charm and beauty tagging efficiencies, to be 10 % and 60 %, respectively. The light quark background in the charm analysis is assumed to be controllable to per cent level, while the charm background in the beauty tagging sample is assumed to be 10 %. The tagging efficiencies and background contaminations affect the statistical error. Moreover, an additional systematic error is assumed in the simulated NC (CC) measurements of 3 (5) %. These results in very promising measurements of the heavier quark distributions: to about $10 - 20$ % total uncertainty on the strange and $3 - 5$ % on the charm and beauty measurements, for typically x between 10^{-4} and 0.1 and Q^2 extending from below threshold m_Q^2 up to a few times $10^4\,\mathrm{GeV}^2$. The knowledge of the heavy quark densities is of prime relevance for understanding nuclear structure and the development of QCD as has often been emphasised.

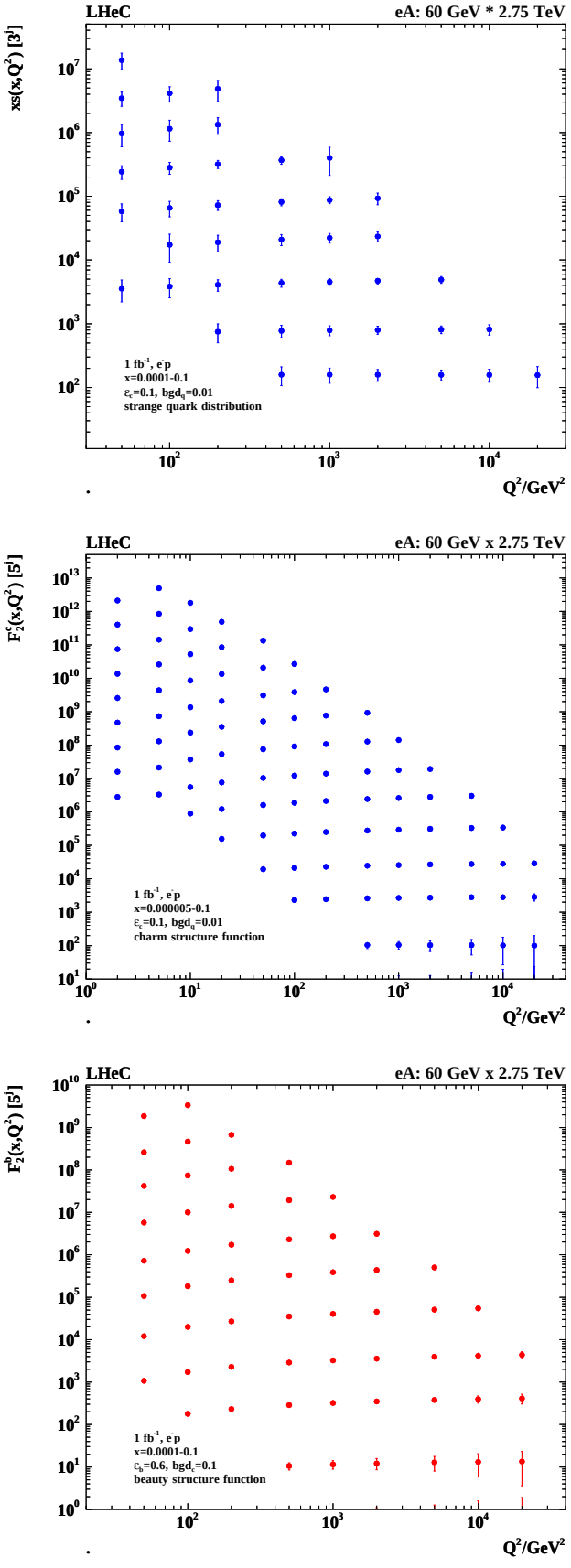

Figure 6.3: *Top*: Simulation of the measurement of the (anti)-strange quark distribution $x\bar{s}(x, Q^2)$ in charged current eA scattering through the t-channel reaction $W^- \bar{s} \to c$; *Middle*: Simulation of the measurement of the charm quark distribution expressed as $F_2^c = e_c^2 x(c+\bar{c})$ in neutral current eA scattering; *Bottom*: Simulation of the measurement of the bottom quark distribution expressed as $F_2^b = e_b^2 x(b+\bar{b})$ in neutral current eA scattering. The data are plotted with full systematic and statistical errors added in quadrature.

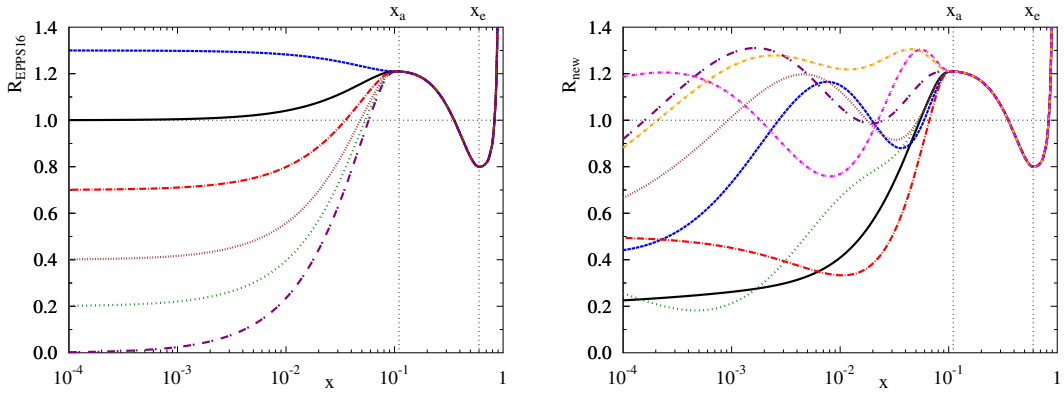

Figure 6.4: Left: Functional behaviour allowed at small x in the EPPS16 analysis. Right: Possible functional variation at small in the extended parametrization.

6.2.2 Nuclear gluon PDFs in a global-fit context [Hannu Paukkunen]

To illustrate the impact of the LHeC e-Pb pseudodata in the global context, they have been added [97] into the EPPS16 global analysis of nuclear PDFs [75]. The EPPS16 strategy is to parametrize the nuclear modification ratios $R_i(x, Q^2)$ between the bound-proton PDFs $f_i^{\mathrm{p/Pb}}$ and proton PDFs f_i^{p},

$$R_i(x, Q^2) \equiv \frac{f_i^{\mathrm{p/Pb}}(x, Q^2)}{f_i^{\mathrm{p}}(x, Q^2)}$$

at the charm mass threshold $Q^2 = m^2_{\mathrm{charm}}$. At higher Q^2 the nuclear PDFs are obtained by solving the standard DGLAP evolution equations at next-to-leading order in QCD. As the LHeC pseudodata reach to significantly lower x than the data that were used in the EPPS16 analysis, an extended small-x parametrization was used for gluons, see Figure 6.4. The framework is almost identical to that in Ref. [98]. The introduced functional form allows for rather wild – arguably unphysical – behaviour at small-x and e.g. significant enhancement is allowed. This is in contrary to the theoretical expectations from the saturation conjecture and looks also as an improbable scenario given the recent LHCb D- and B-meson measurements [99, 100] which impressively indicate [101] gluon shadowing down to $x \sim 10^{-5}$ at interaction scales as low as $Q^2 \sim m^2_{\mathrm{charm}}$. On the other hand, given that there are no prior DIS measurements at these kinematics for other nuclei than the proton, and that the D- and B-meson production in p-Pb collisions could be affected by strong final-state effects (which could eventually be resolved by e.g. measurements of forward prompt photons [102] in p-Pb), we hypothesize that any kind of behaviour is be possible at this stage. Anyway, with the extended parametrization – called here EPPS16* – the uncertainties in the small-x regime get significantly larger than what they are in the standard EPPS16 set. This is reflected as significantly larger PDF error bands in comparison to the projected LHeC pseudodata. This is shown in Figure 6.5 where EPPS16* predictions are compared with the LHeC pseudodata for inclusive neutral- and charged-current reactions, as well as charm production in neutral-current scattering. The uncertainties are estimated using the Hessian method [103] and the same overall tolerance $\Delta\chi^2 = 50$ as in the EPPS16 analysis has been used when defining the error bands. Because there are no small-x data constraints for gluons, the gluon uncertainty is enormous and the Hessian method used for estimating the uncertainties is not particularly accurate, i.e. the true $\Delta\chi^2 = 50$ errorbands are likely to be even larger. At some point the downward uncertainty will be limited by positivity constraints e.g. for F_{L}, but will depend strongly on which Q^2 the positivity constraints are set (in EPPS16 analysis F_{L} is required to remain positive at $Q^2 = m^2_{\mathrm{charm}}$).

Upon including the LHeC e-Pb pseudodata in the fit, the new PDFs adapt to reproduce the pseudodata and the PDF uncertainties are greatly reduced, as shown in Figure 6.6. The overall tolerance has been kept fixed

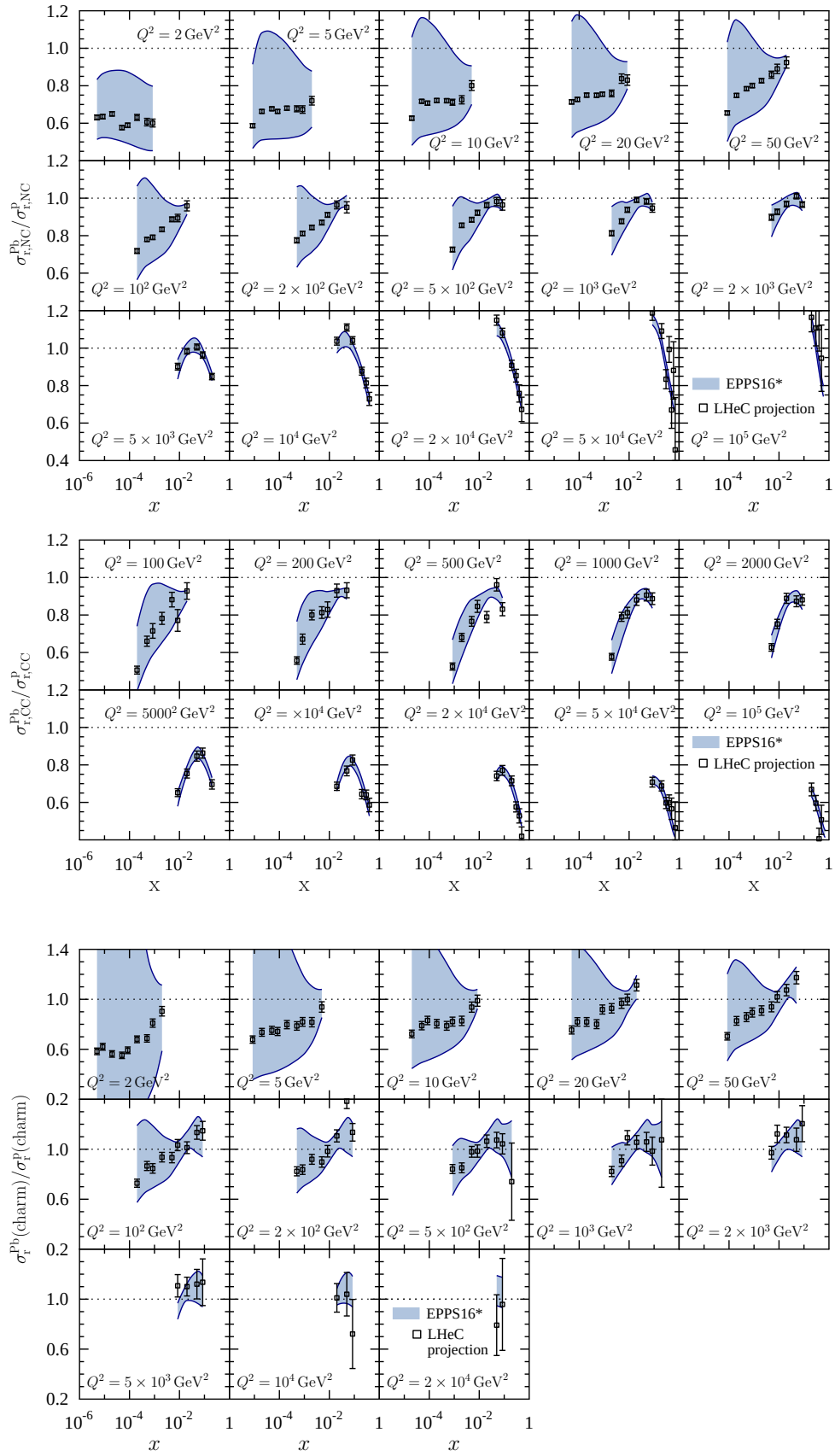

Figure 6.5: Top: Ratios of neutral-current reduced cross sections between e-Pb and e-p collisions compared with the predictions from a EPPS16-type global fit of nuclear PDFs using an exteneded parametrization for gluons. Middle: Charged-current cross sections. Bottom: Neutral-current charm-production cross-section ratios.

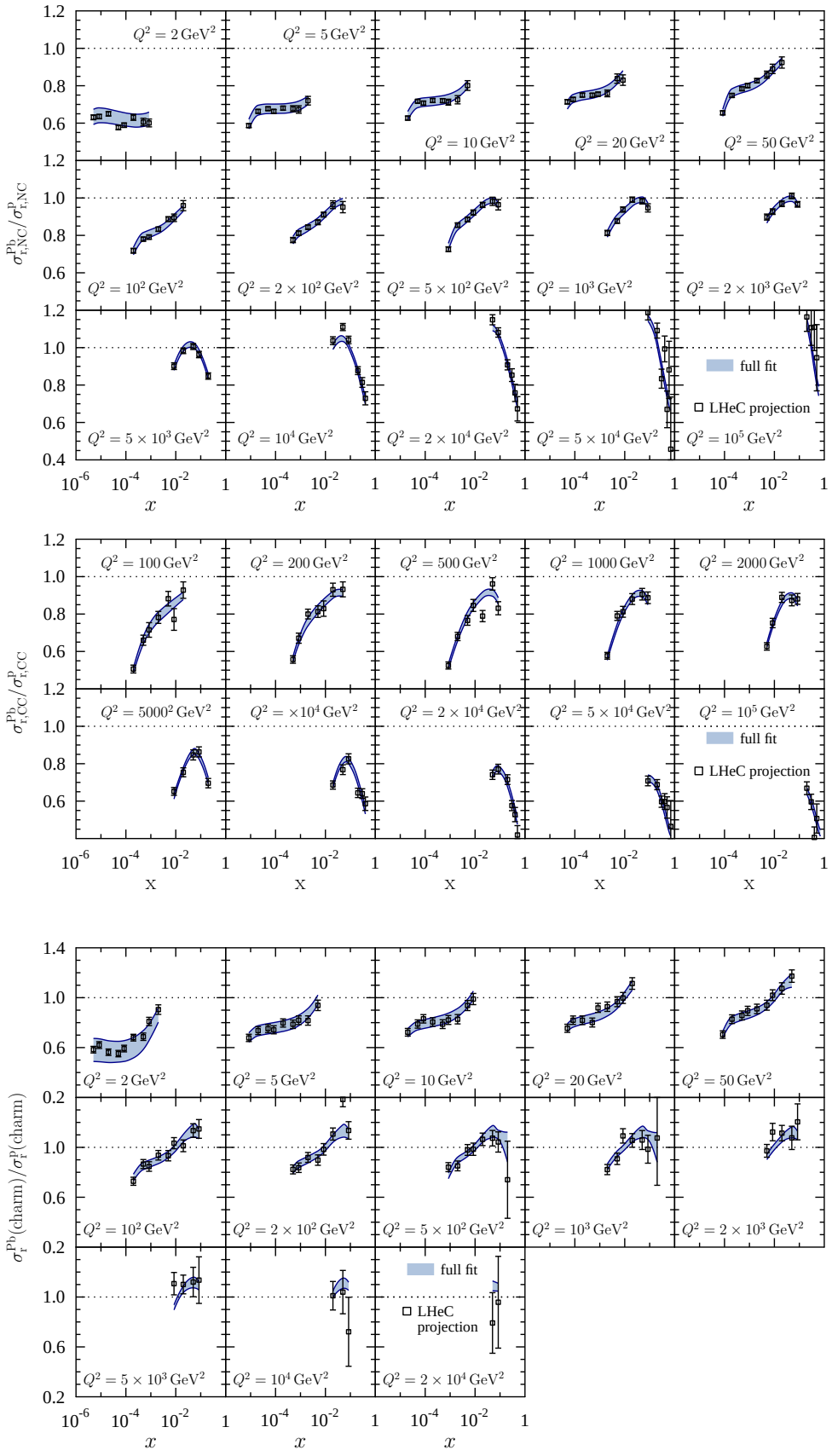

Figure 6.6: As Figure 6.5 but after including the LHeC pseudodata in the global analysis.

to the default value $\Delta\chi^2 = 50$. The impact on the nuclear modification of the gluon PDF is illustrated in Figure 6.7 at two values of Q^2: $Q^2 = 1.69\,\mathrm{GeV}^2$ (the parametrization scale) and $Q^2 = 10\,\mathrm{GeV}^2$. Already the inclusive pseudodata are able to reduce the small-x gluon uncertainty quite significantly, and the addition of the charm data promises even more dramatic reduction in the errors. The analysis indicates that – unless very low Q^2 and very small x is considered – the LHeC would nail the nuclear gluon PDF to a high precision.

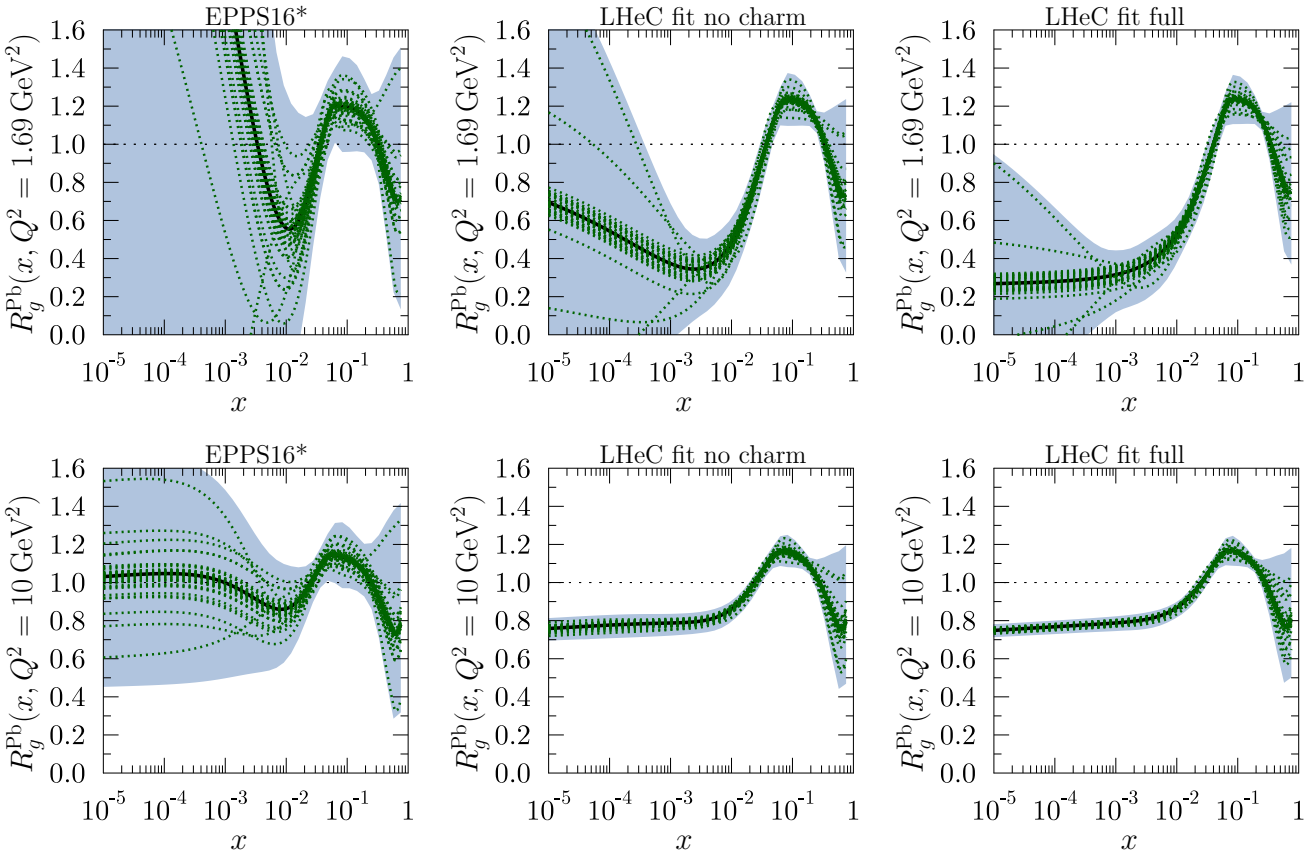

Figure 6.7: Upper panels: The gluon nuclear modification for Pb nucleus at $Q^2 = 1.69\,\mathrm{GeV}^2$ in EPPS16* (left), LHeC analysis without charm pseudodata (middle), and full LHeC analysis (right). The blue bands mark the total uncertainty and the green curves correspond to individual Hessian error sets. Lower panels: As the upper panels but at $Q^2 = 10\,\mathrm{GeV}^2$.

6.2.3 nPDFs from DIS on a single nucleus [Nestor Armesto]

Another approach that becomes possible with the large kinematic coverage and number of data for a single nucleus, Pb, at the LHeC and FCC-eh, is to perform a fit to only Pb data in order to extract the Pb PDFs. Then the corresponding ratios or nuclear modification factors for each parton species can be obtained using either a proton PDF set from a global fit or, as we do here (see [104, 105, 106]), from a fit to proton LHeC and FCC-eh pseudodata. In this way, there is no need of introducing a nuclear size dependence in the parameters for the initial condition for DGLAP evolution. Such nPDFs can then be used for comparing to those obtained from global fits and for precision tests of collinear factorisation in nuclear collisions.

The fits are performed using xFitter [107], where 484 (150) NC and CC Pb data points at the LHeC (FCC-eh) have been used in the fitted region $Q^2 > 3.5$ GeV^2, see Fig. 6.2. A HERAPDF2.0-type parametrisation [71] has been employed to provide both the central values for the reduced cross sections (therefore, the

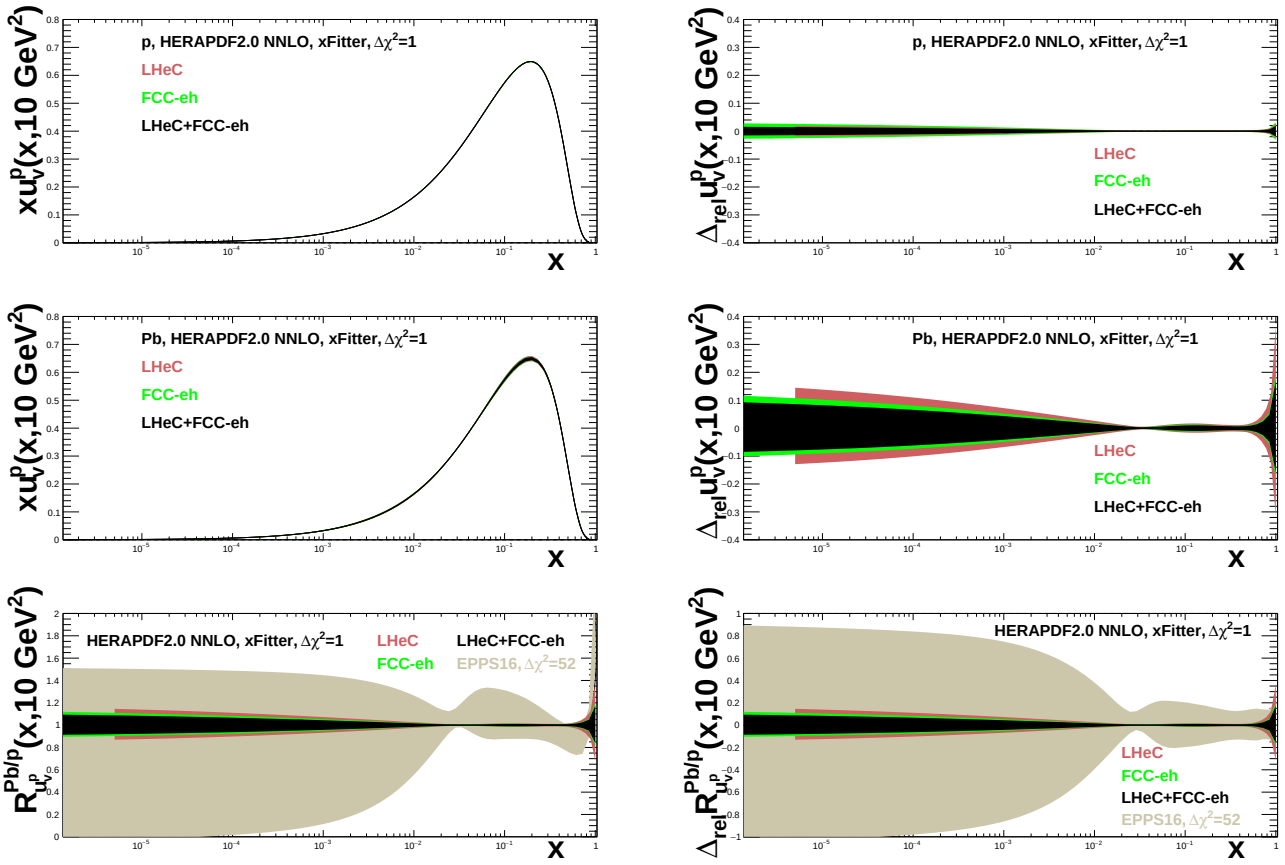

Figure 6.8: Distributions (left) and their relative uncertainties (right) of the valence u-quark density in proton (top), Pb (middle) and the corresponding nuclear modifications factor (bottom) in an analysis of ep and ePb LHeC and FCC-eh NC plus CC pseudodata using xFitter (both a single set of data and all combined), compared to the results of EPPS16 [75], see the text for details.

extracted nuclear modification factors are centered at 1) and the fit functional form; in this way, neither theory uncertainties (treatment of heavy flavours, value of α_s, order in the perturbative expansion) nor the uncertainty related to the functional form of the initial condition – parametrisation bias – are considered in our study, in agreement with our goal of estimating the *ultimate experimental achievable* precision in the extraction of PDFs. We have worked at NNLO using the Roberts-Thorne improved heavy quark scheme, and $\alpha_s(m_Z^2) = 0.118$. The treatment of systematics and the tolerance $\Delta\chi^2 = 1$ are identical to that in the HERAPDF2.0 fits, as achievable in a single experiment.

The results for the relative uncertainties in the nuclear modification factors, are shown in Figs. 6.8, 6.9 and 6.10 for valence, sea and glue respectively. While a very high precision looks achievable at the LHeC and the FCC-eh, for the comparison with EPPS16 (or any other global fit) shown in the plots and with previous works in that setup [98, 97] some caution must be taken. First, the effective EPPS16 tolerance criterium $\Delta\chi^2 = 52$ implies that naively the uncertainty bands should be compared after rescaling by a factor $\sqrt{52}$. Second, the treatment of systematics is rather different, considering correlations in the xFitter exercise and taking them as fully uncorrelated (and added quadratically to the statistical ones) in the EPPS16 one. Finally, EPPS16 uses parametrisations for the nuclear modification factors for different parton species while in xFitter just the PDF combinations that enter the reduced cross sections are parametrised and employed for the fit. In this respect let us note that, in analogy to proton PDFs, full flavour decomposition could be achieved using both NC and CC with heavy flavour identification.

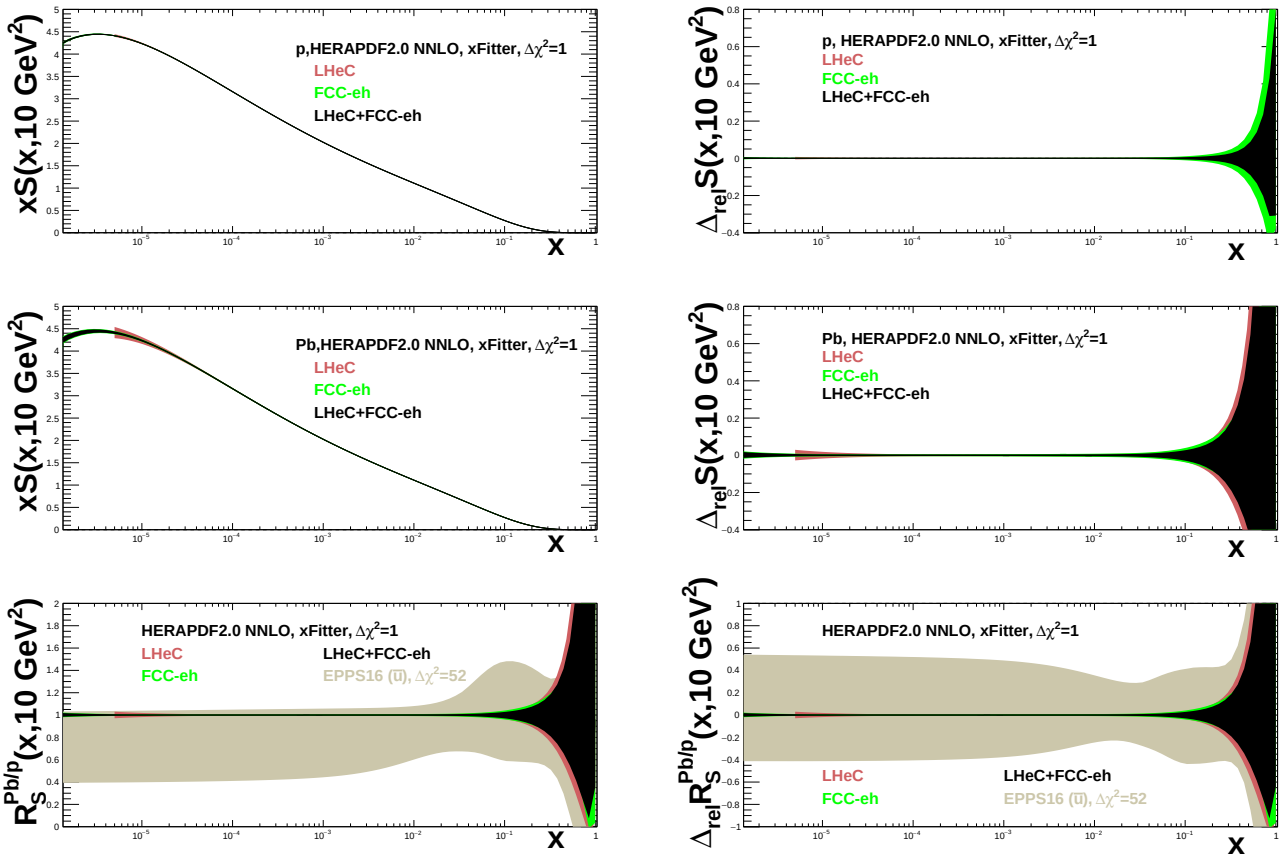

Figure 6.9: Distributions (left) and their relative uncertainties (right) of the sea quark density in proton (top), Pb (middle) and the corresponding nuclear modifications factor (bottom) in an analysis of ep and ePb LHeC and FCC-eh NC plus CC pseudodata using xFitter (both a single set of data and all combined), compared to the results of EPPS16 [75] for $\bar{u}$, see the text for details.

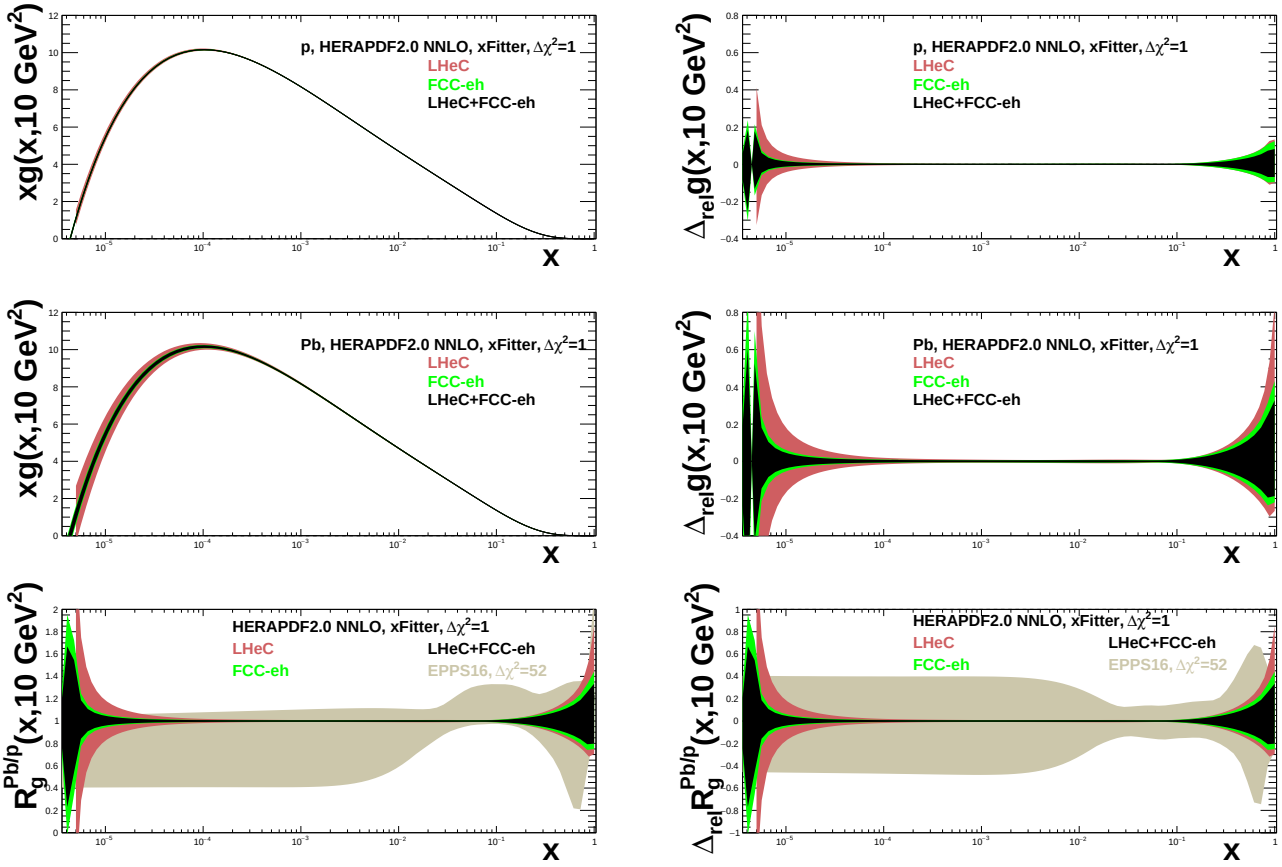

Figure 6.10: Distributions (left) and their relative uncertainties (right) of the gluon density in proton (top), Pb (middle) and the corresponding nuclear modifications factor (bottom) in an analysis of ep and ePb LHeC and FCC-eh NC plus CC pseudodata using xFitter (both a single set of data and all combined), compared to the results of EPPS16 [75], see the text for details.

Here a figure on the coherent vs incoherent diffraction

Figure 6.11: Caption

6.3 Nuclear diffraction [Anna Stasto, Paul Newman]

Here we should include a discussion on coherent versus incoherent diffraction, perspective for elastic VM production (plots by Heikki Mantysaari), nuclear GPDs and nuclear shadowing from diffraction in ep,...

In Sec. 5.4.5 we have discussed specific processes which will allow to probe the details of the 3D structure of the proton. Inclusive diffraction on nuclei can provide important information about the nuclear diffractive parton distribution similarly to the diffraction on the proton, see Sec.5.4.6. Same processes can be studied in the context of electron-ion scattering and used to learn about the partonic structure of nuclei. The diffractive vector meson production can be studied in the nuclear case as well, within the framework of the dipole model suitable for high energy and including non-linear effects in density. In the nuclear case though, one needs to make a distinction between the coherent and incoherent diffraction. In the coherent process, the nucleus scatters elastically and stays intact after the collision, see Fig. **??**. In the coherent diffraction, the nucleus breaks up, and individual nucleons can be set free. Still, there will be a large rapidity gap between the produced diffractive system and the dissociated nucleus, see Fig. **??**. It is expected that this process will dominate the diffractive cross section from medium towards the large values of momentum transfer. It is only in the region of small values of momentum transfer, where the elastic diffraction is the dominant contribution. Dedicated instrumentation in the forward region must be constructed in order to clearly distinguish between the two scenarios. ***We need here some blurb on the ZDC***

6.3.1 Exclusive vector meson diffraction

Calculations in the case of lead nucleus for the elastic diffractive J/ψ production were performed using the dipole model [108]. In order to apply the dipole model calculation to nucleus case one takes the independent scattering approximation that is usually used in Glauber theory [109]. The dipole amplitude can be then repreented in the form

$$N_A(x,\mathbf{r},\mathbf{b}) \;=\; 1-\prod_{i=1}^{A}\left[1-N(x,\mathbf{r},\mathbf{b}-\mathbf{b}_i)\right], \tag{6.1}$$

Here $N(x,\mathbf{r},\mathbf{b}-\mathbf{b}_i)$ is the dipole amplitude for the nucleon, $\mathbf{b}_i$ are the transverse positions of the nucleons in the nucleus. The interpretation of Eq.6.1 is that $1-N$ is the probability not to scatter off an individual nucleon, and thus $\prod_{i=1}^{A}\left[1-N(\mathbf{r},\mathbf{b}-\mathbf{b}_i,x)\right]$ is the probability not to scatter off the entire nucleus.

In addition, in the following simulation one included the fluctuations of the density profile in the proton, following the prescription given in [110, 111, 108]. To include these proton structure fluctuations one assumes that the gluonic density of the proton in the transverse plane is distributed around three constituent quarks (hot spots). These hot spots are assumed to be Gaussian. In practical terms one replaces the proton profile T_p

$$T_p(\mathbf{b}) = \frac{1}{2\pi B_p} e^{-b^2/(2B_p)},$$

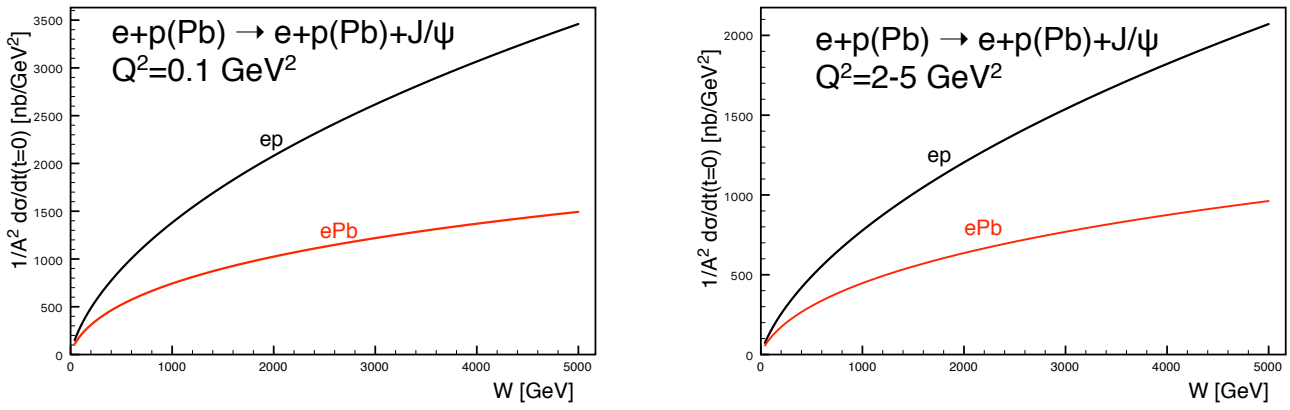

Figure 6.12: Cross section for the elastic diffractive prodcution of the vector meson J/ψ in ePb (red solid curves) and ep (black solid curves) collisions, as a function of the energy W. Left plot: photproduction case $Q^2 \simeq 0$, right plot $Q^2 = 2 - 5$ GeV^2

with the function

$$T_p(\mathbf{b}) = \sum_{i=1}^{3} T_q(\mathbf{b} - \mathbf{b}_{q,i}) \ ,$$

where the 'quark' density profile is given by

$$T_q(\mathbf{b}) = \frac{1}{2\pi B_q} e^{-b^2/(2B_q)} \ .$$

Here $\mathbf{b}_{q,i}$ are the location of hotspots.

They are sampled from a two dimensional Gaussian distribution whose width is given by parameter B_{qc}. The free parameters B_q and B_{qc} were obtained in [111] by comparing with the HERA data on the coherent and incoherent J/ψ production at the photon-proton center of mass energy $W = 75$ GeV, corresponding to $x_{IP} = 10^{-3}$. The proton fluctuation parameters obtained are $B_{qc} = 3.3\text{GeV}^{-2}$, $B_q = 0.7\text{GeV}^{-2}$.

The results for the total cross section for the diffractive elastic production of J/ψ as a function of energy W for fixed values of Q^2 are shown in Figs. 6.12 and Figs. 6.13. The calculations for lead are compared to those on the proton target. We see that the cross sections for nuclear case increase with energy slower than for the proton case and are always smaller. Note that, we have already rescaled the diffractive cross section by factor A^2, as appropriate for comparison of the cross section on proton and nucleus. In the absence of nuclear corrections this ratio should be equal to 1. The difference between the scattering off nucleus and a proton is also a function of Q^2. The differences are largest for smaller values of Q^2 and for photoproduction.

This is understood from the dipole formulae, see Eqs.5.1, 5.2,5.3. As explained previously the larger value of scale Q^2 selects smaller size dipoles, for which the density effects are smaller. Similarly, the differences between the lead and proton case are largest for highest energies. This is because the dipole amplitude grows with the decreasing values of x which are probed when the energy is increased, and thus the non-linear density effects are more prominent at low values of x and low values of Q^2.

These findings case be summarized by inspecting the ratio of the cross sections, presented as a function of x defined as

$$x = \frac{Q^2 + m_{J/\psi}^2}{Q^2 + W^2 + m_{J/\psi}^2 - m_N^2} \ . \tag{6.2}$$

which is presented in Fig.6.14

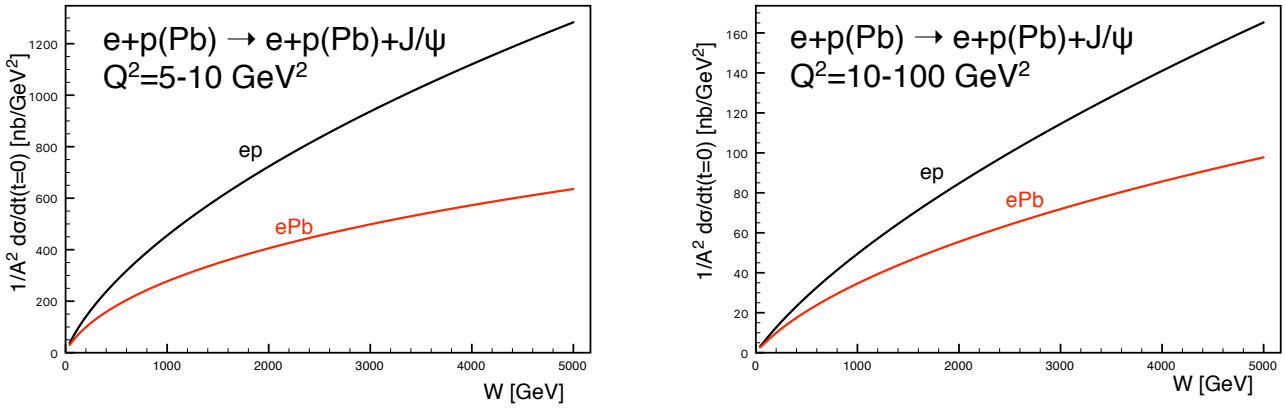

Figure 6.13: Cross section for the elastic diffractive prodcution of the vector meson J/ψ in ePb (red solid curves) and ep (black solid curves) collisions, as a function of the energy W. Left plot: $Q^2 = 5 - 10$ GeV^2, right plot $Q^2 = 10 - 100$ GeV^2.

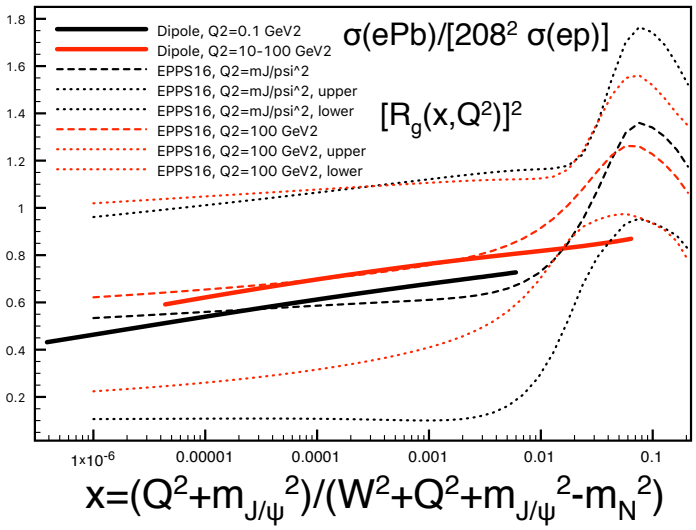

Figure 6.14: Ratio of cross sections for Pb and proton as a function of variable x defined in Eq.6.2. Solid lines: dipole model calculation, for $Q^2 = 0.1$ GeV^2 (black) and $Q^2 = 10 - 100$ GeV^2. Dotted and dashed lines correspond to the nuclear ratio for the gluon density squared using the EPPS16 parametrization of the nuclear parton distribution functions. Black and red dashed line correspond to the central sets for $Q^2 = M^2_{J/\psi}$ and $Q^2 = 100$ GeV^2 correspondingly. The dotted lines correspond to the lowest and highest sets in EPPS16 parametrization. The difference between the two dotted lines is indicative of the parametrization uncertainty for the nuclear ratio.

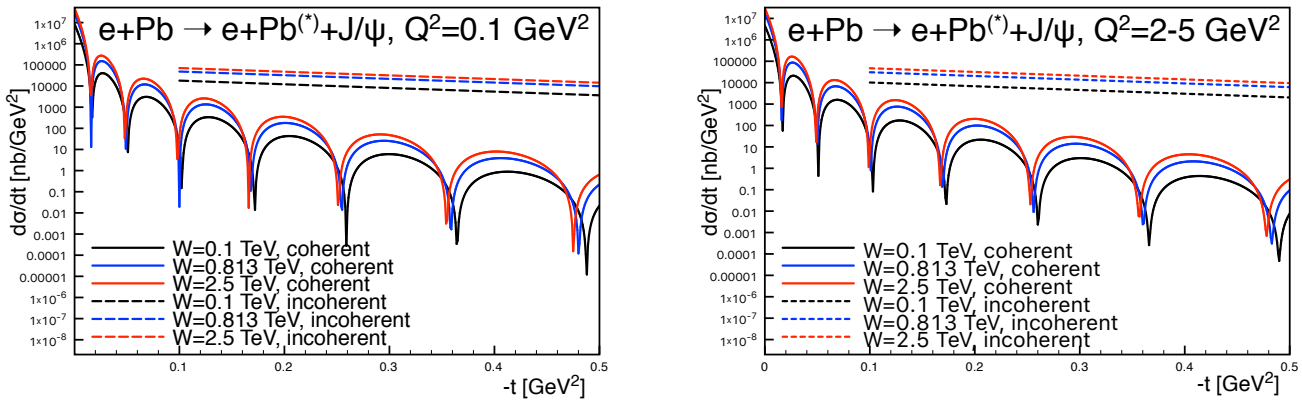

Figure 6.15: The differential cross section for the elastic diffractive production of J/ψ in ePb as a function of the negative momentum transfer $-t$. Left plot: photoproduction $Q^2 \simeq 0$, right plot $Q^2 = 2-5$ GeV^2. Solid lines are for the coherent production, dashed lines - incoherent. Black, blue, red are for $W = 0.1, 0.813, 2.5$ TeV.

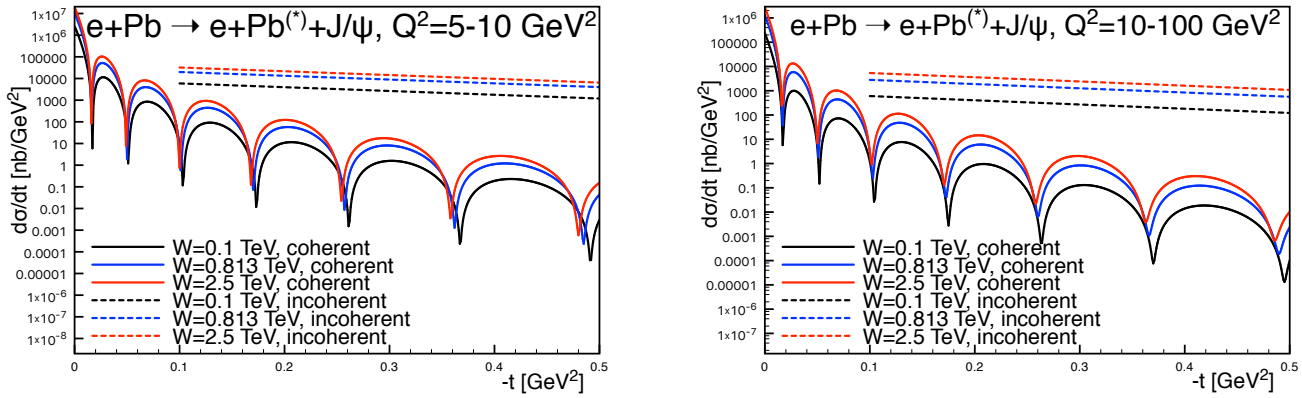

Figure 6.16: The differential cross section for the elastic diffractive production of J/ψ in ePb as a function of the negative momentum transfer $-t$. Left plot: $Q^2 5-10$, right plot $Q^2 = 10-100$ GeV^2. Solid lines are for the coherent production, dashed lines - incoherent. Black, blue, red are for $W = 0.1, 0.813, 2.5$ TeV.

We observe that the ratio is smaller for smaller values of scale Q^2, and it decreases for decreasing value of x. The results from the dipole model calculations are compared with the ratio of the gluon density squared obtained from the nuclear PDFs using the EPPS16 set. The reason why one can compare the diffractive cross section ratios with the ratios for the gluon density squared can be understood from Eqs.(5.1) and (5.2). The diffractive amplitude is proportional to the gluon density $xg(x, Q^2)$. On the other hand the diffractive cross section will be proportional to amplitude squared, thus resulting in the sensitivitiy to the square of the gluon density. The nuclear PDFs have a large range of uncertainties built in, which is indicated by the region between the two sets of dotted lines. The EPPS16 parametrization is practically unconstrained in the region below $x = 0.01$. Nevertheless the estimate based on the dipole model calculation and the central value of the EPPS16 parametrization are consistent with each other.

In Figs. 6.15 and 6.16 we show the differential cross section $d\sigma/dt$ as a function of the negative momentum transfer $-t$ for the case of the coherent and incoherent production. The coherent and incoherent diffraction cross section are computed from the dipole model in the following way. The coherent diffractive cross section is obtained by averaging the diffractive scattering amplitude over the target configurations and taking the square

$$\frac{d\sigma}{dt} = \frac{1}{16\pi}|\langle \mathcal{A}(x,Q,\Delta)\rangle|^2 \, .$$

Here the brackets $\langle \dots \rangle$ refer to averages over different configurations of the target. The incoherent cross section is obtained by subtracting the coherent cross section from the total diffractive cross section. It takes the form of a variance of the diffractive scattering amplitude put here references [13] (see also Refs. [14, 15, 17, 18]):

$$\frac{d\sigma}{dt} = \frac{1}{16\pi}\Big(\langle|\mathcal{A}(x,Q,\Delta)|\rangle^2 - |\langle \mathcal{A}(x,Q,\Delta)\rangle|^2\Big) \, .$$

The t dependence, and the relation between the impact parmeter and t through the Fourier transform, makes diffractive scattering a sensitive probe of the internal geometric structure of hadrons and nuclei. In particular because the incoherent cross section has the form of a variance of the amplitude, it is sensitive to the amount of fluctuations in coordinate impact parameter space.

The results in Figs. 6.15 and 6.16 indicate that the incoherent production is dominant for most values of $-t$, except for the very small momentum transfers, about $|t| < 0.02\text{GeV}^2$. Thus the dedicated instrumentation which will allow to distinguish the two cases is essential if one wants to measure the coherent process in a reasonably wide range of $|t|$. As in the proton case the coherent t distribution exhibits the characteristic dips. However in the case of the nuclear targets the dips occur for much smaller values of momenta t. This is related to the much larger value of the dipole amplitude for a wide range of impact parameters in the case of nuclear targets as compared to the proton targets.

We thus conclude that by investigating the coherent and incoherent diffractive scattering on nuclei, one gets unique insight into the spatial structure of matter in nuclei. The coherent cross section, which is obtained by averaging the amplitude before squaring it, is sensitive to the average spatial density distribution of gluons in transverse space. On the other hand, the incoherent cross section, which is the variance of the amplitude with respect to the initial nucleon configurations N of the nucleus, measures fluctuations of the gluon density inside the nucleus. In the case of a nucleus, the diffractive production rate is controlled by two different scales related to the proton and nucleus size. At momentum scales corresponding to the nucleon size $|t| \sim 1/R_p^2$ the diffractive cross section is almost purely incoherent. The t-distribution in coherent diffractive production off nucleus gives rise to a dip-type structure for both saturation and non-saturation models, while in the case of incoherent production at small $|t|$, both saturation and non-saturation models do not lead to dips [83, 84]. This is in drastic contrast to the diffractive production off proton where only saturation models lead to dip-type structure in the t-distribution at values of $|t|$ that can be experimentally accessible. Therefore, diffractive production offers unique opportunity to measure spatial distribution of partons in the protons and nuclei. It is also excellent tool to investigate the approach to unitarity in high energy limit of QCD.

6.3.2 Inclusive diffraction on nuclei

6.4 New Dynamics at Small x with Nuclear Targets [Nestor Armesto]

As discussed in Sec. 5.4.3, theoretical expectations [112] indicate that fixed-order perturbation theory leading to the DGLAP evolution equations should eventually fail. When x decreases, $\alpha_s \ln 1/x$ becomes large and these large logarithms must be resummed, leading to the BFKL equation. Furthermore, when parton density becomes large the linear approximation that underlies both DGLAP and BFKL breaks, and non-linear processes must be taken into account to compute parton evolution. The CGC [113] offers a non-perturbative but weak coupling effective theory to treat dense parton systems in a systematic and controlled

way. One of the important predictions of the CGC is that the in a dense parton system, parton saturation occurs, with emergence of a new, dynamical scale – saturation scale Q_s, which increases with the energy.

Parton density in a hadron becomes high both through evolution – when energy or $1/x$ becomes large, and when partons are accumulated by overlapping nucleons – when mass number A becomes large in a nucleus. In the nucleus rest frame, the virtual photon fluctuations at small $x < (2m_N R_A)^{-1}$, with m_N the nucleon mass and R_A the nuclear radius, acquire a lifetime larger than the nuclear size and, thus, all partons within a transverse area $\sim 1/Q^2$ are simultaneously probed. Actually, the parameter determining the transition between linear and non-linear dynamics is parton density and, therefore, the onset of this new regime of QCD and its explanation must be tested, as commented in [1], exploring both decreasing values of x and increasing values of A in a kinematic $x - Q^2$ region where, in order to be sensitive to differences in evolution, enough lever arm in $Q^2 \gg \Lambda^2_{\rm QCD}$ at small x is available. The saturation scale Q_s that characterises the typical gluon momentum in a saturated hadron wave function increases with nuclear size, $Q_s^2 \propto A^{1/3}$. Therefore, in eA collisions the perturbatively saturated regime is achieved at parametrically larger x than in a proton – a prediction of the CGC.

The opportunities to establish the existence of saturation in lepton-nucleus collisions are numerous. They include inclusive observables, both total and diffractive cross sections, and less inclusive ones like correlations:

- Tension in DGLAP fits for inclusive observables: As discussed in [1, 66], deviations from fixed-order perturbation theory can be tested by the tension that would appear in the description within a DGLAP fit of observables with different sensitivities to the sea and the glue, for example F_2 and F_L (or reduced cross sections at different energies) or $F_2^{\rm inclusive}$ and $F_2^{\rm heavy\ quarks}$. In [114], such exercise was performed using F_2 and F_L for eAu collisions at the EIC [94] using reweighting techniques. While the results for EIC energies are shown not to be conclusive due to the reduced lever arm in $Q^2 > Q_s^2 \gg \Lambda^2_{\rm QCD}$, the much larger centre-of-mass energies at the LHeC (and FCC-eh) should make possible a search for tensions between different observables.

- Saturation effects on diffraction: A longstanding prediction of saturation [115, 116, 117] is a modification of the diffractive cross section in nuclei with respect to protons, with a suppression (enhancement) at small (large) β due to the approach of the nucleus to the black disk limit, where elastic and diffractive scattering become maximal, and the behaviour of the different Fock components of the virtual photon wave function. Such effects can also be discussed in terms of a competition of nuclear shadowing with the probability that the event remains diffractive in the multiple scattering process [91]. This leads to the generic expectation of an enhancement of the ratio of the diffractive cross section in nucleus over that in protons, in non-linear approaches with respect to linear ones [94].

- Correlations: Correlations have been considered since long ago as sensitive probes of the underlying production dynamics. For example, the cross section for the production of two jets with the same hardness and widely separated in rapidity, called Mueller-Navelet jets [118], was proposed as a sensitive test of BFKL versus DGLAP dynamics, but the effect of saturation has not been widely studied although it has the large potentiality of differentiating linear resummation from non-linear saturation where non-trivial nuclear effects could appear. They were analysed in [1] for the LHeC kinematics, both in inclusive and diffractive events, see the formalism in [119]. On the other hand, the azimuthal decorrelation of particles and jets when saturation effects are at work – at small x, studied by the difference between collisions involving proton and nuclei, was proposed long ago at the Relativistic Hadron Collider [120]. It was studied in [1] for the LHeC kinematics, see recent developments in [121] and the extension to forward dijet production in [122].

Chapter 7

Higgs Physics with LHeC [Uta Klein, Bruce Mellado]

Example reference: LHeC [1]

7.1 Signal Strength and Couplings [Max, Uta Klein]

7.2 Htt Coupling Measurement [Bruce Mellado]

7.3 Higgs Decay into Invisible Particles [Masahiro Kuze]

7.4 ep Measurement Potential in the EFT Framework [Jorge De Blas]

Chapter 8

Searches for Physics Beyond the Standard Model [Georges Azuelos, Oliver Fischer]

Example reference: LHeC [1]

8.1 Extension of the SM Higgs Sector [Oliver Fischer]

8.2 SUSY [Monica D'Onofrio]

8.3 Heavy Neutrinos and Feebly Interacting Particles [Oliver Fischer]

8.4 Dark Matter and Dark Sector [Monica D'Onofrio]

8.5 Contact Interactions and Leptoquarks [Georges Azuelos]

8.6 Anomalous Triple Gauge Couplings [Orhan Carkir]

Chapter 9

The Influence of the LHeC on Physics at HL-LHC [Maarten Boonekamp]

Example reference: LHeC [1]

9.1 Precision Electroweak Measurements at the LHC [Maarten Boonekamp]

9.2 Higgs Physics

9.2.1 Resolving QCD Uncertainties in pp Higgs Physics using LHeC [Max Klein]

9.2.2 Combined ep and pp Higgs Coupling Determinations [Jorge De Blas]

9.3 High Mass Searches at the LHC [Uta Klein]

9.4 Heavy Ion Physics with eA Input [Nestor Armesto]

The study of hadronic collisions at RHIC and the LHC, proton-proton, proton-nucleus and nucleus-nucleus, has produced several observations of crucial importance for our understanding of QCD in complex systems where a large number of partons is involved [123, 124]. The different stages of a heavy ion collision, as we presently picture it, are schematically drawn in Fig 9.1.

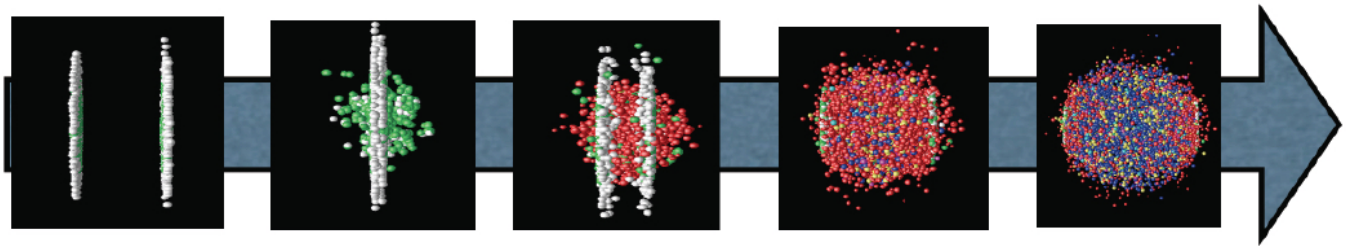

Figure 9.1: Sketch of a heavy ion collision with time running left to right, going from the approach of two ultrarelativistic Lorentz-contracted nuclei, the collision and parton creation in the central rapidity region, the beginning of expansion and formation of the QGP, the expansion of the QGP until hadronisation, and finally the expansion of the hadronic gas.

First, the hot and dense partonic medium created in heavy ion collisions, the quark-gluon plasma (QGP), experiences a collective behaviour of which azimuthal asymmetries and transverse spectra with a specific ordering in particle masses are the most prominent observables. This collectivity can be very well described by relativistic hydrodynamics [125]. For this description, the system has to undergo some dynamics leading to rough isotropisation in a short time, $\lesssim 1$ fm/c, for which both strong and weak coupling explanations have been proposed [126].

Second, collisions between smaller systems, pp and pA, show many of the features [127, 128] that in heavy ion collisions are taken as indicative of the production of a dense hot partonic medium. The most celebrated of such features, the long rapidity range particle correlations collimated in azimuth, named the ridge, has been found in all collisions systems. The dynamics underlying this phenomena, either the formation of QGP and the existence of strong final state interactions, or some initial state dynamics that leaves imprint on the final observables, is under discussion [126].

Finally, the QGP is extremely opaque to both highly energetic partons [129] and quarkonia [130] traversing it. These observables, whose production in pp can be addressed through perturbative methods, are called hard probes [131]. The quantification of the properties of the QGP extracted through hard probes is done by a comparison with predictions based on assuming a nuclear collision to be a superposition of collisions among free nucleons. Such predictions contain uncertainties coming both from nuclear effects other than those in QGP (named cold nuclear matter effects), and from uncertainties in the dynamics determining the interaction between the energetic parton or bound state and the medium. In the case of partons, this has motivated the development of sophisticated jet studies in heavy ion collisions [132].

eA collisions studied in the energy range relevant for the corresponding hadronic accelerator – the LHeC for the LHC – would substantially improve our knowledge on all these aspects and, indeed, of all stages of a heavy ion collisions depicted in Fig 9.1. Besides, they can reduce sizeably the uncertainties in the extracted QGP parameters, the central goal of the heavy program for the understanding of the different phases of QCD. Here we provide three examples of such synergies:

- Nuclear parton densities: The large lack of precision presently existing in the determination of parton densities induce large uncertainties in the understanding of several signatures of the QGP. For example, for J/ψ suppression, its magnitude at midrapidity at the LHC is compatible with the sole effect of nuclear shadowing on nPDFs [130], see Fig. 9.2. While from data at lower energies and at forward and backward rapidities it is clear that this is not the only effect at work, only a reduction on the nPDF uncertainty as feasible at the LHeC , see Sec. 6.2, will make possible a precise quantification of the different mechanisms producing either suppression (screening, gluon dissociation, energy loss) or enhancement (recombination or coalescence), that play a role in this observable.

- Initial conditions for the collective expansion and the small system problem: At present, the largest uncertainty in the determination of the transport coefficients of the partonic matter created in heavy ion collisions [134, 135] (see Fig. 9.3), required in hydrodynamic calculations, and in our understanding of the speed of the approach to isotropisation and of the dynamics prior to it [136], comes from our lack of knowledge of the nuclear wave function and of the mechanism of particle production at small to moderate scales – i.e. the soft and semihard regimes. Both aspects determine the initial conditions for the application of relativistic hydrodynamics. This is even more crucial in the discussion of small systems, where details of the transverse structure of protons are key [137] not only to provide such initial conditions but also to establish the relative role of initial versus final state dynamics. For example, the description of azimuthal asymmetries in pp and pPb collisions at the LHC demands that the proton is modelled as a collection of constituent quarks or hot spots [125, 137]. ep and eA collisions at the LHeC can constrain both aspects in the relevant kinematic region, Secs. 5.4.5 and 6.3. Besides, they can clarify the mechanisms of particle production and the possible relevance of initial state correlations on the final state observables as suggested e.g. by CGC calculations, see Secs. 5.4.3

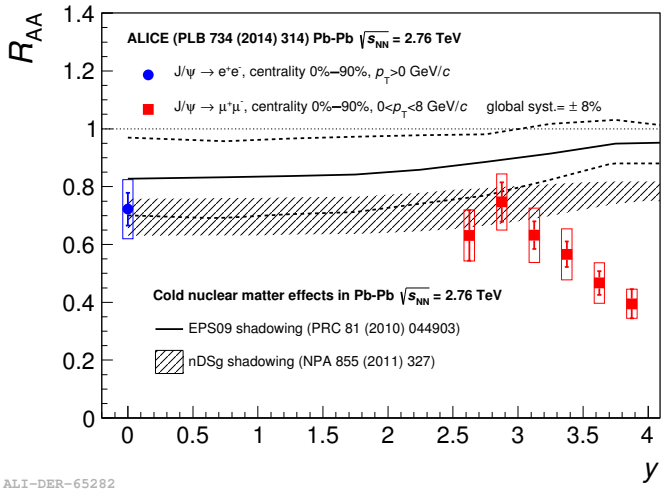

Figure 9.2: ALICE inclusive J/ψ nuclear modification factor versus rapidity [133], compared to nPDF calculations. Taken from [130].

and 6.4, whose relevance for LHC energies can be established at the LHeC.

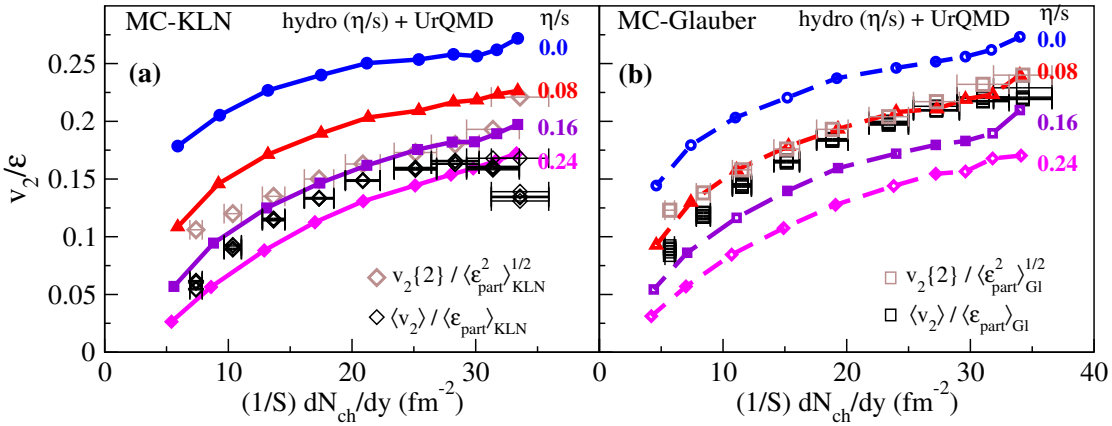

Figure 9.3: Comparison of the universal $v_2(\eta/s)/\varepsilon$ vs. $(1/S)(dN_{\rm ch}/dy)$ curves with experimental data for $\langle v_2\rangle$ [138], $v_2\{2\}$ [139], and $dN_{\rm ch}/dy$ [140] from the STAR Collaboration. The experimental data used in (a) and (b) are identical, but the normalisation factors $\langle\varepsilon_{\rm part}\rangle$ and S used on the vertical and horizontal axes, as well as the factor $\langle\varepsilon^2_{\rm part}\rangle^{1/2}$ used to normalize the $v_2\{2\}$ data, are taken from the MC-KLN model in (a) and from the MC-Glauber model in (b). Theoretical curves are from simulations with MC-KLN initial conditions in (a) and with MC-Glauber initial conditions in (b). Taken from [134].

- Impact on hard probes: Besides the improvement in the determination of nPDFs that affects the quantification of hard probes, commented above, eA collisions can help to understand the dynamics of the probes by analysing the effects of the nuclear medium on them. As two examples, the abundant yields of jets and large transverse momentum particles at the LHeC [1] will allow precise studies of the nuclear effects on jet observables and of hadronisation inside the nuclear medium. These two aspects are of capital importance not only in heavy ion collisions but also in small systems where the lack of jet modification is the only QGP-like characteristics not observed in pPb. On the other hand, measurements of exclusive quarkonium production at the LHeC [1] will allow a better understanding of the cold nuclear matter effects on this probe, on top of which the effects of the QGP will provide a a quantitative characterisation of this new form of QCD matter.

As discussed in Sec. 6.2, pPb and PbPb collisions at the LHC offer possibilities for constraning nPDFs, through the measurement of EW vector boson production [141], dijets [88], D mesons at forward rapidities [101] and exclusive charmonium and dijet photoproduction in ultraperipheral collisions [142, 143, 144]. Specifically, dijets in UPCs could constrain nPDFs in the region $10^{-3} \lesssim x \lesssim 0.7$ and $200 \lesssim Q^2 \lesssim 10^4$ GeV^2. eA collisions would provide more precise nPDFs, whose compatibility with these mentioned observables would clearly establish the validity of collinear factorisation and the mechanisms of particle production in collisions involving nuclei.

Furthermore, eA offers another system where photon-photon collisions, recently measured in UPCs at the LHC [145], can be studied. For example, the observed acoplanarity of the produced muon pairs can be analysed in eA in order to clarify its possible origin and constrain the photon parton densities.

Finally, the possible existence of a new non-linear regime of QCD - saturation - at small x is also under study at the LHC, for example using dijets in the forward rapidity region in pPb collisions [146]. Also, the ridge phenomenon (two particle correlations peaked at zero and π azimuthal angled and strechted along the full rapidity of the detector) observed in all collision systems, pp, pPb and PbPb at the LHC, has been measured in photoproduction on Pb in UPCs at the LHC [147]. For the time being, its existence in smaller systems like e^+e^- [148] at LEP and ep at HERA [149] has been scrutinised but the results are not conclusive. Its search in eA collisions at the smallest possible values of x at the LHeC would be most interesting. These studies are fully complementary to those in ep and eA.

In conclusion, ep and eA collisions as studied at the LHeC will have a large impact on the heavy ion programme, as the comparison of the kinematic reach of DIS and hadronic machines shown in Fig. 9.4 makes evident. It should be noted that there exist proposals for extending such programme into Run 5 and 6 of the LHC [93], by running lighter ions and with detector upgrades in ATLAS and CMS (starting in Run 4) and LHCb (Upgrade II [150]).

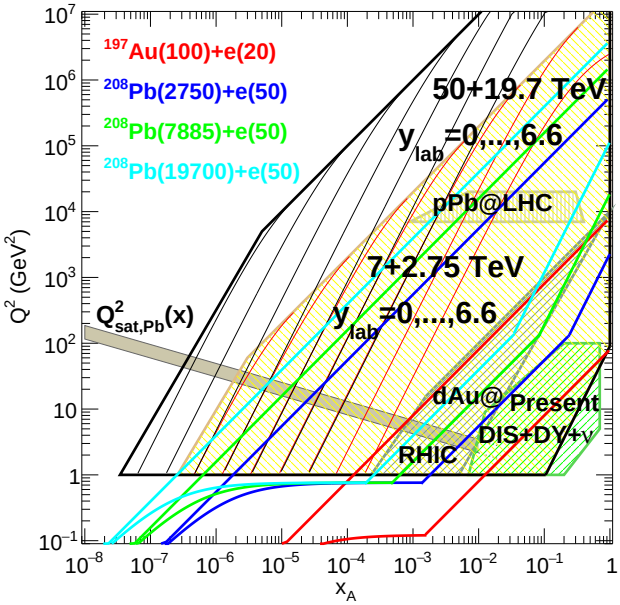

Figure 9.4: Kinematic regions in the $x - Q^2$ plane explored by data sets (charged lepton and neutrino DIS, DY, dAu at RHIC and pPb at the LHC) used in present nPDF analyses [75], compared to the ones achievable at the EIC (red), the LHeC (ERL against the HL-LHC beams, dark blue) and two FCC-eh versions (20 TeV - green and 50 TeV - light blue). Acceptance is taken to be $1^\circ < \theta < 179^\circ$, and $0.01(0.001) < y < 1$ for the EIC (all other colliders). The areas delimitated by brown and black thick lines show the regions accessible in pPb collisions at the LHC and the FCC-hh (50 TeV) respectively, while the thin lines represent constant rapidities from 0 (right) to 6.6 (left).

Chapter 10

The Electron Energy Recovery Linac [Erk Jensen, Gianluigi Arduini, Rogelio Tomas]

We studied different options for the electron accelerator for LHeC in [151], of which the Energy Recovery Linac (ERL) option is retained in this update of the CDR. This is due to the higher achievable luminosity of the Linac-Ring option, as compared to the Ring-Ring option, as well as the interference of the installation of an electron ring in the LHC tunnel with its operation [152].The clear advantage of the ERL compared to its contenders in 2012 is the possibility to keep the overall energy consumption at bay; its disadvantage is that operation at lepton energies above 70 GeV would lead to excessive synchrotron radiation losses and is thus practically excluded. Since there is no fundamental beam loading in an ERL by its principle, higher average currents and thus higher luminosities would not lead to larger power consumption.

10.1 Introduction - Design Goals [Gianluigi Arduini, Erk Jensen, Rogelio Tomas]

The main guidelines for the design of the Electron ERL and the Interaction Region (IR) with the LHC :

- electron-hadron operation in parallel with high luminosity hadron-hadron collisions in LHC/HL-LHC;
- centre-of-mass collision energy in the TeV scale;
- power consumption of the electron accelerator smaller than 100 MW;
- peak luminosity approaching 10^{34} $\mathrm{cm}^{-2}\mathrm{s}^{-1}$;
- integrated luminosity exceeding by at least two orders of magnitude that achieved by HERA at DESY.

The electron energy E_e chosen in the previous version of the CDR [151] was 60 GeV. This could be achieved with an ERL circumference of 1/3 of that of the LHC. Cost considerations and machine–detector performance aspects, in particular the amount of synchrotron radiation losses in the IR, have led to define a new reference configuration with $E_e = 49.19$ GeV and a circumference of ≈ 5.4 km, 1/5 of that of the LHC.

The ERL consists of two superconducting (SC) linacs operated in CW connected by three pairs of arcs to allow three accelerating and three decelerating passes (see Figure 10.1). The length of the high energy return arc following the interaction point should be such to provide a half RF period wavelength shift to allow the deceleration of the beam in the linac structures in three passes down to the injection energy and its safe disposal. SC Cavities with an unloaded quality factor Q_0 exceeding 10^{10} are required to minimize the requirements on the cryogenic cooling power and to allow an efficient ERL operation. The choice of having three accelerating and three decelerating passes implies that the circulating current in the linacs is six times the current colliding at the Interaction Point (IP) with the hadron beam.

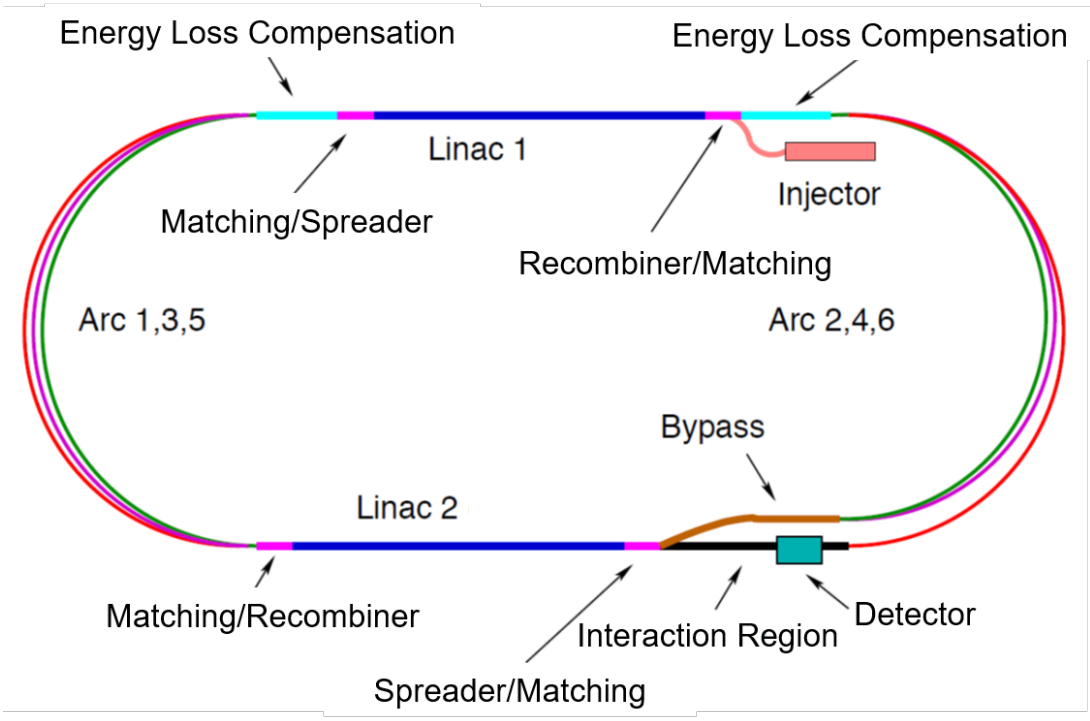

Figure 10.1: Schematic layout of the LHeC design based on an Energy Recovery Linac.

The choice of an Energy Recovery Linac offers the advantages of a high brightness beam and it avoids performance limitations due to the beam-beam effect seen by the electron beam, which was a major performance limitation in many circular lepton colliders (e.g. LEP) and for the LHeC Ring-Ring option. The current of the ERL is limited by its source and an operational goal of $I_e = 20\,\mathrm{mA}$ has been set, corresponding to a bunch current of 500 pC at a bunch frequency of 40 MHz. This implies operating the SRF cavities with the very high current of 120 mA for a virtual beam power (product of the beam current at the IP times the maximum beam energy) of 1 GW. The validation of such performance in terms of source brightness and ERL 3-turn stable and efficient operation in the PERLE facility [153] is a key milestone for the LHeC design.

A small beam size at the IP is required to maximize luminosity and approach peak luminosities of $10^{34}\,\mathrm{cm}^{-2}\mathrm{s}^{-1}$ and integrated luminosities of $1\,\mathrm{ab}^{-1}$ in the HL-LHC lifetime. in particular $\beta^* < 10\,\mathrm{cm}$ needs to be achieved for the colliding proton beam compatibly with the optics constraints imposed by the operation in parallel to proton-proton physics in the other Interaction Points (IPs) during the HL-LHC era [154]. The peak luminosity values quoted above exceed those at HERA by 2-3 orders of magnitude. The operation of HERA in its first, extended running period 1992–2000, provided and integrated luminosity of about $0.1\,\mathrm{fb}^{-1}$ for the H1 and ZEUS experiments, corresponding to the expected integrated luminosity collected over 1 day of LHeC operation!

10.2 The ERL Configuration of the LHeC [Alex Bogacz]

The main parameters of the LHeC ERL are listed in Table 10.1; their choices and optimization criteria will be discussed in the following sections.

Table 10.1: Parameters of LHeC ERL —for reference

Description	unit	parameters
Injector energy	GeV	0.5
Total number of linacs		2
Number of acceleration passes		3
Maximum electron energy	GeV	49.19
Bunch charge	pC	499
Bunch spacing	ns	24.95
Electron current	mA	20
Transverse normalized emittance	µm	20
Total energy gain per linac	GeV	8.114
Frequency	MHz	801.58
Acceleration gradient	MV/m	19.73
Cavity iris diameter	mm	130
Number of cells per cavity		5
Cavity length (active/real estate)	m	0.918/1.5
Cavities per cryomodule		4
Cryomodule length	m	7
Length of 4-CM unit	m	29.6
Acceleration per cryomodule (4-CM unit)	MeV	289.8
Total number of cryomodules (4-CM units) per linac		112 (28)
Total linac length (with with spr/rec matching)	m	828.8 (980.8)
Return arc radius (length)	m	536.4 (1685.1)
Total ERL length	km	5.332

10.2.1 Baseline Design - Lattice Architecture [Alex Bogacz]

The ERL, as sketched in Figure 10.1, is arranged in a racetrack configuration; hosting two superconducting linacs in the parallel straights and three recirculating arcs on each side. The linacs are 828.8 m long and the arcs have 536.4 m radius, additional space of 76 m is taken up by utilities like Spreader/Recombiner, matching and energy loss compensating sections adjacent to both ends of each linac (total of 4 sections) [155]. The total length of the racetrack is 5.332 km: 1/5 of the LHC circumference ($2 \times (828.8 + 2 \times 76 + \pi \times 536.4)$ m). Each of the two linacs provides 8.114 GV accelerating voltage, therefore a 49.19 GeV energy is achieved in three turns. After the collision with the protons in the LHC, the beam is decelerated in the three subsequent turns. The injection and dump energy has been chosen at 0.5 GeV.
Injection into the first linac is done through a fixed field injection chicane, with its last magnet (closing the chicane) being placed at the beginning of the linac. It closes the orbit 'bump' at the lowest energy, injection pass, but the magnet (physically located in the linac) will deflect the beam on all subsequent linac passes. In order to close the resulting higher pass 'bumps', the so-called re-injection chicane is instrumented, by placing two additional opposing bends in front of the last chicane magnet. This way, the re-injection chicane magnets are only 'visible' by the higher pass beams. The second linac in the racetrack is configured exactly as a mirror image of the first one, with a replica of the re-injection chicane at its end, which facilitates a fixed-field extraction of energy recovered beam to the dump.

Linac Configuration and Multi-pass Optics Appropriate choice of the linac optics is of paramount importance for the transverse beam dynamics in a multi-pass ERL. The focusing profile along the linac (quadrupole gradients) need to be set (and they stay constant), so that multiple pass beams within a vast

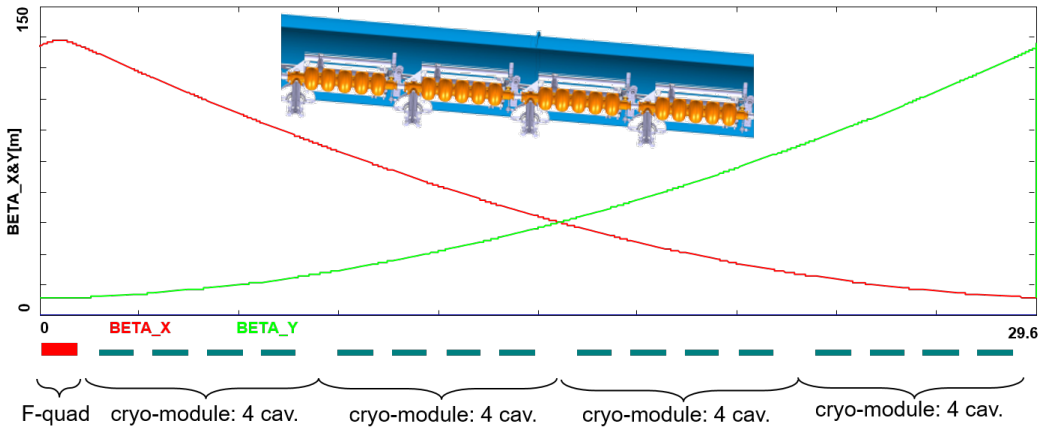

Figure 10.2: Layout of a half-cell composed out of four cryo-modules (each hosting four, 5-cell cavities: top insert) and a focusing quad. Beta functions reflect 130° FODO optics.

energy range may be transported efficiently (provide adequate transverse focusing for given linac aperture).The linac optics is configured as a strongly focusing, 130° FODO. In a basic FODO cell a quadrupole is placed every four cryomodules, so that the full cell contains two groups of 16 RF cavities and a pair of quads (F, D) as illustrated in Figure 10.2. The entire linac is built out of 14 such cells. Energy recovery in a racetrack topology explicitly requires that both the accelerating and decelerating beams share the individual return arcs [156]. This in turn, imposes specific requirements for TWISS function at the linacs ends: TWISS functions have to be identical for both the accelerating and decelerating linac passes converging to the same energy and therefore entering the same arc.

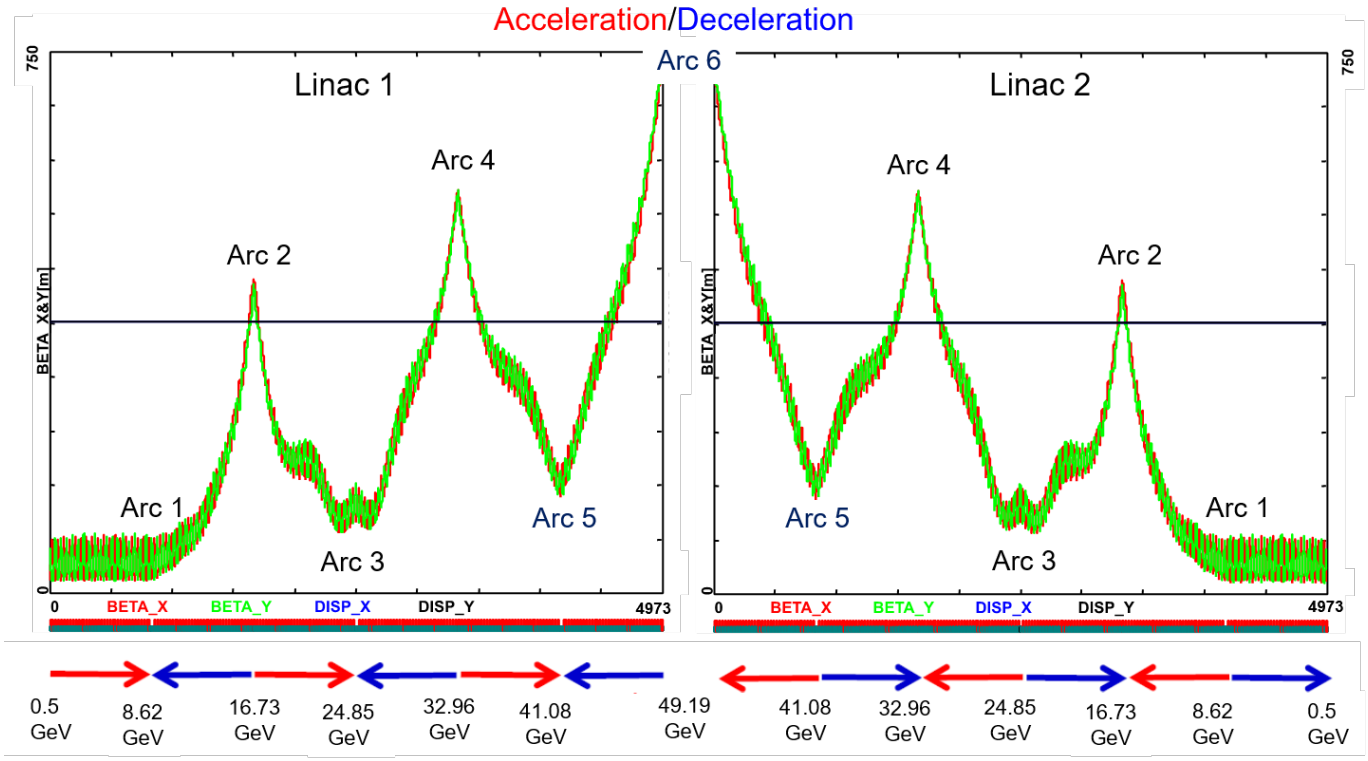

Figure 10.3: Beta function in the optimized multi-pass linacs (3 accelerating passes and 3 decelerating passes in each of two linacs. The matching conditions are automatically built into the resulting multi-pass linac beamline.

To visualize beta functions for multiple accelerating and decelerating passes through a given linac, it is convenient to reverse the linac direction for all decelerating passes and string them together with the interleaved accelerating passes, as illustrated in Figure 10.3. This way, the corresponding accelerating and decelerating passes are joined together at the arc's entrance/exit. Therefore, the matching conditions are automatically built into the resulting multi-pass linac beamline. One can see that both linacs uniquely define the TWISS functions for the arcs: Linac 1 fixes input to all odd arcs and output to all even arcs, while Linac 2 fixes input to all even arcs and output to all odd arcs. The optics of the two linacs are mirror-symmetric; They were optimized so that, Linac 1 is periodic for the first accelerating pass and Linac 2 has this feature for last decelerating one. In order to maximize the BBU threshold current [157], the optics is tuned so that the integral of β/E along the linac is minimized. The resulting phase advance per cell is close to 130°. Non-linear strength profiles and more refined merit functions were tested, but they only brought negligible improvements.

Recirculating Arcs - Emittance Preserving Optics Synchrotron radiation effects on beam dynamics, such as the transverse emittance dilution induced by quantum excitations have a paramount impact on the collider luminosity. All six horizontal arcs are accommodated in a tunnel of 536.4 m radius. The transverse emittance dilution accrued through a given arc is proportional to the emittance dispersion function, H, averaged over all arc's bends, as expressed by Equation 10.1.

$$\Delta\epsilon = \frac{2\pi}{3} C_q r_0 < H > \frac{\gamma^5}{\rho^2}, \tag{10.1}$$

where

$$C_q = \frac{55}{32\sqrt{3}} \frac{\hbar}{mc}$$

and r_0 is the classical electron radius, γ is the Lorentz boost.
Here, $H = (1+\alpha^2)/\beta \times D^2 + 2\alpha \times DD' + \beta \times D'^2$ where D, D' are the bending plane dispersion and its derivative, with $< ... > = \frac{1}{\pi} \int_{bends} ... \, d\theta$.

Therefore, emittance dilution can be mitigated though appropriate choice of arc optics (values of α, β, D, D' at the bends). In the presented design, the arcs are configured with a FMC (Flexible Momentum Compaction) optics to ease individual adjustment of, $< H >$, in various energy arcs.

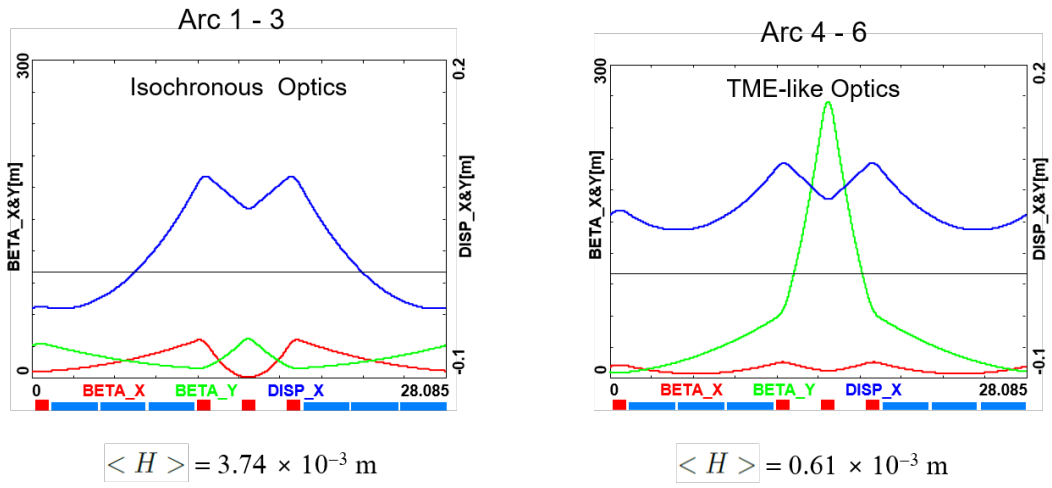

Figure 10.4: Two styles of FMC cells appropriate for different energy ranges. Left: lower energy arcs (Arc 1-3) configured with 'Isochronous' cells, Right: higher energy arcs configured with 'TME-like' cells. Corresponding values of the emittance dispersion averages, $< H >$, are listed for both style cells.

Optics design of each arc takes into account the impact of synchrotron radiation at different energies. At the highest energy, it is crucial to minimize the emittance dilution due to quantum excitations; therefore, the cells are tuned to minimize the emittance dispersion, H, in the bending sections, as in the TME (Theoretical Minimum Emittance) lattice. On the other hand, at the lowest energy, it is possible to compensate for the bunch elongation with isochronous optics which, additionally, contains the bunch-length. All styles of FMC lattice cells, as illustrated in Figure 10.4, share the same footprint for each arc. This allows us to stack magnets on top of each other or to combine them in a single design. Here, we use shorter, 28.1 m, FMC cell configured with six 3 m bends, in groups of flanked by a quadrupole singlet and a triplet, as illustrated in Figure 10.4. The dipole filling factor of each cell is 63 %; therefore, the effective bending radius, ρ, is 336.1 m. Each arc is followed by a matching section and a recombiner (mirror symmetric to spreader and matching section). Since the linacs are mirror-symmetric, the matching conditions described in the previous section, impose mirror-symmetric arc optics (identical betas and sign reversed alphas at the arc ends).

Path length adjusting chicanes were also foreseen to tune the beam time of flight in order to hit the proper phase at each linac injection. Later investigations proved them to be effective only with the lowest energy beam, as these chicanes triggers unbearable energy losses if applied to the higher energy beams. A possible solution may consist in distributing the perturbation along the whole arc with small orbit excitations.

Spreaders and Recombiners The spreaders are placed directly after each linac to separate beams of different energies and to route them to the corresponding arcs. The recombiners facilitate just the opposite:

merging the beams of different energies into the same trajectory before entering the next linac. As illustrated in Figure 10.5, each spreader starts with a vertical bending magnet, common for all three beams, that initiates the separation. The highest energy, at the bottom, is brought back to the horizontal plane with a chicane. The lower energies are captured with a two-step vertical bending adapted from the CEBAF design [158].

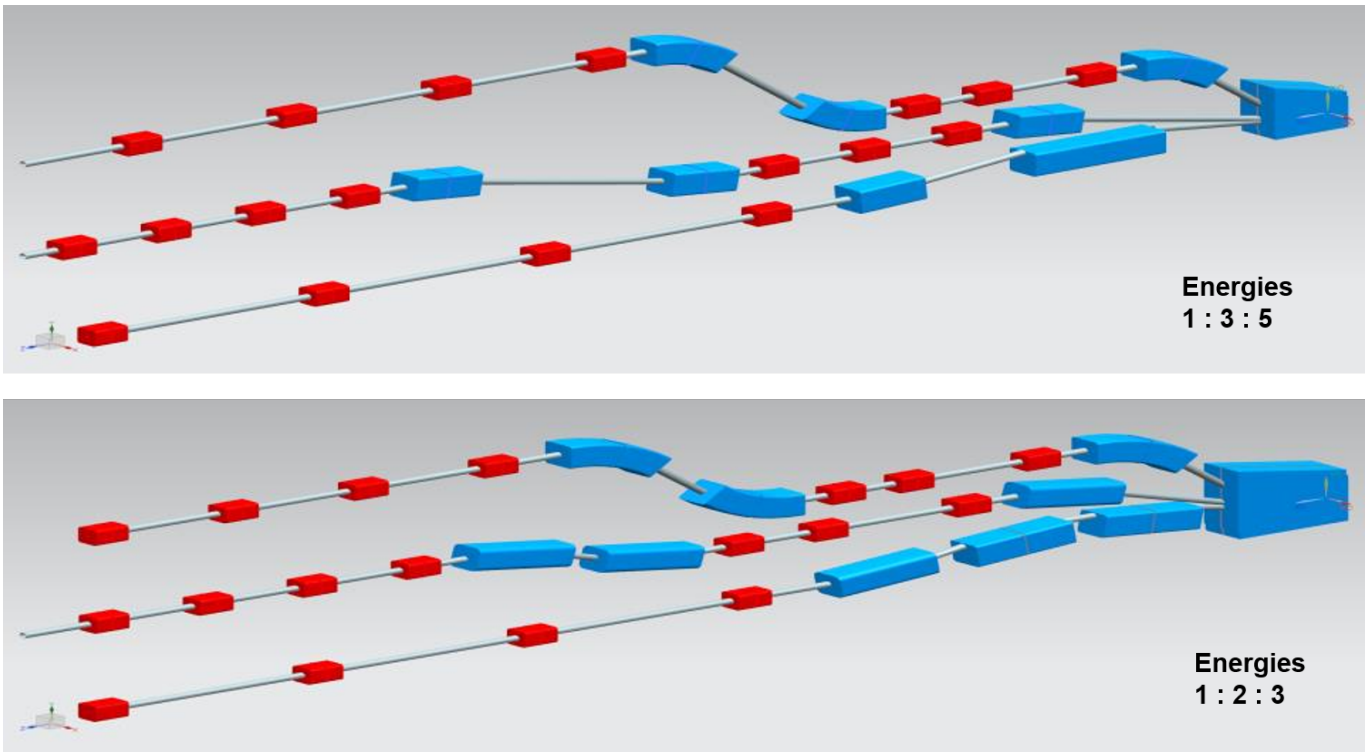

Figure 10.5: Layout of a three-beam switch-yard for different energy ratios: 1 : 3 : 5 and 1 : 2 : 3 corresponding to specific switch-yard geometries implemented on both sides of the racetrack

Functional modularity of the lattice requires spreaders and recombiners to be achromats (both in the horizontal and vertical plane). To facilitate that, the vertical dispersion is suppressed by a pair of quadrupoles located in-between vertical steps; they naturally introduce strong vertical focusing, which needs to by compensated by the middle horizontally focusing quad. The overall spreader optics is illustrated in Figure 10.6. Complete layout of two styles of switch-yard with different energy ratios is depicted in Figure 10.5. Following the spreader, there are four matching quads to 'bridge' the Twiss function between the spreader and the following 180° arc (two betas and two alphas).

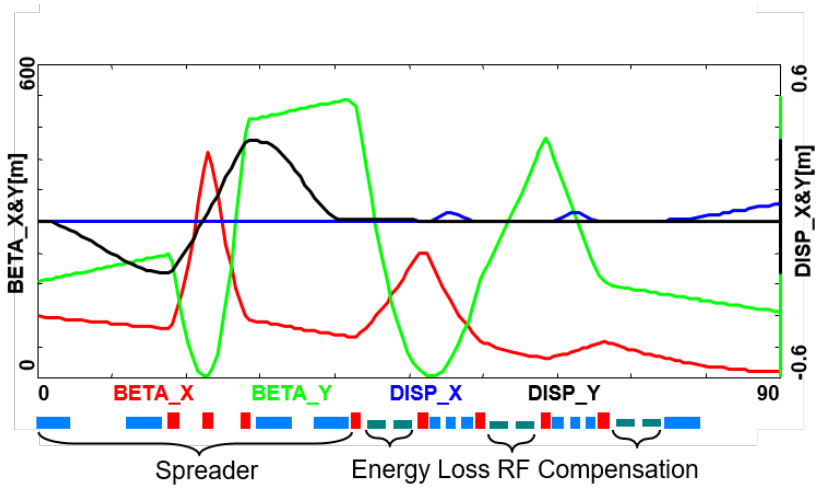

Figure 10.6: Spreader optics; featuring a vertical achromat, pathlength adjucting 'doglegs' and betatron matching quads, interleaved with enerfy loss compensation RF.

Combined spreader-arc-recombiner optics, features a high degree of modular functionality to facilitate momentum compaction management, as well as orthogonal tunability for both the beta functions and dispersion, as illustrated in Figure 10.7.

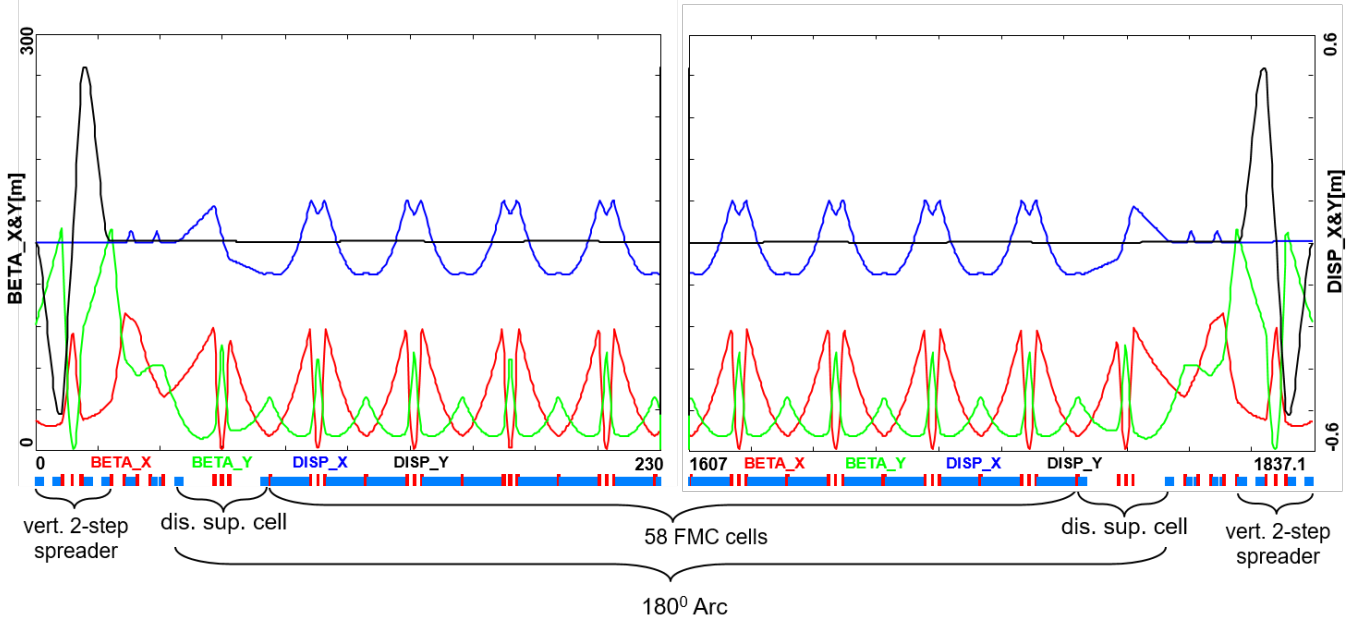

Figure 10.7: Complete Optics for Arc 3 (including switch-yard); featuring: low emittance 180° arc based on DBA-like cells (30 cells flanked by dispersion suppression cell with missing dipoles on each side), spreaders and recombiners with matching sections and doglegs symmetrically placed on each side of the arc proper.

IR Bypasses After the last spreader the 49.19 GeV beam goes straight to the interaction region. However the lower energy beams; at 16.7 and 33.0 GeV, need to be further separated horizontally in order to avoid interference with the detector. Different design options for the bypass section were explored [159] and the one that minimizes the extra bending has been chosen and implemented in the lattice.

Ten arc-like dipoles are placed very close to the spreader, to provide an initial bending, θ, which results in

$X = 10\,\text{m}$ separation from the detector located 120 m downstream. The straight section of the bypass is approximately 240 m long. After the bypass, in order to reconnect to the footprint of Arc 6, 7 of 30 standard cells in Arc 2 and Arc 4 are replaced with 7 higher field, junction cells. The number of junction cells is a compromise between the field strength increase and the length of additional bypass tunnel, as can be inferred from the scheme summarized in Figure . The stronger bending in the junction cells creates a small mismatch, which is corrected by adjusting the strengths of the quadrupoles in the last junction cell and in the first regular cell.

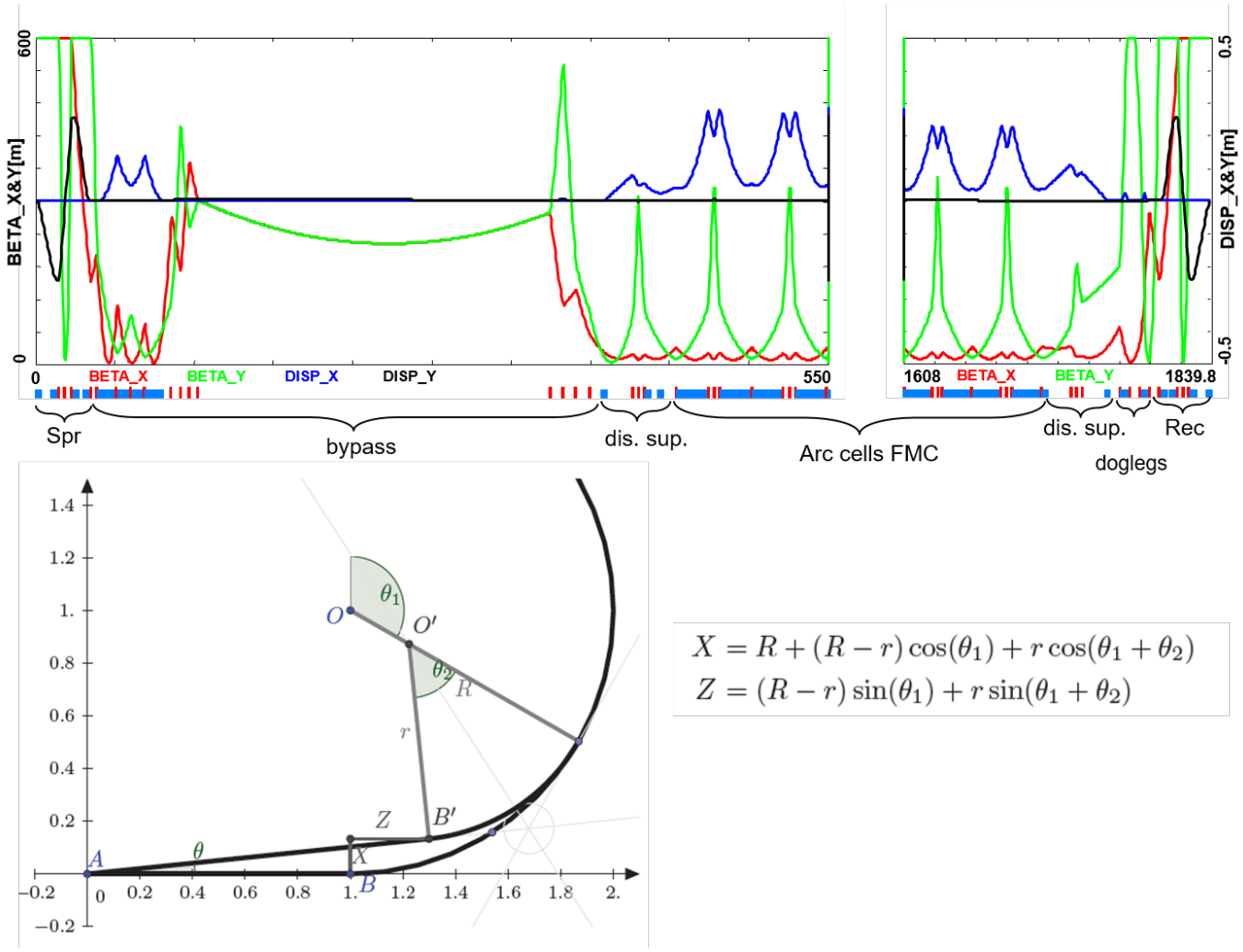

Figure 10.8: Optics and layout of Arc 4 including the detector bypass. The lattice (top insert) features a vertical spreader, an initial horizontal bending , a straight section, a modified dispersion suppressor, seven junction cells, and four regular cells. The bypass geometry (bottom insert), features a long IP line, AB, stretched to about 1/5 of the arc radius. All geometric dependencies of the bypass parameters are summarized in the inserted formulae as well.

Synchrotron Radiation Effects - Emittance Dilution ERL efficiency as a source of multi-GeV electrons for a high luminosity collider is limited by the incoherent synchrotron radiation effects on beam dynamics; namely the transverse emittance dilution and the longitudinal momentum spread (induced by quantum excitations). The fist effect, the transverse emittance increase, will have a paramount impact on the collider luminosity, due to stringent limits on the allowed emittance increase. The second one, accrued momentum spread, governs asymmetries of accelerated and decelerated beam profiles. These asymmetries

substantially complicate multi-pass energy recovery and matching, and ultimately they limit the energy reach of the ERLs due to recirculating arc momentum acceptance.

Arc optics was designed to ease individual adjustment of momentum compaction (needed for the longitudinal phase-space control, essential for operation with energy recovery) and the horizontal emittance dispersion, H, in each arc. Table 10.2 lists arc-by-arc dilution of the transverse, $\Delta\epsilon$, and longitudinal, $\Delta\sigma_{\frac{\Delta E}{E}}$, emittance dilution due to quantum excitations calculated using analytic formulas, Equations 10.2, 10.3 and 10.4, introduced by M. Sands [160].

$$\Delta E = \frac{2\pi}{3} r_0 \; mc^2 \; \frac{\gamma^4}{\rho}, \tag{10.2}$$

$$\Delta\epsilon_N = \frac{2\pi}{3} C_q r_0 < H > \frac{\gamma^6}{\rho^2}, \tag{10.3}$$

$$\frac{\Delta\epsilon_E^2}{E^2} = \frac{2\pi}{3} C_q r_0 \; \frac{\gamma^5}{\rho^2}, \tag{10.4}$$

where

$$C_q = \frac{55}{32\sqrt{3}} \; \frac{\hbar}{mc}.$$

Here, r_0 is the classical electron radius, γ is the Lorentz boost and $C_q \approx 3.832 \times 10^{-13}$ m for electrons (or positrons).

Table 10.2: Energy loss and cumulative emittance dilution (transverse and longitudinal) due to synchroton radiation at the end of a given beamline: Entire ER cycle (3 passes'up' + 3 passes 'down'). Here, $\Delta\sigma_{\frac{\Delta E}{E}} = \sqrt{\frac{\Delta\epsilon_E^2}{E^2}}$

Beamline	Beam energy [GeV]	ΔE [MeV]	$\Delta\epsilon_N$ [mm mrad]	$\Delta\sigma_{\frac{\Delta E}{E}}$ [%]
Arc 1	8.62	1	0.0017	0.00052
Arc 2	16.73	10	0.094	0.0033
Arc 3	24.85	50	1.1	0.011
Arc 4	32.96	155	2.0	0.026
Arc 5	41.08	375	5.2	0.052
Arc 6	49.19	770	14.9	0.092
Arc 5	41.08	375	18.2	0.118
Arc 4	32.96	155	19.1	0.133
Arc 3	24.85	50	20.1	0.140
Arc 2	16.73	10	20.2	0.143
Arc 1	8.62	1	20.2	0.144
Dump	0.5		20.2	0.144

Here, the LHeC luminosity requirement of total transverse emittance dilution (normalized) of 5.2 mm mrad is met by-design, employing low emittance optics arcs, as implemented in our scheme.
Finally, one can see from Equations 10.3 and 10.4 an underlying universal scaling of the transverse and longitudinal emittance dilution with energy and arc radius; they are both proportional to γ^5/ρ^2. This in

turn, has a profound impact on arc size scalability with energy; namely the arc radius should scale as $\gamma^{5/2}$ in order to preserve both the transverse and longitudinal emittance dilutions, which is a figure of merit for a synchrotron radiation dominated ER.

10.2.2 30 GeV ERL Options [Alex Bogacz]

One may think of an upgrade path from 30 to 50 GeV ERL, using the same 1/5 of the LHC circumference (5.4 km), footprint. In this scenario, each linac straight (front end) would initially be 'loaded' with 18 cryo-modules, forming two 5.21 GV linacs. One would also need to decrease the injector energy by factor of 5.21/8.11 The top ERL energy, after three passes, would reach 31.3 GeV. Then for the upgrade to 50 GeV, one would fill the remaining space in the linacs with additional 10 cryo-moduls each; 2.9 GV worth of RF in each linac. This way the energy ratios would be preserved for both 30 and 50 GeV ERL options, so that the same switch-yard geometry could be used. Finally, one would scale up the entire lattice; all magnets (dipoles and quads) by 8.11/5.21 ratio. If one wanted to stop at the 30 GeV option with no upgrade path, then the 1/12 of the LHC circumference (2.2 km) would be a viable footprint for the racetrack, featuring: two linacs, 533 m each, (18 cryo-modules) and arcs of 136 m radius. Again, assuming 0.32 GeV injection energy, the top ERL energy would reach 31.3 GeV.

10.2.3 Component Summary [Alex Bogacz]

This closing section will summarize active accelerator components: RF cavities/cryo-modules and magnets (bends and quads) for both the 50 GeV baseline and 30 GeV ERL Options. They are collected in the Tables below:

10.3 Electron-Ion Scattering [John Jowett]

Besides colliding proton beams, the LHC also provides collisions of nuclear (fully-stripped ion) beams with each other (AA collisions) or with protons (pA). Either of these operating modes offers the possibility of electron-ion (eA) collisions in the LHeC configuration. In pA operation of the LHC the beams may be reversed (Ap) for some part of the operating time. Only one direction (ions in Beam 2) would provide eA collisions while the other would provide ep collisions at significantly reduced luminosity compared to the pp mode, since there would be fewer bunches of lower intensity.

Here we present luminosity estimates for collisions of electrons with $^{208}Pb^{82+}$ nuclei, the species most commonly collided in the LHC. Other, lighter, nuclei are under consideration for future LHC operation [93].

10.4 Beam-Beam Interactions [Kevin Andre, Andrea Latina, Daniel Schulte]

10.5 Arc Magnets [Pierre Thonet, Cynthia Vallerand]

10.6 LINAC and SRF [Erk Jensen]

Each of the two main linacs has an overall length of 828.8 m and provides an acceleration of 8.114 GV. Each linac consists of 112 cryomodules, arranged in 28 units of 4 cryomodules with their focussing elements—each cryomodule contains four 5-cell cavities, optimized to operate with large beam current (up to 120 mA at the HOM frequencies). The operating temperature is 2 K; the cavities are based on modern SRF technology and

are fabricated from bulk Nb sheets; they are described in detail in subsection 10.6.2 below. The nominal acceleration gradient is 19.73 MV/m.

In addition to the main linacs, the synchrotron losses in the arcs will make additional linacs necessary, referred to here as the "loss compensation linacs". These will have to provide different accelerations in the different arcs, depending on the energy of the beams as shown in Table 10.3. The quoted beam energies are at entry into the arc. Their natural placement would be at the end of the arcs just before the combiner, where the different energy beams are still separate. The largest of these linacs would have to compensate the SR losses at the highest energy, requiring a total acceleration of about 700 MV. The loss compensation linacs will be detailed in subsection 10.6.7 below.

Table 10.3: Synchroton radiation losses for the different arc energies

Arc number	Beam energy [GeV]	ΔE [MeV]
1	8.62	1
2	16.73	10
3	24.85	50
4	32.96	155
5	41.08	375
6	49.19	770

Through all arcs but arc 6, the beam passes twice, once while accelerated and once while decelerated. It is planned to operate these additional "loss compensation linacs" at 1603.2 MHz, which allows energy compensation of both the accelerated and the decelerated beam simultaneously. This subject will be discussed in detail in a subsequent section, 1.6.7.

10.6.1 Choice of Frequency [Frank Marhauser]

The RF frequency choice primarily takes into account the constraints of the LHC bunch repetition frequency, f_0, of 40.079 MHz, while allowing for a sufficiently high harmonic, h, for a flexible system. For an ERL with $n_{pass} = 3$ recirculating passes and in order to enable equal bunch spacing for the 3 bunches – though not mandatory – it was originally considered to suppress all harmonics that are not a multiple of $n_{pass} \cdot f_0 = 120.237$ MHz. Initial choices for instance were 721.42 MHz ($h = 18$) and 1322.61 MHz ($h = 33$) in consideration of the proximity to the frequencies used for state-of-the-art SRF system developments worldwide [161]. In synergy with other RF system developments at CERN though, the final choice was 801.58 MHz ($h = 20$), where the bunching between the 3 recirculating bunches can be made similar but not exactly equal. Note that this frequency is also very close to the 805 MHz SRF proton cavities operating at the Spallation Neutron Source (SNS) at ORNL, so that one could leverage from the experience in regard to cryomodule and component design at this frequency.

Furthermore, in the frame of an independent study for a 1 GeV CW proton linac, a capital plus operational cost optimization was conducted [162]. This optimization took into account the expenditures for cavities, cryomodules, the linac tunnel as well as the helium refrigerator expenses as a function of frequency and thus component sizes. Labor costs were included based on the existing SNS linac facility work breakdown structure. It was shown that capital plus operating costs could be minimized with a cavity frequency between 800 MHz and 850 MHz, depending also on the choice of the operating He bath temperature (1.8 K to 2.1 K). Clear benefit of operating in this frequency regime are the comparably small dynamic RF losses per installation length due to a relatively small BCS surface resistance as well as low residual resistance of the niobium at the operating temperature. This could be principally verified as part of the prototyping effort detailed in the next sub-section. Note that the cost optimum also favors cavities operating at rather

moderate field levels ($< 20\,\mathrm{MV/m}$). This comes as a benefit in concern of field emission and associated potential performance degradations.

10.6.2 Cavity Prototype [Frank Marhauser]

Given the RF frequency of 801.58 MHz, JLab has collaborated with CERN, and consequently proposed a five-cell cavity design that was accepted for prototyping, see Fig. 10.9. The cavity shape has also been adopted for PERLE. Table 10.4 summarizes the relevant cavity parameters.

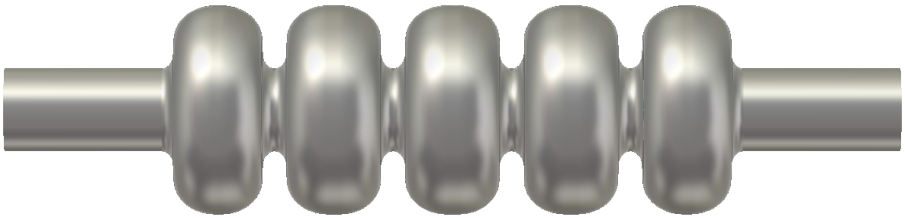

Figure 10.9: Bare 802 MHz five-cell cavity design (RF vacuum) with a 130 mm iris and beam tube aperture.

Table 10.4: Parameter table of the 802 MHz prototype five-cell cavity

Description	unit	parameters
Frequency	MHz	801.58
Number of cells		5
active length l_{act}	mm	917.9
loss factor	$\mathrm{V\,pC^{-1}}$	2.742
R/Q (linac convention)	Ω	523.9
$R/Q \cdot G$ per cell	Ω^2	28788
Cavity equator diameter	mm	327.95
Cavity iris diameter	mm	130
Beam tube inner diameter	mm	130
diameter ratio equator/iris		2.52
E_{peak}/E_{acc}		2.26
B_{peak}/E_{acc}	mT/(MV/m)	4.2
cell-to-cell coupling factor k_{cc}	%	3.21
$\mathrm{TE_{11}}$ cutoff frequency	GHz	1.35
$\mathrm{TM_{01}}$ cutoff frequency	GHz	1.77

The cavity exhibits a rather large iris and beam tube aperture (130 mm) to consider beam-dynamical aspects such as HOM-driven multi-bunch instabilities. Despite the comparably large aperture, the ratio of the peak surface electric field, E_{pk}, respectively the peak surface magnetic field, B_{pk}, and the accelerating field, E_{acc}, are reasonably low, while the factor $R/Q \cdot G$ is kept reasonably high, concurrently to limit cryogenic losses. This is considered as a generically well 'balanced' cavity design [163]. The cavity cell shape also avoids that crucial HOMs will coincide with the main spectral lines (multiples of 801.58 MHz), while the specific HOM coupler development is pending.

Furthermore, as shown in Fig. 10.10 for the case of the bunch recombination pattern considered for PERLE originally, the much denser intermediate beam current lines (green) are not coinciding with cavity HOMs. Here the figure plots the real part of the beam-excited cavity monopole impedance spectrum up to 6 GHz, and denotes the power deposited at each spectral line (in Watt) for an injected beam current of 25 mA.

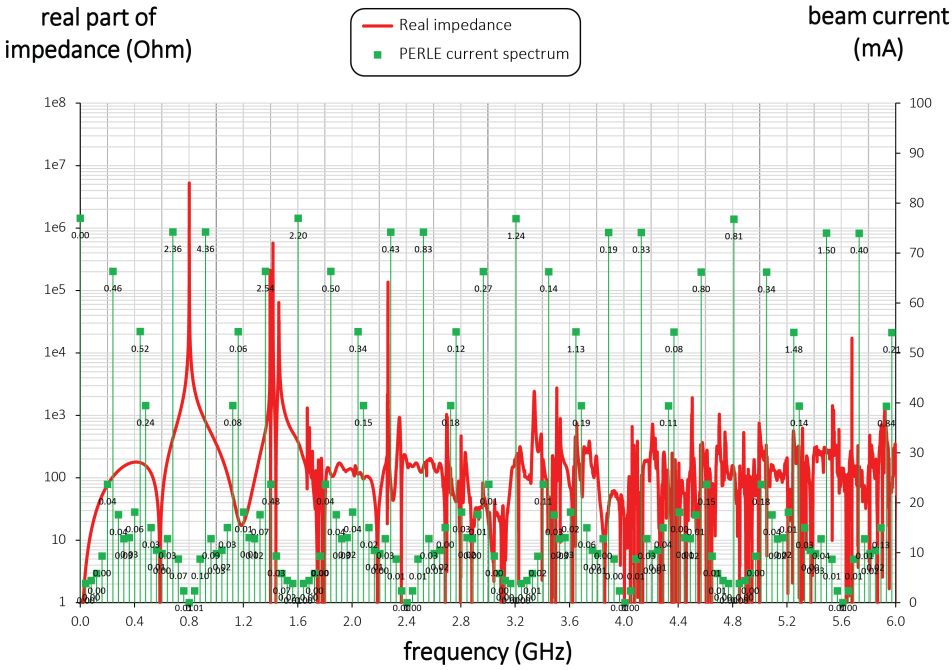

Figure 10.10: Real monopole impedance spectrum of the five-cell 802 MHz cavity prototype (red) together with the considered beam current lines (green) for the 3-pass PERLE machine (25 mA injected current). The numbers associated with the spectral lines denote the power dissipation (in Watt).

For instance, the summation of the power in this spectral range results in a moderate 30 Watts. This covers the monopole modes with the highest impedances residing below the beam tube cutoff frequency. The HOM-induced heat has to be extracted from the cavity and shared among the HOM couplers attached to the cavity beam tubes. The fraction of the power escaping through the beam tubes above cutoff can be intercepted by beam line absorbers.

Note that for Fig. 10.10 a single HOM-coupler end-group consisting of three scaled TESLA-type coaxial couplers was assumed to provide damping. Instead of coaxial couplers, waveguide couplers could be utilized, which for instance have been developed at JLab in the past for high current machines. These are naturally broadband and designed for high power capability, though some penalty is introduced as this will increase the complexity of the cryomodule. Ultimately, the aim is to efficiently damp the most parasitic longitudinal and transverse modes (each polarization). The evaluation of the total power deposition is important for LHeC to decide which HOM coupler technology is most appropriate to cope with the dissipated heat and whether active cooling of the couplers is a requirement.

Though the prototype efforts focused on the five-cell cavity development, JLab also produced single-cell cavities, i.e. one further Nb cavity and two OFE copper cavities. The former has been shipped to FNAL for N-doping/infusion studies, whereas the latter were delivered to CERN for Nb thin-film coating as a possible alternative to bulk Nb cavities. In addition, a copper cavity was built for low power bench measurements, for which multiple half-cells can be mechanically clamped together. Presently, a mock-up can be created with up to two full cells. This cavity has been produced in support of the pending HOM coupler development. Fig. 10.11 shows the ensemble of manufactured cavities resonating at 802 MHz.

Results for the Nb cavities - made from fine grain high-RRR Nb - were encouraging since both cavities reached accelerating fields, E_{acc}, slightly above 30 MV/m ultimately limited by thermal breakdown (quench). Moreover, the RF losses were rather small as a benefit of the relatively low RF frequency as anticipated. The residual resistance extracted from the measurement data upon cooldown of the cavity was $3.2\,\Omega \pm 0.8\,\Omega$. This resulted in unloaded quality factors, Q_0, well above 4×10^{10} at 2 K at low field levels, while Q_0-

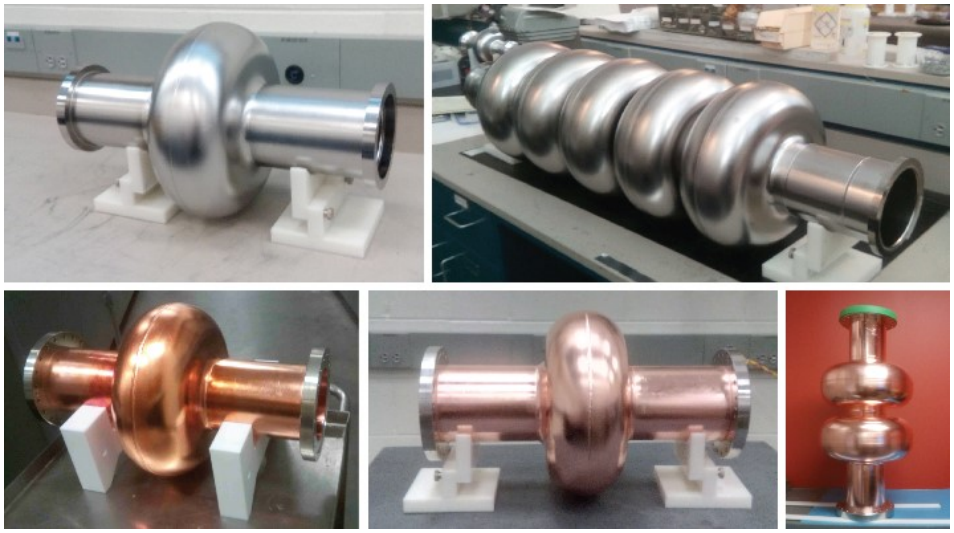

Figure 10.11: Ensemble of 802 MHz cavities designed and built at JLab for CERN. The Nb cavities have been tested vertically at 2 Kelvin in JLab's vertical test area.

values beyond 3×10^{10} could be maintained for the five-cell cavity up to $\sim$27 MV/m (see Fig. 10.12). Only standard interior surface post-processing methods were applied including bulk buffered chemical polishing, high temperature vacuum annealing, light electropolishing, ultrapure high-pressure water rinsing, and a low temperature bake-out. While the vertical test results indicate generous headroom for a potential performance reduction once a cavity is equipped with all the ancillary components and installed in a cryomodule, clean cavity assembly procedure protocols must be established for the cryomodules to minimize the chance of introducing field-emitting particulates.

10.6.3 Dressed Cavity Design [Rama Calaga]

10.6.4 Cavity-CryoModule [Sebastien Bousson]

10.6.5 Sources [Boris Militsyn, Ben Hounsell, Matt Poelker]

Specification of electron sources

Operation of the LHeC with an electron beam, delivered by a full energy ERL imposes specific requirements on the electron source. It should deliver a beam with the charge and temporal structure required at the Interaction Point. Additionally as during acceleration in a high energy ERL both longitudinal and transverse emittances of the beam are increased due to Synchrotron Radiation (SR), the 6D emittance of the beam delivered by electron source should be small enough to mitigate this effect. The general specification of the electron source are shown in Table 10.5. Some parameters in this table such as RMS bunch length, uncorrelated energy spread and normalised transverse emittance are given on the basis of the requirements for the acceleration in ERL and to pre-compensate the effects of SR. The most difficult of the parameters to specify is injector energy. It should be as low as possible to reduce the unrecoverable power used to accelerate the beam before injection into the ERL while still being high enough to deliver short electron bunches with high peak current. Another constraint on the injection energy is the average energy and energy spread of the returned beam. The average energy cannot be less than the energy of electron source, but the maximum energy in the spectrum should not exceed 10 MeV the neutron activation threshold. An injection energy of 7 MeV is a reasonable compromise to meet this constraint.

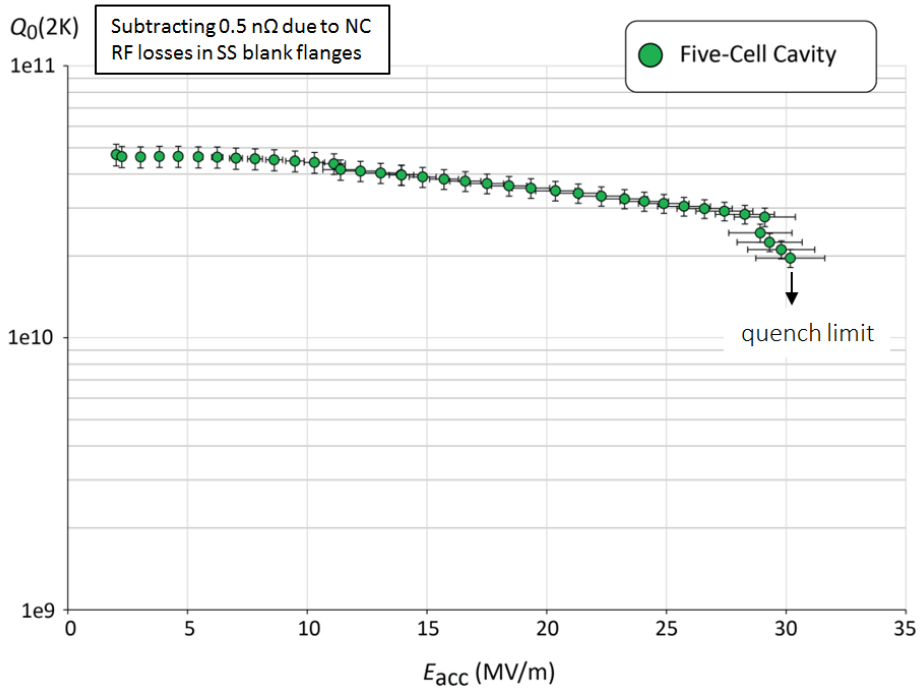

Figure 10.12: Vertical test result of the five-cell 802 MHz niobium cavity prototype.

Table 10.5: General specification of the LHeC ERL electron injector.

Beam parameter	
Injection energy, MeV	7*
Bunch repetition rate, MHz	40.1
Average beam current, mA	20
Bunch charge, pC	500
RMS bunch length, mm	3
Normalised transverse emittance, π·mm·mrad	<6
Uncorrelated energy spread, keV	10
Beam polarisation	Unpolarised/Polarised

The required temporal structure of the beam and the stringent requirements for beam emittance do not allow the use of conventional thermionic electron sources for the LHeC ERL without need for beam losses during the bunching process. While this option cannot completely be excluded as a source of unpolarised electrons. The requirement to deliver polarised beams leaves only one option available, electron sources based on photoemission of electrons.

There are now four possible design of electron sources for delivering unpolarised beams and (potentially) three for delivering polarised beams:

1. A thermionic electron source with RF modulated grid or gate electrode with following (multi)stage compression and acceleration. The electron source could be either a DC electron gun or an RF electron source in this case. Although these sources are widely used in the injectors of IR FELs [164] their emittance is not good enough to meet the specification of the LHeC injector. Moreover, thermionic sources cannot deliver polarised electrons.

2. A VHF photoemission source. This is a type of normal conducting RF source which operates in the frequency range 160 MHz – 200 MHz. The relatively low frequency of these sources means that they

are large enough that sufficient cooling can be provided to permit CW operation. This type of source has been developed for the new generation of CW FELs such as LCLS-II [165], SHINE [166] and European XFEL upgrade [167], but they have not yet demonstrated the average current required for the LHeC injector. The possibility of generating polarised electrons with this type of source has not investigated yet.

3. A superconducting RF photoemission source. This type of sources are under development for different applications such as an option for CW FEL's (ELBE [168], LCLS-II, European XFEL), as a basis of injectors for ERL's (bERLinPro) and for electron cooling (BNL). Though this type of sources has already demonstrated the possibility of delivering the average current, required for the LHeC with unpolarised beams (BNL), and has the potential for operation with GaAs type photocathodes (HZDR) which are required for delivery of polarised beams, the current technology of SRF photoelectron source cannot be considered as mature enough for use in the LHeC.

4. A DC photoemission source. In this type of source the electrons are accelerated immediately after emission by a potential difference between the source cathode and anode. This type of source is the most common for use in ERL injectors. It has been used in the projects which are already completed (JLAB, DL), is being used for ongoing projects (KEK, Cornell/CBeta [169]) and is planned to be used in new projects such as the LHeC prototype PERLE [170]. The technology of DC photoelectron sources is well-developed and has demonstrated the average current and beam emittance required for the LHeC ERL (Cornell). Another advantage of the photoelectron source with DC acceleration is the possibility of operation with GaAs photocathodes for delivering of polarised beam. Currently it's the only source, which can delivery of highly polarized electron beams with the current of up to 6 mA which is already in the range of LHeC specifications (JLab).

Based on this analysis at CDR stage we consider the use of DC photoelectron source as a basic option, keeping in mind that in the course of the injector development other types of electron sources may be considered, especially for providing of unpolarised beam.

The LHeC unpolarised injector

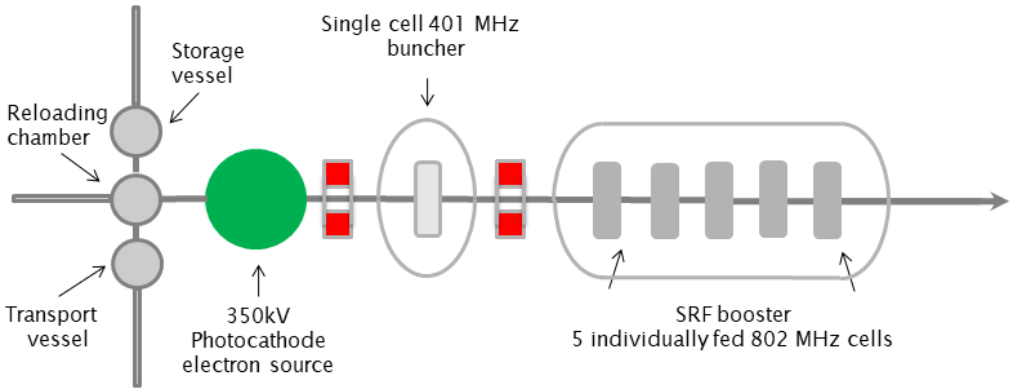

Figure 10.13: The layout of the unpolarised injector.

The injector layout follows the scheme depicted in Fig. 10.13. Its design will be similar to the unpolarised variant of the PERLE injector [170]. The electron source with DC acceleration delivers a CW beam with the required bunch charge and temporal structure. Immediately after the source is a focusing and bunching section consisting of two solenoids with a normal conducting buncher placed between them. The solenoids have two purposes. Firstly to control the transverse size of the space charge dominated beam which will otherwise rapidly expand transversely. This ensures that the beam will fit through all of the apertures in

the injector beamline. Secondly the solenoids are used for emittance compensation to counter the space charge induced growth in the projected emittance. This is then followed by a superconducting booster linac. This accelerates the beam up to its injection energy, provides further longitudinal bunch compression and continues the emittance compensation process.

The DC electron source will have an accelerating voltage of 350 kV using a high quantum efficiency antimonide based photocathode such as Cs_2KSb. The photoinjector laser required for this cathode type will be a 532 nm green laser. There will be a load lock system to allow photocathodes to be replaced without breaking the source vacuum. This significantly reduces the down time required for each replacement which is a major advantage in a user facility such as the LHeC where maximising uptime is very important. The cathode electrode will be mounted from above similar to the Cornell [3] and KEK [171] sources. This electrode geometry makes the addition of a photocathode exchange mechanism much easier as photocathode can be exchanged through the back of the cathode electrode. In addition the cathode electrode will be shaped to provide beam focusing. An example of a Jefferson lab type electron source, with the cathode electrode mounted from behind, optimised for the requirements of the LHeC prototype PERLE can be seen in Fig. 10.14 [172].

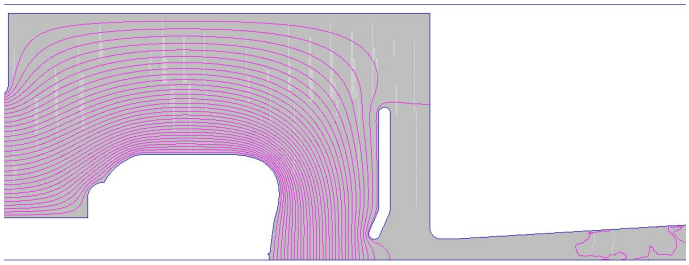

Figure 10.14: The optimised electrode geometry for PERLE. This is a Jefferson lab type gun and is optimised for both 350 kV and 220 kV operation.

The operational voltage of 350 kV for the source was chosen as practical estimate of what is achievable. A higher voltage would produce better performance but would be challenging to achieve in practice. The highest operational voltage successfully achieved is 500 kV by the DC electron source that is used for the cERL injector [4]. However as shown in the following section 350 kV is sufficient to achieve the required beam quality. Fig. 10.14 shows configuration of electrodes in the PERLE electron source optimised for operation in two modes – at voltage 350 kV for unpolarised mode and 220 kV for polarised mode. In addition to the cathode electrode the source is also equipped with an anode electrode biased to few kV positive. The purpose of this electrode is to block back ion stream from low vacuum part of accelerator which can severe damage photocathodes.

The unpolarised variant of the PERLE injector [2] is shown in the previous section as it provides an example of the achievable parameters. The PERLE injector will have similar behaviour to the LHeC injector as it has the same layout but the electron source will be different as unlike PERLE the LHeC source only needs to perform in one operational mode. Beam dynamics in the injector up to the booster exit were simulated with ASTRA and optimised using the many objective optimisation algorithm NSGAIII. The target injection energy and bunch length were chosen as 7 MeV and 3 mm which are the required values for PERLE. A solution was selected from the results of the optimisation and is presented below. The transverse beam size and bunch length are kept small enough by the solenoid and buncher to ensure that there would be no issue with passing through the apertures or RF non-linearities. This can be seen in Fig. 10.15.

The behaviour of the emittances can be seen in Fig. 10.16.

The transverse emittance at the booster exit is 4 mm·mrad which meets the PERLE requirements and should be sufficient for the LHeC. This analysis shows that injector based on a high voltage DC electron source is capable of achieving the required transverse emittances for the LHeC at the necessary bunch charges.

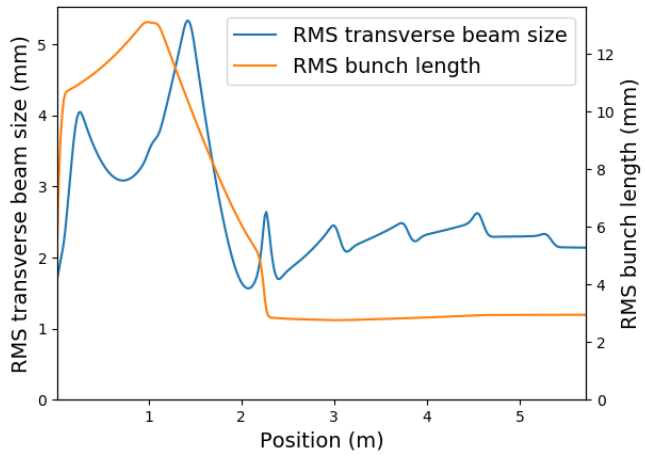

Figure 10.15: The rms beam sizes transversely and longitudinally as the bunch travels along the injector.

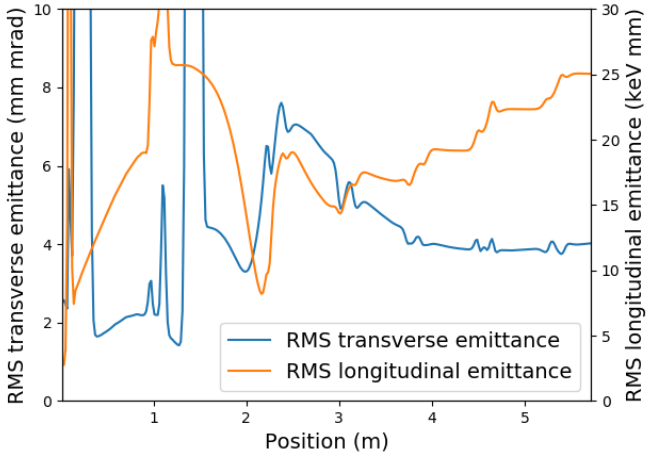

Figure 10.16: The emittances of the bunch as it travels along the injector.

Polarised electron source for ERL

Providing polarised electrons has always been challenging process, especially at relatively high average current as required for the LHeC. The only practically usable production mechanism of polarised electrons is the illumination of activated to Negative Electron Affinity (NEA) state GaAs based photocathodes with circularly polarised laser light. The vacuum requirements for these cathodes mean that this must be done in a DC electron source only. In the course of the last 30 years significant progress has been achieved in improving the performance of polarised electron sources. The maximum achievable polarisation has reached 90% and the maximum Quantum Efficiency (QE) of the photocathode at the laser wavelength of maximum polarisation has reached 6%. Meanwhile the implementation of a polarised electron source into the LHeC remains a challenge as the practical operational charge lifetime of the GaAs based photocathode does not exceed few kC (JLAB) at an operational current of about 5 mA. In Fig. 10.17 a preliminary design of the LHeC polarised injector is shown.

In general, the design of the polarised electrons injector is close to that of the unpolarised injector and is based on a DC electron source where a photocathode is illuminated by a pulsed laser beam. The choice of a DC source is dictated by the necessity of achieving extra high vacuum, with a pressure at a level of

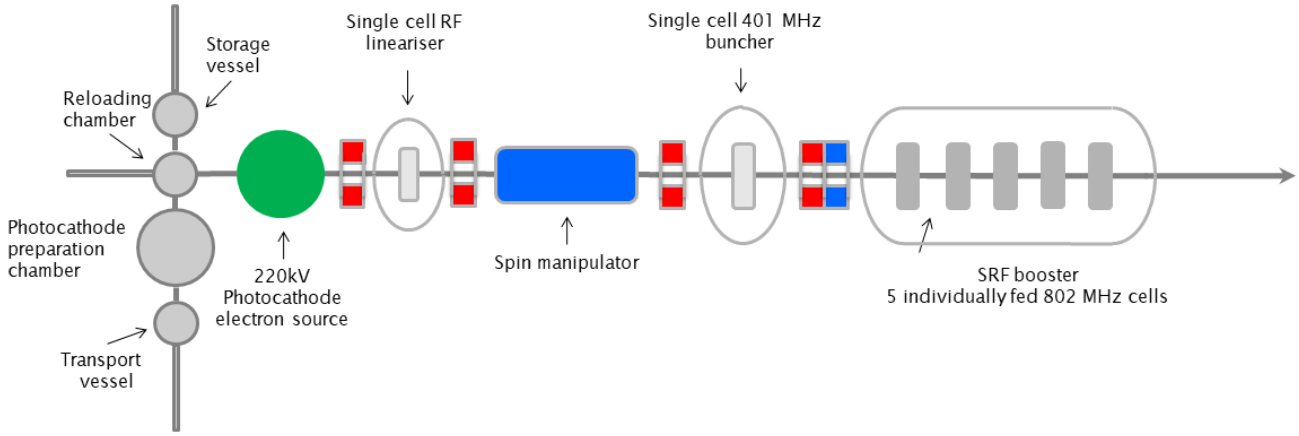

Figure 10.17: The layout of the polarised injector.

10^{-12} mbar, in the photocathode area. This level of vacuum is neccesary for providing long lifetime of the photocathode. In order to reduce photocathode degradation caused by electron stimulated gas desorption accelerating voltage in the source is reduced to 220 kV. The main differences with unpolarised injector are the presence of a photocathode preparation system, permanently attached to the source, and a Wien filter based spin manipulator between the source and the buncher. In order to reduce depolarisation of the beam in the spin manipulator, caused by the space charge induced energy spread of the beam, an RF d is installed between the source and the spin manipulator. The injector is also equipped with a Mott polarimeter to characterise the polarisation of the beam delivered by the source.

An important consideration of the operation with interchangeable photocathodes is minimisation of the down time required for the photocathode exchange. It typically takes few hours to replace the photocathode and to characterise polarisation of the beam. For large facility like LHeC this is unacceptable. A practical solution could be operation with 2 or more electron sources which operate in rotation. Another motivation for using several electron sources is the nonlinear dependence of photocathode charge lifetime on average beam current (JLAB), which reduces with increasing of the average current. In case of 3 electron sources 2 of them can be operated with half operation frequency 20.05 MHz in opposite phase delivering average current of 10 mA each, while the third is in stand by regime with freshly activated photocathode. The only time which is necessary to switch it on is the time required for rising the high voltage. Another advantage of using a 3 source scheme is the reduction of the average laser power deposited on the photocathode and as result relaxing requirements for the photocathode cooling. In order to implement a 3 source polarised electron injector, development of a deflection system which is able to merge the beams from different sources before the spin rotator is required.

Lasers for electron sources

In the proposed design of the LHeC injection system at least 2 lasers must be used. In the unpolarised electron injector, which is going to operate with antimionide-based photocathode, a laser with a wavelength of 532 nm is required. Typical initial QE of these photocathodes is 10% and for practical application reduction of QE up to 1% may be expected. For polarised electron source typical QE varies from 1% down to 0.1% and laser with a wavelength of 780 nm is required. The optimised parameters of the required lasers are summarised in Table 10.6. Laser temporal profile and spot size on the photocathode are given on the basis of source optimisation for operation at 350 kV for unpolarised regime and 220 kV for polarised.

Table 10.6: Parameters of the electron source drive laser.

Laser beam parameter	unpolarised mode	polarised mode
Laser wavelength, nm	532	780
Laser pulse repetition rate, MHz	40.1	
Laser pulse repetition rate, MHz		40.1
Energy in the single pulse at photocathode Qe=1%, μJ	0.12	
Average laser power at photocathode Qe=1%, W	4.7*	
Energy in the single pulse at photocathode Qe=0.1%, μJ		0.79
Average laser power at photocathode Qe=0.1%, W		32*
Laser pulse duration, ps FWHM	118	80
Laser pulse rise time, ps	3.2	3.2
Laser pulse fall time, ps	3.2	3.2
Spot diameter on the photocathode surface, mm	6.4	8
Laser spot shape on the photocathode surface	Flat top	

10.6.6 Injector [Oliver Bruening]

10.6.7 Compensation of Synchrotron Radiation Losses [Alex Bogacz]

Depending on energy, each arc exhibits factional energy loss due to the synchrotron radiation, which scales as γ^4/ρ^2 (see Equations 10.2). Arc-by-arc energy loss was previously summarized in Table 10.3. That energy loss has to be replenished back to the beam, so that at the entrance of each arc the accelerating and decelerating beams have the same energy. Before or after each arc, a matching section adjusts the optics from and to the linac. Adjacent to these, additional cells are placed, hosting the RF compensating sections. The compensation makes use of a second harmonic RF at 1603.2 MHz to replenish the energy loss for both the accelerating and the decelerating beams, therefore allowing them to have the same energy at the entrance of each arc, as shown in Figure 10.18.

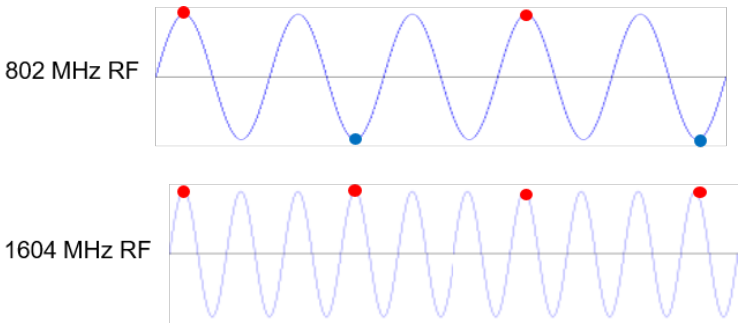

Figure 10.18: The second-harmonic RF restores the energy loss in both the accelerating and decelerating passes.

Parameters of the rf compensation cryomodules, shown in Table 10.7, have been extrapolated from the ILC cavity design, expecting that the higher frequency and lower gradient would support continuous operation.

Table 10.7: A tentative list of parameter for the compensating rf cryomodules extrapolated from the ILC design.

Frequency	1603.2 MHz
Gradient	30 MV/m
Design	Nine cells
Cells length	841 mm
Structure length	1 m
Cavity per cryomodule	6
Cryomodule length	6 m
Cryomodule voltage	150 MV

The compensating cryo-modules are placed into Linac 1 side of the racetrack, before the bending section of Arc 1, Arc 3, and Arc 5 and after the bending section of Arc 2, Arc 4, and Arc 6. This saves space on Linac 2 side to better fit the interaction point (IP) line and the bypasses. Note that with the current vertical separation of 0.5 m it will not be possible to stack the cryomodules on top of each other; therefore, they will occupy 36 m on the Arc 4 and Arc 6 side. Table 10.8 shows the energy loss for each arc and the corresponding synchrotron radiated power, along with number of cryomodules at 1603.2 MHz RF frequency required to replenish the energy loss.

Table 10.8: Arc-by-arc synchrotron radiated power and number of 2-nd harmonic RF cryomodules required to compensate energy loss.

Arc number	ΔE [MeV]	P [MW]	Cryomodules
1	1	0.03	0
2	10	0.5	0
3	50	2.5	1
4	155	7.8	1
5	375	18.7	3
6	770	38.5	5

and 18 m on the Arc3 and Arc 5 side of the racetrack. Each of the compensating cavities in Arc 5 needs to transfer up to 1 MW to the beam. Although a 1 MW continuous wave klystron are available [173], the cryomodule integration and protection system will require a careful design.

10.6.8 LINAC Configuration and Infrastructure [Erk Jensen]

Since the power supplied to the beam in the main linacs will be recovered, the average RF power requirements at 802 MHz are relatively small and determined by the needs to handle transients and microphonics.

The RF power required for the second-harmonic RF system however is substantial - it can be estimated from Table 10.3 with the nominal current of 20 mA:

10.7 Interaction Region [Emilia Cruz Alaniz, Kevin Andre', Bernhard Holzer, Roman Martin, Rogelio Tomas]

10.7.1 Layout [Emilia Cruz Alaniz, Roman Martin, Rogelio Tomas]

The basic principle of the Linac-Ring Interaction Region (IR) design remains unchanged and it is shown in Figure 10.19: the two proton beams are brought onto intersecting orbits by strong separation and recombination dipoles. A collision of the proton beams at the Interaction Point (IP) is avoided via timing. The large crossing angle keeps the long range beam-beam effect small and separates the beams enough to allow septum quadrupoles to focus only the colliding beam (the anti-clockwise rotating LHC beam – Beam 2). The non-colliding beam (the clockwise rotating LHC beam – Beam 1) is unfocused and passes the septum quadrupoles in a field free aperture. The electron beam is brought in with an even larger angle, partly sharing the field free aperture of the septum quadrupoles with the non-colliding beam. A weak dipole in the detector region bends the electron beam into head-on collisions with the colliding proton beam. The two proton beams are also exposed to the dipole field but, due to the large beam rigidity, they are barely affected. After the interaction point a dipole with opposite polarity separates the orbits of the electron and proton beam.

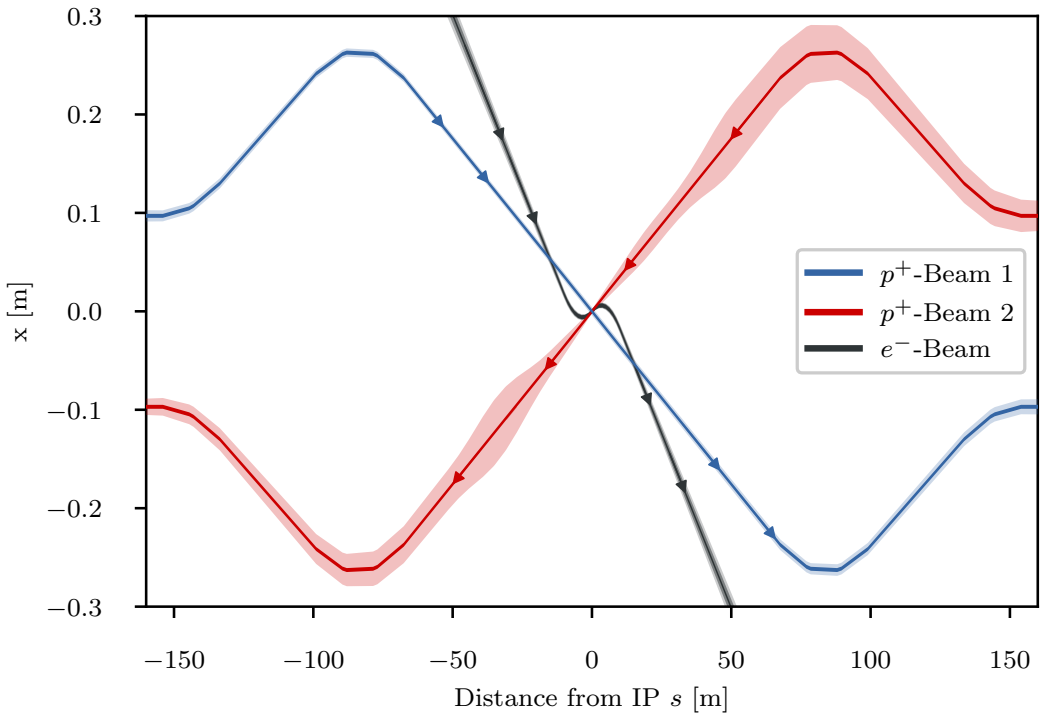

Figure 10.19: Geometry of the interaction region with 10σ envelopes.The electron beam is colliding with the focussed anti-clockwise rotating LHC beam (Beam 2) while the clockwise rotating LHC beam is unfocussed and passes the Interaction Region without interacting with the other two beams

The high electron current (cfr. 10.1) required to approach the goal peak luminosity of $10^{34}\text{cm}^{-2}\text{s}^{-1}$ poses a potential problem for the interaction region (IR) as it increases the already high synchrotron radiation.

The ERL parameters are not the only major change the new IR design has to account for. The first design of the quadrupole septa featured a separation of 68 mm for the two proton beams. However, this design focused strongly on providing a field free region for the non-colliding beam. Unfortunately, this lead to a poor field quality for the strongly focused colliding beam. The first quadrupole Q1 was a half quadrupole

Table 10.9: Parameters of the final focus quadrupole septa. The parameters of Q1A/B and Q2 are compatible with the Nb_3Sn based designs from [176] assuming the inner protective layer of Q2 can be reduced to 5 mm thickness.

Magnet	Gradient [T/m]	Length [m]	Free aperture radius [mm]
Q1A	252	3.5	20
Q1B	164	3.0	32
Q2 type	186	3.7	40
Q3 type	175	3.5	45

Table 10.10: Parameters of the separation and recombination dipoles. The respective interbeam distances are given for the magnet with the lowest value.

Magnet	Field strength [T]	Interbeam distance [mm]	Length [m]	Number
D1	5.6	≥ 496 mm	9.45	6
D2	4.0	≥ 194 mm	9.45	4
IP Dipole	0.21	-	10	-

design effectively acting as a combined function magnet with a dipole component of 4.45 T [174]. The sextupole field component was also prohibitively high. Consequently, a new design approach focusing on the field quality in the quadrupole aperture was necessary. Table 10.9 summarizes the parameters relevant for the interaction region design. It is noteworthy that the minimum separation of the two beams at the entrance of the first quadrupole Q1A increased from 68 mm to 106 mm requiring a stronger bending of the electron beam. This would increase the already high synchrotron radiation in the detector region even more. In order to compensate this increase, it was decided to increase L^* to 15 m, an approach that was shown to have a strong leverage on the emitted power [175].

The increased separation of the two proton beams, the longer L^* and the overall longer final focus triplet make longer and stronger separation and recombination dipoles necessary. The dipoles differ from the arc dipoles in that the magnetic field in both apertures has the same direction. Consequently the cross talk between both apertures is significant and the maximum reachable field is lower. The new geometry keeps the required field below 5.6 T. The required lengths and strength of these dipoles are listed in Table 10.10. It should be noted that the inter–beam distance is different for each of the five magnets per side, so each magnet will likely require an individual design. The design of the D1 dipoles is further complicated by the fact that an escape line for neutral collision debris traveling down the beam pipe will be necessary [151], as well as a small angle electron tagger. These issues have not been addressed so far, further studies will require detailed dipole designs.

The first design of the LHeC interaction region featured detector dipoles occupying almost the entire drift space between the interaction point and first quadrupole. The approach was to have the softest synchrotron radiation possible to minimize the power. However, since the purpose of the dipoles is to create a spacial separation at the entrance of the first quadrupole, it is possible to make use of a short drift between dipole and quadrupole to increase the separation without increasing the synchrotron radiation power. A dipole length of $\frac{2}{3}L^*$ is the optimum in terms of synchrotron radiation power [177]. Compared to the full length dipole it reduces the power by 15.6 % at the cost of a 12.5 % higher critical energy. With an L^* of 15 m the optimum length of the detector dipoles is 10 m. A magnetic field of 0.21 T is sufficient to separate the electron and proton beams by 106 mm at the entrance of the first quadrupole. With these dipoles and an electron beam current of 20 mA at 49.19 GeV the total synchrotron radiation power is 38 kW with a critical energy of 283 keV to be compared with a power of 83 kW and a critical energy of 513 keV for the electron beam energy of 60 GeV **I have rescaled for 49.19 GeV but I still find differences wrt the values quoted later for the original solution (Ref. Design) in Tables ?? and ?? - To be cross checked**

with Kevin .

A schematic layout of the LHeC interaction region with the dipoles discussed above is shown in Fig. 10.20. The corresponding beam optics will be discussed in the next Subsections.

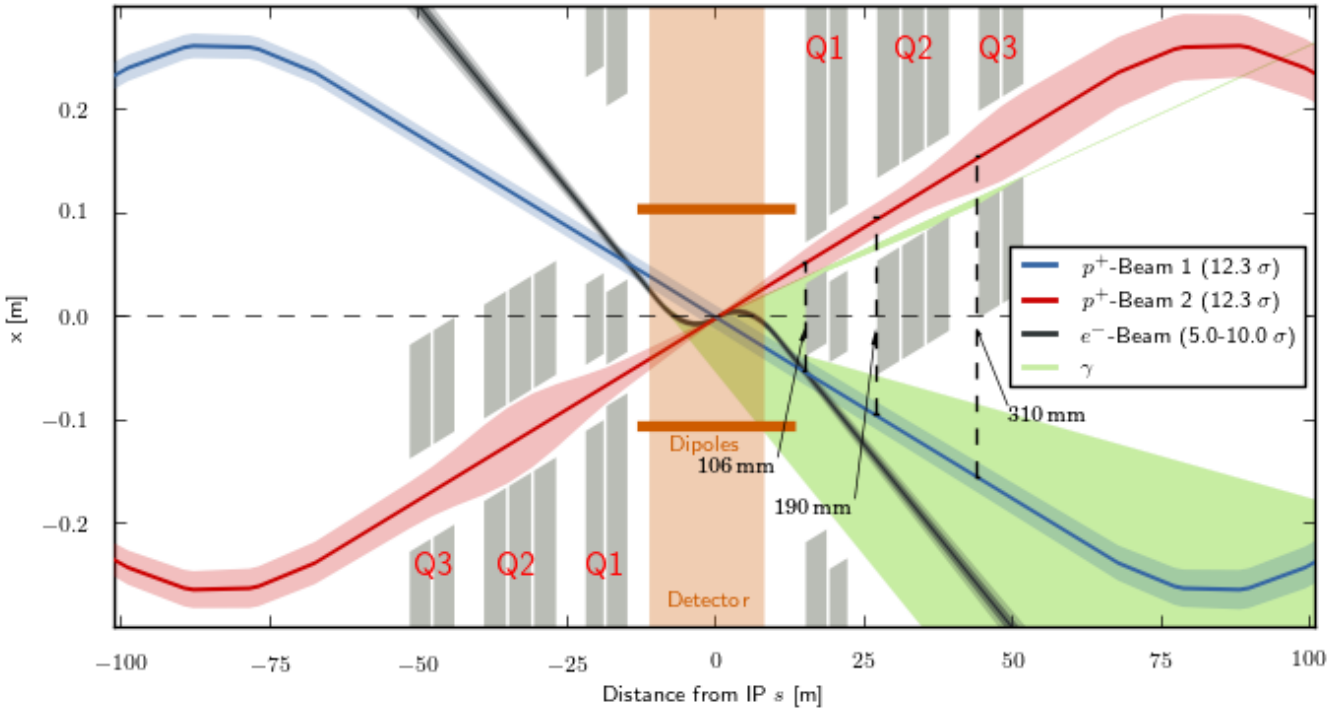

Figure 10.20: Schematic layout of the LHeC interaction region. The colliding proton beam and the electron beam are shown at collision energy while the non-colliding beam is shown at injection energy when its emittance is the largest.

10.7.2 Proton Optics [Emilia Cruz Alaniz]

As discussed above, the L^* was increased to 15 m in order to compensate the increased synchrotron radiation due to the larger separation. The final focus system is a triplet consisting of the quadrupoles Q1A and Q1B (see Table 10.9), three elements of the Q2 type and two of the Q3 type. Between the elements a drift space of 0.5 m was left to account for the magnet interconnects in a single cryostat. Between Q1 and Q2 as well as Q2 and Q3 a longer drift of 5 m is left for cold-warm transitions, Beam Position Monitors (BPMs) and vacuum equipment. Behind Q3, but before the first element of the recombination dipole D1, another 16 m of drift space are left to allow for the installation of non-linear correctors in case the need arises, as well as a local protection of the triplet magnets from asynchronous beam dumps caused by failures of the beam dump kickers (MKD) as discussed later.

As the recombination dipoles D1 and D2 for the LHeC interaction region require more space than the current ALICE interaction region, the quadrupoles Q4 and Q5 had to be moved further away from the IP. The position of Q6 is mostly unchanged but due to a need for more focusing the length was increased by replacing it with two elements of the MQM magnet class of LHC.

With the triplet quadrupole parameters provided in Table 10.9 we were able to match optics with a minimum β^* of 10 cm. The corresponding optics are shown in Fig. 10.21 and feature maximum β functions in the triplet in the order of 20 km. With these large β functions, the free apertures of the quadrupoles leave just

enough space for a beam stay clear of $12.3\,\sigma$, the specification of the LHC. This is illustrated in Fig 10.21. However, since the LHeC is supposed to be incorporated in the HL-LHC lattice, this minimum beam stay clear requires specific phase advances from the MKD kicker to the protected aperture as detailed later. The large β functions not only drive the aperture need in the final focus system, but also the required chromaticity correction in the adjacent arcs. To increase the leverage of the arc sextupoles, the Achromatic Telescopic Squeezing scheme (ATS) developed for HL-LHC [178] was extended to the arc upstream of IP2 for the colliding beam (Beam 2) (see Fig. 10.22). This limited the optical flexibility in the matching sections of IR2, specifically of the phase advances between arc and IP2. As a consequence, the optical solution that has been found (Fig. 10.21) still has a residual dispersion of 15 cm at the IP and the polarities of the quadrupoles Q4 and Q5 on the left side of the IP break up the usual sequence of focusing and defocusing magnets. It needs to be studied whether this is compatible with the injection optics. The latest optics designs can be found in [179].

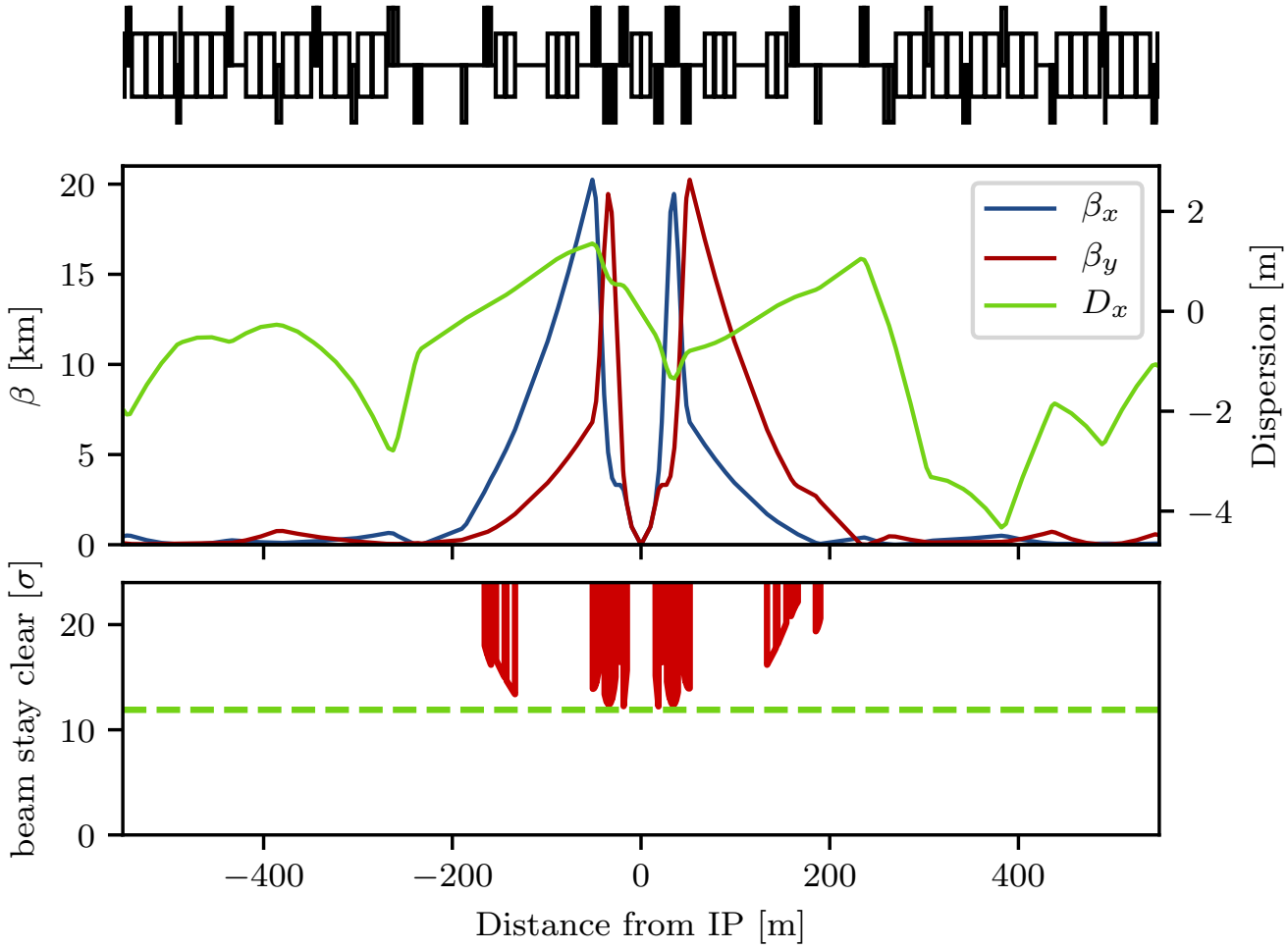

Figure 10.21: Optics (top) and beam stay clear (bottom) of the colliding beam with $\beta^* = 10\,\text{cm}$.

The free apertures given in Table 10.9 include a 10 mm thick shielding layer in Q1 and 5 mm in Q2 and Q3. This is necessary to protect the superconducting coils from synchrotron radiation entering the magnets as can be seen in Figure 10.20. The absorber must also protect the magnets from collision debris. Simulations of both synchrotron radiation and collision debris are yet to be conducted in order to confirm the feasibility of this design.

A separation between the two proton beams in time is currently foreseen, i.e. while the orbits of the

two proton beams do cross, the bunches do not pass through the IP at the same time. This approach is complicated by the fact that the timing of the bunches in the other three interaction points should not be affected. The easiest way to accomplish this is by shifting the interaction point of LHeC by a quarter of a bunch separation, i.e. $6.25\,\text{ns} \times c \approx 1.87\,\text{m}$ upstream or downstream of the current ALICE IP. This will of course have an impact in the integration of the detector in the underground cavern [180], however it seems feasible [181].

The LHC protected aperture in the event of an asynchronous beam dump significantly depends on the phase advance between the MKD kicker and the local aperture protection [182]. This is due to the oscillation trajectory of bunches deflected during the kicker rise time. With a phase advance of 0° or 180° from the kicker to the protected aperture, a direct hit should be unlikely, so aperture bottlenecks should be close to that. For a beam stay clear of $12.3\,\sigma$ a phase advance of less than 30° from either 0° or 180° was calculated to be acceptable [182]. The major complication comes from the fact that not only the final focus system of LHeC, but also of the two main experiments ATLAS and CMS need to have to correct phase advances and since the phase advances between IP2 (LHeC) and IP1 (ATLAS) are locked in the achromatic telescopic squeezing scheme there are few degrees of freedom to make adaptations.

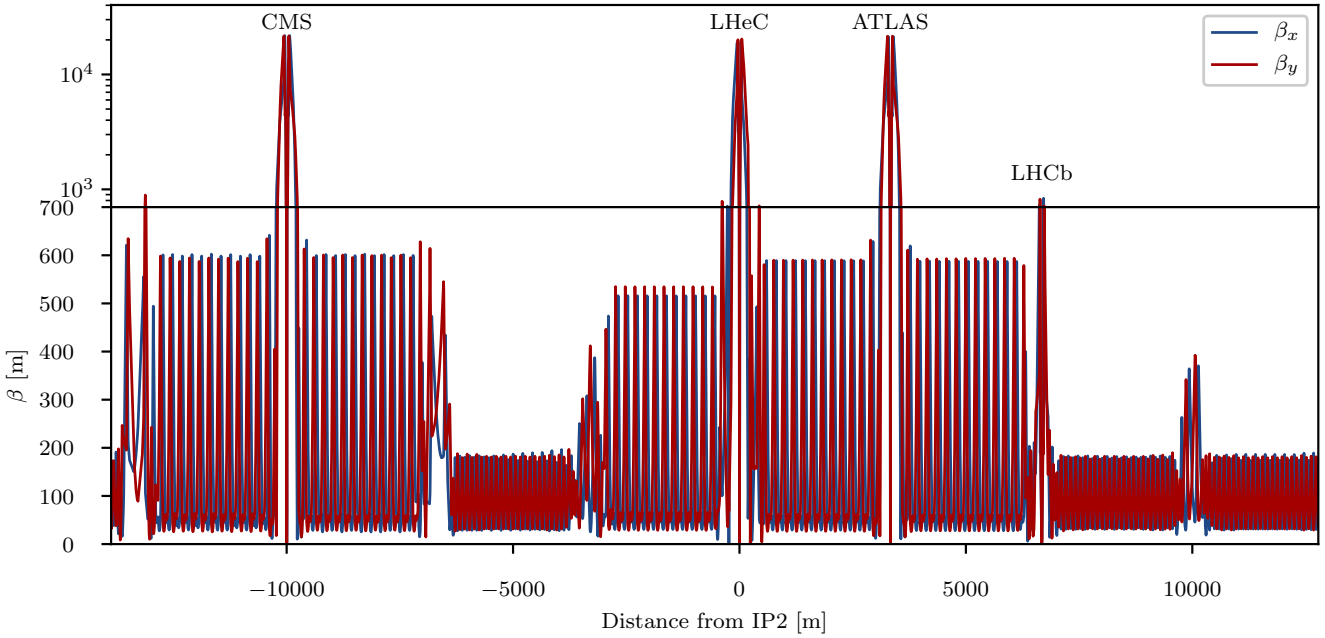

Figure 10.22: Optics of full ring of the colliding beam (Beam 2).

The Achromatic Telescopic Squeezing (ATS) scheme [178] is a novel optical solution proposed for the HL-LHC to strongly reduce the β^* while controlling the chromatic aberrations induced, among other benefits.

The principles of the ATS as implemented for the HL-LHC are as follows: first, in the presqueeze stage, a standard matching procedure is performed in the interaction regions to obtain a value of β^* which is achievable in terms of quadrupole strengths and chromaticity correction efficiency, in the case of HL-LHC this corresponds to IR1 and IR5. A further constraint at this point is to match the arc cell phase advance on the regions adjacent to the low β^* interaction regions to exactly $\pi/2$. Later, at the collision stage, the low β^* insertions remain unchanged and instead the adjacent interaction regions contribute to the reduction of β^*, that is IR8 and IR2 for IR1, and IR4 and IR6 for IR5. The $\pi/2$ phase advance allows the propagation of β-waves in the arc. If phased correctly with the IP, these β-waves will reach their maximum at every other sextupoles, increasing the β function at their location at the same rate that the decrease in β^*. The increase of the β function at the location of the sextupoles will result in an increase of their efficiency, allowing the

system to correct the high chromaticity produced by the high-β function in the inner triplet. This way, the ATS allows a further reduction of the β^* at the same time that correcting the chromaticity aberrations produced in the low β insertions.

Following the experience for HL-LHC, the ATS scheme was proposed for the LHeC project to overcome some of the challenges of this design in terms of limits in the quadrupole strengths of the interaction region and in the chromaticity correction.

A first integration of the LHeC IR into the HL-LHC lattice using the ATS scheme for the previous nominal case with $\beta^* = 10\,\text{cm}$ and $L^* = 10\,\text{m}$ was presented by extending the β wave into the arc 23 [175]. The flexibility of this design was later explored to study the feasibility of minimizing β^*, to increase the luminosity, and increasing L^*, to minimize the synchrotron radiation. It was found that increasing L^* to 15 m provided a good compromise but keeping the β^* to 10 cm.

The changes made to the HLLHCV1.3 lattice [183] to obtain the LHeC lattice and the detailed matching procedure are described in [184]. At the end of this process a lattice for the required collision optics in all IRs (β^*=15 cm for IR1 and IR5 and β^*=10 cm for IR2) has been obtained, with the appropriate corrections (crossing, dispersion, tune and chromaticity). The phases between the MKD kicker in IR6 and the different low β^* triplets were also checked, resulting in 15° from the horizontal for IR1, 22° for IR2 and 26° for IR5, therefore fulfilling the <30° requirement for all three IRs.

Similarly the chromaticity correction for the LHeC lattice further develops from the HL-LHC chromaticity correction scheme [184] allowing to correct the chromaticity for the case with $\beta^* = 10\,\text{cm}$ in IP2 within the available main sextupole strength. Lattices with β^*= 7, 8 and 9 cm and $L^* = 15$ m were also successfully matched in terms of both the β^* and the chromaticity correction. It must be noted however that these cases require a larger aperture in the inner triplet.

Dynamic aperture (DA) studies were performed to analyze the stability of the lattice designs using SixTrack [185] on a thin-lens version of the LHeC lattice at collision ($\beta^* = 0.15\,\text{m}$ in IP1 and IP5, $\beta^* = 10\,\text{cm}$ in IP2) over 10^5 turns with crossing angles on, 30 particles pairs per amplitude step of $2\,\sigma$, 5 angles in the transverse plane and a momentum offset of 2.7×10^{-4}. The energy was set to 7 TeV and the normalised emittance of the proton beam to $\epsilon = 2.5\,\mu\text{m}$. No beam-beam effects were included in this study.

Previous DA studies had been performed for an earlier version of the LHeC lattice [175]. These studies did not include triplet errors of either of the low-β interaction regions, as these errors were not available at that stage. These studies were updated for the newer version of the LHeC lattice described in the previous sections and included errors on the triplets of IR1 and IR5. For the case of IR2 errors tables for the new triplet are not yet available but it was estimated that the same field quality than the triplets for the HL-LHC IR can be achieved for these magnets, and therefore the same field errors were applied but adjusted to the LHeC triplet apertures.

The initial DA resulted in $7\,\sigma$ but following the example of HL-LHC and FCC studies [186] two further corrections were implemented: the use of non-linear correctors to compensate for the non linear errors in the LHeC IR, and the optimization of the phase advance between IP1 and IP5. With these corrections the DA was increased to $10.2\,\sigma$, above the target of $10\,\sigma$. The case for lower β^*, particularly for the case of interest with $\beta^* = 7\,\text{cm}$ proved to be more challenging, as expected, when adding errors on the LHeC IR; however with the use of the latest corrections a DA of $9.6\,\sigma$ was achieved, that is not far off from the target. Fig. 10.23 shows the DA vs angle for both these cases. It is important to point out that the challenge for the β^*=7 cm case comes instead from the quadrupole aperture and gradient requirements, particularly in the first magnet.

β^* values lower than 10 cm require a completely different final focus system as the lower β^* means the beam size in the triplet will become larger. Larger apertures are required and consequently the gradients in the quadrupoles will decrease. However similar integrated focusing strengths will be required so the overall

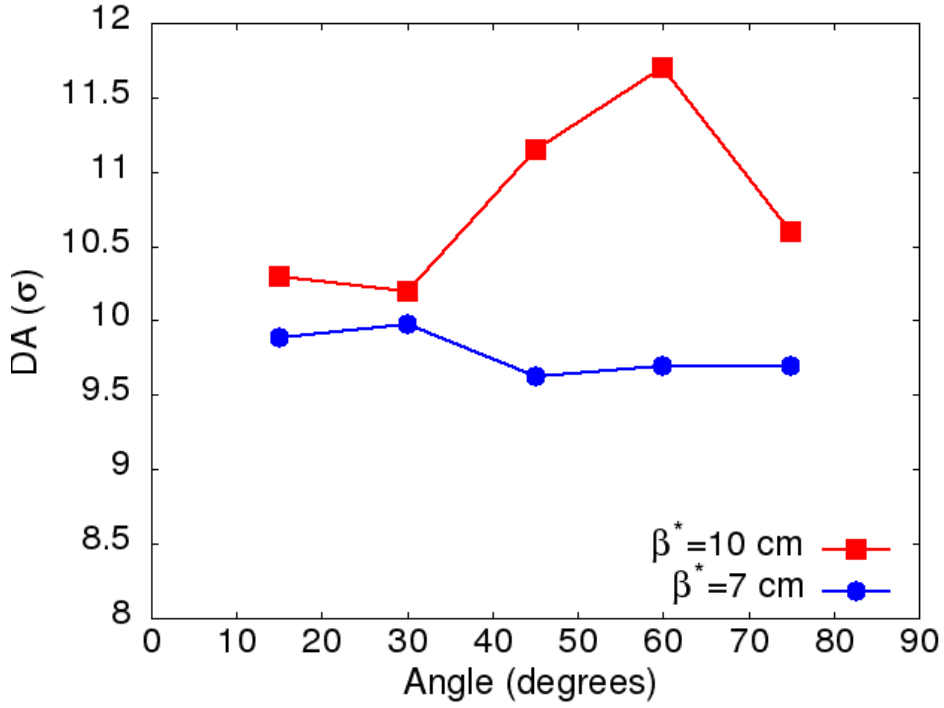

Figure 10.23: Dynamic aperture vs angle for 60 seeds for the LHeC lattice at collision for the cases $\beta^* = 10$ cm (red) and $\beta^* = 5$ cm in IP2.

length of the triplet will increase. As this will in turn increase the β functions in the triplet further it is imperative to optimize the use of the available space. An example of available space is the drift between the detector region dipoles and the triplet magnets as shown in Fig. 10.24. The optimum dipole lengths in terms of synchrotron radiation power was determined to be $2/3 \cdot L^*$ so a drift of 5 m is left. Now it is immediately clear that this region cannot be occupied by a superconducting quadrupole septum as that would effectively decrease L^* and thus increase the synchrotron radiation power as a stronger separation is necessary. Instead it is thinkable that a normal conducting quadrupole septum can be built that either does not require a yoke or similar structure between the beams or has a very thin yoke, or a septum that has a very limited and controlled field in the region of the electron beam trajectory. In the later case it might even be used as part of the final focus system of the electron beam. Either way, it is clear that such a normal conducting septum must have a pole tip field way below the saturation limit of iron. The section on electron optics shows that a normal quadrupole of this kind can also have benefits in terms of synchrotron radiation, but studies remained to be done to make sure the parameters work for both cases. For our calculation a pole tip field of 1 T was assumed. For $\beta^* = 5$ cm an aperture radius of 20 mm is required at a distance of 14 m from the IP, resulting in a pole tip field of 50 T/m for the normal conducting septum called Q0. Possible ratios of apertures and gradients for the remaining triplet magnets were approximately based on the quadrupole parameters shown in Table 10.9, however these parameters would require a magnet design for confirmation. With the quadrupole parameters shown in Table 10.11 we were able to obtain triplet optics that can accommodate a beam with a minimum β^* of 5 cm.

The corresponding optics are shown in Fig. 10.25. So from the triplet point of view it appears possible to reach lower β^*, however many assumptions need verification: First the magnetic design for the normal conducting quadrupole septum must be shown to be possible. If there is a residual field in the space of the electron beam trajectory, the impact on the electron beam and the synchrotron radiation power must be evaluated. The parameters of the modified superconducting triplet quadrupole septa, although scaled conservatively, must be confirmed. Furthermore the larger aperture radius of Q1 might require a larger separation at the entrance of Q1, increasing the synchrotron power that is already critical. Thus a full

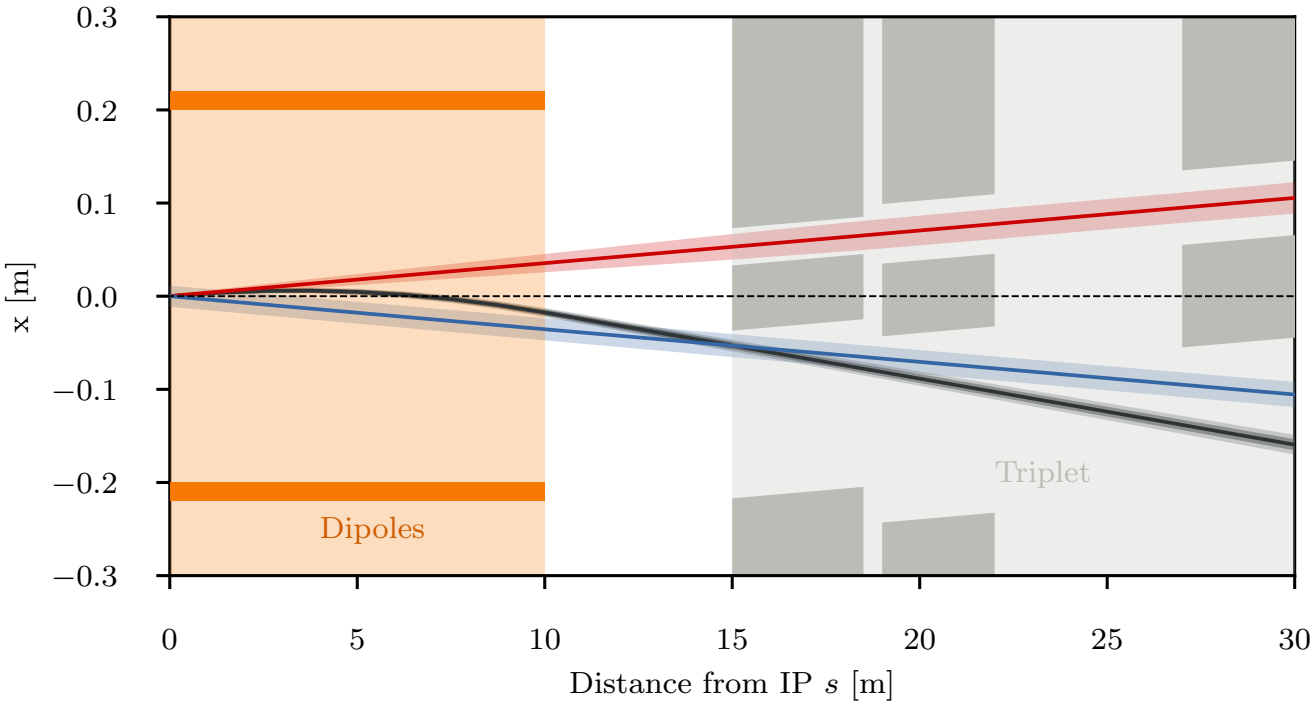

Figure 10.24: Empty space between the detector dipole and the superconducting quadrupoles of the final focus triplet.

Table 10.11: Parameters of the final focus quadrupole septa required to accommodate a β^* of 5 cm. The normal conducting quadrupole is called Q0 although it has the same polarity as Q1A/B.

Magnet	Gradient [T/m]	Length [m]	Aperture radius [mm]
Q0 (nc)	50	3.0	20
Q1A	110	3.5	27
Q1B	162	5.0	37
Q2	123	5.0	62
Q3	123	4.5	62

design of such magnets is required. Lastly, the interaction region must be integrated into the full ring to verify that chromaticity correction is possible. Studies in [184] that were conducted on the normal triplet without regard for aperture constraints suggest that a chromaticity correction is only possible for a β^* down to around 7 cm.

So far the optics of the final focus system featured asymmetrically powered triplets on the two sides of the IP. This is inherited from the ALICE final focus system where the aperture is shared and the antisymmetry guarantees the same optics for both beams and similar chromaticities in both horizontal and vertical planes. In the LHeC final focus system however, the apertures of the quadrupoles are not shared between both beams, so the antisymmetry is not strictly necessary, although it eases the integration in the full ring. An alternative approach that is worth studying is a symmetric doublet. Doublets feature a large β function in one plane and a relatively low one in the other plane. Since the non-colliding proton beam is of no concern for LHeC it makes sense to create doublets on each side of the IP that have the peak β function in the horizontal plane as the chromaticity correction was limited in the vertical plane. Furthermore, in a doublet the integrated focusing strength needed is lower as fewer quadrupoles act against each other. This further reduces the chromaticity and should also reduce the overall length of the final focus system. With

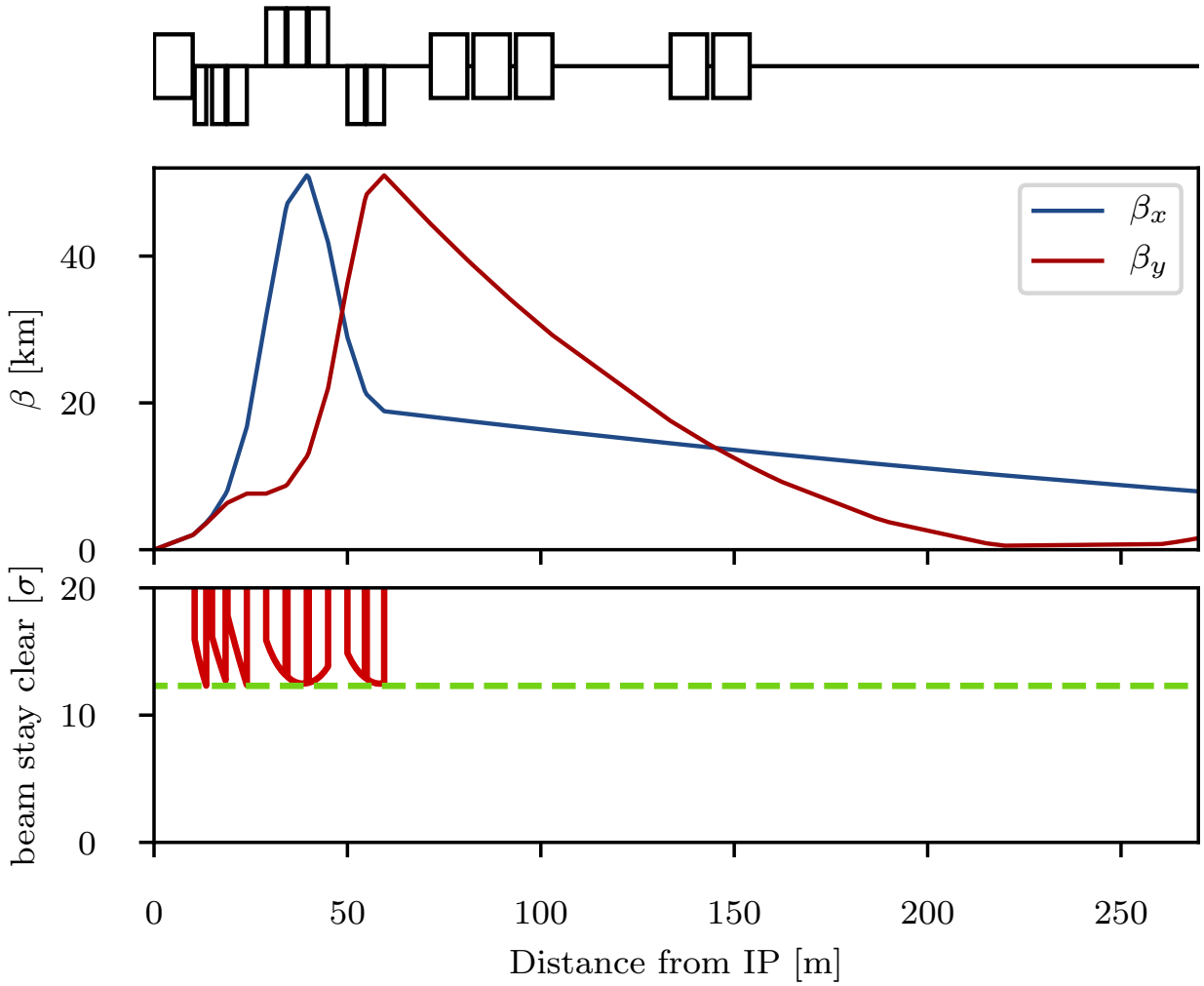

Figure 10.25: Optics (top) and beam stay clear (bottom) in the triplet region of colliding beam with $B^* = 5\,\text{cm}$.

the space saved by the doublet it is possible to either shift the recombination dipoles D1 and D2 closer to the IP, reducing the needed integrated strengths, or even to increase L^* to further reduce the synchrotron radiation power and critical energy. In order to make best use of the available doublet quadrupole aperture, it is also thinkable to collide with flat beams. The main disadvantage of symmetric doublets is the breaking of the sequence of focusing and defocusing quadrupoles. As no changes should be made to the arcs, the left-right symmetry needs to be broken up again in one of the matching sections, either by introducing another quadrupole on one side of the IP, or by overfocusing the beam.

At collision energy the non-colliding beam has no optics specification within the straight section. Consequently the optics should transfer the beam from the left arc to the right arc without hitting the aperture and at a specific phase advance. The same is true at injection energy, but with a larger emittance, making the satisfaction of the aperture constraint more difficult. Thus it is sufficient to find working injection optics, as no squeeze will be required for this beam. This approach of course will require some tuning as at least one arc will apply the ATS scheme at collision, but as the aperture constraint is less tight at higher energy there should be enough degrees of freedom available.

Finding injection optics appears trivial at first but is complicated by the fact that the distance between the IP and the first quadrupole magnet Q4 is larger than 159 m. A total distance of 318 m needs to be bridged

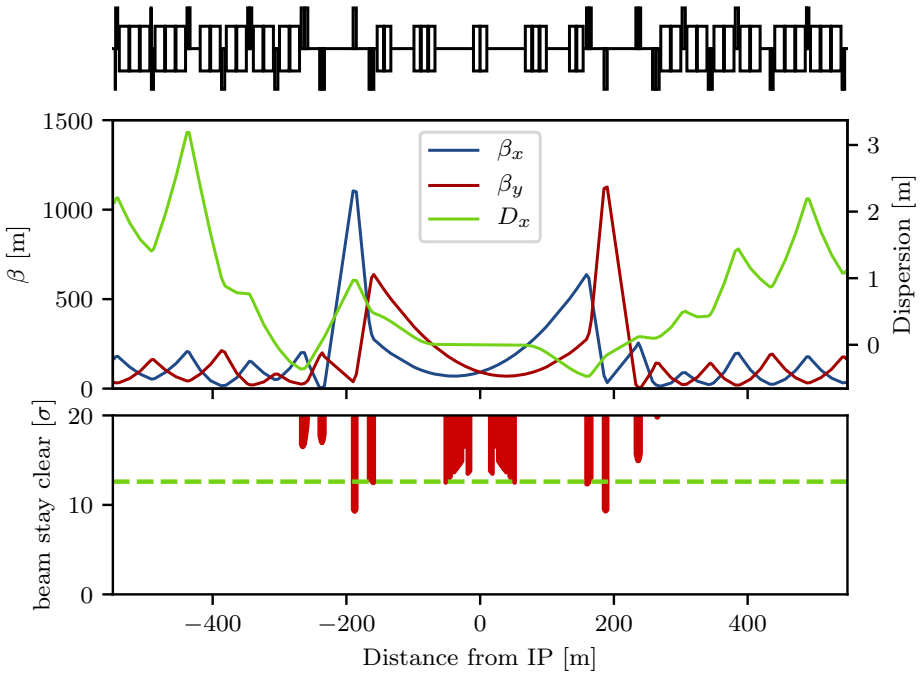

Figure 10.26: Optics (top) and beam stay clear of the non-colliding beam at injection energy. The Q5 quadrupole magnets on either side of the IP currently are aperture bottlenecks. It should be possible to mitigate this problem by replacing the magnets with longer, larger aperture magnets.

without any focusing available. A solution has been found with $\beta^* = 92\,\text{m}$ and $\alpha^* = \pm 0.57$ with the required beam size in the quadrupole septa and Q4 [184]. The corresponding optics are shown in Fig. 10.26. For the magnets Q4 and Q5 LHC quadrupoles of the large aperture MQY type with 70 mm aperture diameter and a 160 T/m gradient were assumed. As can be seen in the aperture plot, the triplet quadrupole septa and Q4 are just below the minimum beam stay clear at injection of $12.6\,\sigma$ but it is expected that nominal aperture can be achieved With some minor optimization. However the Q5 magnets only have a beam stay clear of about $9.2\,\sigma$ with little chance of decreasing the beam size without increasing it both in Q4 and in the quadrupole septa. Consequently it will be necessary to use quadrupoles with apertures larger than 106 mm and make up for the lower gradient by increasing the length or by using Nb_3Sn technology. At injection energy the remaining magnets in the IR have strengths according to the HL-LHC specification and thus do not pose any problems. However the injection optics shown in Fig. 10.26 will require some changes during the ramp as Q4, Q5 and Q6 would become too strong at collision energy. This is not considered a problem though, as the emittance shrinking will ease the aperture requirements.

The non-colliding proton beam does not need to be focused and consequently passes the quadrupole septa of the colliding beam in the field free region.

The large angle of 7200 µrad between the two beams (compared to 590 µrad in the high luminosity IPs) should suffice to mitigate long range beam-beam effects, considering that the shared aperture is only 30 m long as opposed to the main experiments where the shared aperture exceeds a length of 70 m.

10.7.3 Electron Optics [Kevin André, Bernhard Holzer]

First ideas of a possible layout and design of the Interaction Region IR between the LHeC lepton and proton beam have already been presented in [151]. Based on the principles explained there, a further optimisation of the beam separation scheme has been established, with the ultimate goal of lowest synchrotron radiation

power and critical energy in the direct environment of the particle detector. Depending on the requests from the actual detector geometry and shielding, the flexibility of the new IR layout allows to optimise for either side.

The basic principle is - as before - based on the large ratio (approximately 140) of the proton to electron beam momentum (or beam rigidity, $B\rho = p/e$) that makes a magnetic field based separation scheme the straightforward solution to the problem, using effective dipole fields.

Boundary conditions are set however due to the limited longitudinal space, resulting from the distance of the first focusing elements of the proton lattice, located at L*=15m, and the need for sufficient transverse separation, defined by the technical design of this first proton quadrupole. The size of the two beams and - clear enough - the power of the emitted synchrotron radiation P_{syn} and the critical energy E_{crit} have to be taken into account in addition.

Equations 10.5 and 10.6 describe the well known dependencies of these two parameters on the beam energy $E_e = m_e c^2 \gamma$ and bending radius ρ.

$$P_{syn} = \frac{e^2 c}{6\pi\varepsilon_0}\frac{\gamma^4}{\rho^2}. \tag{10.5}$$

$$E_{crit} = \frac{3}{2}\frac{\hbar c \gamma^3}{\rho}. \tag{10.6}$$

The schematic layout of the original design of the electron interaction region shown in Fig. 10.20 is reproduced in Fig. 10.27a. The long dipole magnet B, used to deflect the electron beam, is embedded inside the detector structure which is ranging from -6 m to 4 m around the interaction point, extended by ± 1.65 m of muon chamber. Basic interaction region designs with and without chromaticity correction were presented [187, 188] but were not fully integrated in the ERL. The electron final quadrupoles were placed at 30 m from the IP [189], compatible with the proton layout described above. While this approach is straightforward, the only parameter that can be used to minimize the power of the emitted synchrotron radiaton is the length of the separator-dipole field [177]. In addition, the installation of the first focusing elements of the electron beam downstream of the triplet focussing the colliding proton beam leads to a considerable increase of the electron beam size in the separation plane.

Lattices including chromaticity correction had a significant length of 150 m. However, the whole straight section between Linac and arc is only 290 m long [151] and the IR design did not include a matching and splitting section or a focus system for the spent, outgoing electron beam. Without chromaticity correction in the electron final focus, aberrations at the IP decrease luminosity by about 20% [190].

Investigations have been launched to minimise critical energy and emitted synchrotron radiation power by reducing the separation in two main steps:

- introduce a compact mirror-plate half quadrupole (QNC) in front of Q1A (on the IP side) to focus the colliding proton beam and provide a field free region for the electron and non-interacting proton beam. This reduces the required bending field of the separation dipole B for the same separation at Q1A. In addition, the normal conducting magnet QNC will act as shielding of the superconducting triplet magnets that would otherwise be subject to direct synchrotron radiation. Additional shielding is foreseen, to protect the SC magnets and avoid as much as possible backshining to the detector. In addition, sufficient space will be provided to correct the vertical orbit and coupling of the electrons coming from the solenoid.
- reduce the beam size of the electron beam by a very early focusing of the beam. As positive side effect this leads to a considerable reduction of the chromaticity of the electron lattice.

The first step is sketched in Fig. 10.27b and the corresponding electron beam trajectory is shown in Fig. 10.27c.

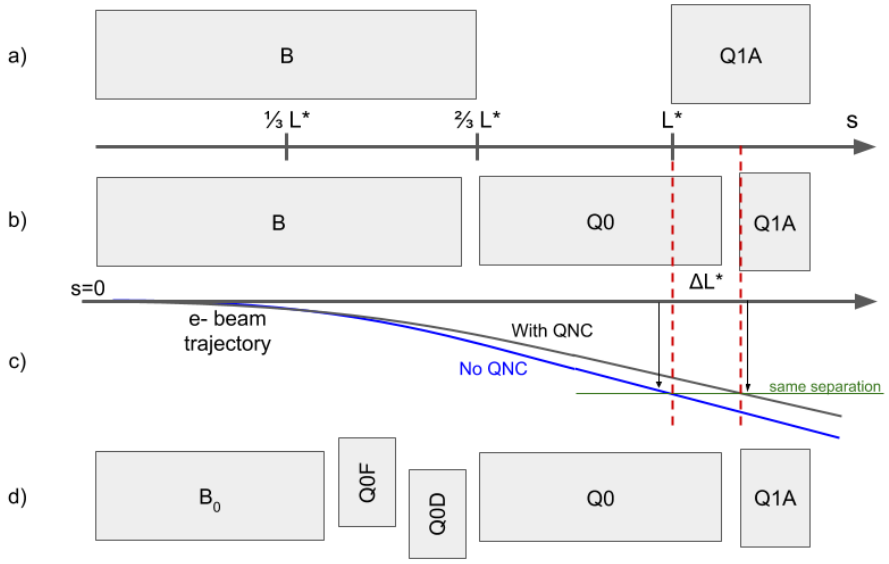

Figure 10.27: Separation scheme based on a long dipole magnet B (a) and improved layout using Q0, a normal conducting half-quadrupole as first focusing element of the proton beam (b). The last design features a doublet of off-centered quadrupoles to minimize the electron beam size at the entrance of Q1A (d).

The introduction of the mirror plate half quadrupole QNC allows to reduce the length of the Q1A quadrupole while conserving the total integrated gradient, therefore leaving the overall focusing properties of the proton lattice quasi untouched. The entry of Q1A is therefore moved away from the IP to relax the separation fields.

Scanning the Q1A entry position leads to either an optimum of the critical energy or to a minimum of the emitted synchrotron power. Both cases are shown in Fig. 10.28 and for each of them the new Q1A entry position has been determined. The power of the emitted radiation is reduced by up to 28%. The colliding proton beam, passing through this half quadrupole with a certain offset to guarantee sufficient beam stay clear, will receive a deflecting kick in the horizontal plane of about 90 µrad. It supports the dipole based beam separation, provided by the so-called D1 / D2 magnets in LHC, and will be integral part of the LHC design orbit.

The resulting beam optics of the protons differs only marginally from the original version and only a slight re-match is needed. However by carefully choosing the gradient of the new magnet the parameters of the superconducting proton quadrupoles are untouched and the phase advance at the end of the interaction region lattice is conserved in both planes.

Improved Electron lattice

A further improvement of the emitted synchrotron power and critical energy is obtained by introducing an early focusing scheme of the electrons, which leads to a reduced electron beam size and thus to softer separation requirements.

The reduction of the electron beam size is obtained by installing a quadrupole doublet in the electron lattice between the separation dipole and the QNC (half-) quadrupole. A carefully matched focusing strength of this doublet will minimise the β function of the electrons at the location of Q1A. At the same time an effective dipole field, that is needed to maintain the separation of proton and electron beams, is provided by shifting the magnet centres of the doublet lenses off axis. The horizontal offset of these quadrupoles has been chosen to provide the same bending radius as the separation dipole, thus leading in first order to the same critical energy of the emitted light in all separation fields. A detailed calculation of the divergence of

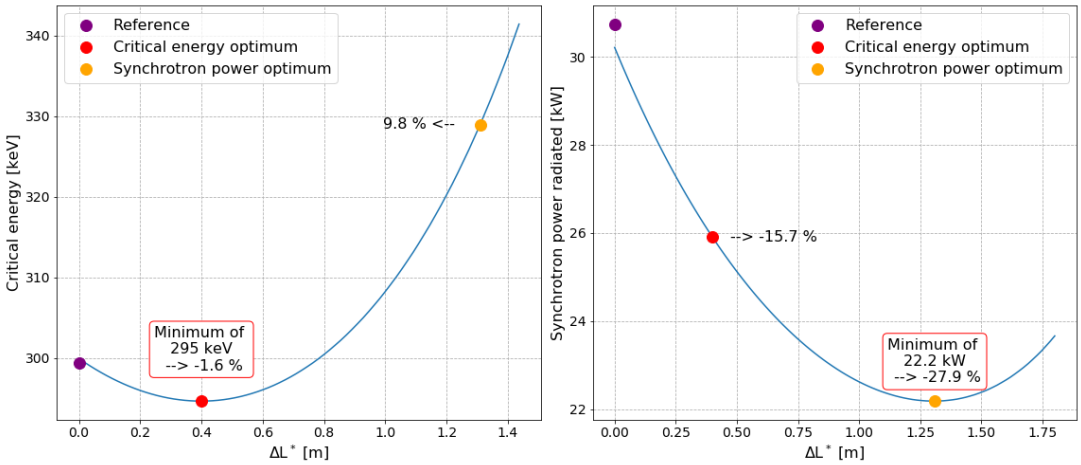

Figure 10.28: Improved critical energy and power of the synchrotron radiation for the half quadrupole based proton lattice. Left side: critical energy, right side: synchrotron radiation power. The horizontal axis refers to the shift ΔL^* of the position of the first proton superconducting magnet Q1A.

the photons, the geometry of the radiation fan and the position of the absorbers and collimators will be one of the essential next steps within the so-called machine-detector-interface considerations.

Fig. 10.27d shows the new layout – compared to the previous version. The doublet providing the early focusing of the electron beam is embedded in the separator dipole, i.e. it is positioned at $s = 6.3\,\mathrm{m}$ and acts in combination with the separation dipole. The quadrupole gradients have been chosen for optimum matching conditions of the electron beam and the transverse shift of the field centres provide the same separation dipole effect as used in the long dipole.

The early focusing of the electron beam allows for a softer separation of the beams, and leads therefore directly to a reduced critical energy E_{crit} and power P_{syn} of the emitted radiation. Fig. 10.29 shows the dependence of E_{crit} and P_{syn} on the β-function at $s = L^*$ for the electron optics for different values of the required electron beam stay-clear expressed in units of the electron beam size σ. The beam separation has been re-calculated and the critical energy and radiation power are plotted. The graphs include different assumptions for the beam size considered. Including orbit tolerances, a beam stay-clear of 20 σ is considered as the most relevant case, which refers to the red curve in the graph.

In order to provide a complete study with the lattice featuring the off-centered quadrupoles, the new interaction region has been embedded in between the high energy end of the acceleration part of the linac and the "arc 6" of the ERL, which marks the start of the energy recovery lattice. An optimum has been found for a beam optics with a beta function in the plane of the beam separation (i.e. horizontal) of $\beta_x = 90$ m at $L^* \approx 15\,\mathrm{m}$

An improvement of about 9 % for the critical energy and close to 25 % of the radiated power is obtained, if an electron beam optics with $\beta_x = 90\,\mathrm{m}$ at the entrance of Q1A is used. For this most promising case the matched beam optics is shown in Fig. 10.30.

The lower β-function of the electron beam at the focusing elements has the additional positive feature of reducing considerably the chromaticity of the new lattice, which is a crucial parameter for the performance of the energy recovery process. (Details are described below in the chapter on tracking calculations). Compared to the dipole based separation and a late focusing, Q' is reduced to a level of 13 % horizontally and to a level of 11 % in the vertical plane. The details are listed in Table 10.12. Furter studies will investigate the orbit correction scheme of the new IR, and an eventual interplay of the solenoid fringe field and the quadrupoles.

The influence of the electron doublet magnets on the proton optics is marginal - as can be expected due to

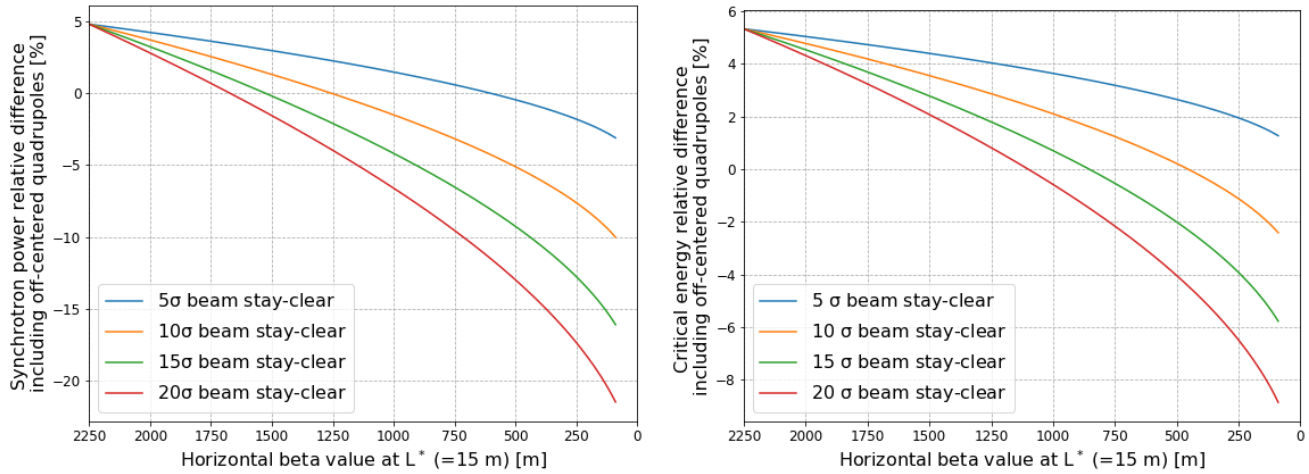

Figure 10.29: Relative difference with respect to the single dipole separation scheme for different values of the required beam stay-clear expressed in σ. Left : for the power of the emitted radiation, as function of the β-function of the electron beam at position s=15m. Left : for the critical energy of the emitted radiation, as function of the β-function of the electron beam at position s=15m. The early focusing of the electron beam allows for a much reduced separation field and thus to a reduced critical energy and power of the emitted radiation. The initial beta value is 2250 m.

the large difference in beam rigidity: If uncorrected, the electron doublet creates a distortion (a so-called beta-beat) of the proton optics of roughly 1%. Still it has been calculated and taken into account in the context of a re-match of the proton beam optics.

Table 10.12: Chromaticity of the dipole based separation scheme and the new lattice based on early focusing, off-axis quadrupole lenses.

	dipole based separation	early focusing scheme
ξ_x	-116	-15
ξ_y	-294	-32

Combining the two improvement factors, namely the effective lengthening of L^* due to the use of a half quadrupole in front of the superconducting triplet, and the early focusing scheme in the lattice of the electrons, leads to an overall improvement of the interaction region with respect to synchrotron radiation power and critical energy that is shown in Fig. 10.31. The overall improvement factor is plotted with reference to the baseline dipole separation design with originally $\beta = 2250$ m at the separation point s=L^*. Using a normal conducting half quadrupole in combination with the early focusing scheme, the power of the emitted synchrotron radiation is reduced by 48 % for an electron beam stay-clear of 20 σ.

The estimated synchrotron radiation power and critical energy for the different optimizations are plotted in Fig. 10.31 and the results are summarized in Table 10.13. Referring to a beam energy of 49.19 GeV and the design current of 20 mA an overall power of 16.2 kW is emitted within one half of the interaction region.

Depending on the boundary conditions imposed by the integration of the particle detector, one of the two optimum layouts can be chosen – or a combination of both, i.e. an overall minimum defined by critical energy and radiated power.

The basic main parameters of the proton mirror plate half quadrupole are summarized in Table 10.14 for the two optimum scenarios explained above: the optimum found for smallest synchrotron radiation power and the optimum for smallest critical energy of the emitted radiation. The values result from the optics studies of the previous sections. The presented gradients lead to a pole tip field of $B_p \approx 1.3$ T.

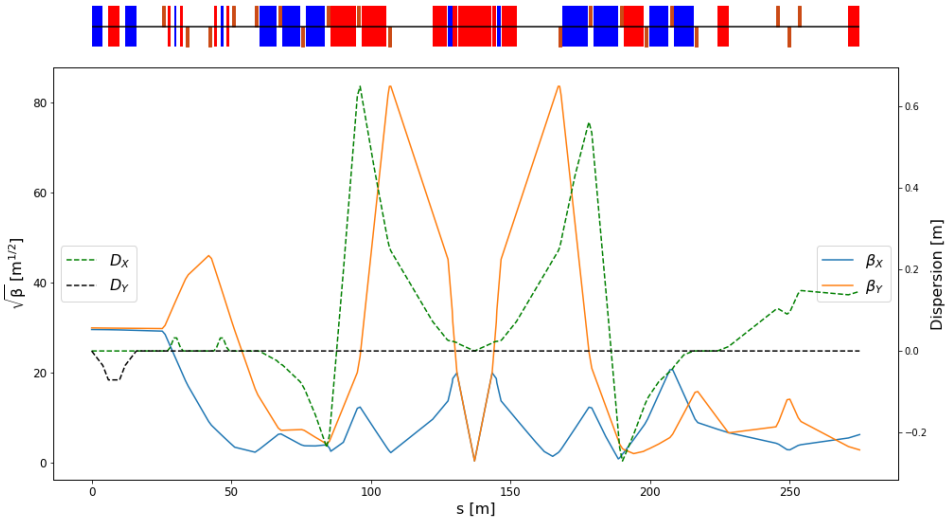

Figure 10.30: Electron beam optics for the new lattice including the early focusing scheme. The offset of the new doublet quadrupoles are chosen to provide the same separation field as in the dipole. The new optics is matched on the left side of the plot to the end of the acceleration linac. The right hand side is connected to arc 6, the beginning of the decelerating ERL part. At the position of the first superconducting proton magnet the β-function in the (horizontal) separation plane of the electron beam is reduced to 90 m for lowest possible synchrotron radiation load.

In both cases, the proton aperture radius has been chosen to include an orbit tolerance of 2 mm, a 10% tolerance on the beam size due to optics imperfections ($\beta-$ beating) and a beam size that corresponds to n=15 σ for a proton beam normalized emittance $\varepsilon_p = 2.50\mu m$. A value that is comfortably larger than the requirements of the HL-LHC standard lattice. The injection proton optics has been taken into account and although it features a larger emittance it clearly fit in the aperture, see the red dashed line in Fig 10.32. The electron beam and the non-colliding proton beam will pass through the field free region delimited by the mirror plate.

The aperture requirements inside the half quadrupole are determined on one side by the colliding proton beam optics in the main aperture of the magnet. The beam separation scheme and optics of electron and non-colliding proton beam on the other side have to fit into the field free region beyond the mid plane of the mirror plate. As described below, a crossing angle of 7 mrad is assumed for the non-colliding protons. Fig. 10.32 illustrates these requirements. For the case of smallest synchrotron radiation power, the three

Table 10.13: Synchrotron radiation power and critical energy for the different optimised separation schemes.

Optimum	Synchrotron Radiation		Critical energy	
	Radiation Power (kW)	Critical Energy (keV)	Radiation Power (kW)	Critical Energy (keV)
Reference design	30.8	300	30.8	300
Dipole length optimum	26.8	336	30.8	300
Half quadrupole optimum	22.2	331	26.1	295
Off-centered quadrupoles opti.	19.3	290	22.1	259
Half quad. + Off-centered quad. opti.	16.2	265	17.4	255

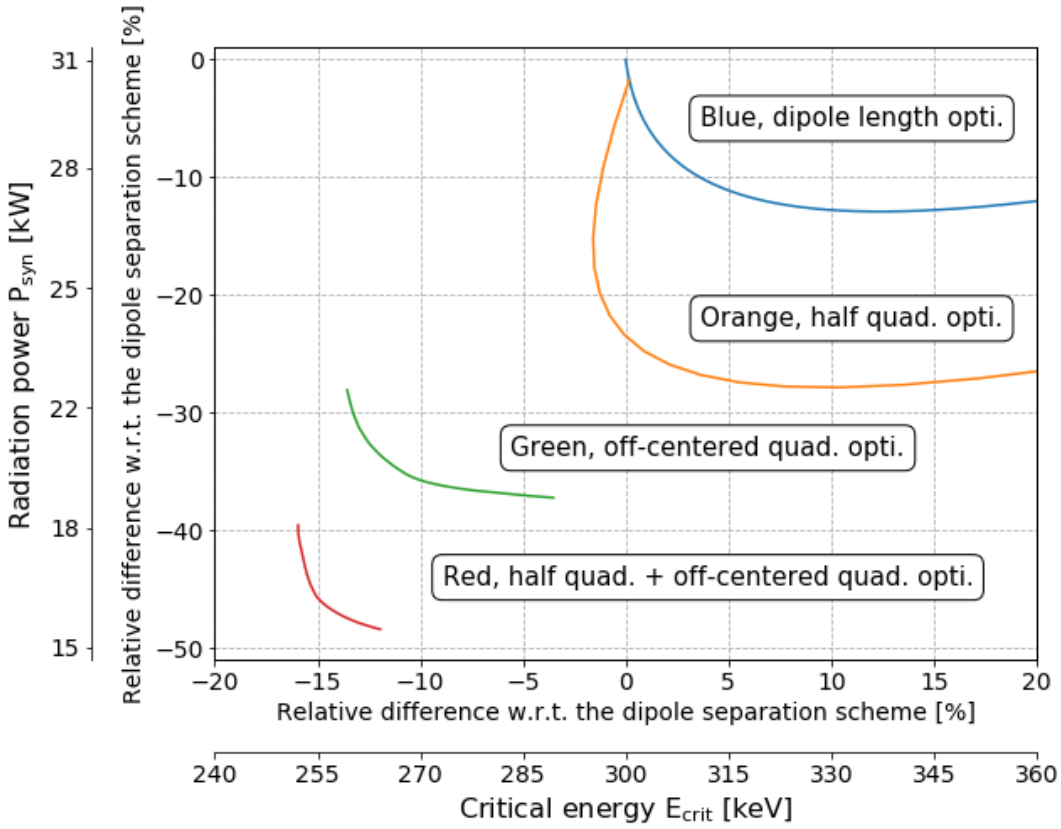

Figure 10.31: Relative differences with respect to the original single dipole separation scheme. The synchrotron radiated power is plotted as a function of the critical energy for different optimization results : only optimizing the dipole length (blue), only using a mirror quadrupole (orange), only using off-centered quadrupoles (green) and combining the mirror quadrupole with an earlier focusing (red).

beams are plotted at the entrance and exit of the quadrupole lens. For both proton beams the beam size shown in the graph corresponds to 15 sigma plus 2 mm orbit tolerance and 10 % beam size beating. Due to the mini-beta optics the colliding proton beam fills nearly the given aperture of the magnet. The non-colliding proton beam follows a relaxed optics with very limited aperture need. The envelope of the electron beam is shown for 20 σ beam size in both transverse planes.

In contrast to the proton half quadrupole, the doublet magnets of the early focusing scheme will house the three beams in one single aperture. In addition to the beam envelopes, the offset that has been chosen to provide the beam separation effect has to be taken into account and included in the aperture considerations. In Fig. 10.33 the situation is visualised. On the left side the first off-center quadrupole (powered as focusing lens) is presented. Following the field direction, the electron beam is offset towards the outer side of the ring (right side of the plot) as defined by the proton beam closed orbit. The right part of the figure shows the

Table 10.14: Magnet gradient of the proposed half quadrupole for lowest synchrotron radiaton power and lowest critical energy. An aperture of 15 σ + 20% beta-beating + 2 mm orbit tolerances has been assumed.

	minimum synch. radiation power	minimum critical energy
$\gamma\varepsilon_p$ [mm.mrad]	2.50	2.50
Gradient [T/m]	48.2	50.7
Aperture radius [mm]	27.0	25.6
Length [m]	6.84	2.08

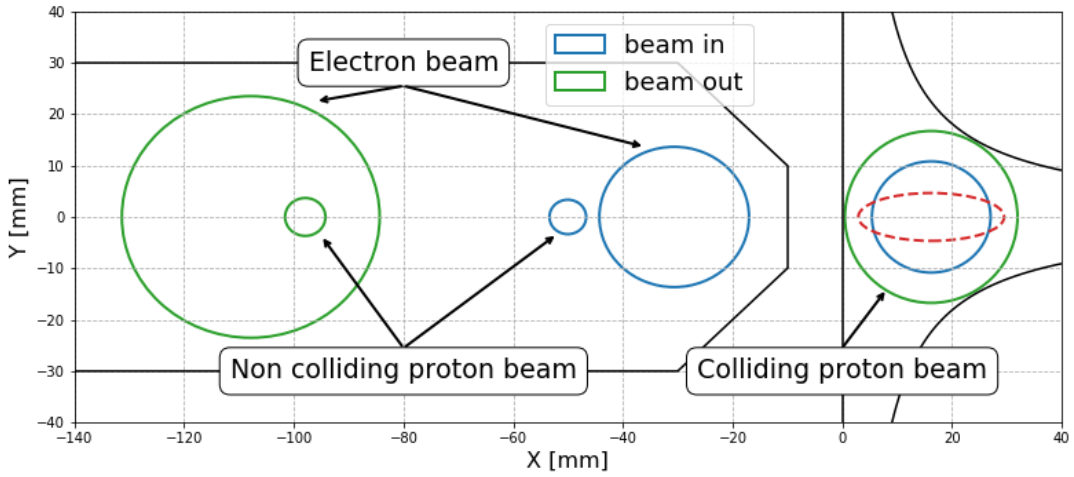

Figure 10.32: The position of the three beams at the entrance (blue) and exit (green) of the half quadrupole. The colliding proton beam is centered inside the main magnet aperture, while the second proton beam and the electrons are located in the field free region. The dashed red line represents the injection proton beam at the output of the half quadrupole.

second quadrupole (powered as defocusing lens) with the electron beam offset shifted to the other direction. In order to provide sufficient aperture for the three beams, an elliptical shape has been chosen for the vacuum chamber. It defines enough space for the beam envelopes and the off-centre design trajectories. The black ellipses correspond to the beams at the entrance of the magnet while the red shapes represent the beams at the exit. From left to right the three beams are respectively the non colliding proton beam (tiny circles), electron beam (squeezed ellipses) and the colliding proton beam. As defined before we refer to a beam size of 20 σ in case of the electrons and 15 sigma plus beta-beating plus 2 mm orbit tolerance for the colliding and non-colliding proton beam.
In this context it should be pointed out that the non-colliding proton beam, travelling in the same direction as the electrons, is shifted in time by half the bunch spacing. While the projected beam envelopes in Fig. 10.33 and 10.32 seem to overlap in the transverse plane, they are well separated by 12.5 ns, corresponding to 3.75m, in the longitudinal direction.

The minimum required gradients and pole tip radius of the quadrupoles of the doublet are listed in Table 10.15. Following the increasing beam size after the IP, the two quadrupoles are optimised for sufficient free aperture for the collidng beams and their design orbits. Accordingly a different layout has been chosen for the magnets, to provide the best conditions for the radiation power and critical energy. An alternative approach has been studied, based on a single quadrupole design for both lenses of the doublet. While an optics solution still is possible, it does however not allow for minimum radiation power and sets more stringent requirements on the shielding and absorption of the synchrotron light fan.

Table 10.15: Magnet gradient and pole tip aperture of the quadrupoles of the doublet for the synchrotron power optimum

	Q0F	Q0D
$\gamma\varepsilon_e$ [mm.mrad]	50	50
$\gamma\varepsilon_p$ [mm.mrad]	2.50	2.50
Max. gradient [T/m]	36.2	26.1
Min. pole-tip radius [mm]	28.9	38.1
Length [m]	1.86	1.86

The Fig. 10.35 shows the chromatic effect of the two lattice versions, as function of the momentum spread.

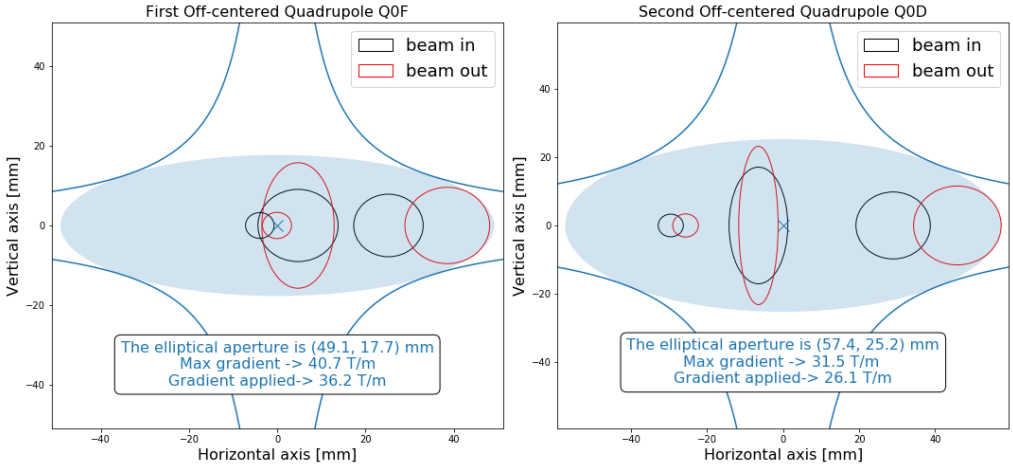

Figure 10.33: The position of the three beams at the entrance (black) and exit (red) of the electron doublet magnets. Following the internal convention, 15 σ plus 20% beta beating plus 2 mm orbit tolerances beam envelopes are chosen for the proton beams. The beam size of the electrons refer to 20 σ. From left to right the three beams are respectively the non colliding proton beam (tiny circles), electron beam (squeezed ellipses) and the colliding proton beam.

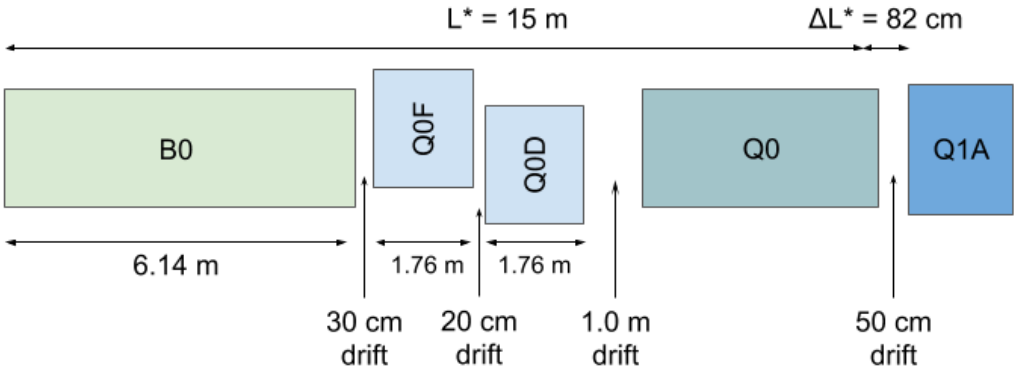

Figure 10.34: Possible optimized design featuring a 1.0 meter drift between the off-centered quadrupoles and the half quadrupole in order to leave space for shielding material.

The lattice based on a single dipole magnet and late focusing of the electron beam, shows an increase of the beta function of up 40% in the vertical plane for particles with a momentum deviation up to the design value of $\frac{\Delta p}{p} = 2.6 \times 10^{-4}$ (vertical cursor line in the graph) and a corresponding luminosity loss of 20% for those particles. The optimised design, based on the early focusing scheme, shows a much reduced chromatic effect and the resulting off-momentum beta-beating at the IP is limited to a few percent. As direct consequence the luminosity loss is well below the 1.5% level. A special local chromaticity correction scheme, therefore, dealing with the aberrations at IP, is thus not considered as necessary. Further studies will include the recirculation of the beam post-collision and the energy recovery performance and might nevertheless highlight the need of explicit sextupoles to mitigate the growing momentum spread through the deceleration process and to avoid beam losses.

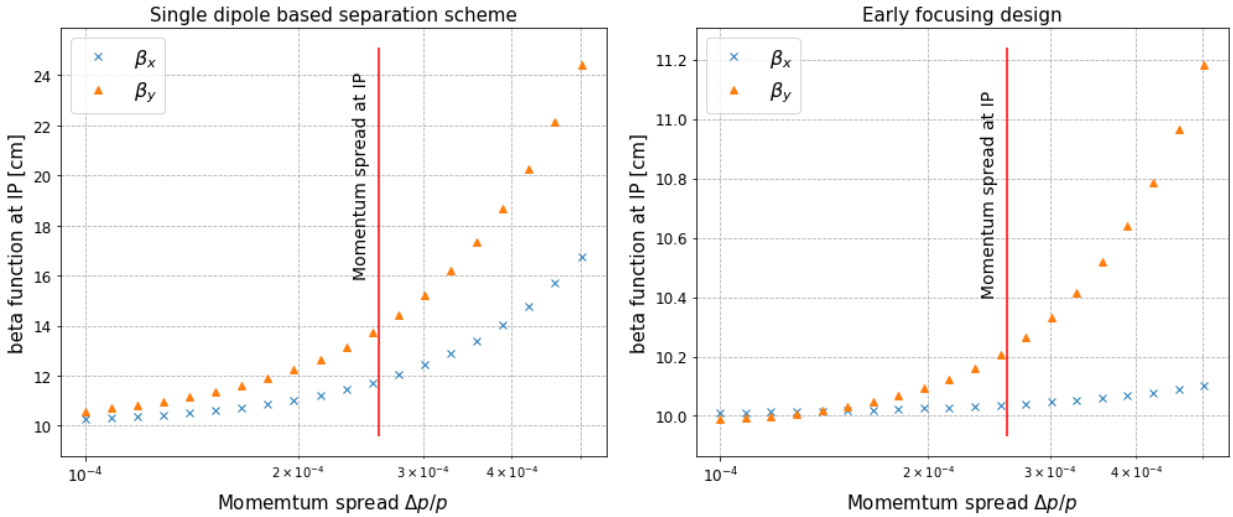

Figure 10.35: Beta function at the IP as a function of the momentum spread. Left : Situation for the single dipole based separation scheme. Right : With the design featuring an earlier focusing. The graphs show the increase of β^* due to the chromaticity of the lattice.

10.7.4 Interaction Region Magnet Design [Stefan Russenschuck, Brett Parker, Kevin Andre', Bernhard Holzer]

Triplet Magnet Design

Part to be provided by Stefan Russenschuck

Normal Conducting Magnet Design

Part to be checked by Stefan Russenschuck

The proposed mini-beta doublet of the electron lattice that is foreseen to establish an early focusing of the beam, and the normal conducting proton-half quadrupole, are new magnet concepts, that have been studied on a first level to determine their technical feasibility and layout.

The geometric layout of the QNC magnet is sketched in Fig. 10.37. Left of the mirror plate the field free region will house the electron beam and the non-colliding proton beam. The thickness of the mirror plate at the magnet mid-plane amounts to 20 mm and allows at the same time for sufficient mechanical stability of the magnet and smallest beam separation need between electron and proton beam.

First field calculations, using the magnet design code ROXIE [191] are presented in Fig. 10.37. The results are promising, the gradient reaches 50 T/m for a current of 400 A, leading to a current density of 21.14 A/mm^2. The cable design used for the study comes from the CERN magnet ID : PXMQNDD8WC, it can support up to 860 A equivalent to 45.45 A/mm^2. The mitigation of the multipole components is under investigation.

The magnet geometry for the quadrupoles Q0F and Q0D quadrupoles, given in Fig. 10.33 and the main specifications provided in Table 10.15 imply a maximum magnetic field at the pole tip of 1.2 T that is well within reach for a normal conducting quadrupole.

10.8 Civil Engineering [Alexandra Tudora, John Osborne]

Since the beginning of the LHeC concept, various shapes and sizes of the eh collider were studied around CERN region.The conceptual study report published in 2012 focused primarily on two main options, namely

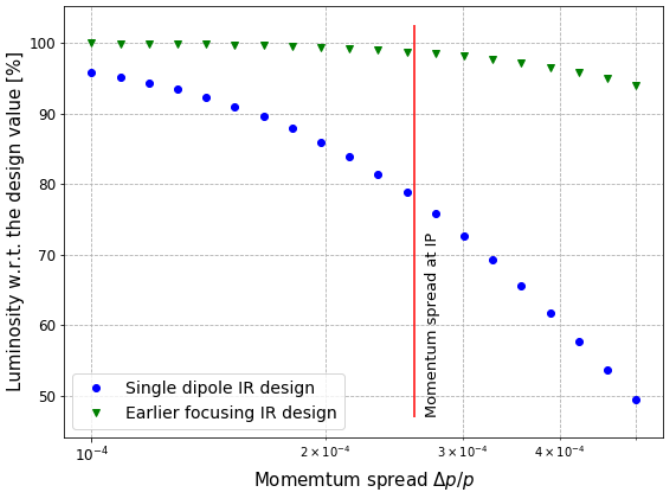

Figure 10.36: The resulting luminosity as a function of the momentum spread for the single dipole based separation scheme (blue circles) and the design featuring an earlier focusing (green triangles).

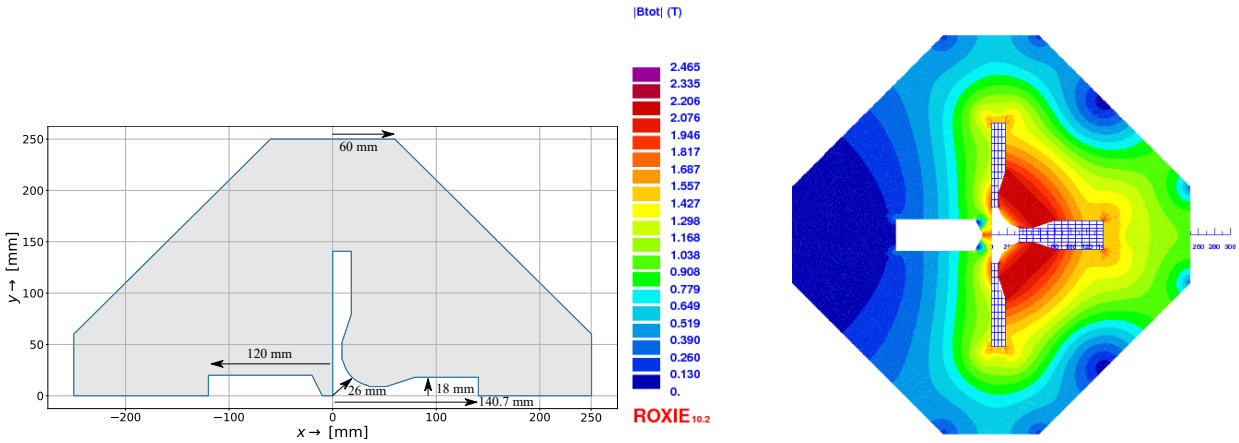

Figure 10.37: Left: Mechanical layout of the new half quadrupole for the proton beam. Right : Field calculation of the new half quadrupole for the proton beam.

the RING-RING and the RING-LINAC options. For civil engineering, these options were studied taking into account geology, construction risks, land features as well as technical constrains and operation of the LHC. The Linac-Ring configuration was selected as preferred due to higher achievable luminosity (see Chapter 1). This chapter describes the civil engineering infrastructure required for an Energy Recovery Linac (ERL) injecting into the LHC ALICE cavern at Point 2 LHC. Figure 10.38 shows three sizes alternatives proposed for the ERL, represented as fractions of the LHC circumference. This chapter focuses on two of these options, specifically the 1/3 and 1/5 of the LHC circumference.

The proposed siting for the LHeC is in the North-Western part of the Geneva region at the existing CERN laboratory. The proposed Interaction Region is fully located within existing CERN land at LHC Point 2, close to the village of St.Genis, in France. The CERN area is extremely well suited to housing such a large project, with well understood ground conditions having several particle accelerators in the region for over 50 years. Extensive geological records exist from previous projects such as LEP and LHC and more recently, further ground investigations have been undertaken for the High-Luminosity LHC project. Any new underground structures will be constructed in the stable molasse rock at a depth of 100-150m in an area with very low seismic activity.

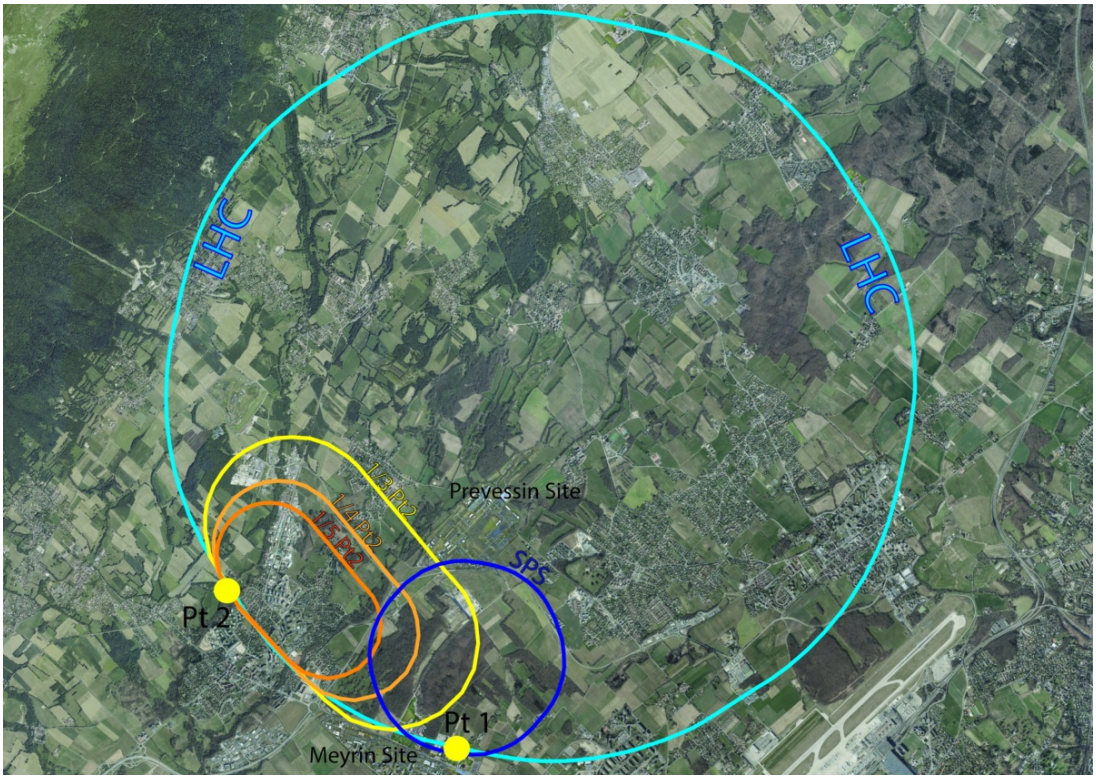

Figure 10.38: Racetrack alternatives proposed for LHeC at Point 2 LHC

The LHeC is situated within the Geneva basin, a sub-basin of the large molassic plateau (Figure 10.39). The molasse formed from the erosion of the Alps and it is a weak sedimentary rock. It comprises of alternating layers of marls and sandstones (and formations of intermediate compositions), which show a high variety of strength parameters. The molasse is overlaid by the Quaternary glacial moraines. Figure 10.40 shows a simplified geological profile of the LHC. Although placed mainly within the molasse plateau, one sector of the LHC is situated in the limestone of the Jura.

The physical positioning of the LHeC has been developed based on the assumption that the maximum underground volume possible should be placed within the molasse rock and should avoid as much as possible any known geological faults or environmentally sensitive areas. Stable and dry, the molasse is considered a suitable rock type for TBM excavation. In comparison, CERN has experienced significant issues with the underground construction of sector 3-4 in the Jura limestone. There were major issues with water ingress at and behind the tunnel face (Cook, 2015). Another challenging factor for limestone is the presence of karsts. They are the result of chemical weathering of the rock and often they are filled with water and sediment, which can lead to infiltration of the tunnel during and after excavation.

The ERL will be positioned inside the LHC Ring, in order to ensure that new surface facilities are located on existing CERN land. The proposed underground structures for a Large Hadron electron Collider (LHeC) at high luminosity aiming for an electron beam energy of 60 GeV is shown in Figure 10.41.

10.8.1 Design requirements and Construction Strategy

Table shows the underground structures proposed for LHeC option 1/3 LHC. This requires 9.1 km of new tunnels of 5.5m diameter and two LINACs. Parallel to the main LINAC tunnels, at 10m distance apart, there are the RF galleries, each 1070m long. Two additional caverns, 25m wide and 50m long are required for general services such as cryogenics and technical services. These are connected to the surface via two

Figure 10.39: Simplified map of Swiss geology

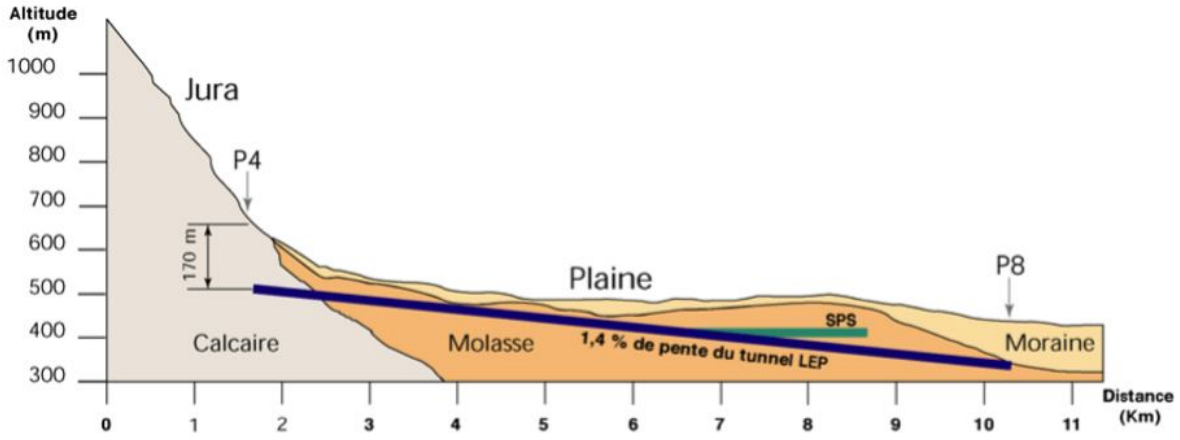

Figure 10.40: Geological profile of the LHC tunnel

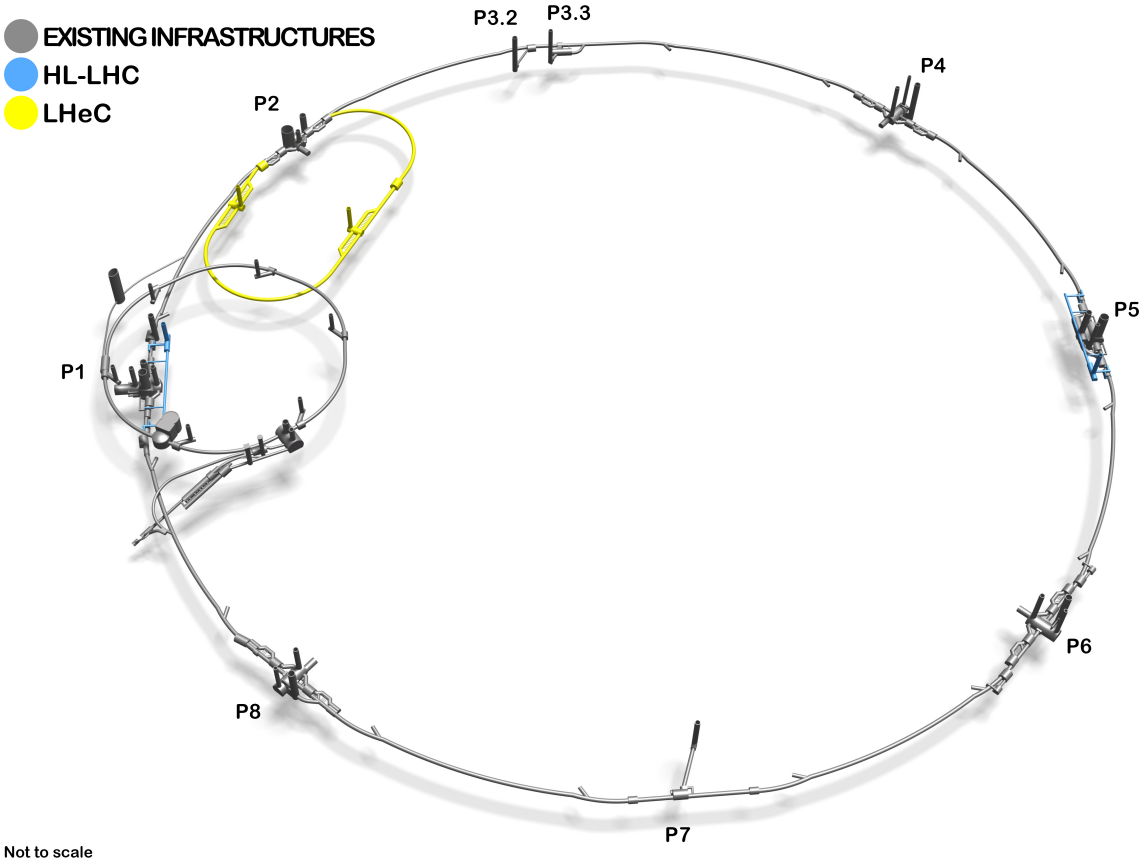

Figure 10.41: 3D Schematic showing proposed underground structures of LHeC (shwon in yellow). The HL-LHC structures are highlighted in blue.

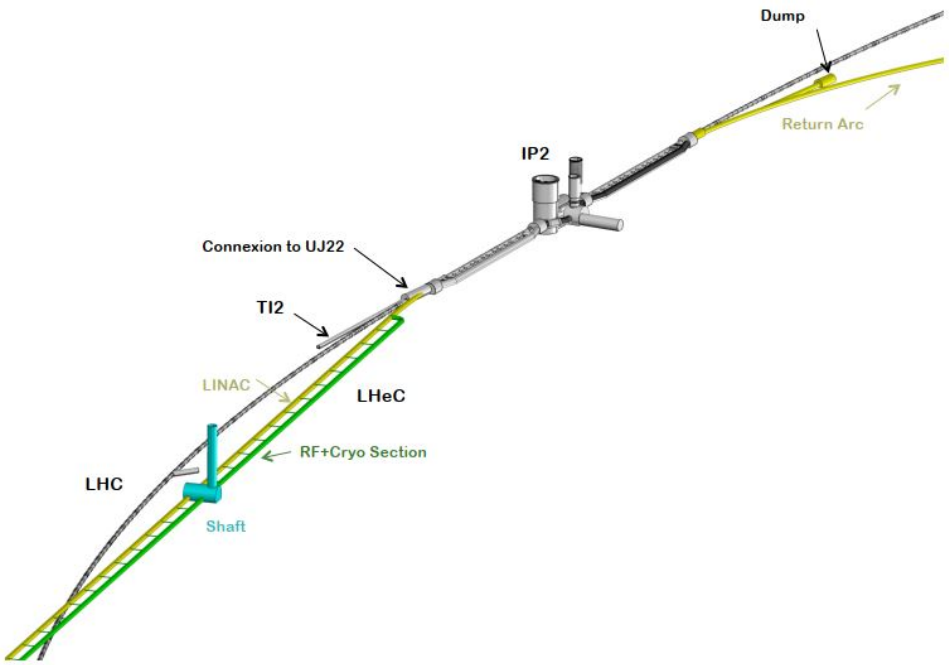

Figure 10.42: ERL injection area into IP2 and junction cavern

9m diameter access, provided with lifts to allow access of equipment and personnel.

Structures	Quantities	Length(m)	Span(m)
Machine tunnels	-	9091	5.5
Service caverns	2	50	25
Service shafts	2	80	9
Injection caverns	1	50	25
Dump cavern	1	90	16.8
Junction caverns	3	20	16.8
RF galleries	2	1070	5.5
Waveguide connections	50	10	1
Connection tunnels	4	10	3

Table 10.16: List of underground structures

Additional caverns are needed to house injection facilities and a beam dump. The underground structures proposed for LHeC option 1/5 LHC are the same as 1/3 options with the exception of the main tunnel which would be 5.4km in circumference and shorter RF galleries, each 830m long.

In addition to the new structures, the existing LHC infrastructure also requires modifications. To ensure connection between LHC and LHeC tunnels, the junction caverns UJ22 and UJ27 need to be enlarged (Figure 10.42).

It is envisaged that a Tunnel Boring Machine (TBM) will be utilised for the excavation of the main tunnel. For the main tunnel construction, a shielded TBM would be employed, with pre-cast segmental lining, and injection grouting behind the lining. Roadheaders and excavators could be utilised for the construction

of the caverns and connection tunnels. Figure shows a similar equipment being used at point 1 for HL-LHC works. Diesel excavators have been modified and equipped with an electric motor in order to reduce vibrations that could disrupt LHC operation.

10.8.2 Schedule and Cost Estimates

A detailed cost estimate was prepared for a 9.1km ERL located at Point 2 of LHC, using the same unit prices as for the civil engineering for the Future Circular Collider. More recently for LHeC, the cost figures were adapted to fit the smaller version, 5.4km racetrack at point 2 (option 1/5 LHC).

Chapter 11

Experimentation at the LHeC [Paul Newman, Peter Kostka]

Example reference: LHeC [1]

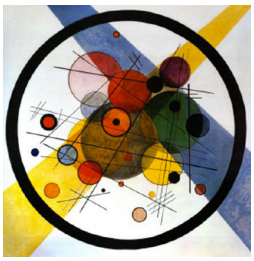

Figure 11.1: Example figure, please remove

11.1 Introduction [Paul Newman]

11.2 Main Detector Elements

Fig. 11.2

Fig. 11.3

Fig. 11.4

Calo$_{LHeC}$ [*Readout,Absorber*]	**FHC** [*Si,W*]	**FEC** [*Si,W*]	**EMC** [*Sci,Pb*]	**HCAL** [*Sci,Fe*]			**BEC** [*Si,Pb*]	**BHC** [*Si,Cu*]
	Plug Fwd	Plug Fwd	Barrel	Ecap Fwd	Barrel	Ecap Bwd	Plug Bwd	Plug Bwd
$\eta_{max/min}$								
[1)] σ_E/E [%] $= \mathbf{a}/\sqrt{E} \oplus \mathbf{b}$	51.8/5.4	17.8/1.4	12.4/1.9	49.3/4.7	48.9/5.3	49.9/4.8	14.4/2.8	49.5/7.9
$\Lambda_I \,/\, X_0$	$\Lambda_I = 9.6$	$X_0 = 48.8$	$X_0 = 30.2$	$\Lambda_I = 10.0$	$\Lambda_I = 8.6$	$\Lambda_I = 8.7$	$X_0 = 30.8$	$\Lambda_I = 9.2$
Area Si $[m^2]$								

[1)] **GEANT4** simulation based fits using crystal ball function

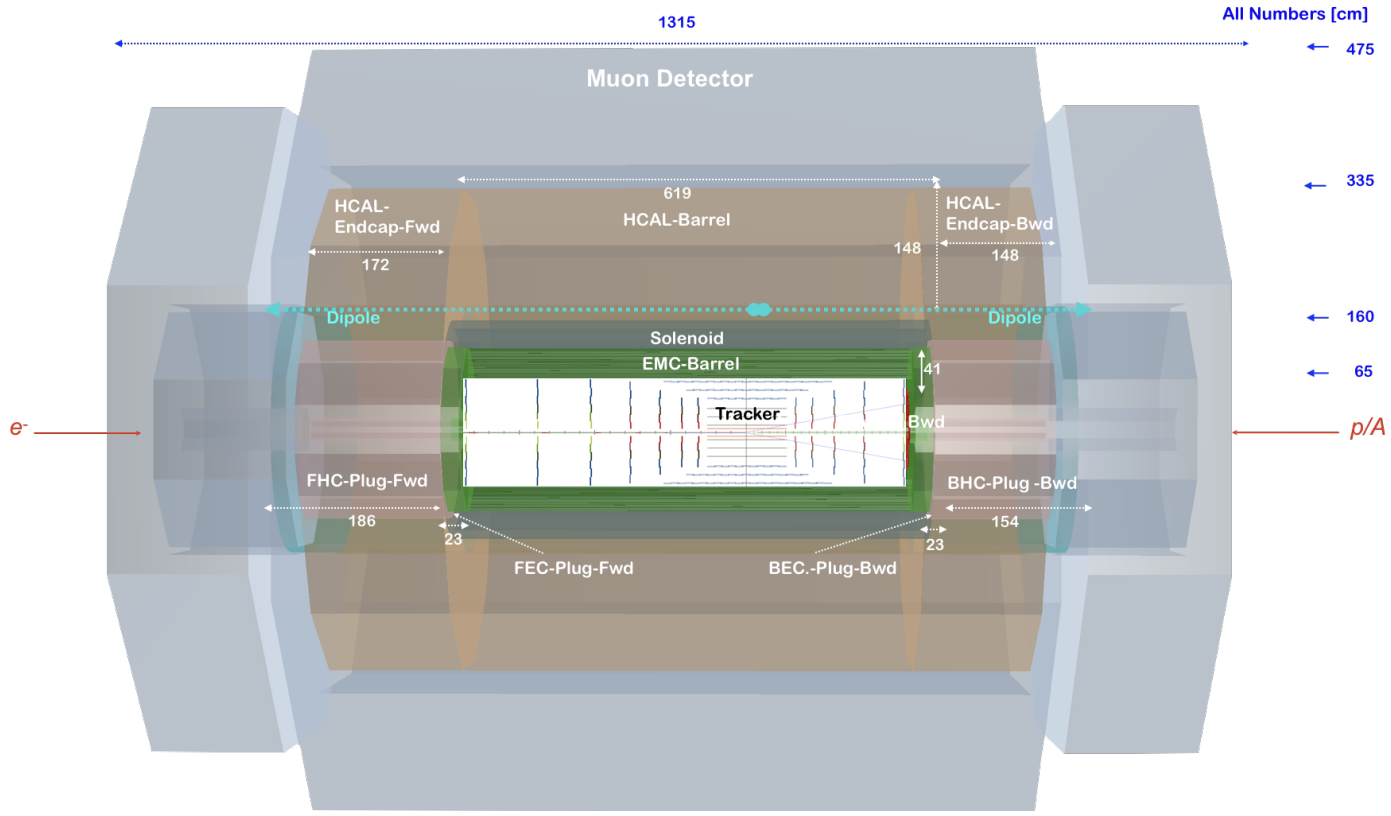

Figure 11.2: Side view of a LHeC concept detector designed using the DD4hep framework [ref.] with essential measures. The lay-over tracker structure optimised using the tkayout-light program [ref.] illustrates the arrangement of pixel, macro-pixel and strip Si-wafers, respectively. The Si-tracker is surrounded by the Electromagnet-Barrel (ECAL-Barrel) and Electromagnet-forward/backward-Plug calorimeters using tungsten (forward) and lead (backward) absorber material and Si-based sensitive readout in both cases. The experiment solenoid is placed between the ECAL-Barrel and Hadronic-Barrel calorimeter (HCAL-Barrel) and housed in a cryostat common with a weak dipole which bends the electron beam into head-on collisions with the colliding proton beam and after the interaction point a dipole with opposite polarity separates the orbits of the electron and proton beam. The steering dipoles extend over the full length of the HCAL-Barrel and HCAL-Plug-forward/backward. The Hadronic Calorimeters Barrel/Endcaps are based on steel structures as absorbing material (of ATLAS type [ref.]) and close the outer field of the central solenoid. The Muon Detector builds an envelope of all other parts of the main LHeC detector.

Calo$_{lowE-FCC-eh}$ [*Readout,Absorber*]	**FHC** [*Si,W*]	**FEC** [*Si,W*]	**EMC** [*Sci,Pb*]	**HCAL** [*Sci,Fe*]			**BEC** [*Si,Pb*]	**BHC** [*Si,Cu*]
	Plug Fwd	Plug Fwd	Barrel	Ecap Fwd	Barrel	Ecap Bwd	Plug Bwd	Plug Bwd
$\eta_{max/min}$								
[1)] σ_E/E [%] $= \mathbf{a}/\sqrt{E} \oplus \mathbf{b}$								
$\Lambda_I \,/\, X_0$	$\Lambda_I = 15.5$	$X_0 = 84.7$	$X_0 = 66.2$	$\Lambda_I = 15.4$	$\Lambda_I = 13.3$	$\Lambda_I = 13.3$	$X_0 = 50.2$	$\Lambda_I = 14.6$
Area Si $[m^2]$								

[1)] **GEANT4** simulation based fits using crystal ball function

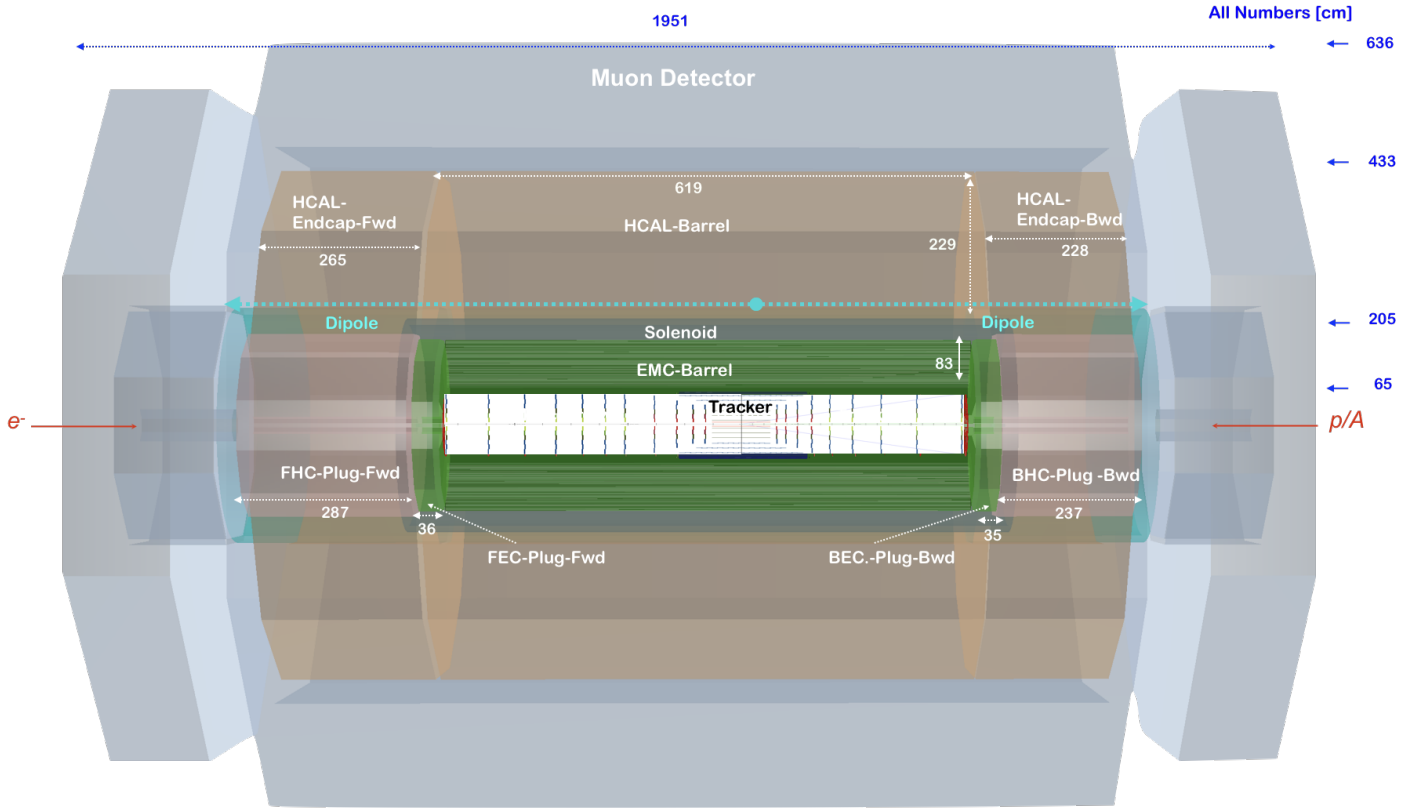

Figure 11.3: Side view of a lowE-FCC-eh (E_p = 20TeV) concept detector designed using the DD4hep framework [ref.] showing essential measures. The principal layout is similar to the LHeC detector. As well as the choice of materials (warm version). The experiment solenoid is placed again between the ECAL-Barrel and Hadronic-Barrel calorimeter (HCAL-Barrel) and housed in a cryostat common with the beam steering dipoles extending over the full length of the HCAL-Barrel and HCAL-Plug-forward/backward. The sizes has been chosen such that the solenoid/dipoles and ECAL-Barrel systems serve also after an upgrade of beam energy to E_p = 50TeV and an upgrade of detector accordingly.

Calo$_{FCC-eh}$ [*Readout, Absorber*]	**FHC** [*Si,W*]	**FEC** [*Si,W*]	**EMC** [*Sci,Pb*]	**HCAL** [*Sci,Fe*]			**BEC** [*Si,Pb*]	**BHC** [*Si,Cu*]
	Plug Fwd	Plug Fwd	Barrel	Ecap Fwd	Barrel	Ecap Bwd	Plug Bwd	Plug Bwd
$\eta_{max/min}$								
[1] σ_E/E [%] $= \mathbf{a}/\sqrt{E} \oplus \mathbf{b}$								
Λ_I / X_0	$\Lambda_I = 20.5$	$X_0 = 112.0$	$X_0 = 66.2$	$\Lambda_I = 20.2$	$\Lambda_I = 17.2$	$\Lambda_I = 16.8$	$X_0 = 69.6$	$\Lambda_I = 19.3$
Area Si $[m^2]$								

[1] **GEANT4** simulation based fits using crystal ball function

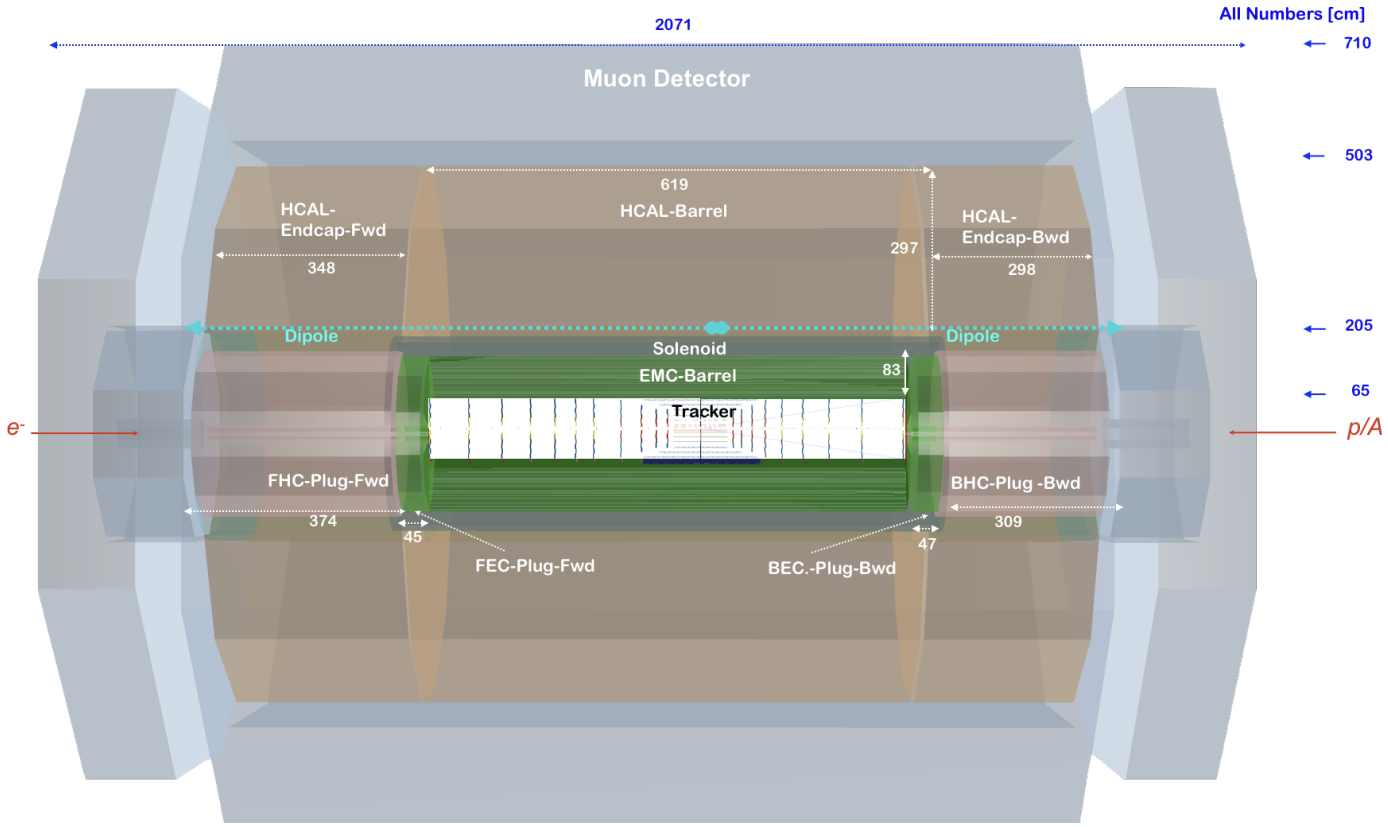

Figure 11.4: Side view of a FCC-eh concept detector designed using the DD4hep framework [ref.] . Essential measures are indicated. The principal layout is similar to the LHeC detector. As well as the choice of materials (warm version). The experiment solenoid is placed again between the ECAL-Barrel and Hadronic-Barrel calorimeter (HCAL-Barrel) and housed in a cryostat common with the beam steering dipoles extending over the full length of the HCAL-Barrel and HCAL-Plug-forward/backward.

11.2.1 Magnets [Hermann ten Kate]

11.2.2 Machine-Detector Interface, Beam Pipe and Radiation [Peter Kostka]

11.2.3 Inner Tracking [Peter Kostka]

11.2.4 Calorimetry [Peter Kostka]

11.2.5 Muon Detector [Alessandro Polini]

11.3 Central Detector Performance [Peter Kostka]

11.4 Forward and Backward Detectors [Paul Newman]

11.5 Detector Installation and Infrastructure [Andrea Gaddi]

Chapter 12

Conclusions [Oliver Bruening, Max Klein]

12.1 Summary [Max Klein]

12.2 Timeline and Future Project Development [Oliver Bruening]

Appendix A

Electron-Hadron Scattering with E_p=20 TeV [Monica D'Onofrio]

A.1 Introduction [Monica D'Onofrio]

Example reference: LHeC [1]

A.2 Performance Parameters [Frank Zimmermann]

A.3 Physics Interest - Case Studies

A.3.1 FCC-hh at 40 TeV: SM and BSM [Maarten Boonekamp, Monica D'Onofrio]

A.3.2 ep at 2.2 TeV cms: PDFs and Higgs [Claire Gwenlan, Max Klein, Jorge De Blas]

A.4 Attaching the ERL to a 100 km Hadron Ring

A.4.1 Scaling the IR [Bernhard Holzer]

A.4.2 Civil Engineering around point L [Alexandra Tudora]

A.5 Scaling the LHeC Detector Design to Higher Proton Energies [Peter Kostka]

Appendix B

ERL Technology and Applications [Alex Bogacz, Walid Kaabi]

B.1 Development of Energy Recovery Linac Technology - Status and Prospects [Chris Tennant]

B.1.1 Introduction

In instances where high beam power is required, the concept of energy recovery presents an attractive solution. Energy recovering linacs (ERLs) are a class of novel accelerators which are uniquely qualified to meet the demands for a wide variety of applications by borrowing features from traditional architectures to generate linac quality beams with near storage ring efficiency [192]. After acceleration through a linac section, the electrons in an ERL are returned 180° out of phase with respect to the radio frequency (RF) accelerating field for energy recovery. The beam deposits energy into cavity fields, which can then accelerate newly injected bunches, thereby effectively canceling the beam loading effects of the accelerated beam. Therefore ERLs can accelerate very high average currents with only modest amounts of RF power. Because the beam is constantly being renewed, it never reaches an equilibrium state. Consequently this provides flexibility to manipulate the phase space and tailor the beam properties for a specific application. Further, since the energy of the decelerated beam is approximately equal to the injection energy, the dump design becomes considerably easier.

B.1.2 ERL Applications

Historically, nearly all ERLs built and operated were used to drive a free-electron laser (FEL). The requirement for high peak current bunches necessitated bunch compression and handling the attendant beam dynamical challenges. In recent years, ERLs have turned from being drivers of light sources toward applications for nuclear physics experiments, Compton backscattering sources and strong electron cooling. Unlike an FEL, these latter use cases require long, high charge bunches with small energy spread. Where once a short bunch length was the key performance metric, now there is a premium on maintaining a small correlated energy spread (with a commensurately long bunch).

B.1.3 Challenges

Energy recovery linacs are not without their own set of challenges. In the following sections a brief survey of some of the most relevant are given. These include collective effects, such as space charge, the multipass beam breakup (BBU) instability, coherent synchrotron radiation (CSR) and the microbunching instability (μBI),

beam dynamic issues such as halo, the interaction of the beam with the RF system and other environmental impedances as well as issues related to common transport lines.

Space Charge The role of space charge forces (both transverse and longitudinal) often dictate many operational aspects of the machine. Maintaining beam brightness during the low energy injection stage is vitally important. In addition to the low energy, ERL injectors must also preserve beam quality through the merger system that directs the beam to the linac axis. Once injected into the linac, the beam energy at the front end is often still low enough that space charge forces cannot be neglected. Just as important is the longitudinal space charge (LSC) force which manifests itself by an energy spread asymmetry about the linac on-crest phase [193]. The LSC wake acts to accelerate the head of the bunch while decelerating the tail. Operating on the rising part of the waveform leads to a decrease in the correlated energy spread, while accelerating on the falling side leads to an increase. These observations inform where acceleration, and how the longitudinal match, is performed.

Beam Breakup Instability The beam breakup instability is initiated when a beam bunch passes through an RF cavity off-axis, thereby exciting dipole higher-order modes (HOMs). The magnetic field of an excited mode deflects following bunches traveling through the cavity. Depending on the details of the machine optics, the deflection produced by the mode can translate into a transverse displacement at the cavity after recirculation. The recirculated beam induces, in turn, an HOM voltage which depends on the magnitude and direction of the beam displacement. Thus, the recirculated beam completes a feedback loop which can become unstable if the average beam current exceeds the threshold for stability [194]. Beam breakup is of particular concern in the design of high average current ERLs utilizing superconducting RF (SRF) technology. If not sufficiently damped by the HOM couplers, dipole modes with quality factors several orders of magnitude higher than in normal conducting cavities can exist, providing a threat for BBU to develop. For single pass ERLs, beam optical suppression techniques – namely, interchanging the horizontal and vertical phase spaces to break the feedback loop between the beam and the offending HOM – are effective at mitigating BBU [195].

Coherent Synchrotron Radiation Coherent synchrotron radiation poses a significant challenge for accelerators utilizing high brightness beams. When a bunch travels along a curved orbit, fields radiated from the tail of the bunch can overtake and interact with the head. Rather than the more conventional class of head-tail instabilities where the tail is affected by the actions of the head, CSR is a tail-head instability. The net result is that the tail loses energy while the head gains energy leading to an undesirable redistribution of particles in the bunch. Because the interaction takes place in a region of dispersion, the energy redistribution is correlated with the transverse positions in the bend plane and can lead to projected emittance growth. While there has been much progress in recent years to undo the effects of CSR in the bend plane with an appropriate choice of beam optics [196], it is more difficult to undo the gross longitudinal distortion caused by the CSR wake. This is particularly true in applications where the intrinsic energy spread is small and/or where the effect can accumulate over multiple recirculations. One possible mitigation is shielding the CSR wake using an appropriately sized beam pipe [197].

Microbunching Instability Microbunching develops when an initial density modulation, either from shot noise or from the drive laser, is converted to energy modulations through short-range wakefields such as space charge and CSR. The energy modulations are then transformed back to density modulations through the momentum compaction of the lattice. Danger arises when a positive feedback is formed and the initial modulations are enhanced. This phenomenon has been studied extensively, both theoretically and experimentally, in bunch compressor chicanes [198, 199]. Only recently has there been a concerted effort to study the microbunching instability in recirculating arcs [200, 201, 202]. Because the beam is subject to

space charge and/or CSR throughout an ERL, density modulations can be converted to energy modulations. And because of the native momentum compaction of the lattice (in arcs, spreaders/recombiners, chicanes, etc.) those energy modulations may be converted back to density modulations. Therefore, ERLs offer potentially favorable conditions for seeding the microbunching instability, which requires careful attention in the early design stages.

Halo Halo is defined as the relatively diffuse and potentially irregularly distributed components of beam phase space that can reach large amplitudes. It is of concern because ERL beams are manifestly non-Gaussian and can have beam components of significant intensity beyond the beam core [203]. Though sampling large amplitudes, halo responds to the external focusing of the accelerator transport system in a predictable manner. It is therefore not always at large spatial amplitude, but will at some locations instead be small in size but strongly divergent. Halo can therefore present itself as "hot spots" in a beam distribution, and thus may be thought of as a lower-intensity, co-propagating beam that is mismatched to the core beam focusing, timing, and energy. Beam loss due to halo scraping is perhaps the major operational challenge for higher-power ERLs. Megawatt-class systems must control losses at unshielded locations to better than 100 parts-per-million to stay within facility radiation envelopes. Scaling to 100 MW suggests that control must be at the part-per-million level. This has been demonstrated – but only at specific locations within an ERL [204].

RF Transients Dynamic loading due to incomplete energy recovery is an issue for all ERLs [205]. In some machines it is due to unintentional errors imposed on the energy recovered beam; for instance, path length errors in large-scale systems. In other machines, such as high power ERL-based FEL drivers, it is done intentionally. In cases where there is the potential for rapid changes in the relative phase of the energy recovered beam, dynamic loading would be difficult to completely control using fast tuners. In such cases adequate headroom in the RF power will have to be designed into the system. These transient beam-loading phenomena are widely unrecognized and/or neglected. RF drive requirements for an ERL are often viewed as "minimal", because in steady-state operation the recovered beam notionally provides RF power for acceleration. It has however been operationally established that RF drive requirements for ERLs are defined not by the steady-state, but rather by beam transients and environmental/design factors such as microphonics [206]. As a result, the RF power required for stable ERL operation can differ dramatically from naïve expectations.

Wakefields and Interaction of Beam with Environment As with other system architectures intended to handle high-brightness beams, ERLs can be performance limited by wakefield effects. Not only can beam quality be compromised by interaction of the beam with environmental impedances, there is also significant potential for localized power deposition in beamline components. Resistive wall and RF heating have proven problematic during ERL operation in the past [207]. Extrapolation of this experience to higher bunch charges and beam powers leads to serious concern regarding heating effects. Careful analysis and management of system component impedances is required.

Multi-turn, Common Transport Future systems must evolve to utilize multiple turns; it is a natural cost optimization method [208] and multi-turn systems can in principle provide performance equal to that of 1-pass up/down ERLs at significantly lower cost. In addition to the use of multiple turns, cost control motivates use of extended lengths of common transport, in which both accelerated and recovered passes are handled simultaneously using the same beam lines. This presents unique challenges for high energy ERLs, like LHeC in particular, where energy loss due to synchrotron radiation cannot be ignored and causes an energy mismatch for common transport lines. But addressing these challenges will open up exciting new opportunities for ERLs. In addition to PERLE and LHeC, a multi-turn ERL design from Daresbury

illustrates the manner in which the cost/complexity optimum lies toward shorter linacs, more turns, and multiple beams in fewer beam lines [209]. This also drives the use of multiple turns in stacking rings for hadron cooling; the more turns the cooling beam can be utilized, the lower the current required from the driver ERL, which mitigates challenges associated with source lifetime [210].

B.1.4 ERL Landscape

One way to view the current state of ERLs globally is the so-called "ERL landscape" shown in Fig. B.1 [211]. Every data point represents a machine that demonstrated energy recovery and is positioned in (maximum) energy and (average) current parameter space. For clarity, the plot is restricted to continuous-wave (CW), SRF-based ERLs only and includes legacy machines, those under construction and currently in operation as well as the LHeC and PERLE (proposed). The size of the marker is indicative of the charge per bunch while a black line around the marker indicates it was/is a "true ERL". That is, where the beam power exceeds the installed RF power (they are represented in the plot by the three FEL drivers that were designed, built, commissioned and operated at Jefferson Laboratory).

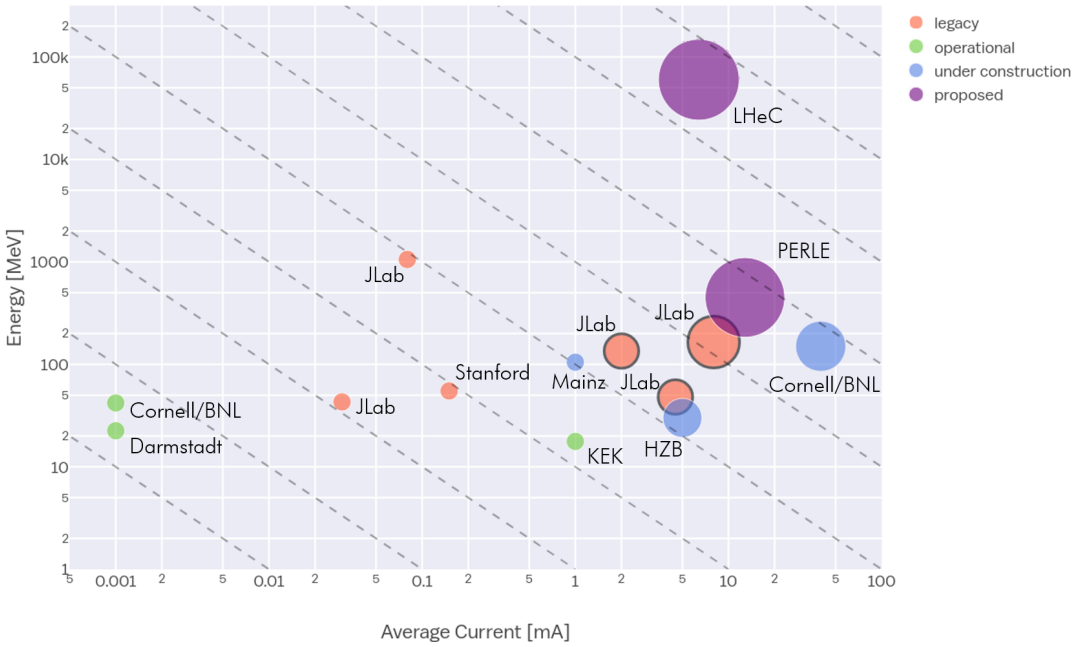

Figure B.1: The "ERL landscape", where data points are restricted to CW, SRF-based ERLs. The dashed lines represent lines of constant beam power – starting from 10 W in the lower left and going to 10 GW in the upper right. Note that both axes use a log scale.

A cursory look at Fig. B.1 illustrates several of the challenges facing the next generation of ERLs. While getting from the current state-of-the-art to the LHeC requires only a modest increase in average current, it requires a significant increase in bunch charge and addressing the consequent collective effects [212]. Most significantly, however, is the leap in energy from systems that have operated in the 100 MeV range to several tens of GeV. Note that PERLE is strategically positioned to address incremental changes in both average current, bunch charge and energy. As such, it provides a convenient test bed facility to address the issues described previously [213]. Several ERLs are still in the nascent stages and as they ramp up beam power, will also be valuable in advancing the state-of-the-art. For instance, though it uses a Fixed Field Alternating Gradient (FFAG) arc, the Cornell/Brookhaven ERL Test Accelerator (CBETA) will address multi-turn energy recovery for the first time in an SRF system [214]. Note that with only minor modifications Jefferson Laboratory's Continuous Electron Beam Accelerator Facility (CEBAF) could be operated with multi-pass

energy recovery at several GeV using common transport with the same topology as LHeC (i.e. bisected linacs of equal energy gain with arcs vertically separated by energy using spreaders and recombiners) [215].

B.2 The ERL Facility PERLE [Walid Kaabi]

B.3 High Eenergy Photo-Nuclear Physics with the LHeC [Norbert Pietralla]

Bibliography

[1] LHeC Study Group Collaboration, J. L. Abelleira Fernandez *et al.*, *J. Phys.* G39 (2012) 075001, arXiv:1206.2913.

[2] O. Bruening, *FCC-ACC-RPT-XXXX* (2018) .

[3] A. Bogacz, *Talk at ERL Workshop, Berlin* (2019) .

[4] FCC Collaboration, A. Abada *et al.*, *Eur. Phys. J. ST* 228 (2019) 755–1107.

[5] LHeC, PERLE Collaboration, O. Bruening and M. Klein, *J. Phys.* G46 (2019) 123001.

[6] xFitter Developers' Team Collaboration, H. Abdolmaleki *et al.*, arXiv:1907.01014.

[7] R. Abdul Khalek, S. Bailey, J. Gao, L. Harland-Lang and J. Rojo, arXiv:1906.10127.

[8] I. I. Balitsky and L. N. Lipatov, *Sov. J. Nucl. Phys.* 28 (1978) 822–829. [Yad. Fiz.28,1597(1978)].

[9] E. A. Kuraev, L. N. Lipatov and V. S. Fadin, *Sov. Phys. JETP* 45 (1977) 199–204. [Zh. Eksp. Teor. Fiz.72,377(1977)].

[10] L. N. Lipatov, *Sov. Phys. JETP* 63 (1986) 904–912. [Zh. Eksp. Teor. Fiz.90,1536(1986)].

[11] V. S. Fadin and L. N. Lipatov, *Phys. Lett.* B429 (1998) 127–134, arXiv:hep-ph/9802290.

[12] M. Ciafaloni and G. Camici, *Phys. Lett.* B430 (1998) 349–354, arXiv:hep-ph/9803389.

[13] J. Blumlein and A. Vogt, *Phys. Rev.* D58 (1998) 014020, arXiv:hep-ph/9712546.

[14] D. A. Ross, *Phys. Lett.* B431 (1998) 161–165, arXiv:hep-ph/9804332.

[15] Y. V. Kovchegov and A. H. Mueller, *Phys. Lett.* B439 (1998) 428–436, arXiv:hep-ph/9805208.

[16] E. Levin, *Nucl. Phys.* B545 (1999) 481–504, arXiv:hep-ph/9806228.

[17] N. Armesto, J. Bartels and M. A. Braun, *Phys. Lett.* B442 (1998) 459–469, arXiv:hep-ph/9808340.

[18] M. Ciafaloni, *Nucl. Phys.* B296 (1988) 49–74.

[19] B. Andersson, G. Gustafson and J. Samuelsson, *Nucl. Phys.* B467 (1996) 443–478.

[20] J. Kwiecinski, A. D. Martin and P. J. Sutton, *Z. Phys.* C71 (1996) 585–594, arXiv:hep-ph/9602320.

[21] J. Kwiecinski, A. D. Martin and A. M. Stasto, *Phys. Rev.* D56 (1997) 3991–4006, arXiv:hep-ph/9703445.

[22] G. P. Salam, *JHEP* 07 (1998) 019, arXiv:hep-ph/9806482.

[23] M. Ciafaloni, D. Colferai and G. P. Salam, *JHEP* 10 (1999) 017, arXiv:hep-ph/9907409.

[24] M. Ciafaloni, D. Colferai and G. P. Salam, *Phys. Rev.* D60 (1999) 114036, arXiv:hep-ph/9905566.

[25] M. Ciafaloni, D. Colferai, D. Colferai, G. P. Salam and A. M. Stasto, *Phys. Lett.* B576 (2003) 143–151, arXiv:hep-ph/0305254.

[26] M. Ciafaloni, D. Colferai, G. P. Salam and A. M. Stasto, *Phys. Lett.* B587 (2004) 87–94, arXiv:hep-ph/0311325.

[27] M. Ciafaloni, D. Colferai, G. P. Salam and A. M. Stasto, *Phys. Rev.* D68 (2003) 114003, arXiv:hep-ph/0307188.

[28] M. Ciafaloni, D. Colferai, G. P. Salam and A. M. Stasto, *JHEP* 08 (2007) 046, arXiv:0707.1453.

[29] G. Altarelli, R. D. Ball and S. Forte, *Nucl. Phys.* B575 (2000) 313–329, arXiv:hep-ph/9911273.

[30] G. Altarelli, R. D. Ball and S. Forte, *Nucl. Phys.* B599 (2001) 383–423, arXiv:hep-ph/0011270.

[31] G. Altarelli, R. D. Ball and S. Forte, *Nucl. Phys.* B621 (2002) 359–387, arXiv:hep-ph/0109178.

[32] G. Altarelli, R. D. Ball and S. Forte, *Nucl. Phys.* B674 (2003) 459–483, arXiv:hep-ph/0306156.

[33] G. Altarelli, R. D. Ball and S. Forte, *Nucl. Phys.* B799 (2008) 199–240, arXiv:0802.0032.

[34] R. S. Thorne, *Phys. Rev.* D64 (2001) 074005, arXiv:hep-ph/0103210.

[35] A. Sabio Vera, *Nucl. Phys.* B722 (2005) 65–80, arXiv:hep-ph/0505128.

[36] M. Bonvini, S. Marzani and T. Peraro, *Eur. Phys. J.* C76 (2016) 597, arXiv:1607.02153.

[37] V. Bertone, S. Carrazza and J. Rojo, *Comput. Phys. Commun.* 185 (2014) 1647–1668, arXiv:1310.1394.

[38] M. Bonvini, S. Marzani and C. Muselli, *JHEP* 12 (2017) 117, arXiv:1708.07510.

[39] A. V. Belitsky, X.-d. Ji and F. Yuan, *Phys. Rev.* D69 (2004) 074014, arXiv:hep-ph/0307383.

[40] U. Amaldi and K. R. Schubert, *Nucl. Phys.* B166 (1980) 301–320.

[41] N. Armesto and A. H. Rezaeian, *Phys. Rev.* D90 (2014) 054003, arXiv:1402.4831.

[42] H. Kowalski and D. Teaney, *Phys. Rev.* D68 (2003) 114005, arXiv:hep-ph/0304189.

[43] H. Kowalski, L. Motyka and G. Watt, *Phys. Rev.* D74 (2006) 074016, arXiv:hep-ph/0606272.

[44] G. Watt and H. Kowalski, *Phys. Rev.* D78 (2008) 014016, arXiv:0712.2670.

[45] B. H. Denby *et al.*, *Phys. Rev. Lett.* 52 (1984) 795–798.

[46] M. E. Binkley *et al.*, *Phys. Rev. Lett.* 48 (1982) 73.

[47] H1 Collaboration, C. Alexa *et al.*, *Eur. Phys. J.* C73 (2013) 2466, arXiv:1304.5162.

[48] H1 Collaboration, A. Aktas *et al.*, *Eur. Phys. J.* C46 (2006) 585–603, arXiv:hep-ex/0510016.

[49] ZEUS Collaboration, S. Chekanov *et al.*, *Nucl. Phys.* B695 (2004) 3–37, arXiv:hep-ex/0404008.

[50] ZEUS Collaboration, S. Chekanov *et al.*, *Eur. Phys. J.* C24 (2002) 345–360, arXiv:hep-ex/0201043.

[51] LHCb Collaboration, R. Aaij *et al.*, *J. Phys.* G41 (2014) 055002, arXiv:1401.3288.

[52] ALICE Collaboration, B. B. Abelev *et al.*, *Phys. Rev. Lett.* 113 (2014) 232504, arXiv:1406.7819.

[53] A. D. Martin, M. G. Ryskin and T. Teubner, *Phys. Rev.* D62 (2000) 014022, arXiv:hep-ph/9912551.

[54] Y. Hatta, B.-W. Xiao and F. Yuan, *Phys. Rev. Lett.* 116 (2016) 202301, arXiv:1601.01585.

[55] M. Klein and T. Riemann, *Z. Phys.* C24 (1984) 151.

[56] MuLan Collaboration, V. Tishchenko *et al.*, *Phys. Rev.* D87 (2013) 052003, arXiv:1211.0960.

[57] D. Britzger and M. Klein, *PoS* DIS2017 (2018) 105.

[58] H1 Collaboration, V. Andreev *et al.*, *Eur. Phys. J.* C78 (2018) 777, arXiv:1806.01176.

[59] ATLAS Collaboration, M. Aaboud *et al.*, *Eur. Phys. J.* C78 (2018) 110, arXiv:1701.07240. [Erratum: Eur. Phys. J.C78,no.11,898(2018)].

[60] A. H. Mueller, *Nucl. Phys.* B335 (1990) 115–137.

[61] R. D. Ball, V. Bertone, M. Bonvini, S. Marzani, J. Rojo and L. Rottoli, *Eur. Phys. J.* C78 (2018) 321, arXiv:1710.05935.

[62] xFitter Developers' Team Collaboration, H. Abdolmaleki *et al.*, *Eur. Phys. J.* C78 (2018) 621, arXiv:1802.00064.

[63] J. Butterworth *et al.*, *J. Phys.* G43 (2016) 023001, arXiv:1510.03865.

[64] S. Carrazza, S. Forte, Z. Kassabov, J. I. Latorre and J. Rojo, *Eur. Phys. J.* C75 (2015) 369, arXiv:1505.06736.

[65] H. Paukkunen and P. Zurita, *JHEP* 12 (2014) 100, arXiv:1402.6623.

[66] J. Rojo and F. Caola, "Parton distributions and small-x QCD at the Large Hadron Electron Collider," in *Proceedings, 17th International Workshop on Deep-Inelastic Scattering and Related Subjects (DIS 2009): Madrid, Spain, April 26-30, 2009*, p. 222, Science Wise Publ. Science Wise Publ., Berlin, Germany, 2009. arXiv:0906.2079.

[67] R. Abdul Khalek, S. Bailey, J. Gao, L. Harland-Lang and J. Rojo, *Eur. Phys. J.* C78 (2018) 962, arXiv:1810.03639.

[68] J. Bartels, K. J. Golec-Biernat and H. Kowalski, *Phys. Rev.* D66 (2002) 014001, arXiv:hep-ph/0203258.

[69] K. J. Golec-Biernat and S. Sapeta, *Phys. Rev.* D74 (2006) 054032, arXiv:hep-ph/0607276.

[70] K. Golec-Biernat and S. Sapeta, *JHEP* 03 (2018) 102, arXiv:1711.11360.

[71] H1, ZEUS Collaboration, H. Abramowicz *et al.*, *Eur. Phys. J.* C75 (2015) 580, arXiv:1506.06042.

[72] J. Gao, L. Harland-Lang and J. Rojo, *Phys. Rept.* 742 (2018) 1–121, arXiv:1709.04922.

[73] S. Forte, E. Laenen, P. Nason and J. Rojo, *Nucl. Phys.* B834 (2010) 116–162, arXiv:1001.2312.

[74] V. Bertone, R. Gauld and J. Rojo, *JHEP* 01 (2019) 217, arXiv:1808.02034.

[75] K. J. Eskola, P. Paakkinen, H. Paukkunen and C. A. Salgado, *Eur. Phys. J.* C77 (2017) 163, arXiv:1612.05741.

[76] B. L. Ioffe, V. S. Fadin and L. N. Lipatov, *Quantum chromodynamics: Perturbative and nonperturbative aspects*, vol. 30. Cambridge Univ. Press, 2010. http://www.cambridge.org/de/knowledge/isbn/item2710695.

[77] J. Collins, *Camb. Monogr. Part. Phys. Nucl. Phys. Cosmol.* 32 (2011) 1–624.

[78] J. C. Collins, D. E. Soper and G. F. Sterman, *Adv. Ser. Direct. High Energy Phys.* 5 (1989) 1–91, arXiv:hep-ph/0409313.

[79] M. Arneodo, *Phys. Rept.* 240 (1994) 301–393.

[80] D. F. Geesaman, K. Saito and A. W. Thomas, *Ann. Rev. Nucl. Part. Sci.* 45 (1995) 337–390.

[81] H. Paukkunen, *PoS* HardProbes2018 (2018) 014, arXiv:1811.01976.

[82] K. J. Eskola, H. Paukkunen and C. A. Salgado, *JHEP* 04 (2009) 065, arXiv:0902.4154.

[83] D. de Florian, R. Sassot, P. Zurita and M. Stratmann, *Phys. Rev.* D85 (2012) 074028, arXiv:1112.6324.

[84] K. Kovarik *et al.*, *Phys. Rev.* D93 (2016) 085037, arXiv:1509.00792.

[85] H. Khanpour and S. Atashbar Tehrani, *Phys. Rev.* D93 (2016) 014026, arXiv:1601.00939.

[86] NNPDF Collaboration, R. Abdul Khalek, J. J. Ethier and J. Rojo, *Eur. Phys. J.* C79 (2019) 471, arXiv:1904.00018.

[87] N. Armesto, *J. Phys.* G32 (2006) R367–R394, arXiv:hep-ph/0604108.

[88] K. J. Eskola, P. Paakkinen and H. Paukkunen, *Eur. Phys. J.* C79 (2019) 511, arXiv:1903.09832.

[89] N. Armesto, H. Paukkunen, J. M. Penín, C. A. Salgado and P. Zurita, *Eur. Phys. J.* C76 (2016) 218, arXiv:1512.01528.

[90] A. Kusina, F. Lyonnet, D. B. Clark, E. Godat, T. Jezo, K. Kovarik, F. I. Olness, I. Schienbein and J. Y. Yu, *Eur. Phys. J.* C77 (2017) 488, arXiv:1610.02925.

[91] L. Frankfurt, V. Guzey and M. Strikman, *Phys. Rept.* 512 (2012) 255–393, arXiv:1106.2091.

[92] N. Armesto, A. Capella, A. B. Kaidalov, J. Lopez-Albacete and C. A. Salgado, *Eur. Phys. J.* C29 (2003) 531–540, arXiv:hep-ph/0304119.

[93] Z. Citron *et al.*, "Future physics opportunities for high-density QCD at the LHC with heavy-ion and proton beams," in *HL/HE-LHC Workshop: Workshop on the Physics of HL-LHC, and Perspectives at HE-LHC Geneva, Switzerland, June 18-20, 2018*. 2018. arXiv:1812.06772.

[94] A. Accardi *et al.*, *Eur. Phys. J.* A52 (2016) 268, arXiv:1212.1701.

[95] M. Klein, *EPJ Web Conf.* 112 (2016) 03002.

[96] J. Blumlein and M. Klein, "Kinematics and resolution at future e p colliders," in *1990 DPF Summer Study on High-energy Physics: Research Directions for the Decade (Snowmass 90) Snowmass, Colorado, June 25-July 13, 1990*, pp. 549–551. 1990.

[97] LHeC study Group Collaboration, H. Paukkunen, *PoS* DIS2017 (2018) 109, arXiv:1709.08342.

[98] E. C. Aschenauer, S. Fazio, M. A. C. Lamont, H. Paukkunen and P. Zurita, *Phys. Rev.* D96 (2017) 114005, arXiv:1708.05654.

[99] LHCb Collaboration, R. Aaij *et al.*, *JHEP* 10 (2017) 090, arXiv:1707.02750.

[100] LHCb Collaboration, R. Aaij *et al.*, *Phys. Rev.* D99 (2019) 052011, arXiv:1902.05599.

[101] K. J. Eskola, I. Helenius, P. Paakkinen and H. Paukkunen, arXiv:1906.02512.

[102] I. Helenius, K. J. Eskola and H. Paukkunen, *JHEP* 09 (2014) 138, arXiv:1406.1689.

[103] J. Pumplin, D. Stump, R. Brock, D. Casey, J. Huston, J. Kalk, H. L. Lai and W. K. Tung, *Phys. Rev.* D65 (2001) 014013, arXiv:hep-ph/0101032.

[104] N. Armesto, "Nuclear pdfs." 2nd FCC Physics Workshop (CERN, January 15th-19th 2018), 2018.

[105] N. Armesto, *PoS* HardProbes2018 (2019) 123.

[106] FCC Collaboration, A. Abada *et al.*, *Eur. Phys. J.* C79 (2019) 474.

[107] S. Alekhin *et al.*, *Eur. Phys. J.* C75 (2015) 304, arXiv:1410.4412.

[108] H. Mäntysaari and B. Schenke, *Phys. Lett.* B772 (2017) 832–838, arXiv:1703.09256.

[109] T. Lappi and H. Mantysaari, *Phys. Rev.* C87 (2013) 032201, arXiv:1301.4095.

[110] H. Mäntysaari and B. Schenke, *Phys. Rev. Lett.* 117 (2016) 052301, arXiv:1603.04349.

[111] H. Mäntysaari and B. Schenke, *Phys. Rev.* D94 (2016) 034042, arXiv:1607.01711.

[112] Y. V. Kovchegov and E. Levin, *Camb. Monogr. Part. Phys. Nucl. Phys. Cosmol.* 33 (2012) 1–350.

[113] F. Gelis, E. Iancu, J. Jalilian-Marian and R. Venugopalan, *Ann. Rev. Nucl. Part. Sci.* 60 (2010) 463–489, arXiv:1002.0333.

[114] C. Marquet, M. R. Moldes and P. Zurita, *Phys. Lett.* B772 (2017) 607–614, arXiv:1702.00839.

[115] N. N. Nikolaev, B. G. Zakharov and V. R. Zoller, *Z. Phys.* A351 (1995) 435–446.

[116] L. L. Frankfurt and M. I. Strikman, *Phys. Lett.* B382 (1996) 6–12.

[117] H. Kowalski, T. Lappi, C. Marquet and R. Venugopalan, *Phys. Rev.* C78 (2008) 045201, arXiv:0805.4071.

[118] A. H. Mueller and H. Navelet, *Nucl. Phys.* B282 (1987) 727–744.

[119] M. Deak, F. Hautmann, H. Jung and K. Kutak, *Eur. Phys. J.* C72 (2012) 1982, arXiv:1112.6354.

[120] J. L. Albacete and C. Marquet, *Phys. Rev. Lett.* 105 (2010) 162301, arXiv:1005.4065.

[121] A. Stasto, S.-Y. Wei, B.-W. Xiao and F. Yuan, *Phys. Lett.* B784 (2018) 301–306, arXiv:1805.05712.

[122] A. van Hameren, P. Kotko, K. Kutak, C. Marquet, E. Petreska and S. Sapeta, *JHEP* 12 (2016) 034, arXiv:1607.03121. [Erratum: JHEP02,158(2019)].

[123] N. Armesto and E. Scomparin, *Eur. Phys. J. Plus* 131 (2016) 52, arXiv:1511.02151.

[124] W. Busza, K. Rajagopal and W. van der Schee, *Ann. Rev. Nucl. Part. Sci.* 68 (2018) 339–376, arXiv:1802.04801.

[125] P. Romatschke and U. Romatschke, *Relativistic Fluid Dynamics In and Out of Equilibrium*. Cambridge Monographs on Mathematical Physics. Cambridge University Press, 2019. arXiv:1712.05815. https://www.cambridge.org/academic/subjects/physics/theoretical-physics-and-mathematical-physics/relativistic-fluid-dynamics-and-out-equilibrium-and-applications-relativistic-nuclear-collisions?format=HB&isbn=9781108483681.

[126] P. Romatschke, *Eur. Phys. J.* C77 (2017) 21, arXiv:1609.02820.

[127] C. Loizides, *Nucl. Phys.* A956 (2016) 200–207, arXiv:1602.09138.

[128] B. Schenke, *Nucl. Phys.* A967 (2017) 105–112, arXiv:1704.03914.

[129] Y. Mehtar-Tani, J. G. Milhano and K. Tywoniuk, *Int. J. Mod. Phys.* A28 (2013) 1340013, arXiv:1302.2579.

[130] A. Andronic *et al.*, *Eur. Phys. J.* C76 (2016) 107, arXiv:1506.03981.

[131] D. d'Enterria, A. Morsch and P. Crochet (eds.), *Proceedings, 9th International Conference on Hard and Electromagnetic Probes of High-Energy Nuclear Collisions: Hard Probes 2018 (HP2018)*, vol. HardProbes2018, SISSA. SISSA, 2018. https://pos.sissa.it/345.

[132] H. A. Andrews *et al.*, arXiv:1808.03689.

[133] ALICE Collaboration, B. B. Abelev *et al.*, *Phys. Lett.* B734 (2014) 314–327, arXiv:1311.0214.

[134] H. Song, S. A. Bass, U. Heinz, T. Hirano and C. Shen, *Phys. Rev. Lett.* 106 (2011) 192301, arXiv:1011.2783. [Erratum: Phys. Rev. Lett.109,139904(2012)].

[135] H. Niemi, K. J. Eskola and R. Paatelainen, *Phys. Rev.* C93 (2016) 024907, arXiv:1505.02677.

[136] J. Liu, C. Shen and U. Heinz, *Phys. Rev.* C91 (2015) 064906, arXiv:1504.02160. [Erratum: Phys. Rev.C92,no.4,049904(2015)].

[137] B. Schenke, P. Tribedy and R. Venugopalan, *Phys. Rev. Lett.* 108 (2012) 252301, arXiv:1202.6646.

[138] J.-Y. Ollitrault, A. M. Poskanzer and S. A. Voloshin, *Phys. Rev.* C80 (2009) 014904, arXiv:0904.2315.

[139] STAR Collaboration, J. Adams *et al.*, *Phys. Rev.* C72 (2005) 014904, arXiv:nucl-ex/0409033.

[140] STAR Collaboration, B. I. Abelev *et al.*, *Phys. Rev.* C79 (2009) 034909, arXiv:0808.2041.

[141] CMS Collaboration, A. M. Sirunyan *et al.*, arXiv:1905.01486.

[142] V. Guzey and M. Zhalov, *JHEP* 10 (2013) 207, arXiv:1307.4526.

[143] J. G. Contreras, *Phys. Rev.* C96 (2017) 015203, arXiv:1610.03350.

[144] V. Guzey and M. Klasen, *Eur. Phys. J.* C79 (2019) 396, arXiv:1902.05126.

[145] ATLAS Collaboration, M. Aaboud *et al.*, *Phys. Rev. Lett.* 121 (2018) 212301, arXiv:1806.08708.

[146] ATLAS Collaboration, M. Aaboud *et al.*, *Phys. Rev.* C100 (2019) 034903, arXiv:1901.10440.

[147] ATLAS Collaboration, T. A. collaboration, .

[148] A. Badea, A. Baty, P. Chang, G. M. Innocenti, M. Maggi, C. Mcginn, M. Peters, T.-A. Sheng, J. Thaler and Y.-J. Lee, arXiv:1906.00489.

[149] ZEUS Collaboration, I. Abt, *PoS* DIS2019 (2019) 113.

[150] R. Aaij *et al.*, "Expression of Interest for a Phase-II LHCb Upgrade: Opportunities in flavour physics, and beyond, in the HL-LHC era," CERN-LHCC-2017-003, CERN, Geneva, Feb 2017. http://cds.cern.ch/record/2244311.

[151] J. L. Abelleira Fernandez *et al.*, *Journal of Physics G: Nuclear and Particle Physics* 39 (2012) 075001. https://doi.org/10.1088/0954-3899/39/7/075001.

[152] O. Brüning, "Accelerator design." Presented at the lhec workshop, June 2015.

[153] A. Klein, M. and. Stocchi, "PERLE: A High Power Energy Recovery Facility for Europe A contribution to the Update of the European Strategy on Particle Physics," CERN-ACC-NOTE-2018-0086, CERN, Geneva, 2018.

[154] I. Apollinari, G. and. Bejar Alonso, O. Brüning, P. Fessia, M. Lamont, L. Rossi and L. Tavian, "High-Luminosity Large Hadron Collider (HL-LHC), Technical Design Report V.0.1," CERN-2017-007-M, CERN, Geneva, 2017.

[155] D. S. D. Pellegrini, A. Latina and S. Bogacz, *Phys. Rev. ST-AB* 121004 (2015) .

[156] S. B. et al, *ICFA Beam Dynamics Newsletter* 71 (2017) 135–144.

[157] G. Hoffstaetter and I. Bazarov, *Phys. Rev. ST-AB* 7 (2004) .

[158] , *Reference Design* (2012) . www.jlab.org/physics/GeV/accelerator.

[159] D. Pellegrini, *Ph.D. Thesis, EPFL, Switzerland* (2016) .

[160] J. Schwinger, *Report No. LBNL-39088,* (1996) .

[161] R. Calaga and E. Jensen, "A Proposal for an ERL Test Facility at CERN," in *Proceedings, 4th International Particle Accelerator Conference (IPAC 2013): Shanghai, China, May 12-17, 2013*, p. WEPWO049. 2013. http://JACoW.org/IPAC2013/papers/wepwo049.pdf.

[162] F. Marhauser, "Cost Rationales for an SRF Proton Linac," in *Proceedings, 5th International Particle Accelerator Conference (IPAC 2014): Dresden, Germany, June 15-20, 2014*, p. THPME053. 2014. http://jacow.org/IPAC2014/papers/thpme053.pdf.

[163] F. Marhauser, "Recent results on a multi-cell 802 mhz bulk nb cavity." Presented at fcc week 2018, https://indico.cern.ch/event/656491/contributions/2932251/attachments/1629681/2597650/5_cell_Cavity_Marhauser.pdf, 2018.

[164] A. T. H.P. Bluem, D. Dowell and L. Young, "High brightness thermionic electron gun performance," in *Proceedings of ERL2011*, pp. 30–35. Association for Computing Machinery, Tsukuba, Japan, 2011. https://accelconf.web.cern.ch/AccelConf/ERL2011/papers/proceed.pdf.

[165] F. Sannibale, K. Baptiste, C. Cork, J. Corlett, M. Decool, S. D. Santis, M. Dickinson, L. Doolittle, J. Doyle, J. Feng, D. Filippetto, D. Gibson, S. Giermann, G. Harris, G. Huang, M. Johnson, M. K. andT. Kramasz, S. Kwiatkowski, D. Leitner, R. Lellinger, R. Li, C. Mitchell, V. Moroz, J. Nasiatka, W. Norum, H. Padmore, C. Pagani, G. Portmann, H. Qian, H. Rasool, J. Schmerge, D. Sertore, D. Syversrud, T. Vecchione, M. Vinco, S. Virostek, R. Wells, F. Zhou and M. Zolotorev, "The vhf-gun, the lbnl high-brightness electron photo-injector for mhz-class repetition-rate applications∗," in *High-Brightness Sources and Light-Driven Interactions*, p. ET1A.1. Optical Society of America, 2016. http://www.osapublishing.org/abstract.cfm?URI=EUVXRAY-2016-ET1A.1.

[166] Z. Wang, Q. Gu, G. Wang and M. Zhao, "Injector Physics Design at SHINE," in *Proc. 10th International Particle Accelerator Conference (IPAC'19), Melbourne, Australia, 19-24 May 2019*, no. 10 in International Particle Accelerator Conference, pp. 1801–1803. JACoW Publishing, Geneva, Switzerland, Jun. 2019. http://jacow.org/ipac2019/papers/tuprb053.pdf. https://doi.org/10.18429/JACoW-IPAC2019-TUPRB053.

[167] G. Shu, Y. Chen, S. Lal, H. Qian, H. Shaker and F. Stephan, "FIRST DESIGN STUDIES OF A NC CW RF GUN FOR EUROPEAN XFEL," in *Proc. 10th International Particle Accelerator Conference (IPAC'19), Melbourne, Australia, 19-24 May 2019*, no. 10 in International Particle Accelerator Conference, pp. 1698–1701. JACoW Publishing, Geneva, Switzerland, Jun. 2019. http://jacow.org/ipac2019/papers/tuprb010.pdf. https://doi.org/10.18429/JACoW-IPAC2019-TUPRB010.

[168] J. Teichert, A. Arnold, H. Büttig, M. Justus, T. Kamps, U. Lehnert, P. Lu, P. Michel, P. Murcek, J. Rudolph, R. Schurig, W. Seidel, H. Vennekate, I. Will and R. Xiang, *Nuclear Instruments and Methods in Physics Research Section A: Accelerators, Spectrometers, Detectors and Associated Equipment* 743 (2014) 114 – 120. http://www.sciencedirect.com/science/article/pii/S016890021400014X.

[169] B. Dunham, J. Barley, A. Bartnik, I. Bazarov, L. Cultrera, J. Dobbins, G. Hoffstaetter, B. Johnson, R. Kaplan, S. Karkare, V. Kostroun, Y. Li, M. Liepe, X. Liu, F. Loehl, J. Maxson, P. Quigley, J. Reilly, D. Rice, D. Sabol, E. Smith, K. Smolenski, M. Tigner, V. Vesherevich, D. Widger and Z. Zhao, *Applied Physics Letters* 102 (2013) 034105, https://doi.org/10.1063/1.4789395. https://doi.org/10.1063/1.4789395.

[170] B. Hounsell, W. Kaabi, M. Klein, B. Militsyn and C. Welsch, "Optimisation of the PERLE injector," in *Proceedings, ERL19*. 2019.

[171] N. Nishimori, R. Nagai, S. Matsuba, R. Hajima, M. Yamamoto, T. Miyajima, Y. Honda, H. Iijima, M. Kuriki and M. Kuwahara, *Applied Physics Letters* 102 (2013) 234103, https://doi.org/10.1063/1.4811158. https://doi.org/10.1063/1.4811158.

[172] B. Hounsell, W. Kaabi, M. Klein, B. Militsyn, T. Noakes and C. Welsch, "Re-optimisation of the ALICE Gun Upgrade Design for the 500-pC Bunch Charge Requirements of PERLE," in *Proceedings, 10th International Particle Accelerator Conference (IPAC2019): Melbourne, Australia, May 19-24, 2019*, p. TUPTS066. 2019.

[173] A. Zaltsman and R. Lambiase, *Proceedings of the 24-th Particle Accelerator Conference, PAC-2011, TUP125* (2011) .

[174] B. Parker, "Latest Developments and Progress on the IR magnet design." presented at the LHeC and FCC-eh Workshop, Sept 2017.

[175] E. Cruz-Alaniz, D. Newton, R. Tomás and M. Korostelev, *Phys. Rev. ST Accel. Beams* 18 (2015) 111001. https://link.aps.org/doi/10.1103/PhysRevSTAB.18.111001.

[176] B. Parker, "Superconducting Magnet Concepts for Electron Hadron Collider IRs." Presented at the electrons for the lhc - lhec/fcceh and perle workshop, Sept 2018.

[177] R. Martin and R. Tomás Garcia, "Length optimization of the detector region dipoles in LHeC and FCC-eh," CERN-ACC-2018-0042, CERN, Geneva, Oct 2018. http://cds.cern.ch/record/2644892.

[178] S. Fartoukh, *Phys. Rev. ST Accel. Beams* 16 (2013) 111002. https://link.aps.org/doi/10.1103/PhysRevSTAB.16.111002.

[179] "Lattice repository." https://gitlab.cern.ch/lhec-optics/lhec-lattice, 2019.

[180] A. Gaddi, "Installation Issues of eh Detectors (LHC and FCC)." Presented at the lhec and fcc-eh workshop, Sept 2017.

[181] A. Gaddi. Private communication, Jan 2019.

[182] R. Bruce, C. Bracco, R. De Maria, M. Giovannozzi, S. Redaelli, R. Tomás Garcia, F. M. Velotti and J. Wenninger, "Updated parameters for HL-LHC aperture calculations for proton beams," CERN-ACC-2017-0051, CERN, Geneva, Jul 2017. https://cds.cern.ch/record/2274330.

[183] R. De Maria *et al.*, "HLLHCV1.3 Optics repository." http://lhc-optics.web.cern.ch/lhc-optics/HLLHCV1.3/.

[184] E. Cruz-Alaniz, R. Martin and R. Tomás, "LHeC optics with $\beta^* = 10$ cm and $L^* = 15$ m," CERN-XXX-2019-XXX, CERN, Geneva, 2019.

[185] Sixtrack web site: http://sixtrack.web.cern.ch/SixTrack/.

[186] E. Cruz-Alaniz, J. L. Abelleira, L. van Riesen-Haupt, A. Seryi, R. Martin and R. Tomás, "Methods to increase the dynamic aperture of the fcc-hh lattice," in *Proc. of International Particle Accelerator Conference (IPAC'18), Vancouver, Canada, 2018*, no. 1 in International Particle Accelerator Conference, pp. 3593–3596. JACoW, Geneva, Switzerland, May 2018. https://accelconf.web.cern.ch/AccelConf/ipac2018/papers/thpak145.pdf.

[187] F. Zimmermann *et al.*, "Interaction-Region Design Options for a Linac-Ring LHeC," in *Proc. of International Particle Accelerator Conference (IPAC'10), Kyoto, Japan, May 23-28, 2010*, no. 1 in International Particle Accelerator Conference, pp. 1605–1607. JACoW, Geneva, Switzerland, May 2010. http://accelconf.web.cern.ch/AccelConf/IPAC10/papers/tupeb037.pdf.

[188] J. L. Abelleira, H. Garcia, R. Tomás and F. Zimmermann, "Final-Focus Optics for the LHeC Electron Beam Line," in *Proc. of International Particle Accelerator Conference (IPAC'12), New Orleans, Louisiana, USA, May 20-25, 2012*, no. 1 in International Particle Accelerator Conference, pp. 1861–1863. JACoW, Geneva, Switzerland, May 2012. http://accelconf.web.cern.ch/AccelConf/IPAC10/papers/tupeb037.pdf.

[189] G. Arduini *et al.*, "Energy frontier DIS at CERN: the LHeC and the FCCeh, PERLE." https://pos.sissa.it/316/183/pdf.

[190] R. Tomás, "LHeC interaction region." Presented at dis 2012 workshop, https://indico.cern.ch/event/153252/contributions/1396962/attachments/160393/226540/SLIDES.pdf, 2012.

[191] S. Russenschuck, *Field computation for accelerator magnets: analytical and numerical methods for electromagnetic design and optimization*. Wiley, Weinheim, 2010. https://cds.cern.ch/record/1221810.

[192] C. Tennant, "Energy Recovery Linacs," in *Challenges and Goals for Accelerators in the XXI Century*, O. Brüning and S. Myers (eds.). World Scientific, 2016.

[193] C. Tennant, "Progress at the Jefferson Laboratory FEL," in *Particle accelerator. Proceedings, 23rd Conference, PAC'09, Vancouver, Canada, May 4-8, 2009*, p. TH3PBI03. 2010. http://www1.jlab.org/Ul/publications/view_pub.cfm?pub_id=8641.

[194] G. H. Hoffstaetter and I. V. Bazarov, *Phys. Rev. ST Accel. Beams* 7 (2004) 054401. https://link.aps.org/doi/10.1103/PhysRevSTAB.7.054401.

[195] D. R. Douglas, K. C. Jordan, L. Merminga, E. G. Pozdeyev, C. D. Tennant, H. Wang, T. I. Smith, S. Simrock, I. V. Bazarov and G. H. Hoffstaetter, *Phys. Rev. ST Accel. Beams* 9 (2006) 064403. https://link.aps.org/doi/10.1103/PhysRevSTAB.9.064403.

[196] S. Di Mitri, M. Cornacchia and S. Spampinati, *Phys. Rev. Lett.* 110 (2013) 014801. https://link.aps.org/doi/10.1103/PhysRevLett.110.014801.

[197] M. G. Fedurin, D. Kayran, V. Yakimenko, A. V. Fedotov, V. Litvinenko and P. Muggli, *Conf. Proc.* C110328 (2011) 1677–1679.

[198] S. Heifets, G. Stupakov and S. Krinsky, *Phys. Rev. ST Accel. Beams* 5 (2002) 064401. https://link.aps.org/doi/10.1103/PhysRevSTAB.5.064401.

[199] Z. Huang and K.-J. Kim, *Phys. Rev. ST Accel. Beams* 5 (2002) 074401. https://link.aps.org/doi/10.1103/PhysRevSTAB.5.074401.

[200] S. Di Mitri and M. Cornacchia, *EPL (Europhysics Letters)* 109 (2015) 62002. https://app.dimensions.ai/details/publication/pub.1064226665.

[201] C.-Y. Tsai, D. Douglas, R. Li and C. Tennant, *Phys. Rev. Accel. Beams* 19 (2016) 114401. https://link.aps.org/doi/10.1103/PhysRevAccelBeams.19.114401.

[202] C.-Y. Tsai, S. Di Mitri, D. Douglas, R. Li and C. Tennant, *Phys. Rev. Accel. Beams* 20 (2017) 024401. https://link.aps.org/doi/10.1103/PhysRevAccelBeams.20.024401.

[203] D. Douglas *et al.* Jefferson Laboratory Technical Note 12-017, 2012.

[204] R. Alarcon *et al.*, *Phys. Rev. Lett.* 111 (2013) 164801. https://link.aps.org/doi/10.1103/PhysRevLett.111.164801.

[205] T. Powers and C. Tennant, "Implications of incomplete energy recovery in srf-based energy recovery linacs," in *Proceedings of the 2007 ICFA Workshop on Energy Recovery Linacs, Daresbury, UK*, p. 75. 2007.

[206] T. Powers, "Control of Microphonics for Narrow Control Bandwidth Cavities," Talk presented at the 2017 International Conference on RF Superconductivity, Lanzhou, China, 2017.

[207] S. Benson *et al.*, *Conf. Proc.* C070625 (2007) 79.

[208] T. Powers, "Optimization of SRF Linacs," in *Proceedings of the 2013 International Conference on RF Superconductivity, Paris, France*, p. 830. 2013.

[209] P. Williams, "A Staged, Multi-User X-Ray Free Electron Laser and Nuclear Physics Facility based on a Multi-Pass Recirculating Superconducting CW Linac," in *Proc. Future Light Sources 2018, Shanghai.* 2018.

[210] S. Benson *et al.*, "Development of a Bunched-Beam Electron Cooler for the Jefferson Lab Electron-Ion Collider," in *Proceedings, 9th International Particle Accelerator Conference (IPAC 2018), Vancouver, BC Canada*, p. MOPMK015. 2018.

[211] C. Tennant. https://userweb.jlab.org/~tennant/.

[212] C. Tennant, "Analysis of the Baseline PERLE Lattice," Jefferson Laboratory Technical Note 18-031, 2018.

[213] D. Douglas *et al.*, ""Why PERLE?" – Historical Context and Technological Motivation," Jefferson Laboratory Technical Note 18-014, 2018.

[214] G. H. Hoffstaetter *et al.*, "CBETA Design Report, Cornell-BNL ERL Test Accelerator," 2017. arXiv:1706.04245.

[215] T. Satogata *et al.*, "ER@CEBAF: A test of 5-pass energy recovery at CEBAF," Program Advisory Committee Proposal, June 2016.